

7
N65-21775

**FABRICATION AND EXPERIMENTAL EVALUATION OF
COMMON DOMES HAVING WAFFLE-LIKE STIFFENING**

PART I - PROGRAM DEVELOPMENT

**NOVEMBER 1964
DOUGLAS REPORT SM-47742**

**MISSILE & SPACE SYSTEMS DIVISION
DOUGLAS AIRCRAFT COMPANY, INC.
SANTA MONICA/CALIFORNIA**



20

FABRICATION AND EXPERIMENTAL EVALUATION OF COMMON DOMES HAVING WAFFLE-LIKE STIFFENING

PART I - PROGRAM DEVELOPMENT

NOVEMBER 1964
DOUGLAS REPORT SM-47742

PREPARED BY:
R.R. MEYER
R.J. BELLIFANTE

PREPARED UNDER THE SPONSORSHIP OF NASA,
GEORGE C. MARSHALL SPACE FLIGHT CENTER,
(CONTRACT NO. NAS8-11542)



APPROVED BY: H.H. DIXON
CHIEF ENGINEER, ADVANCE STRUCTURES
& MECHANICAL DEPARTMENT

DOUGLAS MISSILE & SPACE SYSTEMS DIVISION

Preceding page blank *ii*

NOTICES

When U. S. Government drawings, specifications, or other data are used for any purpose other than a definitely related Government procurement operation, the Government thereby incurs no responsibility nor any obligation whatsoever; and the fact that the Government thereby incurs no responsibility nor any obligation whatsoever; and the fact that the Government may have formulated, furnished, or in any other way supplied the said drawings, specifications, or other data is not to be regarded by implication or otherwise, as in any manner licensing the holder or any other person or corporation, or conveying any rights or permission to manufacture, use, or sell any patented invention that may in any way be related thereto.

This document may not be reproduced or published in any form in whole or in part without prior approval of the Government.

FOREWORD

This report contains the results of the work performed on a study of "Fabrication and Experimental Evaluation of Common Domes Having Waffle-Like Stiffening" initiated under NASA Contract No. NAS 8-11542. The work is administered under the direction of the Propulsion and Vehicle Engineering Division with Mr. Norman C. Schlemmer (R-PVE-SS) acting as Principal Representative.

The Douglas program was conducted under the direction of Mr. H. H. Dixon, Chief, Structures Branch, Advance Space Technology with Mr. R. H. Christensen acting as Study Director.

Mr. R. R. Meyer was the principal investigator of the program and was assisted in the theoretical and analytical phases of the program by Mr. R. J. Bellinfante.

The authors wish to acknowledge the assistance of Mr. H. P. Adam and Mr. P. A. King of the Experimental Stress Analysis Laboratory for their work in the fabrication and testing of the plastic models in the experimental program. Messrs. R. T. Pfaffenberger and T. J. Murphy were responsible for the fabrication and test of the aluminum waffle stiffened dome.

SUMMARY

2/17/75

Experimental and analytical techniques were used to determine the minimum weight shape and stiffening configuration for doubly curved shells subjected to external buckling pressures.

Monocoque shapes considered were spherical, ellipsoidal and torispherical having clamped boundary conditions.

The stiffening configurations considered were meridional, circumferential, combined meridional and circumferential, square-grid and geodesic stiffened domes.

The theory was supported in all phases by experimental tests on plastic models and was concluded by a large scale aluminum test on the best stiffened configuration. It was concluded from this study that:

The minimum weight dome shape for a condition of external pressure is a spherical cap with a half-opening angle of $\theta = 60^\circ$.

The experimental data for the buckling of monocoque spherical domes shows excellent correlation with the theory of Huang.

The geodesic rib-stiffened dome is the most favorable reinforcement arrangement for spherical domes subjected to external pressure.

The geodesic rib-stiffened dome is approximately 30 - 40% heavier than an optimum honeycomb sandwich dome for an external loading condition. However, other loading conditions should be investigated before a final strength to weight comparison can be made for common dome applications.

Huang

TABLE OF CONTENTS

PART I - PROGRAM DEVELOPMENT

	Page
NOTICES	
FOREWORD	
SUMMARY	
TABLE OF CONTENTS	
CHAPTER I - PROBLEM DISCUSSION AND RESULTS OF INVESTIGATION	1
Introduction	1
Phase I - Shape Optimization	1
Monocoque History	1
Results of Optimization Analysis	4
Phase II - Tests to Confirm Shape Optimization	4
Material Property Tests	4
Model Fabrication	6
Test Description	6
Individual Shapes and Results	6
Phase III - Stiffening Optimization	7
Stiffening History	7
Stiffening Theory	8
Geodesic Stiffening	8
General Instability Pressure	8
Panel Instability	9
Rib Crippling	9
Optimum Design	10
Evaluation of Stiffened Results	11
Fabrication of Stiffened Domes	20
Stiffened Model Test Results - Room Temperature	20
Stiffened Model Test Results - Thermal Gradient	20
Phase IV - Metal Dome Fabrication and Test Results	21
Test Description	21
Test Results	21
Conclusions	22

Preceding page blank

	Page
CHAPTER II - MONOCOQUE SHAPE OPTIMIZATION	24
Spherical Cap	24
Thrust Ring of Spherical Cap	27
Ellipsoidal Dome	36
Torispherical Dome	38
Zero-Hoop Stress Dome	41
CHAPTER III - STIFFENED SPHERICAL DOMES UNDER EXTERNAL PRESSURE	45
Meridional Stiffening	45
Introduction	45
Rib Instability	45
Panel Instability	47
Optimum Design	51
Circumferential Stiffening	57
Introduction	57
Shell Segment Instability	57
Ring Instability	62
Optimum Design	64
CHAPTER IV - GEODESIC RIB STIFFENED SPHERICAL DOMES	71
Introduction	71
Basic Relations	71
Rigidity Properties of Equilateral Triangular Rib Grids	78
Bending Rigidity	90
Extensional Rigidity	92
Weight of Construction	92
Rib and Plate Stresses for Pressure Loading	95
Direction of Rib and Plate Stresses	96
Thermal Stresses	99
Primary Modes of Failure	102
General Instability	102
Rib Crippling	105
Panel Buckling	106
Justification for Plate Buckling Approximation	107
Thermal and Residual Stress Considerations	109
Stresses Due to Hot Spots	110
Optimization	113

	Page
General Principles of Grid Optimization	113
Optimum Dimensions	115
Solution of the Optimization Equations	116
Off-Optimum Design	121
Solution for Ribs of Non-Critical Width	121
Other Boundary Conditions for Plate Buckling	123
CHAPTER V - EXPERIMENTAL DATA	126
Plastic Model Testing	126
Model Material	126
Material Property Tests	126
Modulus of Elasticity	126
Strain Rate and Creep	126
Poisson's Ratio	129
Fabrication of Domes	129
Test Set-up	134
Test Procedure - Room Temperature	135
Test Procedure - Thermal Gradient	135
Monocoque Test Results	135
Spherical Domes	135
Ellipsoidal Dome	136
Torispherical Dome	136
Stiffened Spherical Domes - Room Temperature	151
Meridional Stiffened Domes	151
Circumferential Stiffened Dome	164
Combined Meridional and Circumferential Stiffened Dome	166
Square-Grid Stiffened Dome	166
Geodesic Stiffened Domes	168
Stiffened Domes - Thermal Gradient Tests	173
Metal Dome Testing	174
Fabrication of Dome	174
Test Set-up	181
Test Procedure	181
Specimen Design	181
Test Results	183
REFERENCES	188

LIST OF ILLUSTRATIONS

FIGURE	TITLE	PAGE
1.1	Buckling of Monocoque Spherical Caps - Experimental Data	3
1.2	Weight Index of Monocoque Shapes	5
1.3	Monocoque Dome Configurations - Buckling Patterns	12
1.4	Buckling of Monocoque Spherical Caps - Comparison of Tests with Huang's Theory	15
1.5	Stiffened Dome Configurations - Buckling Patterns	16
1.6	Weight Comparison of Deep Spherical Domes Under External Pressure	23
2.1	Edge Forces on Spherical Cap	24
2.2	Effect of Ring Weight Requirement on Spherical Caps	35
2.3	Sketch of Ellipsoidal Dome	36
2.4	Sketch of Torispherical Dome	38
2.5	Sketch of Zero-Hoop Stress Dome	41
3.1	Load Distribution for Meridionally Stiffened Dome	45
3.2	Panel Radius Versus Number of Ribs	49
3.3	Local Panel Buckling of Meridionally Stiffened Spherical Caps Under External Pressure	52
3.4	Index of Structural Efficiency of Meridional Stiffened Domes	56
3.5	Estimated Effect of Curvature	60
3.6	Efficiency of Circumferentially Stiffened Spherical Dome - $\theta = 60^\circ$	70
4.1	Icosahedron Inscribed in Sphere	71
4.2	Symmetric Grid Layout	78
4.3	Displacements of Triangular Grid Pattern	79

LIST OF ILLUSTRATIONS (con't)

FIGURE	TITLE	PAGE
4.4	Distortion of Triangular Grid	83
4.5	Equivalent Tee-Shaped Cross Section	89
4.6	Equivalent Bending Rigidity	90
4.7	Division of Pattern for Weight Consideration	92
4.8	Typical Section Through Panel	92
4.9	Typical Segment Showing Rib and Plate	96
4.10	Local Deformation Between Rib and Plate	98
4.11	Loaded Rectangular Panel	105
4.12	Loaded Triangular Panel	106
4.13	Plate Buckling Curve	107
4.14	Free Body of Spherical Cap	111
5.1	Tensile Modulus of Elasticity of Polyvinyl Chloride Versus Thickness	127
5.2	Typical Tensile Stress-Strain Curve (PVC)	128
5.3	Machining Vacuum Mold Cavity Using Hydraulic Tracing Attachment	131
5.4	Completed Spherical Mold and Plastic Dome	132
5.5	Forming Plastic Dome Model	133
5.6	Typical Holding Block Arrangement for Stiffened Domes	137
5.7	Plastic Dome Testing Fixture	138
5.7a	Typical Experimental Arrangement	139
5.8	Sketch of Thermal Gradient Buckling Test Setup	140
5.9	Typical Experimental Arrangement - Thermal Gradient	141
5.10	Location of Displacement Transducers for Monocoque Domes	144

LIST OF ILLUSTRATIONS (con't)

FIGURE	TITLE	PAGE
5.11	Radial Deflections of Spherical Monocoque Domes - #1-S, #2-S	145
5.12	Radial Deflections of Spherical Monocoque Domes - #3-S, #4-S	146
5.13	Radial Deflections of Ellipsoidal Dome - #5-E	147
5.14	Radial Deflections of Ellipsoidal Dome - #6-E	148
5.15	Radial Deflections of Torispherical Dome - #7-E	149
5.16	Buckling of Ellipsoidal Domes - Experimental	150
5.17	Location of Displacement Transducers on #1-G, #2-G and #3-G Geodesic Domes	155
5.18	Location of Displacement Transducers on #1-C and #1-MC Circumferential and Meridional - Circumferential Domes	156
5.19	Location of Displacement Transducers on #1-M, #2-M and #3-M Meridional Domes	157
5.20	Location of Displacement Transducers on #4-M and #1-SG Meridional and Square Grid Stiffened Domes	158
5.21	Radial Deflections for Geodesic Stiffened Domes	159
5.22	Radial Deflections for Circumferential and Meridional - Circumferential Stiffened Domes	160
5.23	Radial Deflections for Meridionally Stiffened Domes	161
5.24	Radial Deflections for Square-Grid Stiffened Dome	162
5.25	Failure of Geodesic and Square-Grid Dome - Thermal Gradient Test	175
5.26	Thermocouple Location for Geodesic and Square-Grid Domes - Thermal Gradient Test	176
5.27	Location of Displacement Transducers on Geodesic and Square-Grid Domes - Thermal Gradient Test	177

LIST OF ILLUSTRATIONS (con't)

FIGURE	TITLE	PAGE
5.28	Radial Deflections for Geodesic and Square-Grid Domes - Thermal Gradient Test	178
5.29	Stress-Strain Diagram for Aluminum Geodesic Dome	179
5.30	Working Drawing of Geodesic Dome Layup	180
5.31	Fabrication of Aluminum Geodesic Dome	184
5.32	Experimental Arrangement for Aluminum Geodesic Dome	185
5.33	Location of Instrumentation - Aluminum Geodesic Dome	186
5.34	Failure of Aluminum Geodesic Dome	187

LIST OF TABLES

TABLE	TITLE	PAGE
1.1	Summary of Experimental Results for Monocoque Domes Under External Pressure	14
1.2	Summary of Experimental Results for Stiffened Domes Under External Pressure	19
2.1	Evaluation of Optimum Angle for Spherical Domes	26
2.2	Zero-Hoop Stress Constants	44
5.1	Plastic Dome Shapes Fabricated	129
5.2	Thickness Measurements of Monocoque Spherical Domes	142
5.3	Thickness Measurements of Ellipsoidal and Torispherical Monocoque Domes	143
5.4	Thickness Measurements of Shells - Stiffened Configurations	154
5.5	Rib Requirements of Circumferential Stiffened Dome	165

CHAPTER I - PROBLEM DISCUSSION AND RESULTS OF INVESTIGATION

INTRODUCTION

The objective of this study was to determine the minimum weight shape and rib stiffening pattern of a common bulkhead subjected to external pressure separating two tandem cryogenic tanks of a space vehicle. The rib stiffened reinforcement concept is a potential replacement candidate for sandwich construction of common domes. The study was prompted by the difficulties in fabrication and inspection techniques currently experienced with sandwich construction.

This effort was divided into four phases. In Phase I, analytical techniques were used to select the least weight monocoque dome shape for subsequent reinforcement studies. Phase II involved corroborations of the Phase I analysis by tests on small scale plastic monocoque spherical, ellipsoidal, and torisphere shapes. Phase III consisted of analysis and tests of stiffened domes under external pressure to optimize the distribution of the reinforcing members on the shell shape selected from Phase I and II studies. Phase IV was a test of a larger aluminum dome fabricated in the best stiffening configuration to verify the plastic dome results.

PHASE I - SHAPE OPTIMIZATION

MONOCOQUE HISTORY

Prior dome buckling investigations were confined to monocoque construction. The first attempt was made by R. Zoelly (reference 1) in a dissertation at Zurich in 1915. From the prebuckled equilibrium deflections of a complete sphere, he assumed a small axisymmetric perturbation shape and determined the load which would maintain either of the two possible equilibrium configurations. Later in 1932, Van der Neut (reference 2) gave a more general solution, considering also unsymmetrical buckling. Unfortunately, tests of domes gave critical pressures which were far below the predicted values. Various theories were advanced to explain the discrepancy. In 1934, Donnell (reference 3) introduced the concept of imperfection in the geometry as a possible cause for discrepancies between test and theory of cylindrical shells. An imperfection parameter was inserted into the equations which resulted in lowered critical pressures. Unfortunately, actual physical measurements of the imperfection parameter could not be made prior to a test.

Then in 1942 Von Karmen and Tsien (reference 4) investigated the problem using a large deflection set of equations for a shallow spherical dome and predicted an upper and lower equilibrium load for the dome under axisymmetric deformation. Little further progress was made until 1960, when Grigolyuk (reference 5) succeeded in obtaining an unsymmetrical solution to the large deflection shallow dome equation. His solution, however,

was theoretical only, and no actual computations were carried out. The final step was made in 1963 by Huang (reference 7), who obtained numerical results for a deformation process starting with a central dimple, followed by a circle of circumferential dimples occurring at a pressure roughly 80% of the value given by Zoelly for a complete sphere. These results were confirmed by Parmeter (reference 6) a year later, in 1964.

The existing experimental buckling data before the initiation of this study, as depicted in Figure 1.1 shows a lack of consistency between various investigators which complicates any attempted correlation with theoretical predictions. The reason for this large scattering of test data may be attributed to the significant influencing factors of imperfections, boundary conditions, residual and prebuckling bending effects (non-linear theory). Where:

1. Imperfections of geometry consist of deviations of the shell midsurface from that of a perfect sphere and variation in thickness. Of these two, the most serious is midsurface spherical deviations of the flat spot type covering regions of dimple size or larger.
2. Boundary conditions which lack rotational symmetry cause edge disturbances which propagate deeply into the shell interior before damping out. Regions of dimple size are stressed to values considerably above the average $pR/2t$ membrane stresses assumed in theory and precipitate premature failure.
3. Residual stresses can effect stability in two ways. First, by causing a release in residual strain energy occasioned by the buckling change of shape, and secondly by causing overstressed regions to become prematurely plastic.
4. Prebuckled bending effects influence the local geometric radii of curvature of the shell in a similar fashion to that of local flat spots with an accompanying drop in the critical pressure. The magnitude of prebuckled bending is greater for very thin shells (generally those with large R/t ratios). This aspect is incorporated in the large deformation theory, but not in the earlier "classical" theory of Zoelly.

As an example of the effects of boundary conditions, Litle, at MIT, (reference 26) fabricated dome specimens with hat-like brims which were clamped to the testing fixture. Since the material was highly elastic, the domes could be retested with the brim removed, and the edge cemented into a ring. The second set of test pressures were 100% higher than the first. Any efforts to correlate such tests with imperfection theory would be misleading. It could be equally misleading, when residual

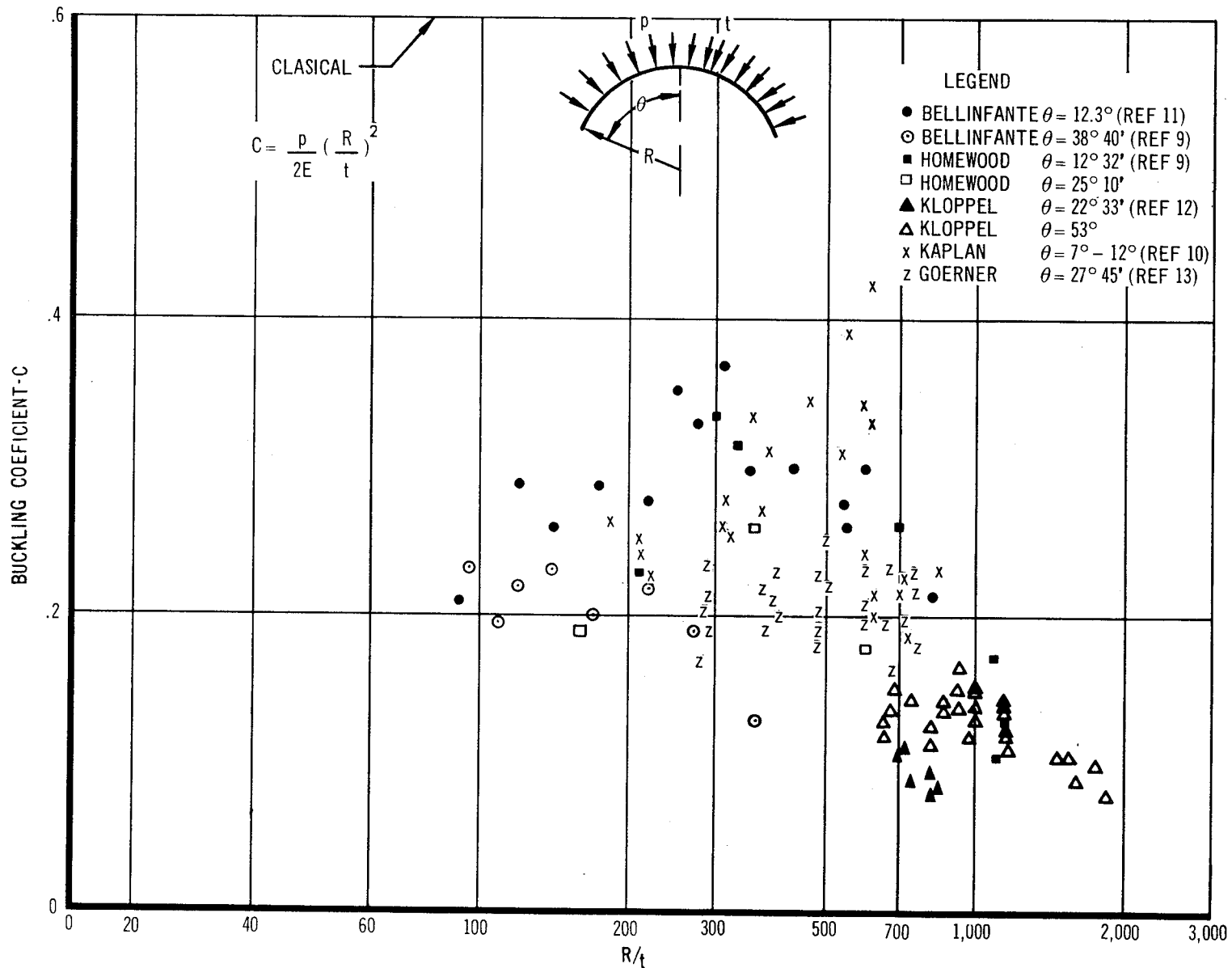


FIGURE 1.1 BUCKLING OF MONOCOQUE SPHERICAL CAPS - EXPERIMENTAL DATA

stresses are high, to compare domes made by essentially different processes, since the magnitude and distribution of residual stresses depend upon the fabrication technique.

RESULTS OF OPTIMIZATION ANALYSIS

The shape is considered to be optimized for the least weight dome configuration to support a given external pressure. Since the dome divides two common tandem tanks, no cylindrical material is considered in the weight comparison. The shapes to be investigated will consist of constant thickness ellipsoids, spherical caps, torispheres and zero-hoop-stress domes. The buckling criteria will be taken as a modified form of the Zoelly equation, i.e., $p = 2CE \left(\frac{t}{R}\right)^2$ where C is an experimentally determined coefficient, and R is the maximum radius of curvature of the dome according to the theory of local stability developed by Mushtari and Galimov, (reference 8).

The optimization analysis is effected by computing a weight index obtained by factoring out the dimensions, the buckling coefficient, and the dome density from the dome weight vs. the a/b (base radius to height) ratio of the dome for the shapes of interest. The results of this weight indexing are shown in Figure 1.2. From the figure, the minimum weight is obtained for spherical cap with an $a/b = \sqrt{3}$, at a half-opening angle $\theta = 60^\circ$.

Although it may appear that a dome shape which frames into a cylinder at an angle will require a large ring to accommodate the hoop thrust from the dome at the juncture with the cylinder, a more careful analysis matching the radial displacements of ring and dome shows that a considerable portion of the hoop load is taken by the dome itself. For this reason, a small ring is adequate. See Chapter II, Figure 2.4.

PHASE II - TESTS TO CONFIRM SHAPE OPTIMIZATION

MATERIAL PROPERTY TESTS

To establish basic material properties of the polyvinyl chloride plastic material used in making experimental models, the following tests were made at the start of the program:

- (a) Elastic Modulus. Standard tensile specimens were fabricated from sheet material supplied by the manufacturer to obtain values in both directions of the sheet, from different areas of the sheet, and different thickness of sheets. The results give an average Young's Modulus of 465,000 psi with a maximum deviation from the mean of 3.5%. Figures 5.1 and 5.2 in Chapter V show the variation in the modulus and a typical stress-strain curve from the experimental results.

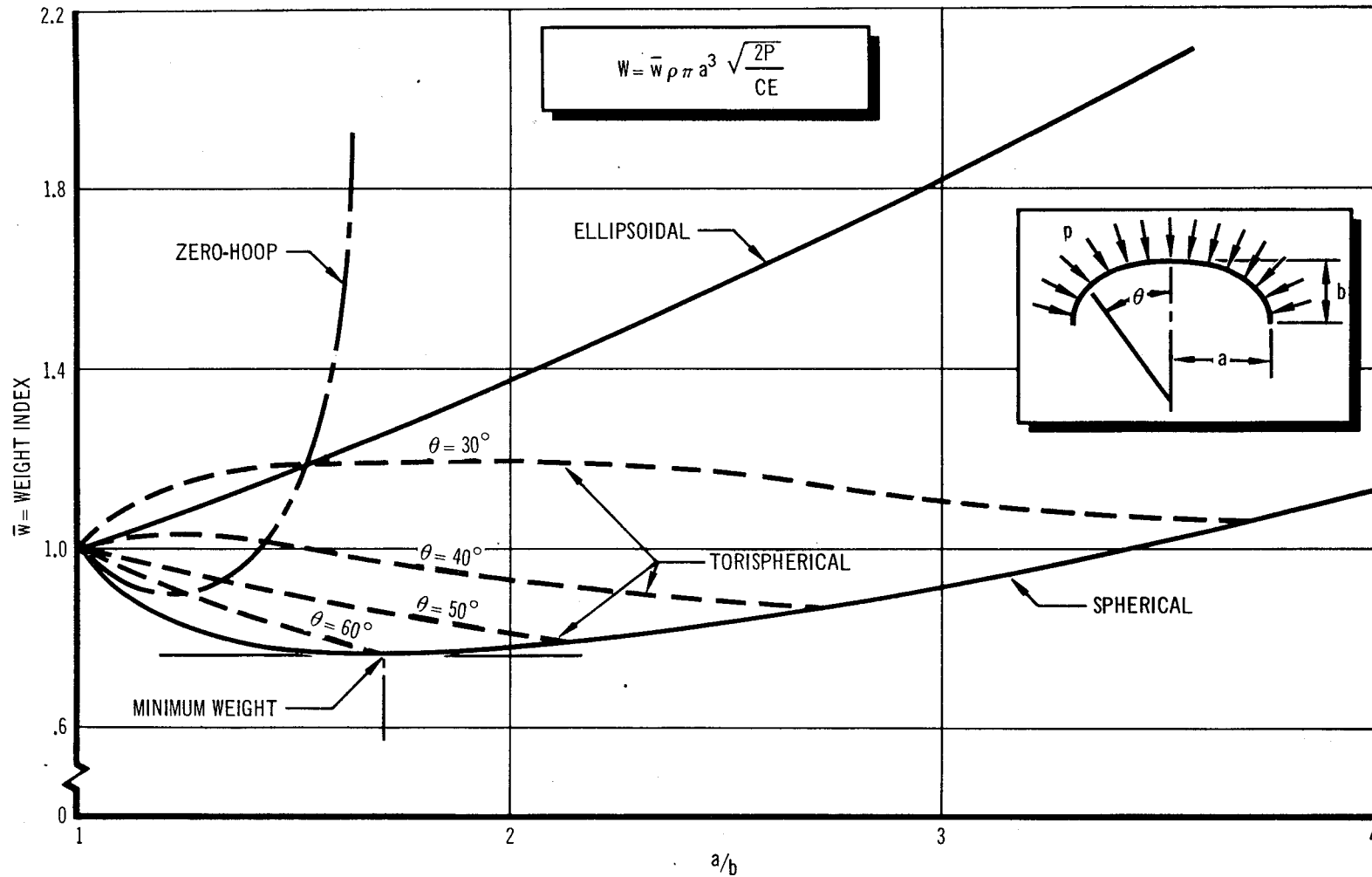


FIGURE 1.2 WEIGHT INDEX OF MONOCOQUE DOMES UNDER UNIFORM EXTERNAL PRESSURE

- (b) Poisson's Ratio. Several tests established Poisson's ratio to be 0.37 with very little scatter.
- (c) Creep. Constant loads were maintained for several minutes at stress levels below the proportional limit, with no detectible creep.

MODEL FABRICATION

The plastic sheets were pressure formed into a metal mold at 240°F, cooled, and finish machined in the mold. They were then cemented into a heavy plastic ring. The physical structure of the plastic is analogous to that of a sponge saturated with water and frozen. Heating melts the water so that the sponge may be formed. The water is then frozen and the resulting new shape is virtually free of residual stresses. This material and fabrication technique minimized the major factors contributing to the test scatter and the reduction of the buckling coefficient.

TEST DESCRIPTION

A wooden block rests between the dome's inner surface and the base of the test fixture with a gap of approximately 1/8" separating them. The purpose of the block is to prevent complete collapse of the specimen so that it may be used for further testing. A vacuum pump evacuates the air beneath the dome thus subjects the dome to an equivalent external differential pressure. The plungers of six transformer displacement transducers are aligned normal to the surface along a dome meridian to measure normal displacement. The output of six pressure gages are recorded with each corresponding transducer and plotted automatically on an X-Y recorder to give pressure vs. displacement for each of the six positions. At the instant of buckling, as recorded on the graphs, the six pressure readings are averaged to obtain the critical pressure.

INDIVIDUAL SHAPES AND RESULTS

- (a) Spherical shapes tested had base radii/height ratios of 1.00, 2.00, 3.33 and 4.78 with a constant base diameter of 16 inches. The buckling coefficients were $C = 0.48; 0.50; 0.50; \text{ and } 0.50$ respectively. The buckling patterns on the models are shown in Figure 1.3.

These buckling coefficients are plotted in Figure 1.4 and demonstrate that C is independent of the R/t and of the half-opening angle of the dome in this range. These tests also show excellent correlation with the shallow shell, clamped edge buckling theory of Huang (reference 7) extrapolated to include deep domes. It is the authors opinion that the large number of dimples appearing on the deep domes are the reason for extrapolated correlation since a shallow shell slice from a deep dome demonstrates the typical deformation pattern.

- (b) Ellipsoidal shapes tested had base radii/height ratios of 2.00 and 3.33. The buckling coefficients, based upon the maximum radius of curvature theory of Mushtari-Galimov (reference 8), were $C = 0.54$ and 0.49 . On the first dome, a single dimple appeared at the apex and was followed by a ring of sausage shaped dimples surrounding it. On the second dome, two adjacent, equal size, circular dimples appeared, with their common point of tangency at the apex. (Figure 1.3).
- (c) A single torisphere with a spherical radius of 11.50 in. and a knuckle radius of 1.71 in. was tested and gave a buckling coefficient $C = 0.33$, based upon the spherical radius. This specimen, with a reduced buckling coefficient, had a single circle of dimples girdling the junction between the spherical cap and the toroidal base, in the vicinity where discontinuity stresses were high (Figure 1.3). It appears that the discontinuity geometry has to be included in buckling correlation of such domes, and that, in general, they will be less efficient than the spherical or ellipsoidal shapes based upon the shape optimization analysis shown in Figure 1.2.

The zero-hoop stress dome was not tested in this program because of its apparent inefficiency based upon the analytical investigation (Figure 1.2) and the need to reduce the scope of experimentation in this program. The results of these tests confirm the optimum shape analysis, showing the lightest weight monocoque dome shape to be the spherical cap with an $a/b = 3$. The reduced buckling coefficient obtained for the torisphere will shift the curve shown in Figure 1.2 relatively higher, and make it less competitive than anticipated. The results of the four monocoque spherical dome tests plotted on the theoretical buckling curve of Huang (Figure 1.4), together with the experimental results of Parmerter (reference 6) shows the scatter of the Parmerter tests compared with the consistency of the present results. Parmerter's copper specimens had some residual stresses and surface roughness which probably accounts for the scatter. Table I shows the summary of the experimental results for the monocoque domes tested in this program.

Considering the mass of conflicting data hitherto existing relating to monocoque dome buckling, it may be said that a remarkable correlation of test and theory has finally been achieved for spherical domes under external pressure.

PHASE III - STIFFENING OPTIMIZATION

Stiffening History

Since the buckling phenomena is considered as a bifurcation of equilibrium mechanism involves a transfer of strain energy from the membrane condition to the bending condition, it was early appreciated that a redistribution of material to increase the bending rigidity of the shell with no increase in

weight should increase the buckling pressure.

The first analysis to include this effect was the stiffened cylinder dissertation of D. D. Dschou in 1935 (Reference 14). Subsequent analysis and testing was confined to shapes of single curvature (cylinders and cones). The major reason for this emphasis was the use of such shapes in aircraft construction.

With the coming of age of the space industry, attention has now been focused upon shapes of double curvature forming end closures of large pressure vessels. Until very recently, the only attack on this problem was experimental. In Germany, Ebner; Kloppel and Jungbluth; and Kloppel and Roos, (References 16, 12, 15 respectively) tested models stiffened by meridional and meridional-circumferential ribs. Semi-empirical analysis was developed for flat meridian-stiffened spherical domes by treating them as arches subjected to triangular loading. Stiffened models of the circumferential, meridian, and waffle-type were also tested by Krenzke at David-Taylor Model Basin. (Reference 17)

Stiffening Theory

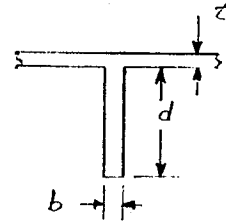
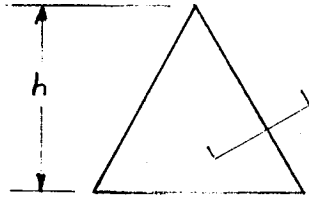
It has been the custom to stiffen spherical domes by placing ribs in the meridian and/or circumferential direction in order to achieve an improvement in the structural weight efficiency compared to monocoque domes. These stiffening configurations suffer from the defect that all directions on a sphere are principal directions and no orientation of the pattern can be assigned. Aware of these possible drawbacks, semi-empirical analyses are developed in this study for meridian and circumferential stiffening, and appropriate optimization procedures are applied. Chapter III contains the details of the analytical investigation. Since a spherical cap, which is the minimum weight shape for monocoque construction, has homogeneous, isotropic, geometrical properties, the major analysis was directed towards obtaining a stiffening concept that is homogeneous and isotropic over the shell mid-surface. A geodesic stiffening configuration, with equilateral triangular grids, meets this criteria of homogeneity and isotropy if the grid spacing is close and the elastic properties are independent of the grid orientation. The increase in efficiency inherent in this geodesic concept is supported by the experimental tests conducted in this study.

A brief outline of the more important aspects of the geodesic stiffening analyses is discussed in the preceding paragraphs. The detailed analysis is presented in Chapter IV.

Geodesic Stiffening

General Instability Pressure - In terms of non-dimensional ratios, the general instability pressure is expressed as

$$p_0 = C_0 E \left(\frac{t}{R}\right)^2 \gamma$$



where

$$\gamma = [3\alpha(1 + \delta)^2 + (1 + \alpha)(1 + \alpha \delta^2)]^{1/2}$$

$$\alpha = \frac{bd}{th}, \quad \delta = \frac{d}{t}$$

In terms of the Zoelly equation for the buckling of a monocoque spherical shell

$$p = C_o E \left(\frac{t^*}{R}\right)^2$$

where

$$t^* = t \sqrt{\gamma}, \quad \gamma > 1$$

Panel Instability - It is assumed that there is no coupling between panel and general instability and that the panels may be conservatively approximated as flat with hinged edges. The panel instability pressure is then:

$$p_1 = C_1 \frac{t}{R} \left(\frac{b}{d}\right)^2 (1 + \alpha) \left[\left(\frac{d}{h}\right)^2 + \bar{C}_1\right]$$

Rib Crippling - Rib crippling assumes no coupling with either panel or general instability, ignores rib curvature and assumes the ribs to be hinge connected to both the panels and to the rib inter-sections. The pressure for rib crippling, on this basis is:

$$p_2 = C_2 \frac{t}{R} \left(\frac{t}{h}\right)^2 (1 + \alpha)$$

Optimum Design - If p_0 , p_1 , and p_2 are continuous, strictly increasing functions of the distributions of material to general, panel and rib crippling modes of failure, it can be shown that the least weight solution for a given pressure occurs when

$$p_{cr} = p_0 = p_1 = p_2$$

Equating these values, and successively eliminating unknowns, yields the solution:

$$\frac{p_{cr}}{E} = \left\{ \frac{\alpha^2 (4 + \alpha)^2 \sqrt{\frac{C_2}{\epsilon} (1 + \alpha) \left[C_3 + \sqrt{C_3^2 + \frac{4C_4}{\alpha^2}} \right]}}{2[-3 + \sqrt{9 + (4 + \alpha) g(\alpha)}]^2} \right\}^2$$

where

$$g(\alpha) = \left(\frac{C_2}{C_0 \epsilon} \right)^2 \frac{(1 + \alpha)^2}{\alpha} - \frac{1 + 4\alpha}{\alpha}$$

$$C_3 = \frac{C_1 \epsilon}{C_2}, \quad C_4 = \frac{C_1 \bar{C}_1 \epsilon^2}{C_2}$$

and ϵ is a grid size parameter given by the relation

$$h^2 = \epsilon R t$$

For the panel to be approximated as a plate, it is necessary that

$$\epsilon \leq 4.0$$

By assuming values for ϵ and α , p/E may be determined and δ , γ are then given by the relations

$$\delta = \frac{-3 + \sqrt{9 + (4 + \alpha) g(\alpha)}}{4 + \alpha}$$

$$\gamma = [3\alpha(1 + \delta)^2 + (1 + \alpha)(1 + \alpha \delta^2)]^{1/2}$$

The ratio of stiffened weight/monocoque weight, is:

$$\eta = \frac{\bar{t}}{t^*} = \frac{1 + 3\alpha}{\sqrt{\gamma}}$$

if the same value of the general instability coefficient, $C_0 = 2C$ is assumed for both monocoque and geodesic stiffened constructions. By holding p/E constant and varying ϵ in the previous equations, a minimum weight construction may be found.

Evaluation of Stiffened Results - The assessment of the quality of a monocoque dome is made by observing how closely the general instability coefficient C comes to the upper limit value. The larger C is, the lighter weight is the dome for a given pressure.

In stiffened domes, one may compute two coefficients of merit \bar{C} and C^* from the equivalent weight thickness or effective buckling thickness of the dome.

$$\bar{p} = 2 \bar{C} E \left(\frac{\bar{t}}{R}\right)^2,$$

$$p^* = 2 C^* E \left(\frac{t^*}{R}\right)^2$$

where $\bar{t} = t(1 + \alpha)$ is the smeared out thickness, which may be computed from the above formula or from the actual weighed dome, and $t^* = t \sqrt{\gamma}$ is the effective thickness. Apparently C^* should have the same upper limit value as the monocoque C found from the previously determined experimental results.

That is

$$C^* = C = \frac{0.80}{\sqrt{3(1 - \nu^2)}} = 0.50$$

for $\nu = \frac{1}{3}$

For equal weight of monocoque and stiffened domes, one has $t = \bar{t}$ giving

$$\frac{\bar{p}}{p} = \frac{2 \bar{C} E \left(\frac{\bar{t}}{R}\right)^2}{2 C E \left(\frac{t}{R}\right)^2} = \frac{\bar{C}}{C}$$

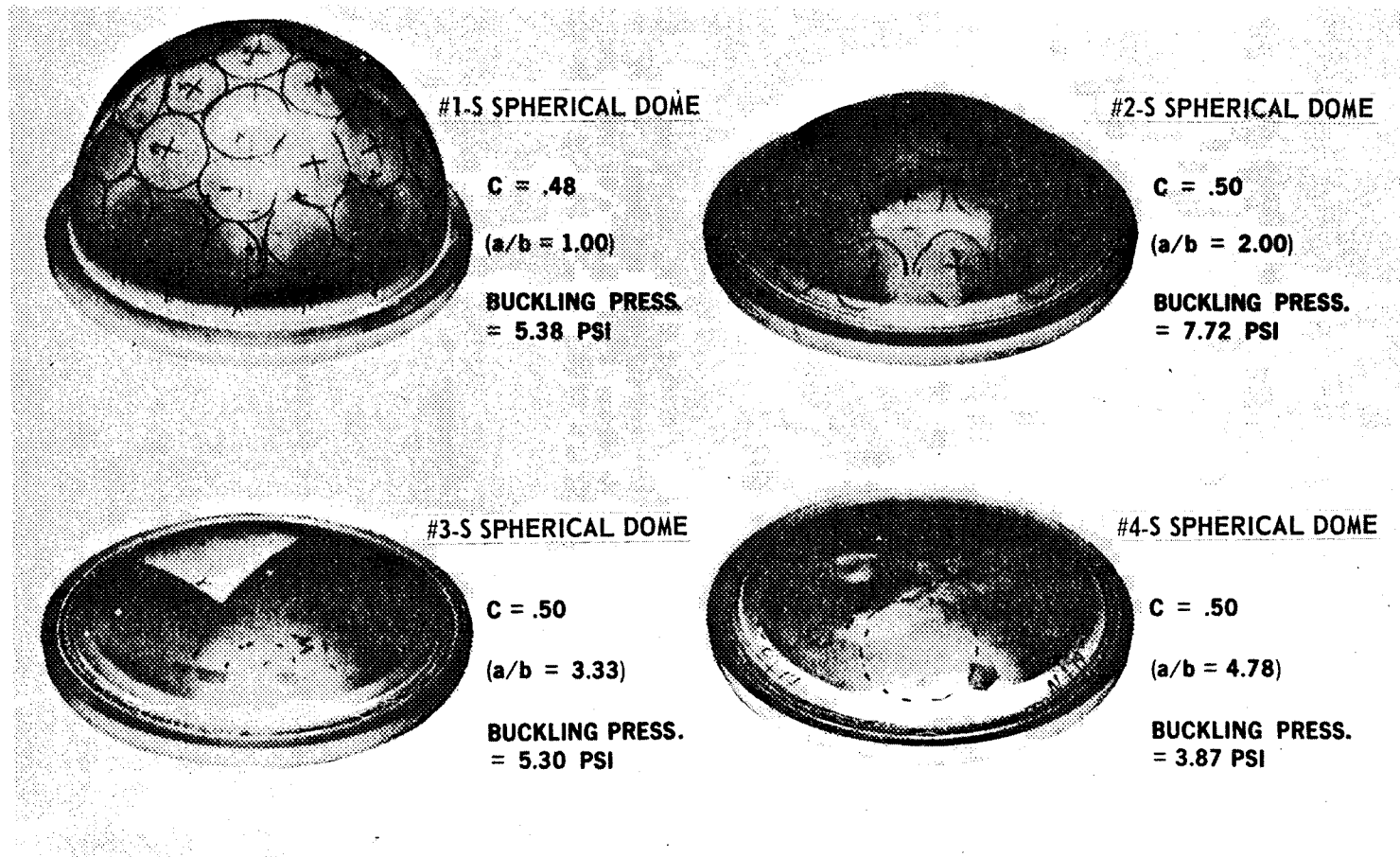


FIGURE 1.3 MONOCOQUE DOME CONFIGURATIONS

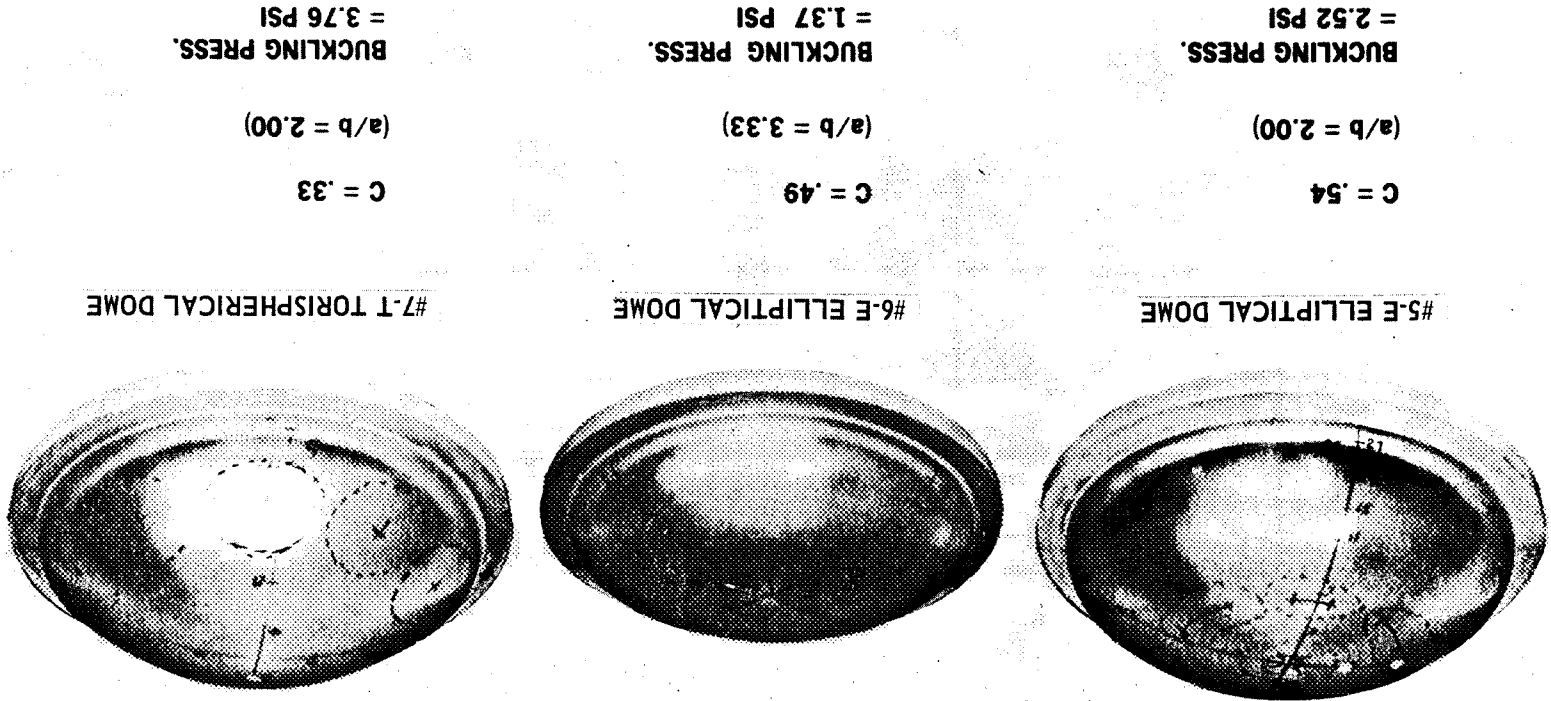


FIGURE 1.3 MONOCOQUE DOME CONFIGURATIONS (CONT)

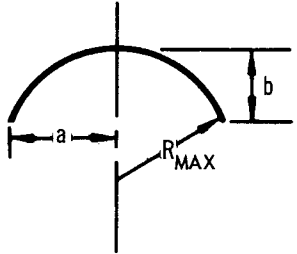
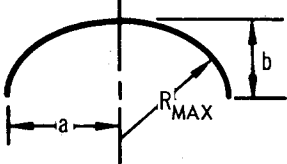
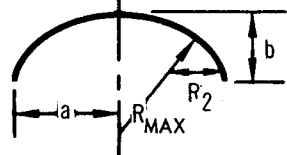
CONFIGURATION	a = 8.0 IN. (CONSTANT)	a/b	R _{MAX}	R ₂	t _{avg}	R _{MAX} /t	P _f -P.S.I.	C	W/ρ
SPHERICAL - #1-S		1.0	8.0	-	.0277	289	5.38	.48	11.14
SPHERICAL - #2-S		2.0	10.0	-	.0409	245	7.72	.50	10.20
SPHERICAL - #3-S		3.33	14.5	-	.0490	296	5.30	.50	10.70
SPHERICAL - #4-S		4.78	20.0	-	.0580	345	3.87	.50	12.60
ELLIPSOIDAL - #5-E		2.0	16.0	-	.0368	435	2.52	.54	9.8
ELLIPSOIDAL - #6-E		3.33	26.6	-	.0461	578	1.37	.49	10.8
TORISPHERICAL - #7-T		2.0	11.5	1.711	.0401	287	3.76	.33	10.8

TABLE 1.1

$$C = \frac{p}{2E} \left(\frac{R_{MAX}}{t} \right)^2$$

SUMMARY OF EXPERIMENTAL RESULTS
FOR MONOCOQUE DOMES UNDER EXTERNAL PRESSURE

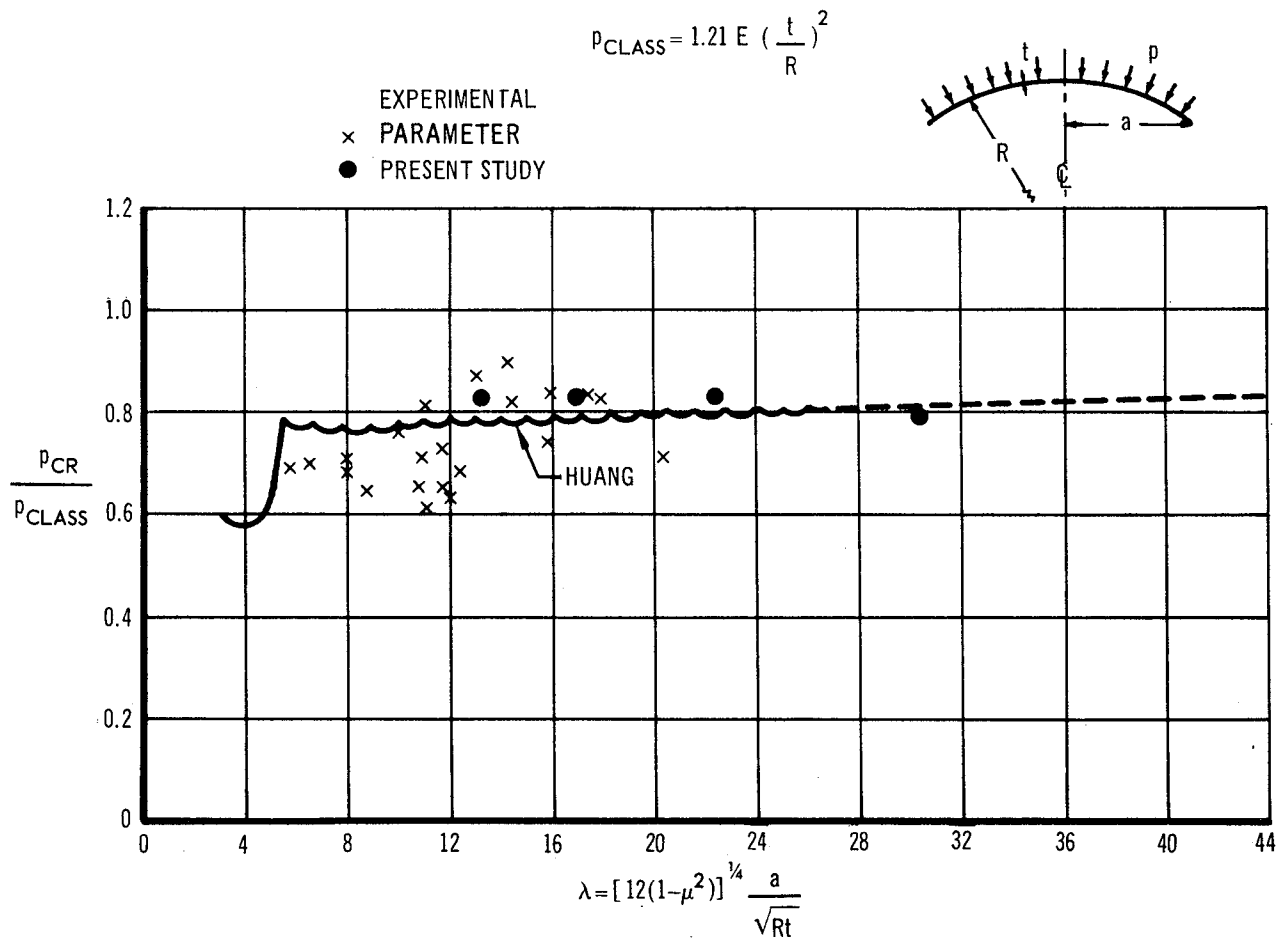
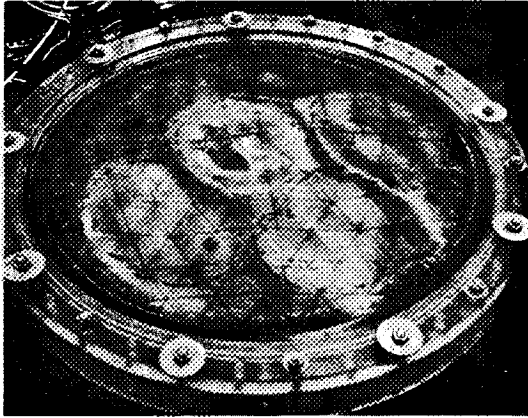
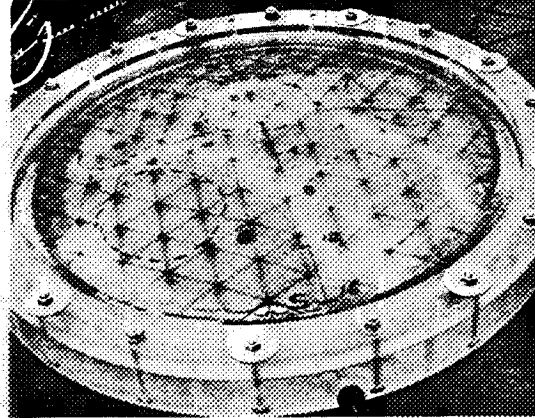


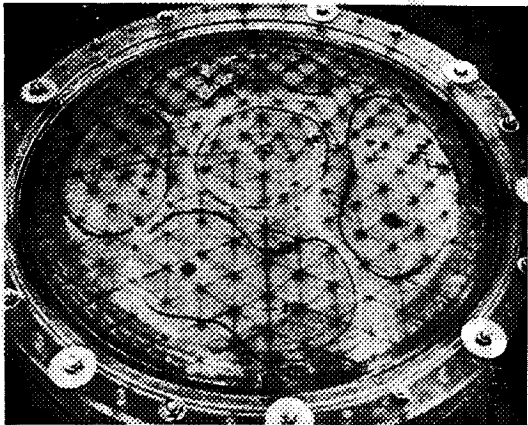
FIGURE 1.4 BUCKLING OF MONOCOQUE SPHERICAL CAPS
 COMPARISON OF TESTS WITH HUANG'S THEORY



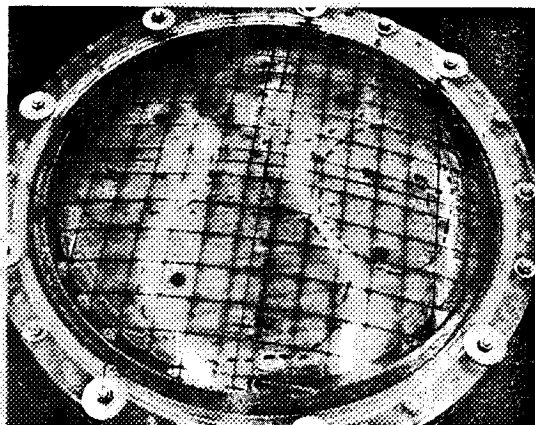
1-G GEODESIC STIFFENING
 (a/b = 4.78) $\bar{c}/c = 1.50$
 BUCKLING PRESSURE = 5.87 P.S.I.



2-G GEODESIC STIFFENING
 (a/b = 4.78) $\bar{c}/c = 1.60$
 BUCKLING PRESSURE = 6.54 P.S.I.



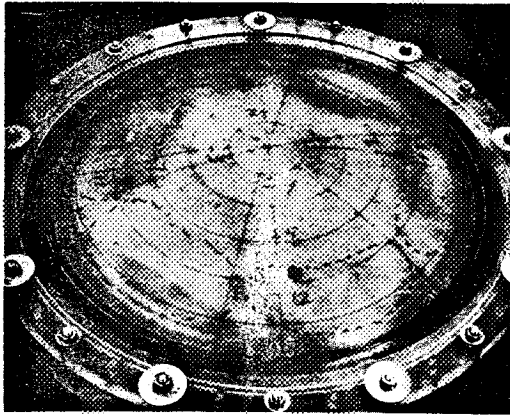
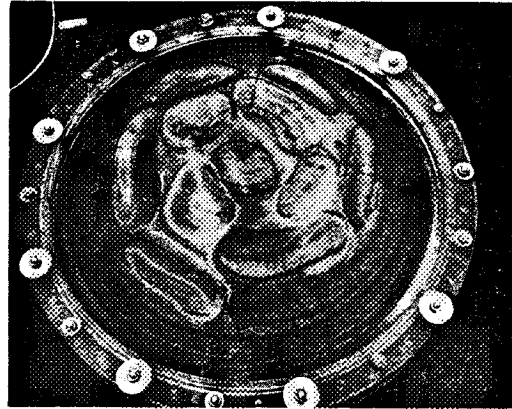
3-G GEODESIC STIFFENING
 (a/b = 4.78) $\bar{c}/c = 2.27$
 BUCKLING PRESSURE = 3.96 P.S.I.



1-SG SQUARE-GRID STIFFENING
 (a/b = 4.78) $\bar{c}/c = 1.58$
 BUCKLING PRESSURE = 9.48 P.S.I.

FIGURE 1.5 STIFFENED DOME CONFIGURATIONS

1-c CIRCUMFERENTIAL STIFFENED
($a/b = 2.0$) $\bar{c}/c = .92$
BUCKLING PRESSURE = 4.09 P.S.I.



1-mc CIRCUMFERENTIAL & MERIDIONAL STIFFENED
($a/b = 4.78$) $\bar{c}/c = .82$
BUCKLING PRESSURE = 1.53 P.S.I.

1-m MERIDIONALLY STIFFENED
($a/b = 4.78$) $\bar{c}/c = .88$
BUCKLING PRESSURE = 1.41 P.S.I.

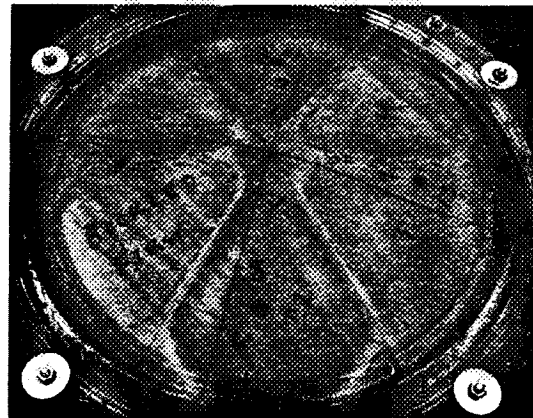
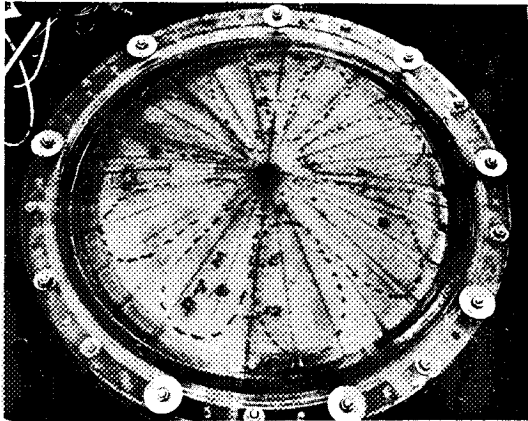
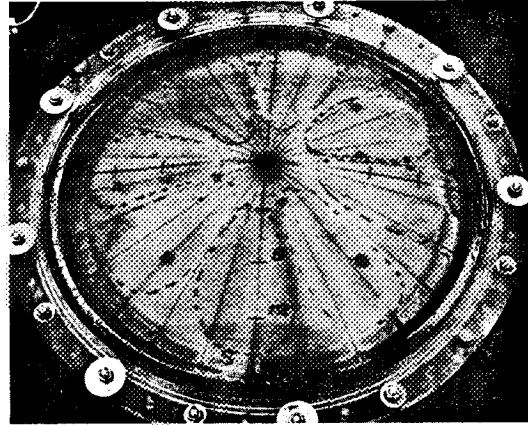


FIGURE 1.5 STIFFENED DOME CONFIGURATIONS

2-m MERIDIONALLY STIFFENED
($a/b = 4.78$) $\bar{c}/c = 1.12$
BUCKLING = 2.09 P.S.I.



3-m MERIDIONALLY STIFFENED
($a/b = 4.78$) $\bar{c}/c = 1.38$
BUCKLING PRESSURE = 2.87 P.S.I.

4-m MERIDIONALLY STIFFENED
($a/b = 4.78$) $\bar{c}/c = 1.24$
BUCKLING PRESSURE = 2.87 P.S.I.

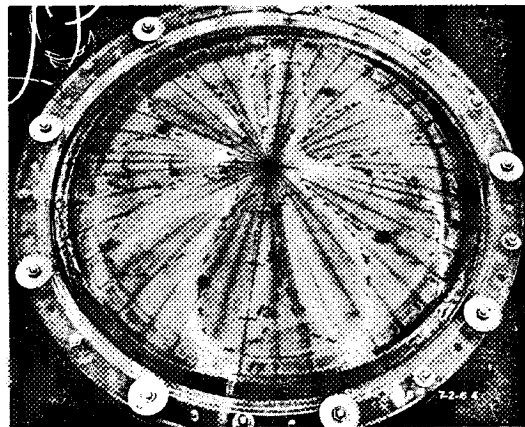


FIGURE 1.5 STIFFENED DOME CONFIGURATIONS

STIFFENING CONFIGURATION	CONSTANT $a = 8$ IN.	R	a	d	b	t_s	NO OF RIBS	$P_{S\text{Fail}}$	$\bar{\tau}$	\bar{c}/c	REMARKS
GEODESIC - 1-G		20	1.57	.230	.0191	.0474		5.87	.0580	1.50	GENERAL INSTABILITY FAILURE
GEODESIC - 2-G		20	1.60	.226	.0239	.0479		6.54	.0592	1.60	GENERAL INSTABILITY FAILURE
GEODESIC-3-G		20	1.25	.205	.0153	.0296		3.96	.0387	2.27	GENERAL INSTABILITY FAILURE
CIRCUMFERENTIAL-1-c		10		VARYING		.0260	10	4.09	.0390	.92	PRIMARY FAILURE BY RIB INSTABILITY
MERIDIONAL - 1-m		20		.25	.0191	.0349	6	1.41	.0371	.88	PANEL INSTABILITY FAILURE
MERIDIONAL - 2-m		20		.30	.0191	.0349	26	2.09	.0402	1.12	RIB INSTABILITY FAILURE
MERIDIONAL - 3-m		20		.30	.0191	.0349	26	2.87	.0424	1.38	RIB INSTABILITY FAILURE
		20		.25	.0191						RIB INSTABILITY FAILURE
		20		.30	.0239	.0272	38	1.69	.0343	1.24	RIB INSTABILITY FAILURE
MERIDIONAL AND CIRCUMFERENTIAL-1-mc		20		.25	.0191	.0349	6 M 5 C	1.53	.0401	.82	PRIMARY FAILURE BY CIRCUMFERENTIAL RIB INSTABILITY
SQUARE-GRID - 1-SG		20	1.16	.302	.0287	.0576		9.48	.072	1.58	PRIMARY FAILURE BY GENERAL INSTABILITY

TABLE 1.2

SUMMARY OF EXPERIMENTAL RESULTS OF STIFFENED SPHERICAL CAPS UNDER UNIFORM EXTERNAL PRESSURE

If C is taken as its upper limit value $C = 0.50$, then

$$\frac{\bar{p}}{p} \geq \frac{\bar{C}}{0.50}$$

for an increase of strength to weight for the stiffened dome.

Fabrication of Stiffened Domes

The shells of the stiffened dome configurations were fabricated using the same technique as the monocoque dome configurations. The ribs were cut from various sheet material thicknesses and bonded on the concave surface of the shell. The stiffening configurations fabricated were:

Meridional Stiffened

Circumferential Stiffened

Combined Meridional and Circumferential Stiffened

Square-Grid Stiffened

Geodesic Stiffened

Stiffened Model Test Results - Room Temperature

The detailed geometry and test results of the stiffened dome configurations for the room temperature condition are tabulated in Table 1.2. Figure 1.5 depicts the resulting buckle patterns of stiffened plastic domes at the failing pressures indicated in the figure.

The highest strength to weight ratio was achieved using a geodesic stiffening pattern as shown in the summary table of the experimental results. It was also indicated that the circumferential and the combined meridional-circumferential stiffening arrangement was less efficient than that of the meridionally stiffened dome arrangement.

The experimental values of C^* for the three geodesic domes and the square-grid dome were less than 0.50 achieved for the monocoque domes. The reasons for not achieving the upper limit for C^* are not clear. The cause could be due to rib fabrication stresses, edge effects and imperfect grid mapping on the spherical surface.

Stiffened Model Test Results - Thermal Gradient

A combined loading condition of thermal stress and external pressure was used to test a geodesic and a square-grid stiffened dome to assess the influence of thermal stresses upon the buckling pressure. In both tests the applied thermal gradient produced a higher buckling pressure than was previously recorded for the room temperature condition. This increase in the buckling pressure was attributed to the difference between the shell and the support ring which introduced a relieving tensile load in the shell.

Phase IV - Metal Dome Fabrication and Test Results

An aluminum dome with a half-opening angle of $\theta = 60^\circ$ and a spherical radius of $R = 27.3$ inches, with a geodesic stiffening pattern, was fabricated and tested to verify the plastic dome results.

The spherical shell was spun using 2014 - T6 aluminum material and the geodesic rib pattern was formed by a hand routing procedure.

Test Description

The finished dome was mounted in a heavy steel base ring with a deep trough machined in the ring. The dome was seated into this trough and then filled with Cero-bend. Pressure was applied on the convex surface using oil as the pressurizing medium, and continuous instrumentation records were taken up to failure.

Test Results

Failure of the dome occurred at 62.2 psi. The buckling coefficient for this geodesic dome at the failing pressure was calculated to be $C = 0.26$. It is suspected that this buckling coefficient was less than that obtained for the plastic dome specimens ($C = .35$) because of the high residual and pressure stresses causing plastic behavior of the material.

CONCLUSIONS

The experimental and analytical investigation concluded shows that a spherical cap with a half-opening angle $\theta = 60^\circ$, with a geodesic waffle arrangement, results in the minimum weight shape and rib stiffening arrangement. However, since this study was initiated to develop a stiffened dome that would be a possible replacement candidate for honeycomb sandwich common domes in tandem propellant tanks of large space vehicles, a comparison between these two dome concepts is necessary.

Figure 1.6 is an estimate of the weight of a near optimum geodesic dome construction compared to that of monocoque and honeycomb dome constructions based upon a spherical radius $R = 100$ inches and 2014-16 material. The general instability coefficient $C = .50$ is assumed constant for this particular example, but in general will be a variable dependent upon the fabrication details. The honeycomb design curve includes a realistic bond weight of 3 lb/ft^2 , dictated by previous fabrication experience, and a core density of 4 lb/ft^3 .

Since a common dome in space vehicles serves the dual purpose of withstanding the resulting differential pressure and temperature between the propellants, the insulation requirement is included in the weight estimation shown in the figure. This is shown by the solid line for the monocoque and geodesic dome construction. The honeycomb core inherently provides a good thermal barrier, therefore, no weight penalty is associated with this design concept. An example of typical geometrics for the three constructions is shown in the figure for an assumed external pressure condition of $P = 30$ psi.

Before drawing general conclusions of comparative strength to weight ratios between rib stiffened and alternate monocoque and composite dome constructions, one must be aware of the other loading conditions, and varying influence of the fabrication variables upon the general instability coefficient.

For example, in honeycomb construction a large differential temperature between the inner and outer face sheets produce high thermal stresses that may have a significant effect upon the overall weight and geometric proportion. On the other hand, in stiffened and monocoque construction these thermal stresses are of minor importance and in general do not have a significant effect upon the weight. Another example of loading influencing the final design weight is that due to an internal pressure condition. Often in the design of common domes the internal pressure may be greater than the external pressure condition, thus resulting in high tensile stress on the bulkhead. From Figure 1.6, assuming $p = 30$ psi, it may be shown that if $P_{int.} \geq 3P$ that the comparative weight between the honeycomb and geodesic stiffened construction are approximately equal.

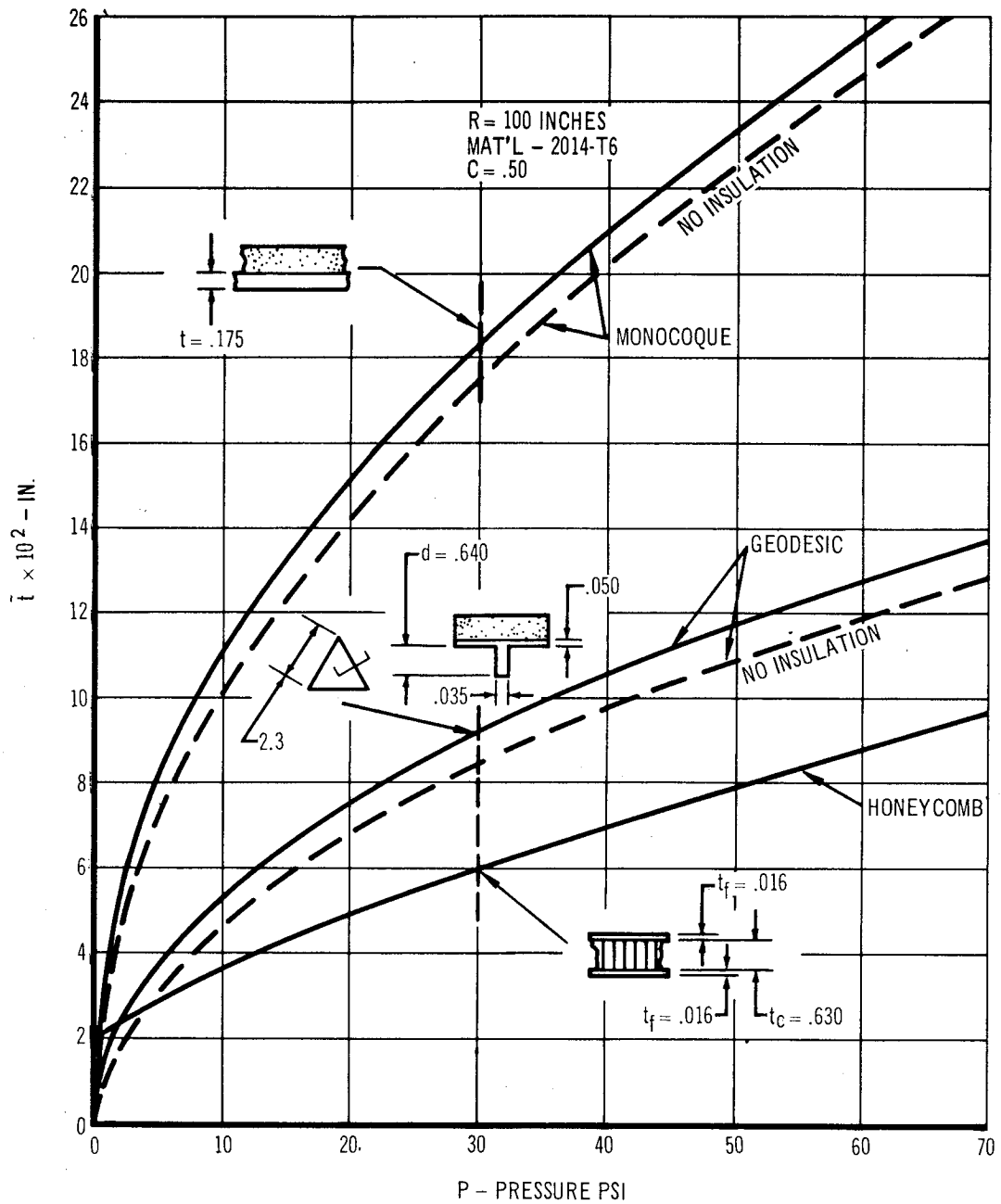


FIGURE 1.6 WEIGHT COMPARISON OF DEEP SPHERICAL DOMES UNDER EXTERNAL PRESSURE

CHAPTER II - MONOCOQUE SHAPE OPTIMIZATION

SPHERICAL CAP

When a hemisphere or an ellipsoid joins a cylinder, due to continuity of the tangents at the juncture, no out-of-balance membrane loads exist at the joint. For a spherical cap, however, the discontinuity in the tangent causes transverse shears and bending moments at the joining point (see Figure 2.1) which results in local bending and hoop forces. When the dome is worked in tension, a thickening of material around the joint, frequently in the form of a ring, is required to resist buckling. However, when the dome is sized for compressive loads but local tensile edge effects occur, ring requirements will depend upon the out-of-balance forces and compatible displacements between the cylinder, ring and dome for the allowable tensile stress. In bulkheads separating two tanks where both pressure loadings may occur, this effect should be considered.

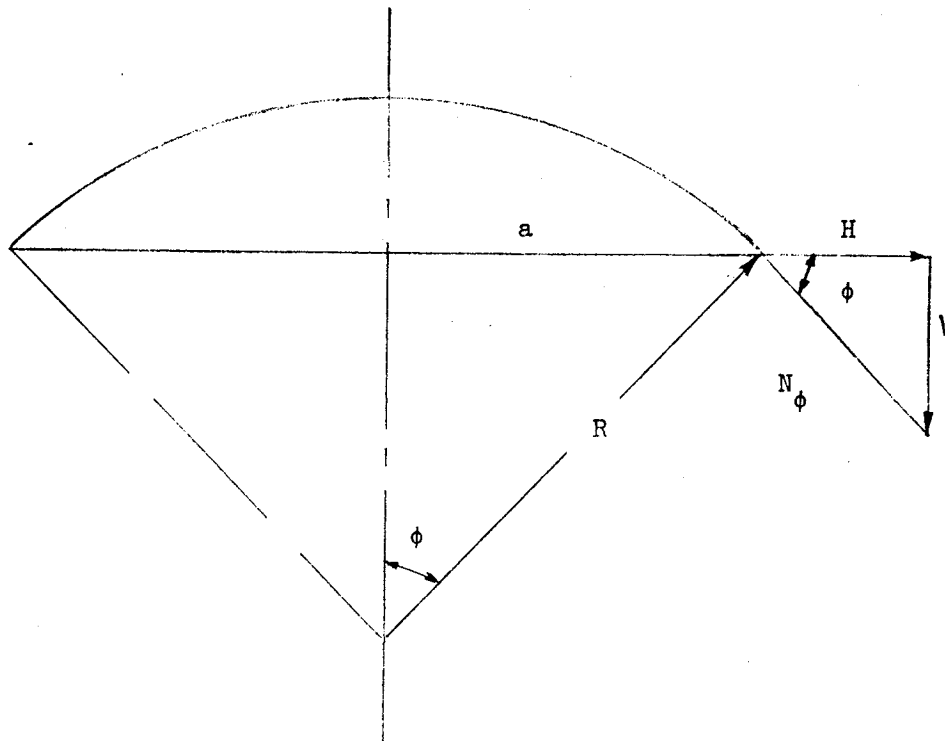


Figure 2.1 - EDGE FORCES ON SPHERICAL CAP

The surface area of the spherical cap is,

$$A = \int_0^{\phi} 2 \pi R \sin \phi R d \phi$$

$$A = 2 \pi R^2 (1 - \cos \phi)$$

the spherical cap weight is

$$W = \rho A t = 2 \pi \rho R^2 (1 - \cos \phi) t$$

Since the allowable compressive stress is,

$$\sigma = C E \frac{t}{R} = \frac{PR}{2t}$$

or in terms of the thickness

$$t = R \sqrt{\frac{P}{2CE}}$$

From figure 2.1

$$R = \frac{a}{\sin \phi}$$

Substituting into the weight equation gives

$$W = 2 \pi \rho a^3 \sqrt{\frac{P}{2CE}} \frac{1 - \cos \phi}{\sin^3 \phi}$$

$$W = 2 \pi \rho a^3 \sqrt{\frac{P}{2CE}} \phi$$

where

$$\phi = \frac{1 - \cos \phi}{\sin^3 \phi}$$

the term ϕ is evaluated in table 2.1 for $0^\circ < \phi \leq 90^\circ$

Table 2.1

ϕ	$\frac{1}{\sin \phi}$	$\frac{1}{\sin^3 \phi}$	$\cos \phi$	$1 - \cos \phi$	$\phi(\phi)$
10°	5.76	190.5	.984	.016	3.05
20°	2.92	24.9	.941	.059	1.470
30°	2.00	8.0	.866	.134	1.072
40°	1.553	3.75	.766	.234	0.877
50°	1.304	2.22	.643	.357	0.831
60°	1.153	1.535	.500	.500	0.766
70°	1.062	1.198	.342	.658	0.789
80°	1.016	1.048	.1737	.8263	0.867
90°	1.000	1.00	0	1.000	1.000

From the table, the minimum value of ϕ occurs at $\phi = 60^\circ$.

Proof that $\phi = 60^\circ$ gives a minimum value of ϕ is shown below.

$$\phi' = \frac{\sin^3 \phi (\sin \phi) - (1 - \cos \phi) 3 \sin^2 \phi \cos \phi}{\sin^6 \phi} = 0$$

and since

$$\phi \neq 0, \sin \phi \neq 0$$

$$\sin^3 \phi - 3 \cos \phi (1 - \cos \phi) = 0,$$

giving

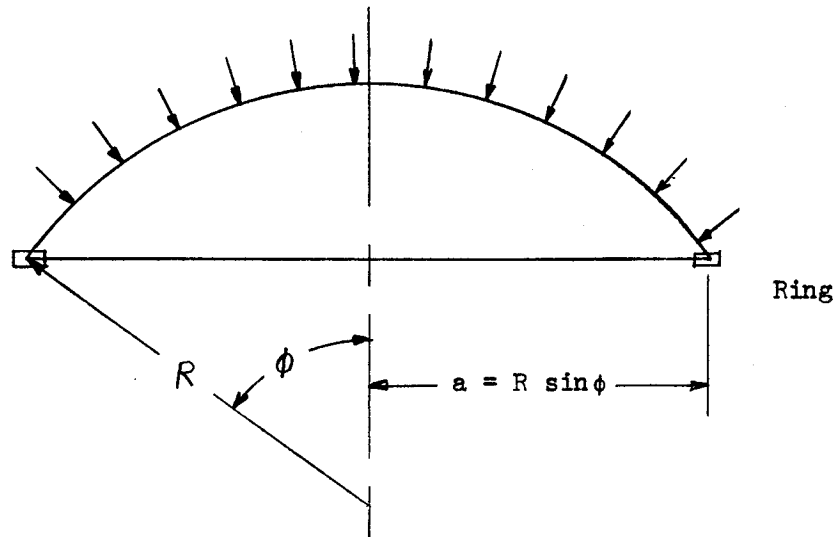
$$2 \cos^2 \phi - 3 \cos \phi + 1 = 0,$$

$$\cos \phi = \frac{3 \pm 1}{4}, \phi = 60^\circ,$$

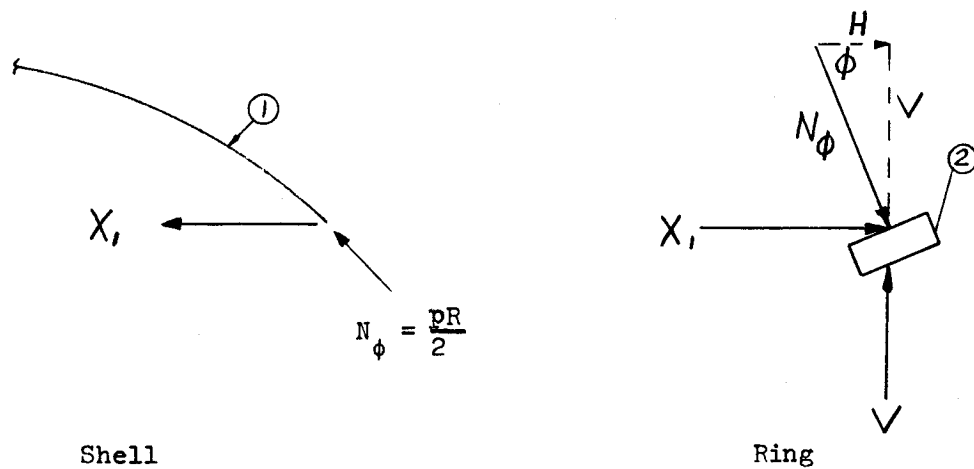
since

$$\phi \neq 0$$

Thrust Ring of Spherical Cap



Due to membrane loading, the spherical cap will be in compression while the ring will be in tension. Assuming that the rotational resistance of the ring is small compared to its hoop rigidity, the following forces will exist at the juncture between the shell and the ring.



Shell (1)

Due to the pressure,

$$N_{\theta} = N_{\phi} = -\frac{pR}{2}$$

The displacement at and in the direction of X_1 is, (reference 22)

$$\delta_{1p}^{(1)} = -\frac{a}{Et} (N_{\theta} - \nu N_{\phi}) = \frac{p R^2 \sin \phi}{2 Et} (1 - \nu)$$

The displacement due to $X_1 = 1$ is:

$$\delta_{11}^{(1)} = \frac{2 \lambda R \sin^2 \phi}{Et}, \quad \lambda^4 = 3(1 - \nu^2) \left(\frac{R}{t}\right)^2$$

Ring (2)

The horizontal ring loading due to the shell pressure is,

$$H = N_{\phi} \cos \phi = \frac{pR}{2} \cos \phi$$

and the ring stress is,

$$\sigma_{\theta} = \frac{Ha}{A} = \frac{p R^2}{2A} \sin \phi \cos \phi$$

where A is the ring cross-sectional area.

The displacement at and in the direction of X_1 , due to p, is

$$\delta_{1p}^{(2)} = \epsilon_{\theta} a = \frac{\sigma_{\theta}}{E} a = \frac{p R^3}{2 AE} \sin^2 \phi \cos \phi$$

The displacement due to $X_1 = 1$ is

$$\delta_{11}^{(2)} = \frac{\sigma_{\theta}}{E} a = \frac{R^2}{AE} \sin^2 \phi$$

since

$$\sigma_{\theta} = \frac{a}{A}, \quad \text{for } X_1 = 1$$

Relative displacements are obtained by adding absolute displacements,

$$\delta_{lp} = \delta_{lp}^{(1)} + \delta_{lp}^{(2)} = \frac{p R^2 \sin \phi (1 - \nu)}{2 E t} + \frac{p R^3 \sin^2 \phi \cos \phi}{2 A E}$$

$$\delta_{ll} = \delta_{ll}^{(1)} + \delta_{ll}^{(2)} = \frac{2 \lambda R \sin^2 \phi}{E t} + \frac{R^2 \sin^2 \phi}{A E}$$

combining terms

$$\delta_{lp} = \frac{p R^2 \sin \phi}{2 E} \left[\frac{1 - \nu}{t} + \frac{R \sin \phi \cos \phi}{A} \right]$$

$$\delta_{ll} = \frac{R \sin^2 \phi}{E} \left[\frac{2 \lambda}{t} + \frac{R}{A} \right]$$

The compatibility equation is:

$$X_1 \delta_{ll} + \delta_{lp} = 0, \quad X_1 = - \frac{\delta_{lp}}{\delta_{ll}}$$

$$X_1 = - \frac{p R}{2 \sin \phi} \left[\frac{\frac{1 - \nu}{t} + \frac{R}{A} \sin \phi \cos \phi}{\frac{2 \lambda}{t} + \frac{R}{A}} \right]$$

$$X_1 = - \frac{p R}{2 \sin \phi} \left[\frac{(1 - \nu) + \frac{t R}{A} \sin \phi \cos \phi}{2 \lambda + \frac{t R}{A}} \right]$$

The total ring load is:

$$H + X_1 = \frac{\sigma_\theta A}{a}, \quad \sigma_\theta = \frac{R \sin\phi}{A} (H + X_1) = F_t$$

where F_t is the allowable ring stress.

$$F_t = \frac{R \sin\phi}{A} \left[\frac{pR}{2} \cos\phi - \frac{pR}{2 \sin\phi} \frac{(1 - \nu) + \frac{tR}{A} \sin\phi \cos\phi}{2\lambda + \frac{tR}{A}} \right]$$

$$F_t = \frac{p R^2 \sin\phi}{2 A} \left[\cos\phi - \frac{(1 - \nu) + \frac{tR}{A} \sin\phi \cos\phi}{2\lambda \sin\phi + \frac{tR}{A} \sin\phi} \right]$$

The thickness will be given by the critical pressure,

$$p = 2 C E \left(\frac{t}{R}\right)^2, \quad \frac{t}{R} = \sqrt{\frac{p}{2CE}} = K,$$

and

$$\frac{F_t}{p} = \frac{R^2 \sin\phi}{A} \left[\cos\phi - \frac{(1 - \nu) + \frac{KR^2}{A} \sin\phi \cos\phi}{2\lambda \sin\phi + \frac{KR^2}{A} \sin\phi} \right]$$

But

$$\lambda^4 = 3(1 - \nu^2) \left(\frac{R}{t}\right)^2 = \frac{3(1 - \nu^2)}{K^2}$$

$$\frac{F_t}{p} = \frac{R^2 \sin\phi}{A} \left[\cos\phi - \frac{(1 - \nu) + \frac{KR^2}{A} \sin\phi \cos\phi}{\frac{2 \sin\phi [3(1 - \nu^2)]^{1/4}}{\sqrt{K}} + \frac{KR^2}{A} \sin\phi} \right]$$

Now let

$$2 \sin \phi [3(1 - \nu^2)]^{1/4} = b \sin \phi$$

$$\frac{R^2}{A} = x$$

So that

$$\begin{aligned} \frac{2}{\sin \phi} \frac{F_t}{p} &= x \left[\cos \phi - \frac{(1 - \nu) + K x \sin \phi \cos \phi}{\frac{b \sin \phi}{\sqrt{K}} + K x \sin \phi} \right] \\ &= x \frac{\frac{b}{\sqrt{K}} \sin \phi \cos \phi - (1 - \nu)}{\frac{b}{\sqrt{K}} \sin \phi + K x \sin \phi} \end{aligned}$$

Solving for x ,

$$x = \frac{\frac{2b}{\sqrt{K}} \left(\frac{F_t}{p}\right)}{\frac{b}{\sqrt{K}} \sin \phi \cos \phi - (1 - \nu) - 2K \left(\frac{F_t}{p}\right)} = \frac{R^2}{A}$$

and the ring area is,

$$A = \frac{R^2}{2 \left(\frac{F_t}{p}\right) \frac{b}{\sqrt{K}}} \left[\frac{b}{\sqrt{K}} \sin \phi \cos \phi - (1 - \nu) - 2K \left(\frac{F_t}{p}\right) \right]$$

$$A = \frac{R^2}{2 \left(\frac{F_t}{p}\right)} \left[\sin \phi \cos \phi - \frac{\sqrt{K}}{b} [(1 - \nu) + 2K \left(\frac{F_t}{p}\right)] \right]$$

$$A = \frac{a^2}{2 \sin^2 \phi \left(\frac{F_t}{p}\right)} \left[\sin \phi \cos \phi - \frac{\sqrt{K}}{b} [(1 - \nu) + 2K \left(\frac{F_t}{p}\right)] \right]$$

i.e. $A = a^2 \psi$, where

$$\psi = \frac{1}{2 \sin^2 \phi \left(\frac{F}{p}\right)} \left[\sin \phi \cos \phi - \frac{\sqrt{K}}{b} \left[(1 - \nu) + 2K \left(\frac{F}{p}\right) \right] \right] \quad (2.2)$$

The ring weight is:

$$W_r = 2 \pi \rho a A = 2 \pi \rho a^3 \psi$$

$$W_r = 2 \pi \rho a^3 \sqrt{\frac{p}{2CE}} \cdot \frac{\psi}{K}$$

since:

$$\sqrt{\frac{p}{2CE}} \cdot \frac{1}{K} = 1$$

The spherical cap weight was shown to be

$$W_s = 2 \pi \rho a^3 \sqrt{\frac{p}{2CE}} \cdot \phi, \quad \text{where } \phi = \frac{1 - \cos \phi}{\sin^3 \phi}$$

and the total weight is:

$$W = W_r + W_s = 2 \pi \rho a^3 \left\{ \frac{\psi}{K} + \phi \right\} \quad (2.3)$$

Which is restricted to solutions such that

$$\psi \geq 0$$

(For values of $\psi < 0$, the ring is in compression)

Substituting the appropriate expressions for ψ and ϕ into the above equation results in:

$$W = \pi \rho a^3 \left\{ 2 \sqrt{K} \frac{1 - \cos \phi}{\sin^3 \phi} + \frac{1}{\sin^2 \phi} \frac{F t}{p} \left[\sin \phi \cos \phi - \frac{K}{2\sqrt{3}(1 - \nu^2)} \left[(1 - \nu) + 2K \frac{F t}{p} \right] \right] \right\}$$

The importance of the ring weight may now be evaluated by only considering the magnitude of the ratio, \bar{W}_r/\bar{W}_s in the above equation.

Substituting the appropriate values for \bar{W}_r and \bar{W}_s gives:

$$\frac{\bar{W}_r}{\bar{W}_s} = \frac{\frac{\cos \phi}{\sin \phi} \frac{F t}{p}}{2 K \frac{1 - \cos \phi}{\sin^3 \phi}}$$

simplifying the above gives:

$$\frac{\bar{W}_r}{\bar{W}_s} = \frac{\cos \phi (1 + \cos \phi)}{\frac{F t}{p} 2 \sqrt{K}}$$

where

$$K = \frac{t}{R}$$

substituting

$$\frac{\bar{W}_r}{\bar{W}_s} = \frac{\cos \phi (1 + \cos \phi)}{2 \frac{F t}{p}} \sqrt{\frac{R}{t}}$$

where

$$\frac{2 \sqrt{K} (1 - \cos \phi)}{\sin^3 \phi} = \bar{W}_s$$

(weight index of spherical cap)

and

$$\frac{1}{\sin^2 \phi} \frac{F_t}{p} \left\{ \sin \phi \cos \phi - \frac{K}{2\sqrt{3(1-\nu^2)}} \left[(1-\nu) + 2K \frac{F_t}{p} \right] \right\} = \bar{W}_r$$

(weight index of ring)

A conservative first approximation of the ring weight would be to neglect the second term of the above equation, thus giving

$$\frac{\cos \phi}{\sin \phi} \frac{F_t}{p} = \bar{W}_r$$

Letting

$$\frac{W}{\pi \rho a^3} = \bar{W}_T \quad (\text{total weight index})$$

therefore:

$$\bar{W}_T = \bar{W}_s + \bar{W}_r = \bar{W}_s \left(1 + \frac{\bar{W}_r}{\bar{W}_s} \right)$$

Using a conservative estimate of $R/t = 1000$, and reasonable values of the ratio F_t/p for varying half angle dome openings, the equation is plotted and shown in Figure 2.2.

It may be seen that for all practical ranges of interest that the ring weight is a negligible portion of the total weight of the bulkhead and need not be considered in the present optimization study.

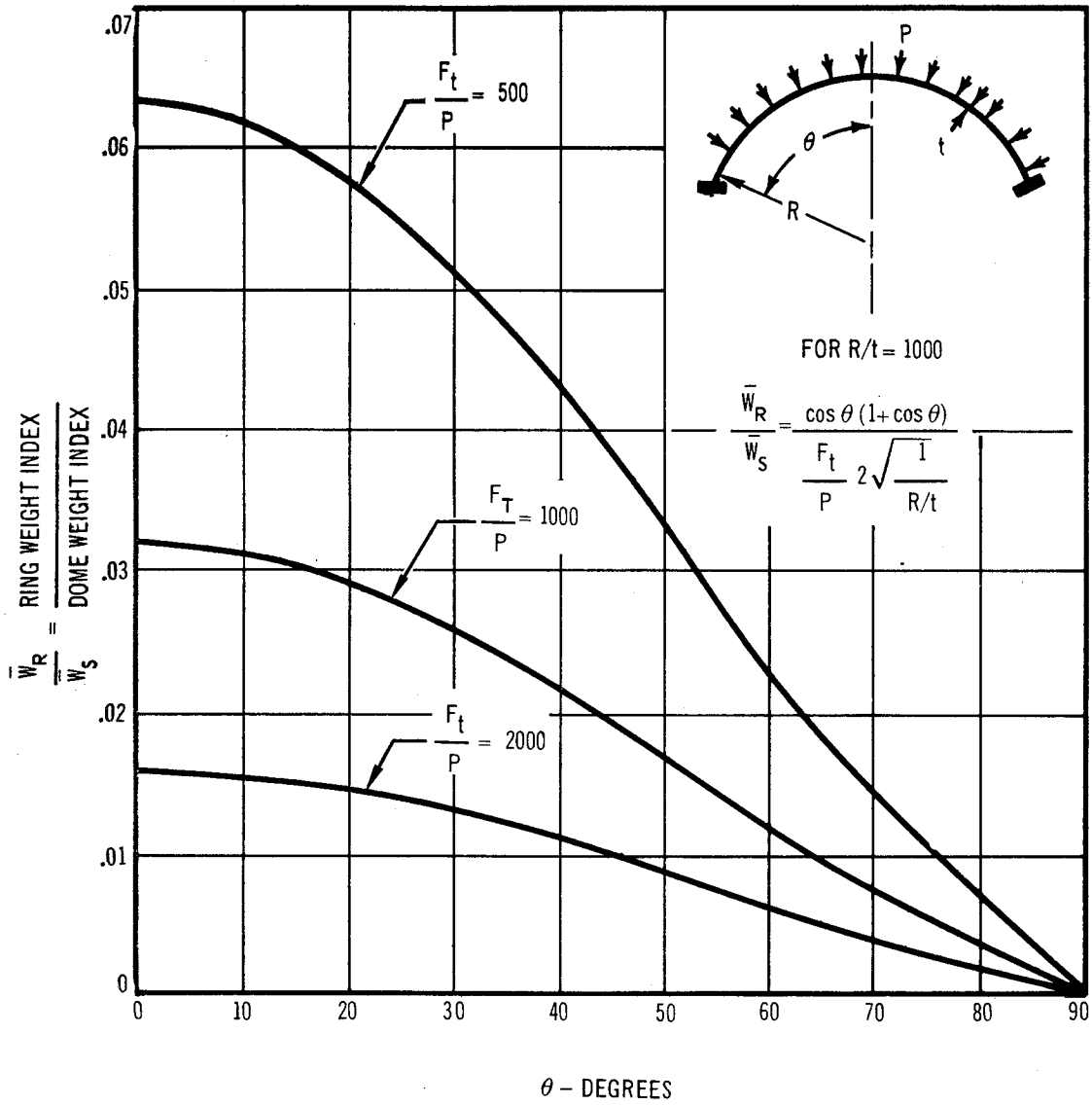


FIGURE 2.2 EFFECT OF RING WEIGHT REQUIREMENT ON SPHERICAL CAPS

ELLIPSOIDAL DOME

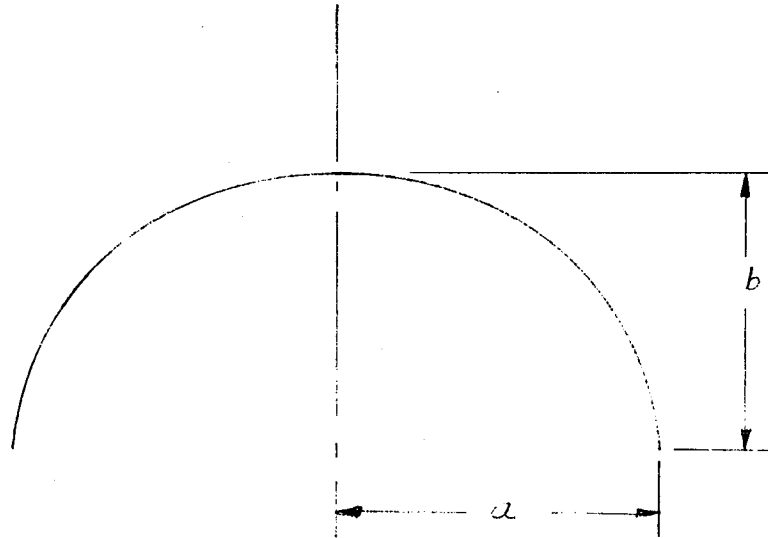


Figure 2.3 - SKETCH OF ELLIPSOIDAL DOME

The surface area of an ellipsoid of revolution from Figure 2.3 is

$$A = \pi \left[a^2 + \frac{a b^2}{\sqrt{a^2 - b^2}} \ln \frac{a + \sqrt{a^2 - b^2}}{b} \right]$$

letting $\beta = \frac{b}{a}$

$$A = \pi a^2 \left[1 + \frac{\beta^2}{\sqrt{1 - \beta^2}} \ln \frac{1 + \sqrt{1 - \beta^2}}{\beta} \right] \quad (2.4)$$

The weight of the dome may therefore be expressed as

$$W = \rho V = \rho A t = \pi \rho a^2 \left[1 + \frac{\beta^2}{\sqrt{1 - \beta^2}} \ln \frac{1 + \sqrt{1 - \beta^2}}{\beta} \right] t$$

The critical buckling pressure for an oblate ellipsoid of revolution, according to Mushtari-Galimov (reference 8) is given as:

$$p = 2CE \left(\frac{t}{a}\right)^2 \beta^2 \quad (2.5)$$

or in terms of the thickness, t , is

$$t = \frac{a}{\beta} \sqrt{\frac{p}{2CE}}$$

so that

$$W = \pi \rho a^3 \sqrt{\frac{p}{2CE}} \left[\frac{1}{\beta} + \frac{\beta}{\sqrt{1-\beta^2}} \ln \frac{1+\sqrt{1-\beta^2}}{\beta} \right]$$

$$W = \pi \rho a^3 \sqrt{\frac{p}{2CE}} \cdot \tau \quad (2.6)$$

where

$$\tau = \frac{1}{\beta} + \frac{\beta}{\sqrt{1-\beta^2}} \ln \frac{1+\sqrt{1-\beta^2}}{\beta}$$

The value of β which minimizes τ in equation (2.6) is required for minimum weight. The table below evaluates this parameter (τ) for various values of β .

β	.10	.20	.30	.40	.50	.60	.70	.80	.90	1.000
τ	10.301	5.468	3.923	3.184	2.760	2.491	2.307	2.174	2.075	2.000

From the table the minimum value of τ occurs at $\beta = 1.0$, or when $a = b$; i.e., a hemisphere. The proof of this is as follows:

$$\lim_{\beta \rightarrow 1} \frac{\beta}{\sqrt{1-\beta^2}} \ln \frac{1+\sqrt{1-\beta^2}}{\beta} = \lim_{\mu \rightarrow 0} \frac{\ln(\mu + \sqrt{1+\mu^2})}{\mu}$$

If $\mu = \frac{\sqrt{1-\beta^2}}{\beta}$, and the limit by L'Hospital is

$$\lim_{\mu \rightarrow 0} \frac{\frac{1}{\mu + \sqrt{1+\mu^2}} (1 + \frac{\mu}{\sqrt{1+\mu^2}})}{1} = 1$$

so that

$$\tau = 2.0$$

One sees that τ decreases monotonically and that the minimum value lies at the end of the range where $\beta = 1$.

TORISPHERE

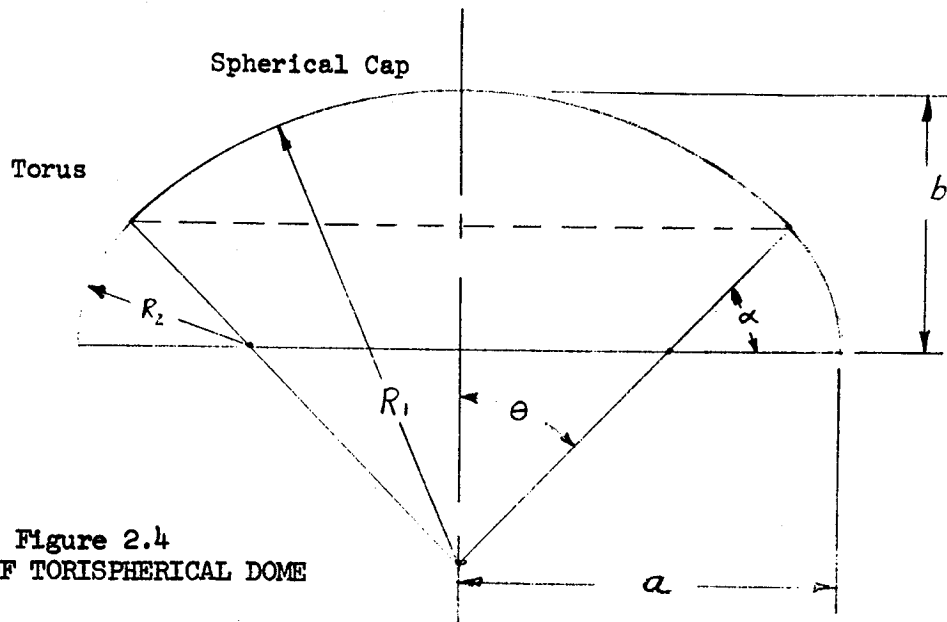


Figure 2.4
SKETCH OF TORISPHERICAL DOME

The surface area of the Torus section from figure 2.4 is:

$$R = (R_1 - R_2) \sin\theta + R_2 \cos\alpha \quad (2.7)$$

$$ds = R_2 d\alpha$$

$$dA_T = 2 \pi R ds = 2 \pi R_2 [(R_1 - R_2) \sin\theta + R_2 \cos\alpha] d\alpha$$

$$A_T = 2 \pi R_2 (R_1 - R_2) \int_0^{\frac{\pi}{2} - \theta} \left[\sin\theta + \frac{R_2}{R_1 - R_2} \cos\alpha \right] d\alpha$$

$$A_T = 2 \pi R_2 (R_1 - R_2) \left[\frac{\pi}{2} \sin\theta - \theta \sin\theta + \frac{R_2}{R_1 - R_2} \cos\theta \right] \quad (2.8)$$

The surface area of the spherical cap section is

$$A_C = 2 \pi R_1^2 (1 - \cos\theta)$$

Total area of torispherical bulkhead is then

$$A = A_T + A_C$$

$$A = 2 \pi R_1^2 \left[(1 - \cos \theta) + \frac{J-1}{J^2} \left(\frac{\pi}{2} \sin \theta - \theta \sin \theta + \frac{\cos \theta}{J-1} \right) \right] \quad (2.8)$$

where

$$J = \frac{R_1}{R_2}$$

Since in torispherical domes $R_1 > R_2$ it may be assumed that the larger radius defining the spherical cap will have a lower buckling state than that of the torus portion. That is, we may substitute R_1 for the radius in the stability equation for spherical domes under normal external pressure.

Therefore:

$$p = 2CE \left(\frac{t}{R_1} \right)^2 \quad (2.9)$$

expressing t in terms of weight gives:

$$W = A t \rho$$

where

A = surface area

t = shell thickness

ρ = density of material

$$\text{or } t = \frac{W}{A\rho} \quad (2.10)$$

substituting equation (2.10) into equation (2.9) gives

$$\frac{p}{E} = \frac{2 C W^2}{\rho^2 R_1^2 A^2} \quad (2.11)$$

substituting equation (2.8) into equation (2.11) results in

$$\frac{p}{E} = \frac{C W^2}{2\pi^2 \rho^2 R_1^6 \left[(1 - \cos \theta) + \frac{J-1}{J^2} \left(\frac{\pi}{2} \sin \theta - \theta \sin \theta + \frac{\cos \theta}{J-1} \right) \right]} \quad (2.12)$$

In general, it is sometimes more advantageous to express the geometry in terms of a and b instead of R_1 and R_2 . From figure 2.4 the following relationships are developed.

$$a = R_1 \sin\theta - R_2 \sin\theta + R_2$$

or

$$b = R_1 - R_1 \cos\theta + R_2 \cos\theta$$

By some algebraic manipulation

$$R_1 = \frac{a \cos\theta + b (\sin\theta - 1)}{\sin\theta + \cos\theta - 1} \quad (2.13)$$

$$R_2 = \frac{b(\sin\theta + \cos\theta - 1) + (\cos\theta - 1)[a \cos\theta + b(\sin\theta - 1)]}{\cos\theta (\sin\theta + \cos\theta - 1)} \quad (2.14)$$

Since $J = \frac{R_1}{R_2}$ this may be expressed as

$$J = \frac{\cos\theta}{\frac{\sin\theta + \cos\theta - 1}{a/b \cos\theta + \sin\theta - 1} + \cos\theta - 1} \quad (2.15)$$

equation (2.13) may be further simplified to read

$$aR_1' = R_1 = \frac{a \left[\cos\theta + \frac{\sin\theta - 1}{a/b} \right]}{\sin\theta + \cos\theta - 1} \quad (2.16)$$

Letting

$$Q = R_1'^6 \left[(1 - \cos\theta) + \frac{J-1}{J^2} \left(\frac{\pi}{2} \sin\theta - \theta \sin\theta + \frac{\cos\theta}{J-1} \right) \right]^2$$

Equation (2.12) may be expressed as:

$$\frac{P}{E} = \frac{C W^2}{2\pi^2 \rho^2 a^6 Q} \quad (2.17)$$

Assuming a constant buckling coefficient C and constant values of ρ and a, the parameter Q is an index of the efficiency. That is, minimum weight occurs when the parameter Q takes on a minimum value.

To evaluate the parameter Q for a minimum value as a function of θ and a/b , a numerical computer program was used. These results are plotted in figure 1.2. From the figure, the minimum value of Q occurs at $a/b = 1.73$ for an angle $\theta = 60^\circ$.

For $\theta = 60^\circ$, $\sin\theta = \frac{\sqrt{3}}{2}$, $\cos\theta = \frac{1}{2}$ and $1.73 = \sqrt{3}$, so that $\frac{a}{b} = \sqrt{3}$

Substituting these values into the expressions for a and b yield,

$$\sqrt{3} b = R_1 \frac{\sqrt{3}}{2} - R_2 \frac{\sqrt{3}}{2} + R_2, \text{ i.e.}$$

$$b = \frac{R_1}{2} - \frac{R_2}{2} + \sqrt{3} R_2 = R_1 - \frac{R_1}{2} + \frac{R_2}{2}$$

Giving $R_2 = 0$, $\theta = 60^\circ$

This is the same geometry as the optimized shape of the spherical cap.

Zero-Hoop Stress Bulkhead

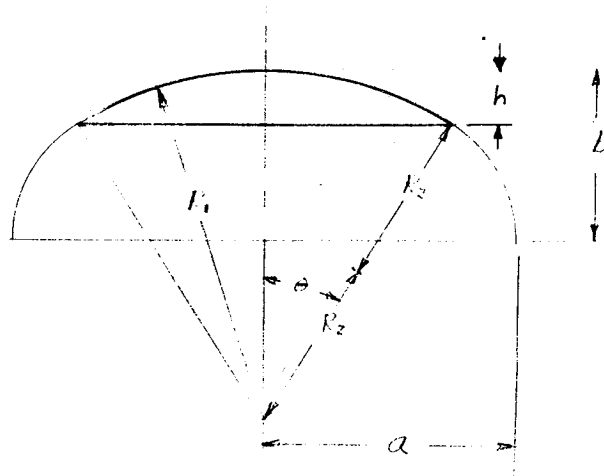


Figure 2.5 - SKETCH OF ZERO-HOOP STRESS BULKHEAD

The total surface area of the dome is

$$A = A_{sc} + A_t \tag{2.18}$$

where A_{sc} = area of spherical cap

and A_t = area of zero-hoop stress torus

The surface area of spherical cap is

$$A_{sc} = 2 \pi R_1^2 (1 - \cos\theta) \quad (2.19)$$

The surface area of zero-hoop torus is

$$A_t = \pi a^2 \left(\frac{\pi}{2} - \theta\right) \quad \text{Reference 26 p. 12} \quad (2.20)$$

substituting equation (2.19) and (2.20) into equation (1) gives

$$A = 2 \pi R_1^2 (1 - \cos\theta) + \pi a^2 \left(\frac{\pi}{2} - \theta\right) \quad (2.21)$$

Since the zero-hoop stress bulkhead is difficult to express analytically, a graphical method is employed using the constants tabulated in Table 2.2. Expressing the spherical radius R_1 in Figure a in terms of the base radius a and the coefficient C_3 from the relationship shown in Table 2.2 results in

$$R_1 = 2 a C_3$$

Substituting the above relationship into equation (2.21) gives

$$A = \pi a^2 [8 C_3^2 (1 - \cos\theta) + \frac{\pi}{2} - \theta] \quad (2.22)$$

From Figure 2.5 since $R_1 = 2 R_2$ and because of the lack of compressive hoop stress in the torus portion of the dome, it may be realistically assumed that the spherical cap will have a lower buckling allowable than that of the zero-hoop stress torus. Substituting R_1 for the radius in the stability equation for spherical domes under normal external pressure gives

$$p = 2CE \left(\frac{t}{R_1}\right)^2 \quad (2.23)$$

Expressing t in the above equation in terms of the dome weight gives

$$W = A t \rho \quad (2.24)$$

where A = total surface area
 t = shell thickness
 ρ = density of material

Substituting equation (2.24) into equation (2.23) gives

$$\frac{p}{E} = \frac{2 C W^2}{\rho^2 A^2 R_1^2} \quad (2.25)$$

Substituting the previous expressions for A and R_1 into the above equation gives

$$\frac{p}{E} = \frac{C W^2}{2 \rho^2 a^6 \pi^2 C_3^2 [8 C_3^2 (1 - \cos \theta) + \frac{\pi}{2} - \theta]^2} \quad (2.26)$$

Letting

$$Q = C_3^2 [8 C_3^2 (1 - \cos \theta) + \frac{\pi}{2} - \theta]^2$$

in equation (2.26) results in

$$\frac{p}{E} = \frac{C W^2}{2 \rho^2 a^6 \pi^2 Q} \quad (2.27)$$

Assuming a constant buckling coefficient C and constant values of ρ and a, the parameter Q is an index of the weight efficiency. That is minimum weight occurs where the parameter Q takes on a minimum value.

Equation (2.27) may also be expressed in terms of the weight efficiency index \bar{w} , by simple algebraic manipulation.

Rewriting equation (2.27) in the form

$$W^2 = Q \rho^2 a^6 \pi^2 \frac{2 p}{C E}$$

$$W = \sqrt{Q} \rho a^3 \pi \sqrt{\frac{2 p}{C E}}$$

Letting $\sqrt{Q} = \bar{w}$

$$W = \bar{w} \rho a^3 \pi \sqrt{\frac{2 p}{C E}}$$

Since it is desirable to compare the results of this configuration with that of the other configurations investigated, it is necessary to express the geometry in terms of the base to height ratio a/b .

From Figure 2.5 where

$$b = y + h \quad \text{and} \quad h = R_1 (1 - \cos\theta)$$

and from Table 2.2 where

$$R_1 = 2aC_3 \quad \text{and} \quad y = aC_2$$

substituting the relationships for y , h , and R_1 results in the following expression for a/b as a function of θ , C_2 and C_3 .

$$\frac{a}{b} = \frac{1}{C_2 + 2C_3 (1 - \cos\theta)}$$

The final results are plotted in Figure 1.2.

Table 2.2

θ	$C_2 = \frac{y}{a}$	$C_3 = \frac{R_1}{2a}$	$\frac{a}{b}$
90	0	0.5000	1
85	.0436	0.5009	1.044
80	.0871	0.5038	1.087
75	.1302	0.5087	1.131
70	.1728	0.5158	1.174
57.5	.2762	0.5444	1.282
45	.3726	0.5946	1.387
32.5	.4590	0.6821	1.486
20	.5318	0.8549	1.572
15	.5559	0.9828	1.606
10	.5764	1.1999	1.630
5	.5924	1.6936	1.650

CHAPTER III - STIFFENED SPHERICAL DOMES UNDER EXTERNAL PRESSURE

MERIDIONAL STIFFENING

Introduction

The state-of-the-art for predicting the buckling pressure for meridionally stiffened spherical caps is essentially based upon a few experimental investigations. Little effort has been expended to develop a stability analysis for this type of stiffened configuration. Basically, the experimental investigations have been limited to exploratory tests in an effort to determine the possible improvement of the buckling pressure of meridionally stiffened domes compared to monocoque domes having the same weight.

Kloppel and Jungbluth's experimental investigations (Reference 12) of meridionally stiffened domes were unsuccessful in their attempt to show an increase in the structural efficiency over that of unstiffened domes. Ebner's experimental program (Reference 16) resulted in an apparent inconsistency for the structural efficiency of the two domes tested in his investigation of meridionally stiffened domes. Recently Krenzke (Reference 17) tested machined meridional stiffened hemispherical domes of small diameter and concluded from his results that the structural efficiency of this reinforcement design is less than that for monocoque domes.

Rib Instability

The variation of the rib spacing along the shell surface results in a load distribution of varying intensity along a meridional rib as shown in Figure 3.1 below:

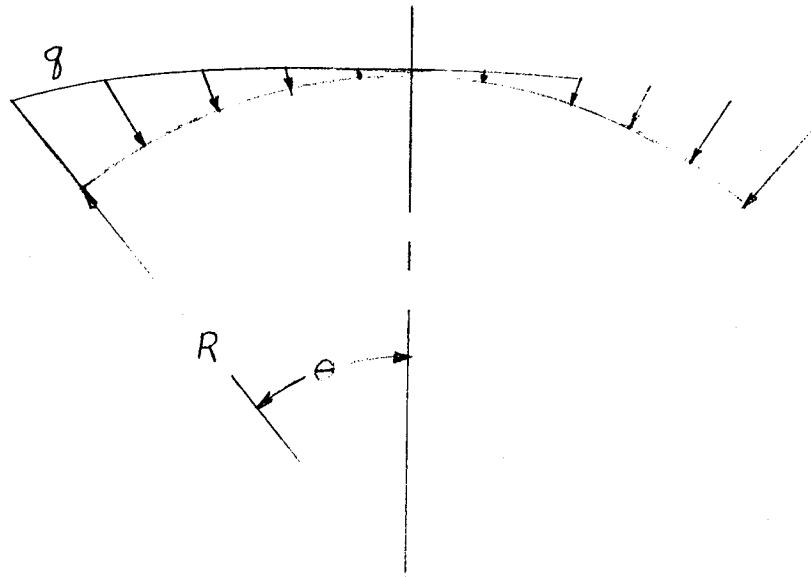


Figure 3.1 - LOAD DISTRIBUTION FOR MERIDIONALLY STIFFENED DOME

Lacking a sufficiently simple analytical method of predicting the stability of the meridional ribs in such a reinforced dome configuration, an approximation of the expected rib stability will be based upon the analysis of a fixed end arch under a uniformly distributed pressure as given by Timoshenko (Reference 20)

Since with the non-uniform loading condition the buckling load will support greater loading than the uniformly loaded arch, a correction coefficient B will be applied to the stability equation of an arch as given by (Reference 20) to reflect the increased failing pressure.

That is

$$q_R = \frac{B' E I'}{R^3} [k^2 - 1] \quad (3.1)$$

where

- q = Loading intensity
- B' = Correction coefficient
- I' = Effective moment of inertia of rib and skin
- R = Radius of arch
- k = Buckling coefficient evaluated by trial from the equation $k \tan \theta \cot k \theta = 1$.

If it is assumed that failure will initiate at the point of the maximum inscribed radius considered for panel instability, then equation (3.1) may be expressed as

$$p_R = \frac{B' E I'}{2 r R^3} [k^2 - 1] \quad (3.2)$$

If a simplifying assumption is made that local panel failure occurs just prior to rib instability, the resulting post buckling strength of the rib need not consider an effective skin acting with the rib. That is, I' may be replaced with I_R in equation (3.2)

Therefore

$$p_R = \frac{B E I}{r R^3} [k^2 - 1] \quad (3.3)$$

where

$$B = \frac{B'}{2}$$

From experiment the correction factor B may be determined.

The experimental result from the first meridionally stiffened dome (#1-M) using equation (3.3) showed that B had a value of 5.0. Although primary failure was due to panel instability there was no secondary rib failure. Therefore, B = 5.0 describes a lower bound of the correction factor. Higher values of B are to be expected in subsequent tests when rib failure occurs. A value of B = 5.0 will be assumed adequate in a preliminary evaluation of rib stability in the proceeding analysis

Panel Stability

The allowable panel buckling of the skin between the radial stiffeners will be based upon the theory of Huang (Reference 7) in the region where the nondimensional parameter λ is > 4 , and for the region of $\lambda < 4$ plate stability will be based upon flat plate theory, since the effects of curvature become small. The validity of these assumptions will be justified later in the analysis by experimental data.

The non-dimensional parameter λ is defined as

$$\lambda = [12 (1 - \nu^2)]^{1/4} \frac{a}{\sqrt{Rt}} \quad (3.4)$$

where

- R = Spherical radius of curvature
- t = Thickness of dome
- ν = Poisson's ratio
- a = Base radius of dome

To make the above non-dimensional parameter λ applicable to local panel instability it is necessary to substitute for a, the radius of the largest inscribed panel between the meridional ribs. This radius is depicted in the sketch.

Therefore, for panel instability

$$\lambda = [12 (1 - \nu^2)]^{1/4} \frac{r}{\sqrt{Rt}} \quad r = \psi R \quad (3.5)$$

where the variable ψ may be shown to be

$$\psi = \arcsin \left(\frac{\sin a \operatorname{sinc}}{\operatorname{sind}} \right)$$

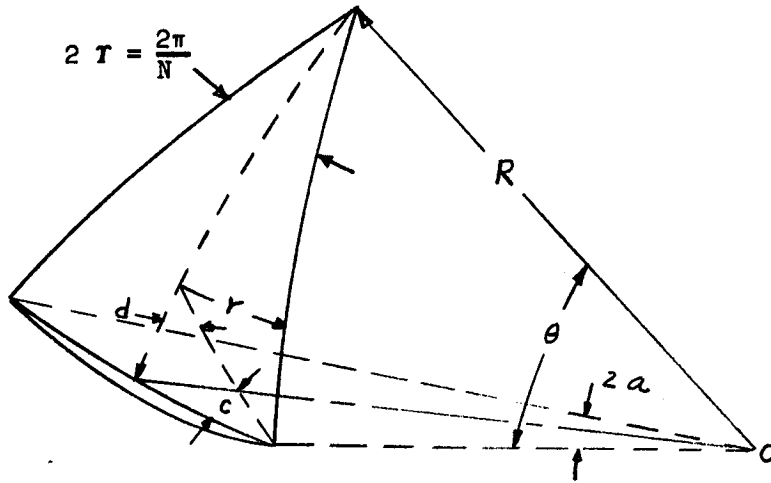
where

$$a = \frac{\text{arc cos}}{2} (\cos^2 \theta + \sin^2 \theta \cos 2 \tau)$$

$$c = \text{arc sin} \left(\frac{\sin 2 \tau \sin \theta}{\sin 2 a} \right)$$

$$d = \text{arc cos} (\sin c \cos a)$$

(ψ versus N is plotted in Figure 3.2 for $\theta = 23^\circ 35'$ and $\theta = 60^\circ$.)



From (Reference 20) the stability of a flat circular plate is expressed as

$$\sigma_{cr} = \frac{K E}{(1 - \nu^2)} \left(\frac{t}{r} \right)^2 \quad (3.6)$$

where K is the edge fixity coefficient.

Equating $\sigma_{cr} = \frac{P_{cr} R}{2 t}$ with equation (3.6) results in

$$P_{cr} = \frac{2 K E t^3}{(1 - \nu^2) R r^2} \quad (3.7)$$

to express the above equation in non-dimensional form using the parameters of λ and P_{cr}/P_{class} the following manipulations are necessary.

Dividing both sides of equation (3.7) by P_{class} where

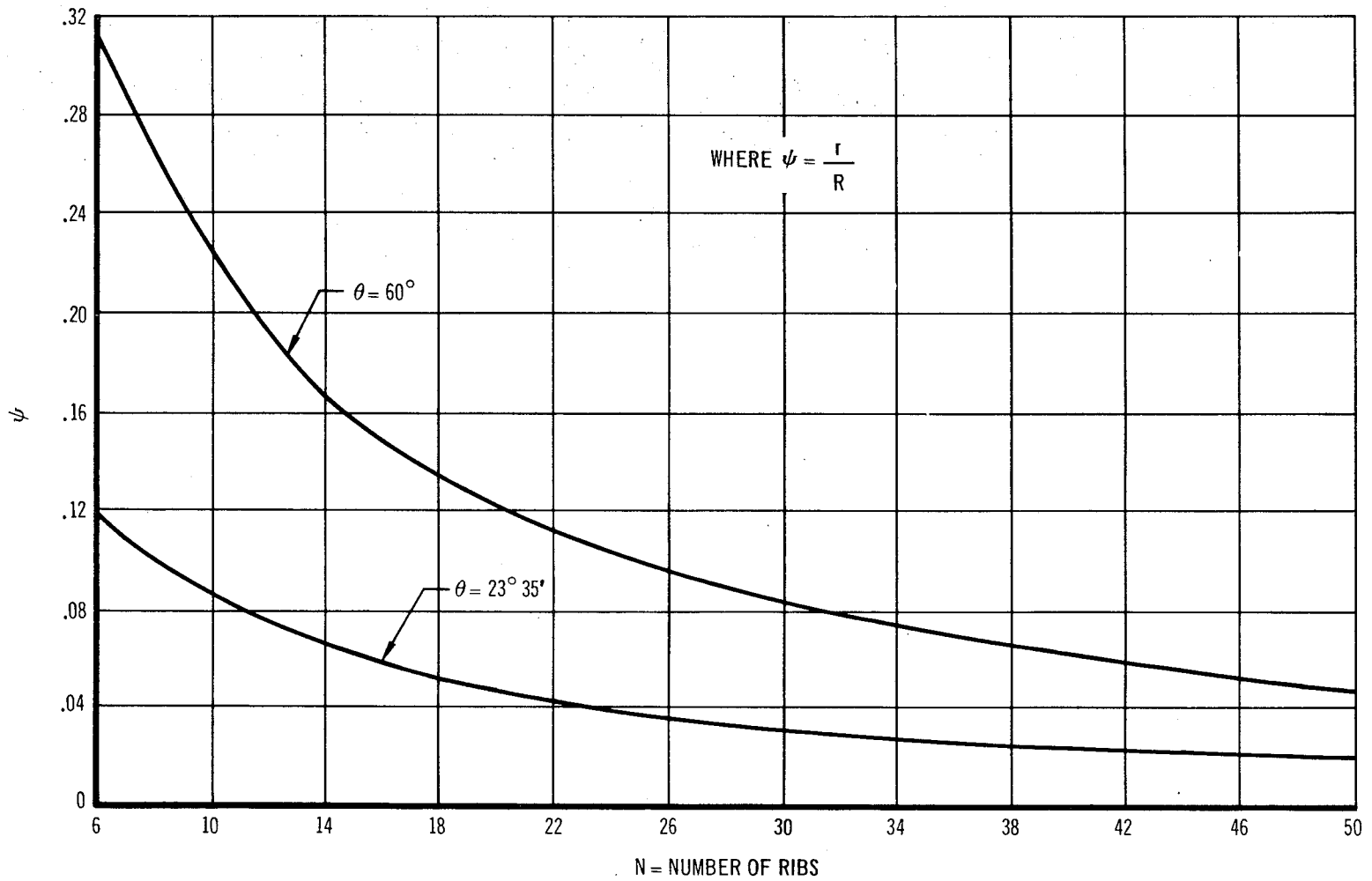


FIGURE 3.2 PANEL RADIUS VERSUS NUMBER OF RIBS

$$P_{\text{class}} = \frac{1.156 E}{\sqrt{1 - \nu^2}} \left(\frac{t}{R}\right)^2$$

results in

$$\frac{P_{\text{cr}}}{P_{\text{class}}} = \frac{2 K t R}{1.156 r^2 \sqrt{1 - \nu^2}} \quad (3.8)$$

Substituting equation (3.5) into equation (3.8) and simplifying gives

$$\frac{P_{\text{cr}}}{P_{\text{class}}} = \frac{6.0 K}{\lambda^2} \quad (3.9)$$

where $K = 1.22$ for clamped edge support
 $K = 0.35$ for simply supported edges

Since the actual condition of edge restraint for the circular inscribed panels between the meridional ribs is unknown, equation (3.9) will be plotted in figure (3.3) using both conditions of edge restraint. To test the validity of this predicted panel buckling equation, Ebner's experimental results on meridionally stiffened spherical caps (Reference 16) are plotted in the same figure. It is not clear from the experiments as to the primary mode of failure, but from the agreement with the predicted panel instability equation, it seems that panel failure was incipient. Since the test points fit more closely to the condition of clamped edge, this condition will be assumed in the prediction of the local panel stability. That is substituting $K = 1.22$ into equation (3.7) results in

$$P = \frac{2.44 E t^3}{(1 - \nu^2) R r^2} \quad (3.10)$$

It was previously stated that the theory for the stability of spherical caps rigidly supported at the base as developed by Huang in Reference 7, was also applicable to the prediction of local panel stability of an inscribed circular plate between the meridional stiffeners. This assumption is substantiated when a comparison between Huang's theory and the experimental tests conducted by Krenzke (Reference 17) and this paper. The results are shown in Figure 3.3. The experimental domes show clearly that primary failure occurred by panel instability between the rib supports.

It may be concluded from the figure that, for plate geometry's resulting in $\lambda < 3$ that panel stability is the limiting mode of failure and cannot exceed the ratio of $P/P_{class} \approx 0.80$. This implies that all reinforced domes falling into this region of λ , the structural efficiency will be less than a monocoque dome of equivalent weight.

The region of interest for reinforced domes is therefore confined in $\lambda < 3$ where panel stability is greater than the limit imposed by Huang's theory. This region may be obtained by introducing a sufficient number of stiffeners such that the radius of the unsupported plate is small. Therefore, the proceeding analysis will be concerned with the arrangement of stiffeners that allow $\lambda < 3$.

Optimum Design

In general, failure of reinforced meridional domes may be attributed to two distinct modes of failure; Panel instability of the unsupported skin between the ribs, and general instability of the meridional ribs. For an optimal arrangement of reinforcement the two modes of failure occurs simultaneously. Although coupling or interaction between the failing modes normally exist, for an approximate analysis the two failure modes will be considered to be independent of each other.

Using the equations previously developed it is now possible to arrive at an optimum design for the meridional stiffened domes.

The total weight of the dome may be expressed as

$$W_t = W_s + W_R \quad (3.11)$$

where

- W_t = total weight of dome
- W_s = weight of shell
- W_R = weight of ribs

the weight of the shell and ribs are given as

$$W_s = \rho_s 2 \pi R^2 t (1 - \cos\theta) \quad (3.12)$$

and

$$W_R = \rho_R N R \theta A_R \quad (3.13)$$

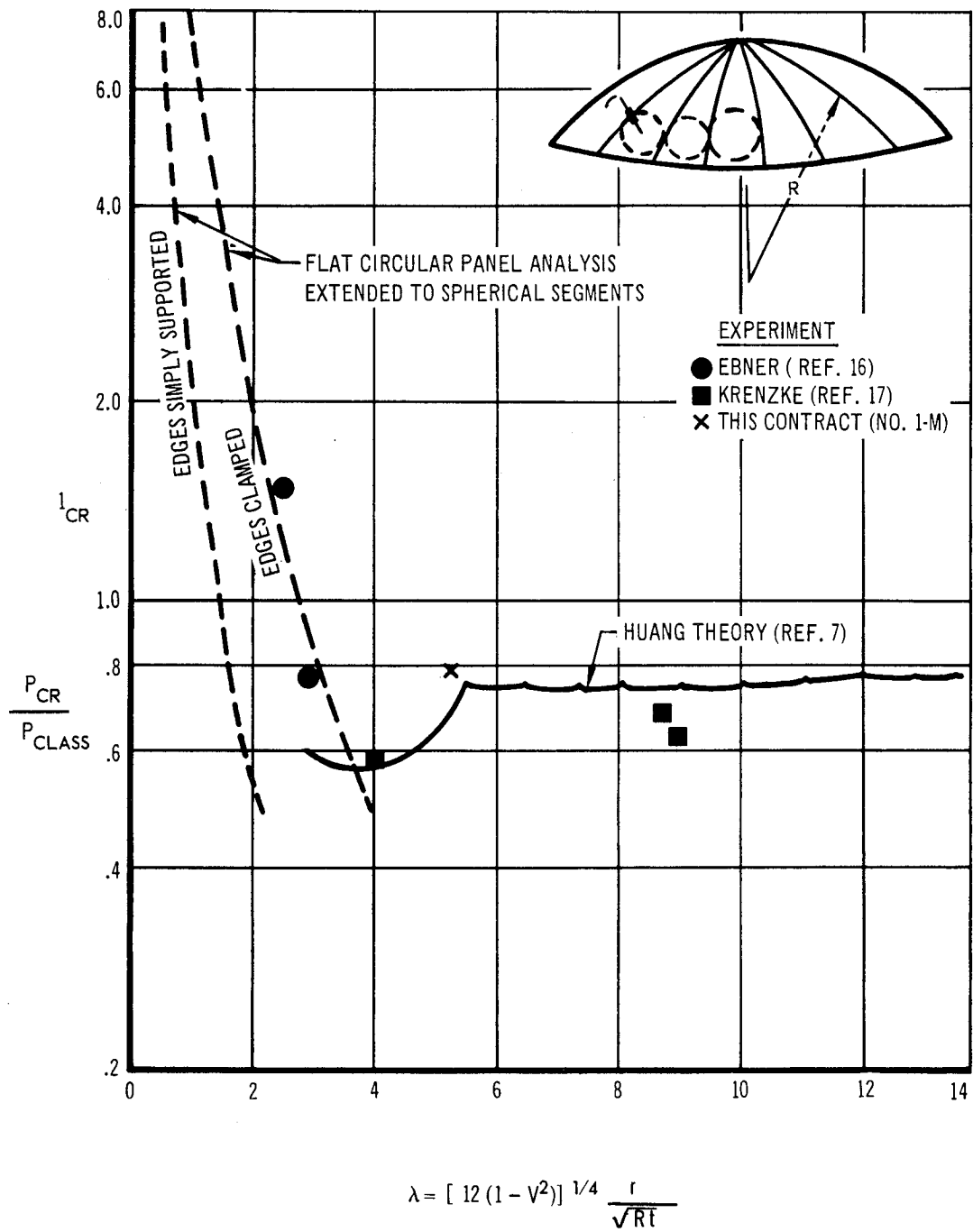


FIGURE 3.3 LOCAL PANEL BUCKLING OF MERIDIONALLY STIFFENED SPHERICAL CAPS UNDER EXTERNAL PRESSURE

where

- ρ_s, ρ_R = Density of material of shell and ribs respectively
 θ = Half opening angle of dome
 N = Number of meridional ribs
 A_R = Area of rib
 t = Shell thickness

Substituting equations (3.12) and (3.13) into equation (3.11) and assuming $\rho_s = \rho_R$ results in

$$W_t = \rho [2 \pi R^2 t (1 - \cos\theta) + N R \theta A_R] \quad (3.14)$$

From equation (3.7) the critical buckling pressure of the panel was given as

$$p_p = \frac{2 K E t^3}{(1 - \nu^2) R r^2} \quad (3.15)$$

or this may be expressed in terms of the shell thickness as

$$t = \frac{p_p^{1/3} R^{1/3} r^{2/3} (1 - \nu^2)^{1/3}}{K^{1/3} E^{1/3} 2^{1/3}} \quad (3.16)$$

and from equation (3.3) the stability of the meridional rib was given as

$$p_R = \frac{B E I_R (k^2 - 1)}{r R^3}$$

since

$$I_R = \Gamma^2 A_R$$

where Γ = radius of gyration of rib.

Substituting into the above equation and solving in terms of the rib area results in

$$A_R = \frac{p_R R^3 r}{B E \Gamma^2 (k^2 - 1)} \quad (3.17)$$

Substituting equations (3.16) and (3.17) into equation (3.14) results in

$$W_T = \frac{2 \pi R^2 (1 - \cos \theta) p_p^{1/3} R^{1/3} r^{2/3}}{K^{1/3} E^{1/3} 2^{1/3} (1 - \nu^2)^{1/3}} + \frac{N R \theta R^3 r p_R}{B E \Gamma^2 (k^2 - 1)} \quad (3.18)$$

Since optimum design assumes that both panel and rib failure occur simultaneously,

$$p_p = p_R = p$$

by proper substitution, equation (3.18) may be expressed as

$$\frac{W_T}{\rho} = \left(\frac{p}{E}\right)^{1/3} \left[\frac{2 \pi R^2 (1 - \cos \theta) R^{1/3} r^{2/3}}{K^{1/3}} + \frac{N \theta K'^{2/3} t^2 R^{10/3}}{B \Gamma^2 (k^2 - 1) r^{1/3}} \right] \quad (3.19)$$

where

$$K' = \frac{K}{1 - \nu^2}$$

letting $\psi = \frac{r}{R}$ and simplifying the above equation results in

$$\frac{W_T}{\rho} = \left(\frac{p}{E}\right)^{1/3} \frac{R^3 \psi^{2/3}}{K^{1/3}} \left[2 \pi (1 - \cos \theta) + \frac{N \theta t^2 K'}{\psi B \Gamma^2 (k^2 - 1)} \right]$$

It is desired to express the total weight W_T in terms of an average weight thickness \bar{t} . Where

$$\bar{t} = \frac{W_T}{\rho 2 \pi R^2 (1 - \cos \theta)}$$

Substituting the above relationship into equation (3.19) and simplifying gives

$$\frac{\bar{t}}{R} = \left(\frac{p}{E}\right)^{1/3} \left[\frac{\psi^{2/3}}{K^{1/3}} \left(1 + \frac{N \theta K' t^2}{B 2 \pi (1 - \cos \theta) (k^2 - 1) \Gamma^2} \right) \right]$$

where the expression inside the brackets [] is defined as the inverse of the efficiency η

That is

$$\eta = \frac{1}{\frac{\psi^{2/3}}{K'^{1/3}} \left(1 + \frac{N \theta K' t^2}{B 2 \pi (1 - \cos \theta)(k^2 - 1) \Gamma^2} \right)} \quad (3.20)$$

therefore

$$\frac{t}{R} = \frac{1}{\eta} \left(\frac{p}{E} \right)^{1/3} \quad (3.21)$$

For optimum design it is necessary that the efficiency term η be maximized in equation (3.21).

Substituting the empirically determined coefficients of K' and B of $2.44/1 - v^2$ and 5.00 respectively into equation (3.20) results in

$$\eta = \frac{1}{\frac{(1 - v^2)\psi^{2/3}}{1.346} \left(1 + \frac{N \theta 2.44 t^2}{10\pi(1 - \cos \theta)(k^2 - 1)(1 - v^2)\Gamma^2} \right)}$$

The equation above is solved for half-dome opening angles of $\theta = 23^\circ$, $35'$ and $\theta = 60^\circ$ for various ratios of $(t/\Gamma)^2$. The results are plotted in Figure 3.4.

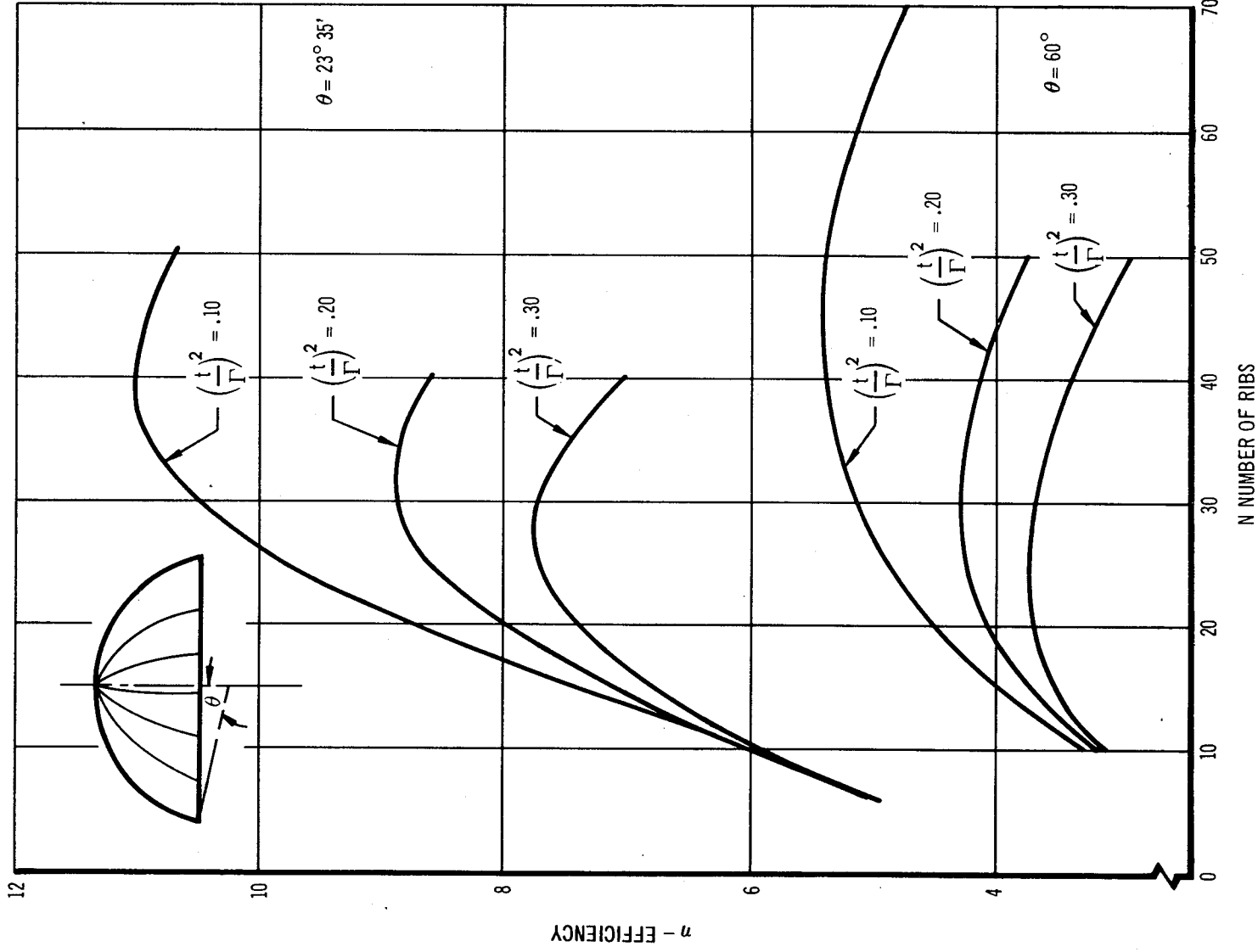


FIGURE 3.4 INDEX OF STRUCTURAL EFFICIENCY OF MERIDIONAL STIFFENED DOMES

CIRCUMFERENTIAL STIFFENING

Introduction

In the present study, a semi-empirical optimization analysis will be applied to a special case of dome reinforcement; that of circumferential ring stiffeners. This semi-empirical formulation assumes that the stability of a spherical dome may be approximated by short cone elements bounded by circumferential frames subjected to external pressures. The boundary condition will be sufficient to provide a simply supported cone element whose buckling mode consists of one-half wave in longitudinal direction and many waves in the circumferential direction. With sufficient bending rigidity in the closure frames to prevent frame instability, the problem is reduced to the study of local panel failure between the frames. Basically the optimization study then consists of selecting the frame areas and spacing so that all panels fail simultaneously under a given pressure with a minimum amount of weight.

Shell Segment Instability

To idealize a spherical dome subjected to external pressure by short cone elements, a necessary condition that must be satisfied is that the membrane loads are compatible.

The membrane loads in a spherical cap under uniform pressure are

$$N_{\phi} = N_{\theta} = \frac{pR}{2} \quad (3.22)$$

where

N_{ϕ} = Meridional Load lb/in

N_{θ} = Hoop Load lb/in

R = Radius of Curvature in

P = Pressure - lb/in²

The membrane loads in a conical shell under uniform hydrostatic pressure are expressed as

$$N_{\phi} = \frac{p_c R}{2} ; \quad N_{\theta} = p_c R \quad (3.23)$$

where the radius (R) is assumed to be the average radius of curvature of the conical shell.

Since the membrane loads are not compatible with equation (3.22), an axial load will be applied such that

$$N_{\phi} = \frac{p_c R}{2}; \quad N_{\theta} = 0 \quad (3.24)$$

Summing the total membrane loads as given by equations (3.23) and (3.24) results in

$$N_{\phi} = N_{\theta} = p_c R \quad (3.25)$$

Equating equations (3.22) and (3.25) and solving for p results in

$$p = 2 p_c \quad (3.26)$$

From reference 25 the allowable buckling pressure for a cone under uniform external pressure may be expressed as

$$p_c = .92 E \left(\frac{t}{R_{avg}} \right)^{5/2} \frac{R_{avg}}{l} \quad (3.27)$$

where

l = slant length of cone

R_{avg} = average radius of cone

substituting $p = 2 p_c$ from equation (3.26) into equation (3.27) gives

$$p = 1.84 E \left(\frac{t}{R_{avg}} \right)^{5/2} \frac{R_{avg}}{l} \quad (3.28)$$

The approximation of a spherical cap by small cone elements neglects the important effect of the increased stability due to the curvature of the shell. An estimate of this effect may be studied empirically by evaluating the experimental results from reference 17 for hemispherical domes under uniform external pressure, reinforced by circumferential rings. The increase in the buckling stability due to the curvature effect will be based upon the following empirical relationship.

$$\frac{P_{\text{exp}}}{P} = f \left(\frac{h}{\ell} \right) \quad (3.29)$$

where

- P_{exp} = Experimental Buckling Pressure
- P = Buckling Pressure From Equation (3.28)
- h = Curvature Index
- ℓ = Slant Length of Cone

A plot of this functional relationship is shown in figure 3.5 using the selected experimental data resulting in $p_{\text{exp}}/P > 1$. A solid line is drawn through the test data and extrapolated for values of $h/\ell < .03$. For the purpose of evaluating the curvature effect, the empirical curve in figure 3.5 will be expressed analytically. A parabolic function of the form $y = a + bx^n$ seems to adequately describe the curve within the region of primary interest and is indicated by the dotted line in figure 3.5. Determining the constants yields the following equation

$$P_{\text{exp}} = P \left[1.0 + 94 \left(\frac{h}{\ell} \right)^2 \right] \quad (3.30)$$

for the limit $h/\ell < .05$.

Since the empirical data is probably conservative, because the failures indicated the the circumferential rings did not provide the necessary condition of edge restraint as assumed by the cone analysis, the equation is a more optimistic estimate of the curvature effect.

Substituting equation (3.28) into the above equation gives

$$P_{\text{exp}} = \frac{1.84 E}{\ell/R_{\text{avg}}} \left(\frac{t}{R_{\text{avg}}} \right)^{5/2} \left[1.0 + 94 \left(\frac{h}{\ell} \right)^2 \right] \quad (3.31)$$

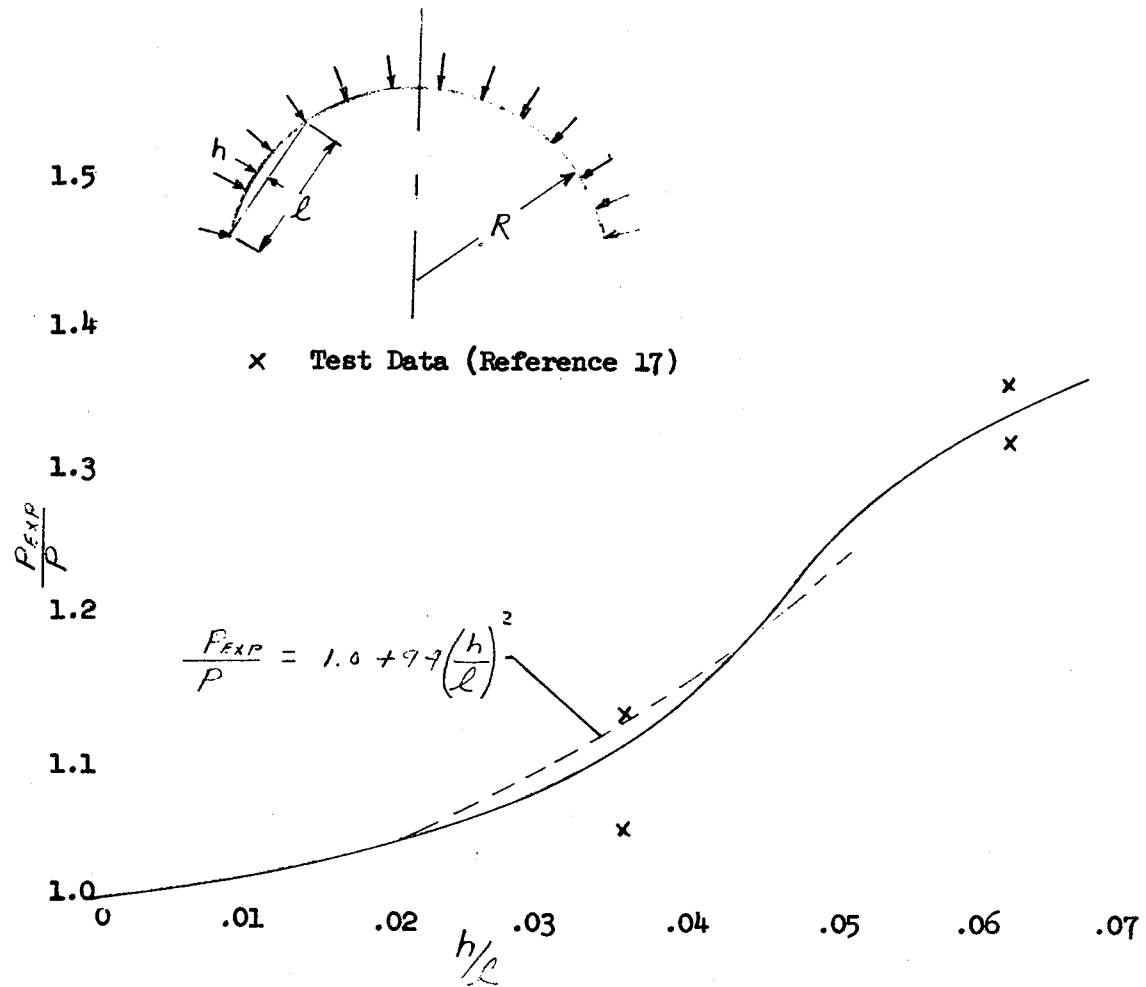
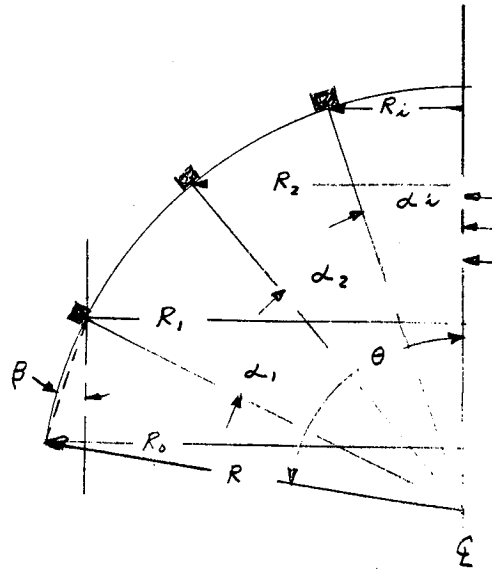


Figure 3.5 - Estimated Effect of Curvature



Optimization of First Cone Element

The total weight of the first cone element is composed of the weight of the skin panel and the weight of the circumferential ring. The total weight is expressed as

$$W_1 = W_{p_1} + W_{R_1} \quad (3.32)$$

where

W_1 = Total weight of first cone element

W_{p_1} = Panel weight of first cone element

W_{R_1} = Ring weight of first cone element

A_{R_1} = Ring cross sectional area associated with "first cone"

ρ = Density of material

From the sketch

$$W_{p_1} = 2\pi R_1^2 t_1 (\cos\alpha_1 - \cos\theta) \quad (3.33)$$

$$W_{R_1} = 2\pi R_1 A_{R_1} \quad (3.34)$$

Ring Instability

Since there is no rigorous analytical method of determining the area of the rings necessary to prevent general instability failure of the cone, an approximate analysis developed by Shanley (reference 18) for approximation. From the reference the cross sectional area of the frame necessary to prevent general instability buckling is given as

$$A_R = \left(\frac{C_F}{K}\right)^{1/2} \frac{D M^{1/2}}{l^{1/2} E_F^{1/2}} \quad (3.35)$$

where

C_F = Dimensionless empirical coefficient

K = Shape coefficient for frame

E_F = Modulus of Elasticity of frame

D = Diameter

M = Bending moment

l = Distance between frames

Expressing M in terms of the equivalent loading index N gives

$$M = \frac{N \pi D^2}{4}$$

where N may be expressed as a function of pressure by $N = \frac{PR}{2}$, substituting the above equations into equation (3.35) results in

$$A_R = \left(\frac{2 \pi C_F}{K}\right)^{1/2} \frac{R^{5/2} p^{1/2}}{l^{1/2} E_F^{1/2}} \quad (3.36)$$

Neglecting the effect of curvature, the critical buckling pressure of the cone element as given by equation (3.28) is

$$P = 1.84 E \left(\frac{t}{R_{avg}} \right)^{5/2} \frac{R_{avg}}{\ell}$$

substituting the above equation in equation (3.36) (assuming $E_F = E$) and simplifying results in

$$A_R = \frac{t R^2}{N' \ell \left(\frac{R}{t} \right)^{1/4}}$$

where

$$N' = \sqrt{\frac{K}{3.68 \pi C_F}} \quad (3.37)$$

since $(R/t)^{1/4}$ is relatively insensitive over a wide range of values it will be treated as a constant

that is

$$N = \left(\frac{R}{t} \right)^{1/4} N'$$

therefore

$$A_R = \frac{t R^2}{N \ell} \quad (3.38)$$

Since the development of the constant in equation (3.37) is very approximate, it will be evaluated experimentally.

Design Optimization

Substituting equation (3.38) into equation (3.34) and evaluating equation (3.32) results in

$$W_1 = 2 \pi R^2 t_1 \rho (\cos \alpha_1 - \cos \theta) + \frac{2 \pi R_1^3 t_1 \rho}{N l_1} \quad (3.39)$$

since

$$R_1 = R \sin \alpha_1$$

$$l_1 = 2 R \sin \left(\frac{\theta - \alpha_1}{2} \right)$$

substituting and simplifying

$$W_1 = 2 \pi R^2 t_1 \rho \left[\cos \alpha_1 - \cos \theta + \frac{\sin^3 \alpha_1}{2 N \sin \left(\frac{\theta - \alpha_1}{2} \right)} \right] \quad (3.40)$$

solving for t_1 gives

$$t_1 = \frac{W_1}{2 \pi R^2 \rho \left[\cos \alpha_1 - \cos \theta + \frac{\sin^3 \alpha_1}{2 N \sin \left(\frac{\theta - \alpha_1}{2} \right)} \right]} \quad (3.41)$$

substituting equation (3.41) into the stability equation (3.31) for the dome gives

$$\frac{p_1}{E_1} = \frac{1.84 \left[1.0 + 94 \left(\frac{h}{l_1} \right)^2 \right] W_1^{5/2}}{\frac{l_1}{R_{avg}} R_{avg}^{5/2} \left\{ 2 \pi R^2 \rho \left[\cos \alpha_1 - \cos \theta + \frac{\sin^3 \alpha_1}{2 N \sin \left(\frac{\theta - \alpha_1}{2} \right)} \right] \right\}^{5/2}} \quad (3.42)$$

where from the figure for the first cone element

$$h = R \left[1 - \cos \left(\frac{\theta - \alpha_1}{2} \right) \right]$$

$$\lambda_1 = 2 R \sin \left(\frac{\theta - \alpha_1}{2} \right)$$

$$R_{\text{avg}} = \frac{R_0 + R_1}{2 \cos \beta} = \frac{R}{2} \left[\frac{\sin \theta + \sin \alpha_1}{\cos \left[\frac{\pi}{2} - \frac{\theta_1 + \alpha_1}{2} \right]} \right]$$

substituting into equation (3.42) and simplifying gives

$$\frac{P_1}{E_1} = \frac{1.84}{2 \pi^{5/2} R^5} \left(\frac{W_1}{R \rho} \right)^{5/2} \left\{ \quad \right\} \quad (3.43)$$

where the terms inside the brackets $\left\{ \quad \right\}$ is

$$1 + 94 \left[\frac{1 - \cos \left(\frac{\theta - \alpha_1}{2} \right)}{2 \sin \left(\frac{\theta - \alpha_1}{2} \right)} \right]^2$$

$$\left[\frac{\sin \theta + \sin \alpha_1}{\cos \left[\frac{\pi}{2} - \frac{\theta_1 + \alpha_1}{2} \right]} \right]^{3/2} \left[\cos \alpha_1 - \cos \theta + \frac{\sin^3 \alpha_1}{2 N \sin \left(\frac{\theta - \alpha_1}{2} \right)} \right]^{5/2} \left[2 \sin \left(\frac{\theta - \alpha_1}{2} \right) \right]$$

In the above equation substituting λ_1 , Q_1 and J where

$$\lambda_1 = \frac{1 + 94 \left[\frac{1 - \cos \left(\frac{\theta - \alpha_1}{2} \right)}{2 \sin \left(\frac{\theta - \alpha_1}{2} \right)} \right]^2}{2 \sin \left(\frac{\theta - \alpha_1}{2} \right) \left[\frac{\sin \theta + \sin \alpha_1}{\cos \left[\frac{\pi}{2} - \frac{\theta + \alpha_1}{2} \right]} \right]^{3/2}}$$

$$Q_1 = \cos \alpha_1 - \cos \theta + \frac{\sin^3 \alpha_1}{2 N \sin \left(\frac{\theta - \alpha_1}{2} \right)}$$

$$J = \frac{1.84}{2 \pi^{5/2} R^5 (R \rho)^{5/2}}$$

results in

$$\frac{p_1}{E_1} = \frac{J W_1^{5/2} \lambda_1}{Q_1^{5/2}} \quad (3.44)$$

The weight of the first cone element (W_1) from equation (3.40) was shown to be

$$W_1 = 2 \pi R^2 t_1 \rho \left[\cos \alpha_1 - \cos \theta + \frac{\sin^3 \alpha_1}{2 N \sin\left(\frac{\theta - \alpha_1}{2}\right)} \right]$$

This may be simplified by substituting Q_1 from the previous relationship, therefore

$$W_1 = 2 \pi R^2 t_1 \rho Q_1 \quad (3.45)$$

For the succeeding cone elements

$$\frac{p_2}{E_2} = \frac{J W_2^{5/2} \lambda_2}{Q_2^{5/2}}$$

$$\frac{p_3}{E_3} = \frac{J W_3^{5/2} \lambda_3}{Q_3^{5/2}}$$

or

$$\frac{p_i}{E_i} = \frac{J W_i^{5/2} \lambda_i}{Q_i^{5/2}}$$

and also the weights of the succeeding cone element may be expressed as

$$W_2 = 2 \pi R^2 t_2 \rho Q_2$$

$$W_3 = 2 \pi R^2 t_3 \rho Q_3$$

or

$$W_i = 2 \pi R^2 t_i \rho Q_i$$

The total weight of the stiffened dome may be expressed as

$$W_T = W_1 + W_2 + \dots W_i + W_{i+1} \quad (3.46)$$

Using the previously developed equations, it may be shown that the total weight, as given by equation (3.46), may be expressed as

$$W_T = \left(\frac{p_1}{E_1 J}\right)^{2/5} \frac{Q_1}{\lambda_1^{2/5}} + \left(\frac{p_2}{E_2 J}\right)^{2/5} \frac{Q_2}{\lambda_2^{2/5}} + \dots + \left(\frac{p_i}{E_i J}\right)^{2/5} \frac{Q_i}{\lambda_i^{2/5}} + \left(\frac{p_{i+1}}{E_{i+1} J}\right)^{2/5} \frac{Q_{i+1}}{\lambda_{i+1}^{2/5}}$$

Since optimum design requires that all cone elements fail simultaneously then, $p_1 = p_i$

Assuming that $E_1 = E_i$, the above equation is further simplified to read

$$W_T = \left(\frac{p}{E J}\right)^{2/5} \left[\frac{Q_1}{\lambda_1^{2/5}} + \frac{Q_2}{\lambda_2^{2/5}} + \dots + \frac{Q_i}{\lambda_i^{2/5}} + \frac{Q_{i+1}}{\lambda_{i+1}^{2/5}} \right] \quad (3.47)$$

By proper substitution it may be shown that

$$p = J(2 \pi R^2 t_1 \rho)^{5/2} \lambda_1 = J(2 \pi R^2 t_2 \rho)^{5/2} \lambda_2 = J(2 \pi R^2 t_i \rho)^{5/2} \lambda_i$$

Assuming that the thickness of the shell (t) is constant.

That is

$$t_1 = t_2 = t_i$$

therefore

$$\lambda_1 = \lambda_2 = \lambda_i$$

Substituting these relationships into equation (3.47) results in

$$W_T = \left(\frac{p}{E J \lambda_1} \right)^{2/5} [Q_1 + Q_2 + \dots + Q_i + Q_{i+1}] \quad (3.48)$$

or this may be expressed as

$$p = \frac{J W_T^{5/2} \lambda_1}{[Q_1 + Q_2 + \dots + Q_i + Q_{i+1}]^{5/2}} \quad (3.49)$$

where

$$Q_1 = \left[\cos \alpha_1 - \cos \theta + \frac{\sin^3 \alpha_1}{2 N \sin\left(\frac{\theta - \alpha_1}{2}\right)} \right]$$

$$Q_2 = \left[\cos \alpha_2 - \cos \alpha_1 + \frac{\sin^3 \alpha_1 + \sin^3 \alpha_2}{2 N \sin\left(\frac{\alpha_1 - \alpha_2}{2}\right)} \right]$$

$$Q_i = \left[\cos \alpha_i - \cos \alpha_{i-1} + \frac{\sin^3 \alpha_{i-1} + \sin^3 \alpha_i}{2 N \sin\left(\frac{\alpha_{i-1} - \alpha_i}{2}\right)} \right]$$

$$Q_{i+1} = \left[1 - \cos \alpha_i + \frac{\sin^3 \alpha_i}{2 N \sin \frac{\alpha_i}{2}} \right]$$

letting

$$\eta = \frac{\lambda_i}{[Q_1 + Q_2 + \dots + Q_i + Q_{i+1}]^{5/2}}$$

Equation (3.49) may be expressed as

$$\frac{p}{E} = J \eta W_T^{5/2} \quad (3.50)$$

where η is the efficiency of the circumferentially stiffened dome. For optimum design η is to be maximum.

The efficiency η is evaluated for a specific case of a dome half opening angle $\theta = 60^\circ$. The results are shown in figure 3.6 for assumed values of $N = 200, 300$ and 400 . It may be seen that for increasing values of N that the efficiency does not increase linearly. At $N = 400$ the maximum efficiency is shown to be at $\alpha_1 = 55^\circ$.

An interesting result develops in the selection of the succeeding frame spacings for optimum design requirements. As a consequence of equating $\lambda_1 = \lambda_i$ in the previous equations, a unique solution exists that shows for optimum design the frame spacings are equal. That is equating $\lambda_1 = \lambda_i$ results in

$$\begin{aligned} & \frac{1 + 94 \left[\frac{1 - \cos\left(\frac{\theta - \alpha_1}{2}\right)}{2 \sin\left(\frac{\theta - \alpha_1}{2}\right)} \right]^2}{2 \sin\left(\frac{\theta - \alpha_1}{2}\right) \left[\frac{\sin\theta + \sin\alpha_1}{\cos\frac{\pi}{2} - \frac{\theta - \alpha_1}{2}} \right]^{3/2}} \\ &= \frac{1 + 94 \left[\frac{1 - \cos\left(\frac{\alpha_{i-1} - \alpha_i}{2}\right)}{2 \sin\left(\frac{\alpha_{i-1} - \alpha_i}{2}\right)} \right]^2}{2 \sin\left(\frac{\alpha_{i-1} - \alpha_i}{2}\right) \left[\frac{\sin\alpha_{i-1} + \sin\alpha_i}{\cos\frac{\pi}{2} - \frac{\alpha_{i-1} + \alpha_i}{2}} \right]^{3/2}} \end{aligned}$$

It may be shown that the equality may only exist if

$$\theta - \alpha_1 = \alpha_{i-1} - \alpha_i$$

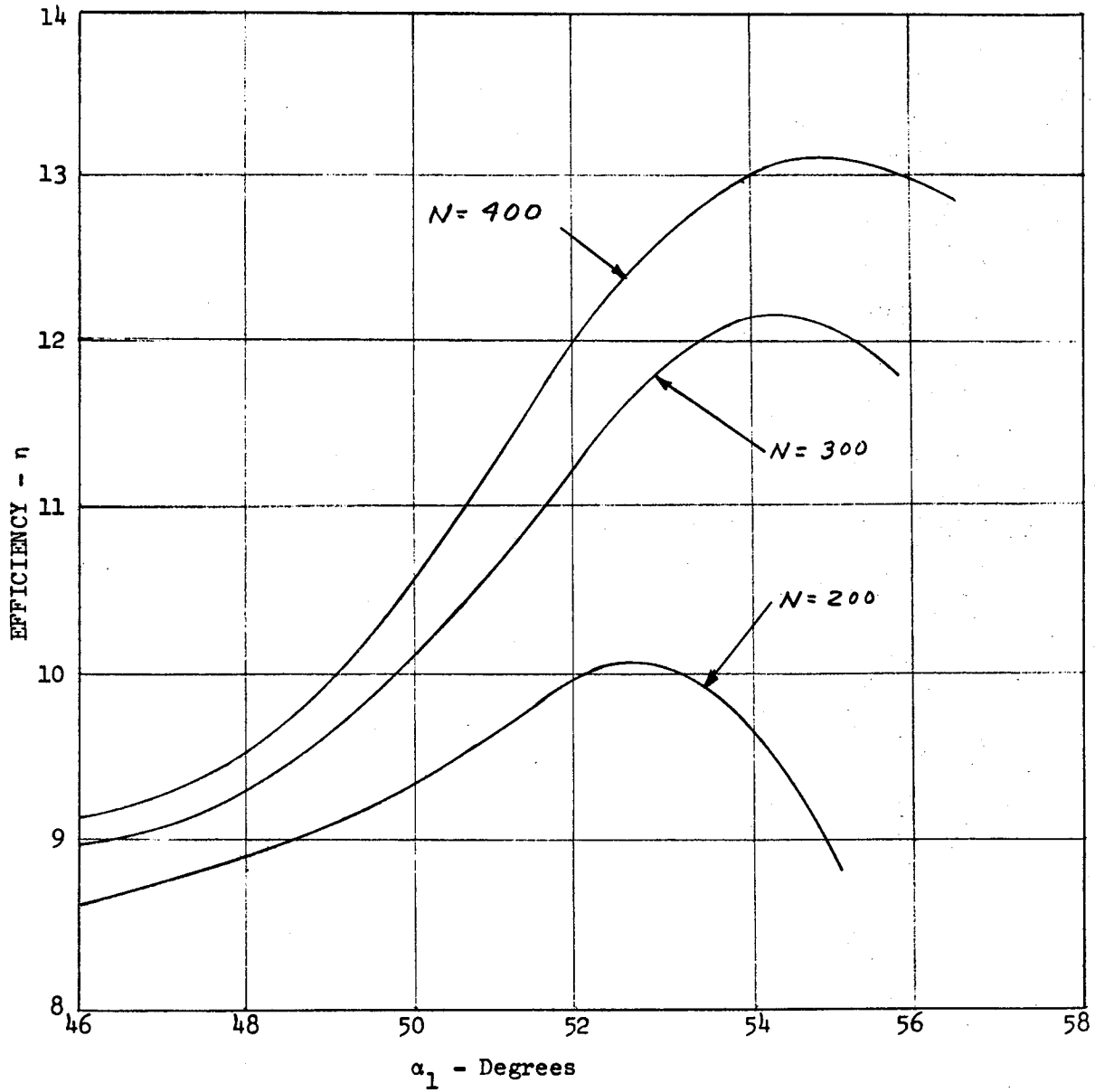


Figure 3.6 - EFFICIENCY OF CIRCUMFERENTIALLY STIFFENED SPHERICAL DOME - $\theta = 60^\circ$

CHAPTER IV - GEODESIC RIB-STIFFENED SPHERICAL DOMES

Introduction

For spherical domes, it has been the custom to orient the ribs in the meridian and circumferential directions. This arrangement suffers from the defect that all directions on a spherical surface are directions of principal curvature, so that no particular directions of the grid stiffening should be assignable. In other words, the grid elastic properties should be invariant with respect to rotation. In addition, the elastic properties should be homogeneous over the surface.

Basic Relations - Approximate solutions to the uniform grid problem are provided by the "geodesic dome" concept by which a mesh of small triangles which are approximately of constant equilateral size are mapped upon the spherical surface. The term "geodesic" refers to the fact that the mesh of lines on the spherical surface consist of arcs of great circles which are geodesic lines, i.e., lines of minimal length between specified points. An exact solution is provided for equilateral triangles in only three particular cases, the regular tetrahedron, the regular octahedron and the regular icosahedron. Of these three, the icosahedron with 20 faces has the maximum number of faces. Since the mesh size must be much smaller than this, an approximation may be made by further triangular subdivision of a face of the icosahedron. An approximately uniform pattern is thus obtained on the sphere circumscribing the basic icosahedron by a ray from the center of the sphere which traverses the triangulation of each face of the icosahedron.

A slight variant of this procedure will be employed and is described in the following.

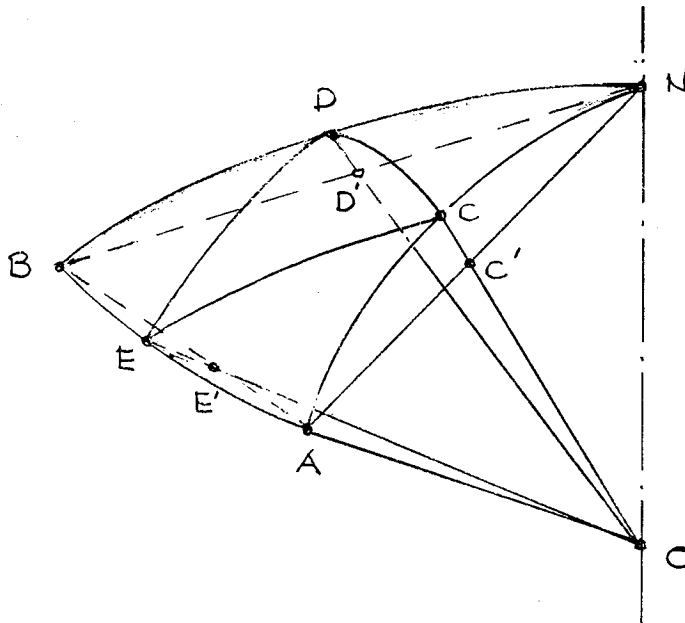
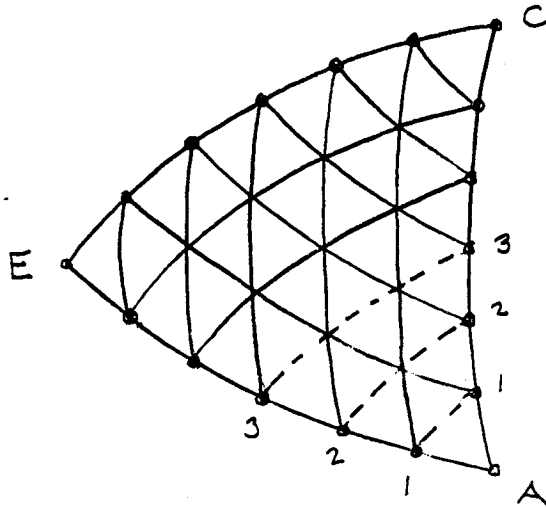


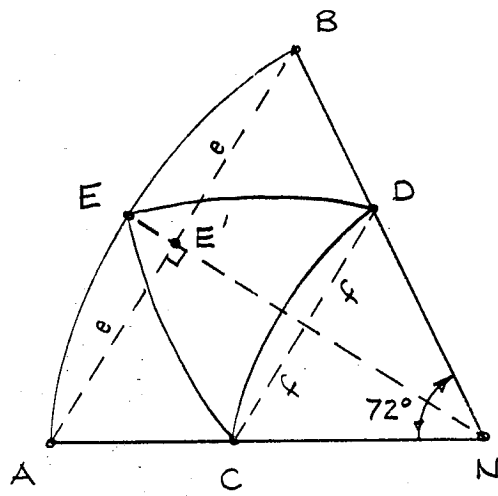
Figure 4.1 - ICOSAHEDRON INSCRIBED IN SPHERE

Figure 4.1 shows a typical face of the icosahedron inscribed in the sphere with north pole, N and center O. The face of the icosahedron is given by its vertices A, B, and N. The midpoints of the edges at C', D', and E' are projected onto the sphere to C, D, and E. Then the spherical triangle ABN is subdivided into four spherical triangles ACE, EDB, NDC, and DCE. The first three of these are congruent isosceles spherical triangles and the fourth is equilateral.

The plane triangles ACE, EDG, NDC, and DCE associated with the spherical triangles are now subdivided along their edges and these points are projected onto the edges of the spherical triangles may be connected by great circle arcs in pairs from each vertex to obtain the grid subdivision on the sphere.

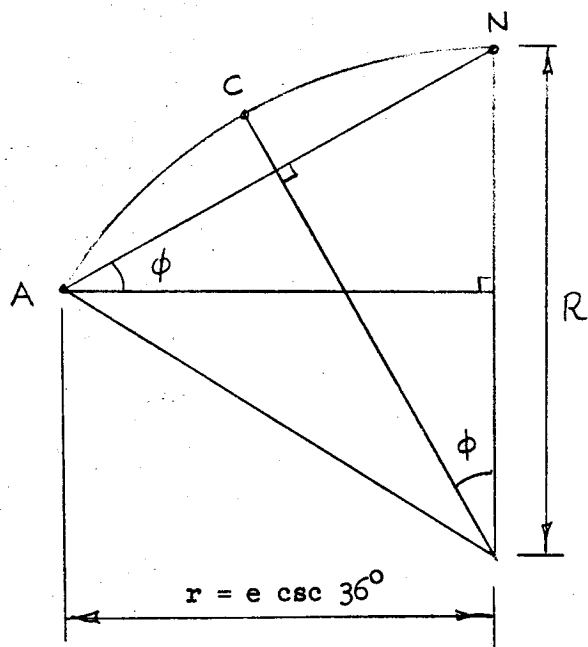
This is equivalent to subdividing the plane faces and projecting the triangle subdivision onto the sphere.





From the half-face of the icosahedron AE'N, it is apparent that the distance of the vertex A from the axis is $r = e \csc 36^\circ$ where $2e$ is the length of an edge of the icosahedron. For the angle θ , one has:

$$\cos \theta = 1/2 \csc 36^\circ$$



By spherical trigonometry, the central angle for the great circle arc CD is given by:

$$\cos \psi = \cos^2 \phi + \sin^2 \phi \cos 72^\circ$$

Where:

$$\psi = \text{arc } \widehat{CD}$$

Thus:

$$\begin{aligned} \cos \psi &= 1/4 \csc^2 36^\circ + (1 - 1/4 \csc^2 36^\circ) \cos 72^\circ \\ &= 1/4 (1 - \cos 72^\circ) \csc^2 36^\circ + \cos 72^\circ \\ &= 1/2 \sin^2 36^\circ \csc^2 36^\circ + \cos 72^\circ \end{aligned}$$

$$\cos \psi = 1/2 + \cos 72^\circ = \cos 36^\circ$$

$$\psi = 36^\circ$$

*

The half-chordal distance e will be:

$$e = R \sin \phi$$

$$e = R \sqrt{1 - 1/4 \csc^2 36^\circ}$$

4.1

* Since:

$$\cos 72^\circ = \frac{\sqrt{5}-1}{4}, \quad \cos 36^\circ = \frac{\sqrt{5}+1}{4}$$

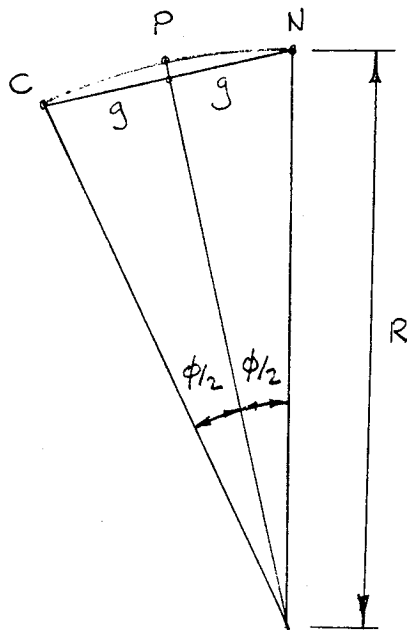
The half-chordal distance f is:

$$f = R \sin \psi$$

$$f = R \sin 36^\circ$$

(4.2)

Designate the chordal distance CN by $2g$.



From the sketch the distance g is:

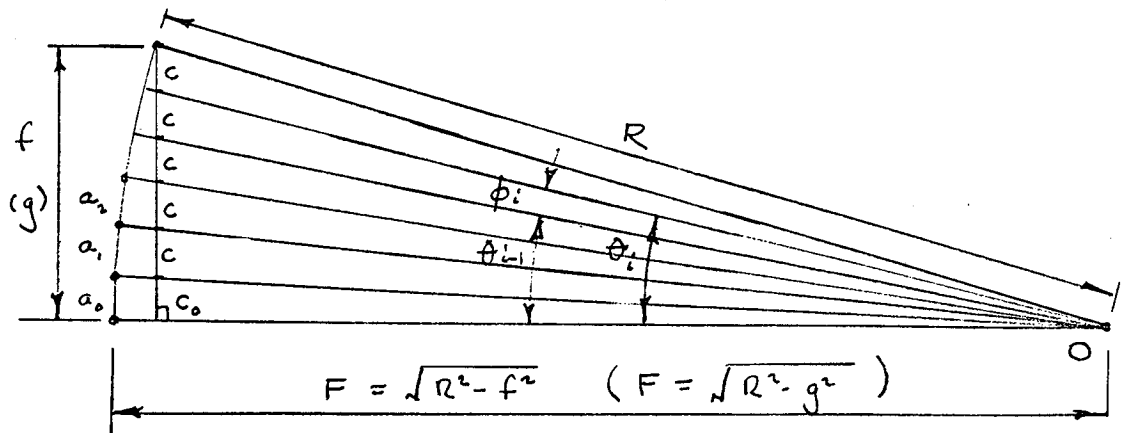
$$g = R \sin \frac{\phi}{2} = R \sqrt{\frac{1}{2} - \frac{1}{2} \cos \phi} =$$

$$R \sqrt{\frac{1}{2} - \frac{1}{4} \csc 36^\circ}$$

$$g = \frac{R}{2} \sqrt{2 - \csc 36^\circ} \quad (4.3)$$

The chords $2f$ and $2g$ are now subdivided into equal segments respectively, to be projected onto the spherical arcs \widehat{NC} and \widehat{CD} . These points will define the grid pattern.

Due to symmetry, it suffices to consider the half-chords f and g . For odd and even subdivisions the first interval will be a half or a full interval.



Thus:

$$C_o = \begin{cases} c/2, & n \text{ odd} \\ c, & n \text{ even} \end{cases}$$

Where n is the number of division of the full chord.

Then:

$$\begin{aligned} \theta_o &= \phi_o = \tan^{-1} \frac{C_o}{F} \\ \theta_i &= \tan^{-1} \frac{C_o + iC}{F}, \quad i = 1, 2, \dots \begin{cases} \frac{n-1}{2}, & n \text{ odd} \\ \frac{n-2}{2}, & n \text{ even} \end{cases} \\ \phi_i &= \theta_i - \theta_{i-1} \end{aligned}$$

$$a_i = R \phi_i$$

a_i is the required arc subdivision of \widehat{NC} and \widehat{CD} .

Obviously one has:

$$\widehat{AC} = \widehat{AE} = \widehat{BD} = \widehat{BE} = \widehat{NC}$$

and

$$\widehat{EC} = \widehat{ED} = \widehat{CD}$$

Thus, all control points may be laid out. Values are computed for unit radius and added cumulatively to facilitate layout from a vertex.

Rigidity Properties of Equilateral Triangular Rib Grids

The extensional - compressive and bending rigidities of equilateral triangular rib grids attached integrally to plate elements will be computed by obtaining the Hooke's law relation for each construction separately and then combining the plate and rib elements. In obtaining the grid properties, the assumptions are that the grid spacing is close enough that the construction may be approximated as a two dimensional continua and that depth-wise shear deformation (Love-Kirchhoff hypothesis) through the ribs may be neglected.

Hooke's law, which expresses the elastic properties of the material at a point, will be developed by considering homogeneous stresses and strains in the gridwork.

A symmetric grid orientation will be chosen for simplicity and it will then be shown that the elastic properties are equivalent to that of an isotropic plate, and hence, independent of direction.

Figure 4.1 shows such a symmetric grid layout.

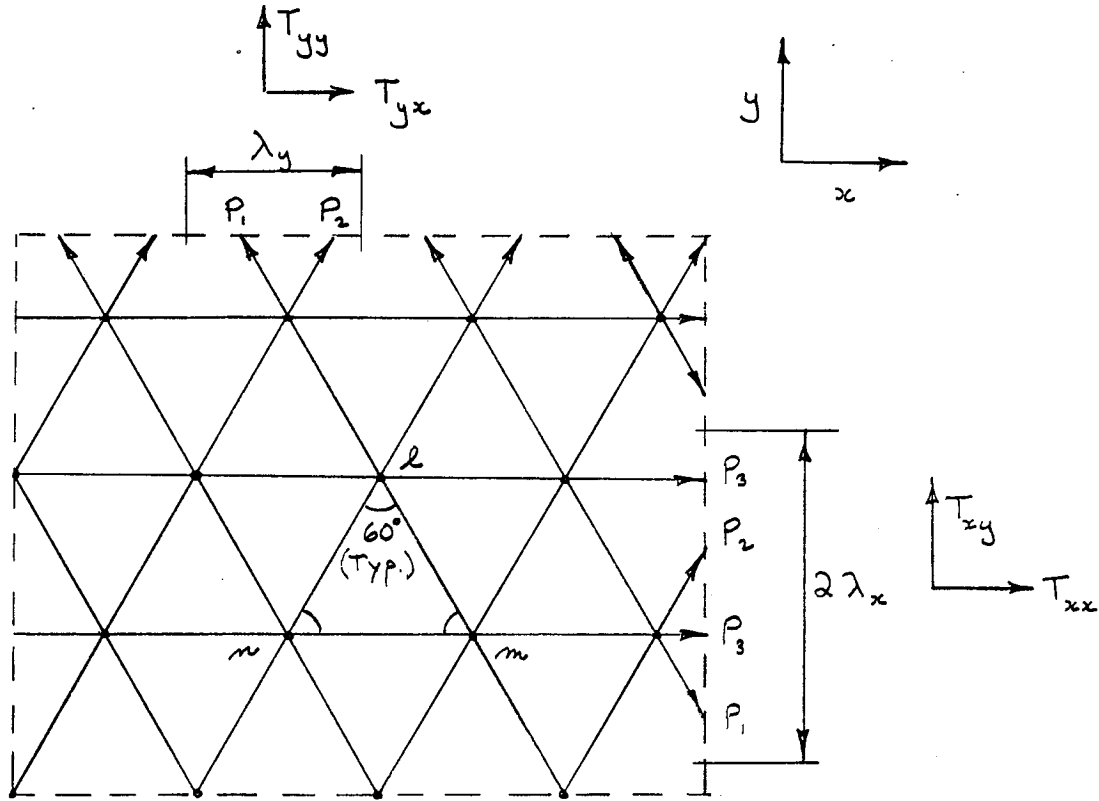


Figure 4.2 - SYMMETRIC GRID LAYOUT

The original bar lengths L_i , ($i = 1, 2, 3$) are equal to the grid spacing, a . The deformed bar lengths L_i' are obtained by projection of u and v onto the original lengths using the customary infinitesimal deformation approximations.

The changes in bar lengths are:

$$\left. \begin{aligned} \Delta L_1 &= \frac{1}{2} (u_m + \sqrt{3} v_m) \\ \Delta L_2 &= \frac{1}{2} (u_n + \sqrt{3} v_n) \\ \Delta L_3 &= u_m + u_n \end{aligned} \right\} \quad (4.4)$$

These are related to bar loads, P_i ,

$$\begin{aligned} e_1 &= \frac{\Delta L_1}{L_1} = \frac{\sigma_1}{E} = \frac{P_1}{AE} = \frac{1}{2a} (u_m + \sqrt{3} v_m) \\ e_2 &= \frac{\Delta L_2}{L_2} = \frac{\sigma_2}{E} = \frac{P_2}{AE} = \frac{1}{2a} (u_n + \sqrt{3} v_n) \\ e_3 &= \frac{\Delta L_3}{L_3} = \frac{\sigma_3}{E} = \frac{P_3}{AE} = \frac{1}{a} (u_m + u_n) \end{aligned}$$

Where A is the bar cross-sectional area.

One obtains the load-displacement relation for the bars,

$$\left. \begin{aligned} P_1 &= \frac{AE}{2a} (u_m + \sqrt{3} v_m) \\ P_2 &= \frac{AE}{2a} (u_n + \sqrt{3} v_n) \\ P_3 &= \frac{AE}{a} (u_m + u_n) \end{aligned} \right\} \quad (4.5)$$

From Figure (4.6), the periodic distances $2\lambda_x$ and λ_y are:

$$2\lambda_x = 2 a \cos 30^\circ = \sqrt{3} a, \quad \lambda_y = a$$

Edge loads $T_{\alpha\beta}$, $\alpha, \beta = x, y$ are related to bar loads by the equilibrium relations:

$$T_{yy} \lambda_y = (P_1 + P_2) \cos 30^\circ = \frac{\sqrt{3}}{2} (P_1 + P_2) = T_{yy} a$$

$$T_{yx} \lambda_y = (-P_1 + P_2) \cos 60^\circ = \frac{1}{2} (-P_1 + P_2) = T_{yx} a$$

$$2T_{xx} \lambda_x = 2P_3 + (P_1 + P_2) \cos 60^\circ = 2P_3 + \frac{1}{2} (P_1 + P_2) = T_{xx} \sqrt{3} a$$

$$2T_{xy} \lambda_x = (-P_1 + P_2) \sin 60^\circ = \frac{\sqrt{3}}{2} (-P_1 + P_2) = T_{xy} \sqrt{3} a$$

i.e.

$$\left. \begin{aligned} T_{xx} &= \frac{1}{2\sqrt{3}a} (P_1 + P_2 + 4P_3) \\ T_{yy} &= \frac{\sqrt{3}}{2a} (P_1 + P_2) \\ T_{yx} &= T_{xy} = \frac{1}{2a} (-P_1 + P_2) \end{aligned} \right\} (4.6)$$

One observes that the stress symmetry relations are a natural consequence of the internal bar loads as related to boundary stresses.

A symmetric set of loads $T_{xx}, T_{yy} \neq 0, T_{xy} = 0$, will now be applied to the grid.

Equation (4.6) shows that for this loading, $P_1 = P_2$, which implies that the displacements in equation (4.5) may be given from:

$$\left. \begin{aligned} P_1 &= P_2 = \frac{AE}{2a} (u + \sqrt{3} v) \\ P_3 &= \frac{2AE}{a} u \end{aligned} \right\} (4.7)$$

Where

$$u_m = u_n = u, \quad v_m = v_n = v$$

The strains $\epsilon_{\alpha\beta}$ along the x and y axes are: (See Figure 4.3)

$$\epsilon_{xx} = \frac{m' n' - m n}{m n} = \frac{2u}{a} \quad (4.8)$$

$$\epsilon_{yy} = \frac{l_o' - l_o}{l_o} = \frac{v}{a \cos 30^\circ} = \frac{2v}{\sqrt{3} a}$$

Eliminating u and v from equation (4.7) and (4.8),

$$\epsilon_{xx} = \frac{P_3}{AE}, \quad \epsilon_{yy} = \frac{1}{3AE} (4 P_1 - P_3) \quad (4.9)$$

From equation (4.6) for $P_1 = P_2$,

$$T_{xx} = \frac{1}{\sqrt{3} a} (P_1 + 2 P_3), \quad T_{yy} = \frac{\sqrt{3}}{a} P_1 \quad (4.10)$$

and eliminating P_1 and P_3 from (4.9) and (4.10)

$$\epsilon_{xx} = \frac{a \sqrt{3}}{2AE} (T_{xx} - \frac{1}{3} T_{yy})$$

$$\epsilon_{yy} = \frac{a \sqrt{3}}{2AE} (T_{yy} - \frac{1}{3} T_{xx})$$

(4.11)

These are the extensional stress-strain relations for the grid network.

Next a skew-symmetric set of loads $T_{xx} = T_{yy} = 0, T_{xy} \neq 0$ will be applied to the grid.

From equation (4.6) one sees that this loading gives the bar loads:

$$P_1 + P_2 = 0 \quad P_3 = 0$$

These bar loads substituted into equation (4.5) gives:

$$u_m + u_n = 0, \quad v_m + v_n = 0, \quad \text{i.e.}$$

$$u = u_n = -u_m, \quad v = v_n = -v_m$$

The distorted triangle is shown in Figure 4.4

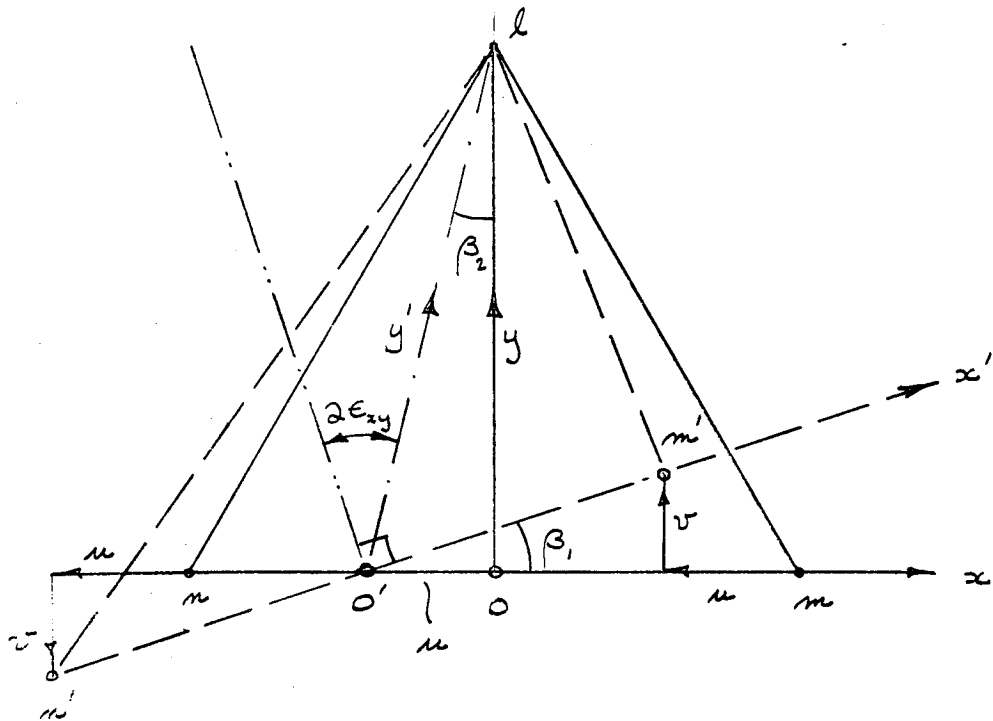


Figure 4.4 - DISTORTION OF TRIANGULAR GRID

The local origin O moves to O' with displacement u . The angular strain $2 \epsilon_{xy}^*$ is defined as the decrease in the right angle between the x and y axes when they are deformed into the x' , y' axes under the load.

From Figure (4.4) one obtains the angular relation,

$$2 \epsilon_{xy} = \beta_1 + \beta_2$$

For the customary small angle linear strains,

$$\beta_1 = \frac{2v}{a}, \quad \beta_2 = \frac{2u}{a\sqrt{3}}$$

while

$$\epsilon_{xx} = \epsilon_{yy} = 0$$

thus

$$2 \epsilon_{xy} = \frac{2}{a} \left(v + \frac{u}{\sqrt{3}} \right) = \frac{2}{a\sqrt{3}} (u + \sqrt{3} v)$$

From equation (4.5) for $P_2 = -P_1$,

$$P_2 = -P_1 = \frac{AE}{2a} (u + \sqrt{3} v) = \frac{\sqrt{3}}{2} AE \epsilon_{xy} \quad (4.12)$$

Equation (4.6) gives

$$-P_1 + P_2 = 2a T_{xy} \quad (4.13)$$

*This is a tensor strain and is related to engineering shearing strain e_{xy} by the relation,

$$2 \epsilon_{xy} = e_{xy}$$

Eliminating P_1 and P_2 from (4.12) and (4.13) gives:

$$\begin{aligned} 2 \epsilon_{xy} &= \frac{4a}{\sqrt{3} AE} T_{xy} \\ \epsilon_{xx} &= \epsilon_{yy} = 0 \end{aligned} \tag{4.14}$$

These are the shear stress-strain relations for the grid network.

Consider now a grid net of unit thickness and width b . The bar cross-sectional area becomes:

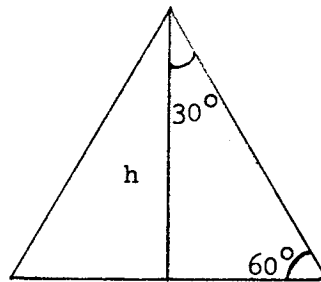
$$A = b$$

and the line loads $T_{\alpha\beta}$ become:

$$T_{\alpha\beta} = \tau_{\alpha\beta}$$

When $\tau_{\alpha\beta}$ are unit stresses along the edges of the grid.

If, in addition, one replaces the grid distance a by the height of the triangle, h



$$h = \frac{\sqrt{3}}{2} a$$

The stress-strain relation (4.11) and (4.14) become;

$$\begin{aligned}
 \epsilon_{xx} &= \frac{h}{bE} \left(\tau_{xx} - \frac{1}{3} \tau_{yy} \right) \\
 \epsilon_{yy} &= \frac{h}{bE} \left(\tau_{yy} - \frac{1}{3} \tau_{xx} \right) \\
 2 \epsilon_{xy} &= \frac{8h}{3bE} \tau_{xy}
 \end{aligned}
 \tag{4.15}$$

by superposition.

Comparing equation (4.15) for the bar grid with the Hooke's law relations for an isotropic plate of unit thickness with Young's modulus E_o and Poisson's ration ν ,

$$\begin{aligned}
 \epsilon_{xx} &= \frac{1}{E_o} (\tau_{xx} - \nu \tau_{yy}) \\
 \epsilon_{yy} &= \frac{1}{E_o} (\tau_{yy} - \nu \tau_{xx}) \\
 2 \epsilon_{xy} &= \frac{\tau_{xy}}{G} = \frac{2(1+\nu)}{E_o} \tau_{xy}
 \end{aligned}
 \tag{4.16}$$

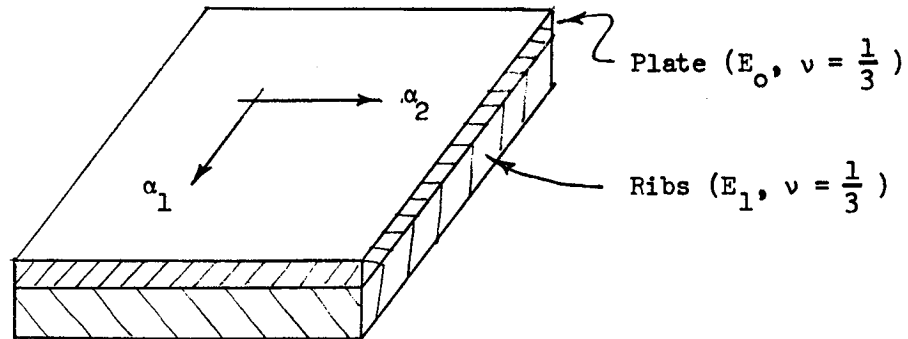
One sees that the equations are equivalent if one sets:

$$\begin{aligned}
 E_o &= \frac{b}{h} E \\
 \nu &= \frac{1}{3}
 \end{aligned}$$

Now since equations (4.16) by virtue of their isotropic property are independent of the choice of x,y axes directions, it follows that the equivalent relations, (4.15) also possesses this property. The internal bar loads, however, may depend upon the choice of axes although the overall grid elasticity does not. Since the grid is imagined to be infinitesimal in size, the Hooke's law relations developed for homogeneous stress and strain conditions in the large may be shrunk to a point to express local properties.

A composite structure consisting of a plate with ribs integrally attached may now be considered.

Assign elastic constants: $E_0, \nu_0 = 1/3$ to the plate, and $E_1 = b/h E_0, \nu_1 = 1/3$ to the grid.



Since both materials are isotropic and have equal Poisson's ratios, loads may be applied in any planar direction without transverse stress coupling between the materials.

Designating the arbitrary axes as α_1 and α_2 , one may solve equations (4.15) and (4.16) for the stresses to obtain:

$$\left. \begin{aligned} \tau_{11}^{(o)} &= \frac{E_0}{1 - \nu^2} (\epsilon_{11} + \nu \epsilon_{22}) \\ \tau_{22}^{(o)} &= \frac{E_0}{1 - \nu^2} (\nu \epsilon_{11} + \epsilon_{22}) \\ \tau_{12}^{(o)} &= \frac{E_0}{1 + \nu} \epsilon_{12} \end{aligned} \right\} \quad (4.17)$$

in the plate.

And,

$$\begin{aligned}\tau_{11}^{(1)} &= \frac{E_1}{1-\nu^2} (\epsilon_{11} + \nu \epsilon_{22}) \\ \tau_{22}^{(1)} &= \frac{E_1}{1-\nu^2} (\epsilon_{22} + \nu \epsilon_{11}) \\ \tau_{12}^{(1)} &= \frac{E_1}{1+\nu} \epsilon_{12}\end{aligned}\tag{4.18}$$

in the ribs.

The flat plate relations (4.17) and (4.18) may now be extended to a thin curved shell using the Love-Kirchhoff approximation as is done in Reference 8, p. 40, 41.

$$\begin{aligned}\epsilon_{11} + \nu \epsilon_{22} &\rightarrow \epsilon_{11} + \nu \epsilon_{22} + z (\chi_{11} + \nu \chi_{22}) \\ \epsilon_{22} + \nu \epsilon_{11} &\rightarrow \epsilon_{22} + \nu \epsilon_{11} + z (\chi_{22} + \nu \chi_{11}) \\ \epsilon_{12} &\rightarrow \epsilon_{12} + z \chi_{12}\end{aligned}\tag{4.19}$$

Substituting the stresses into the stress resultant integrals;

$$\begin{aligned}T_{ik} &= \int_h \tau_{ik} dz \\ & \qquad \qquad \qquad i,k = 1,2 \\ M_{ik} &= \int_h \tau_{ik} z dz\end{aligned}\tag{4.20}$$

Where h is the total height and z is measured from a shell surface such that axial loads produce no resultant moment (neutral surface).* By such a device one obtains the uncoupled stress-resultant deformation relations:

* $\int_h E_j z dz = 0, \quad j = 0,1$

$$T_{11} = K(\epsilon_{11} + \nu\epsilon_{22}), T_{12} = T_{21} = K(1-\nu)\epsilon_{12}, T_{22} = K(\epsilon_{22} + \nu\epsilon_{11}) \quad (4.21)$$

$$M_{11} = D(\chi_{11} + \nu\chi_{22}), M_{12} = M_{21} = D(1-\nu)\chi_{12}, M_{22} = D(\chi_{22} + \nu\chi_{11})$$

The quantities K and D are,

$$K = \frac{1}{1-\nu^2} \int_h E_j dz = \frac{9}{8} \int_h E_j dz \quad (4.22)$$

$$D = \frac{1}{1-\nu^2} \int_h E_j z dz = \frac{9}{8} \int_h E_j z dz$$

where $j = 0$, when the integration is in region 0 and $j = 1$, when the integration is in the region 1.

These integrals may be evaluated very simply if one observes that

$$E_1 = \frac{b}{h} E_0$$

gives an equivalent tee-shaped cross-section of dimensions:

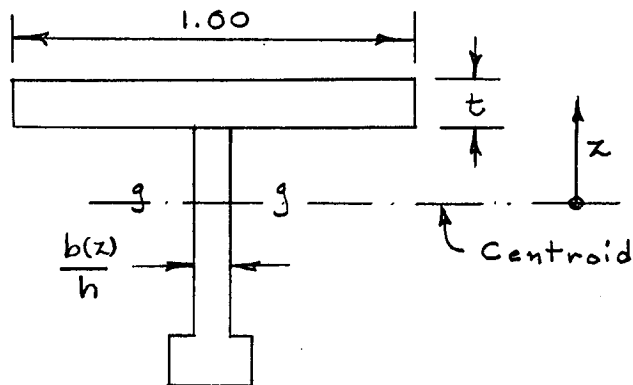


Figure 4.5 - EQUIVALENT TEE-SHAPED CROSS SECTION

The integrals (4.22) become simply:

$$K = \frac{9}{8} E_o A, \quad D = \frac{9}{8} E_o I_{gg} \quad (4.23)$$

where A is the cross-sectional area shown in figure 4.5 and I_{gg} is the second moment of area of A about the centroidal axis gg .

Due to the finite size of the grid, certain small errors will occur. These are due to the following:

- (a) Curvature of the shell between the rib joints.
- (b) Non-homogeneous stress-strain conditions will result in increments of bar loads P_1, P_2, P_3 being transferred in shear from the plate between the rib joints.
- (c) Differential bar loads will result in complex stress distribution at the joints where principal stresses change direction.
- (d) Neglect of fillet radii.

In addition, the Poisson ratio for the plate may differ from 1/3 and cause coupled stress effects in the transverse direction. For most metals, however, Poisson's ratio is very close to 1/3.

Bending Rigidity

The equivalent elastic cross-section for computation of D is shown in figure 4.6, assuming constant rib width, b.

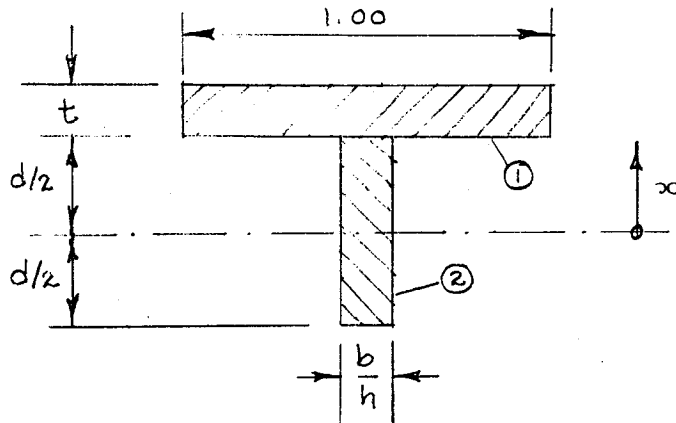


Figure 4.6 - EQUIVALENT BENDING RIGIDITY

Part	Area	x	Ax	Ax ²	I _o
1	t	$\frac{1}{2}(t+d)$	$\frac{t}{2}(t+d)$	$\frac{t}{4}(t+d)^2$	$\frac{1}{12}t^3$
2	$\frac{bd}{h}$	0	0	0	$\frac{1}{12}\frac{b}{h}d^3$
Σ	$t(1 + \frac{bd}{th})$		$\frac{t}{2}(t+d)$	$\frac{t}{4}(t+d)^2$	$\frac{1}{12}(t^3 + \frac{b}{h}d^3)$

Define

$$\alpha = \frac{bd}{th}, \quad \delta = \frac{d}{t}$$

$$\bar{x} = \frac{\Sigma Ax}{\Sigma A} = \frac{t(t+d)}{2t(1+\alpha)} = \frac{t+d}{2(1+\alpha)}$$

$$I_{xx} = \Sigma Ax^2 + \Sigma I_o = \frac{t^3}{4}(1+\delta)^2 + \frac{t^3}{12}(1+\alpha\delta^2)$$

$$I_{gg} = I_{xx} - A\bar{x}^2 = I_{xx} - t(1+\alpha)\frac{t^2(1+\delta)^2}{4(1+\alpha)^2}$$

$$I_{gg} = \frac{\alpha}{1+\alpha}\frac{t^3}{4}(1+\delta)^2 + \frac{t^3}{12}(1+\alpha\delta^2)$$

Then

$$I_{gg} = \frac{t^3}{12(1+\alpha)} \{3\alpha(1+\delta)^2 + (1+\alpha)(1+\alpha\delta^2)\}$$

And

$$D = \frac{9}{8} E_o I_{gg}$$

the bending rigidity, D, is:

$$D = \frac{9}{8} E_o \frac{t^3}{12(1+\alpha)} \{3\alpha(1+\delta)^2 + (1+\alpha)(1+\alpha\delta^2)\} \quad (4.24)$$

Extensional Rigidity

The extensional rigidity, K is obtained from:

$$K = \frac{9}{8} E_o A$$

$$K = \frac{9}{8} E_o t(1 + \alpha) \tag{4.25}$$

Weight of Construction

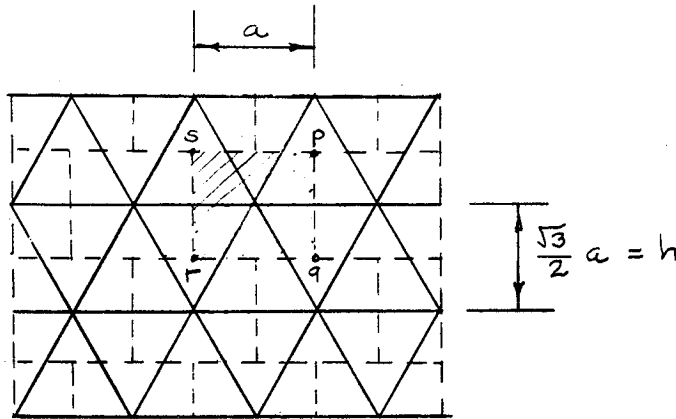


Figure 4.7 - DIVISION OF PATTERN FOR WEIGHT CONSIDERATION

Figure 4.7 shows the rib configuration divided into typical rectangles each with sides of length a and h .

A section through pq is shown in Figure 4.8

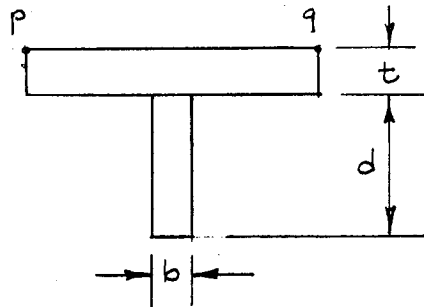


Figure 4.8 - TYPICAL SECTION THROUGH PANEL

The stresses become:

$$\tau_{11} = \tau_{22} = \frac{1}{1 + \alpha} \frac{pR}{2t} \quad (4.27)$$

in the plate, and

$$\sigma = \frac{P}{bd}, \quad \sigma_1 = \sigma_2 = \sigma_3 = \frac{1}{1 + \alpha} \frac{pR}{3t} \quad (4.28)$$

in the ribs.

These quantities are to be set equal to the allowable stresses for local panel stability and rib crippling stability.

are proportional to the equivalent area of plate and ribs in the composite construction.

$$T_{11}^{(1)} = T_{22}^{(1)} = \frac{A_1}{A_1 + A_2} \frac{pR}{2} = c^{(1)}$$

$$T_{11}^{(2)} = T_{22}^{(2)} = \frac{A_2}{A_1 + A_2} \frac{pR}{2} = c^{(2)}$$

Where A_1 is the equivalent plate area, $A_1 = t$ and A_2 is the equivalent rib area, $A_2 = \frac{bd}{h}$ for ribs of constant width.

From equation (4.6) for the rib stress resultants,

$$T_{11}^{(2)} = T_{22}^{(2)}, \quad \frac{1}{\sqrt{3} a} (P_1 + 2P_3) = \frac{\sqrt{3}}{a} P_1 = c^{(2)}$$

$$\text{i.e. } P_1 + 2P_3 = 3P_1, \quad P_3 = P_1$$

and using equation (4.6)

$$P_1 = P_2 = P_3 = \frac{a c^{(2)}}{\sqrt{3}} = \frac{2}{3} h c^{(2)}$$

in the ribs

$$T_{11}^{(1)} = T_{22}^{(1)} = c^{(1)}$$

in the plate.

Now,

$$c^{(1)} = \frac{A_1}{A_1 + A_2} \frac{pR}{2} = \frac{t}{t(1 + \alpha)} \frac{pR}{2}$$

and

$$c^{(2)} = \frac{A_2}{A_1 + A_2} \frac{pR}{2} = \frac{t\alpha}{t(1 + \alpha)} \frac{pR}{2}$$

The length of the ribs in spqr is $3a$, and the volume of rib material is:

$$V_r = 3abd$$

The volume of skin material is:

$$V_s = aht$$

This gives a total volume of:

$$V = a(3bd + th)$$

The equivalent weight thickness (i.e. smeared out thickness) is equal to this volume divided by the rectangular area.

$$\bar{t} = \frac{V}{A} = \frac{a(3bd + th)}{ah}$$

$$\bar{t} = t(1 + 3\alpha)$$

(4.26)

Where, as in previous calculation, $\alpha = \frac{bd}{th}$. This slightly over-estimates the weight where the rib areas overlap at the joints where they cross each other but ignores fillet weight.

Rib and Plate Stresses for Pressure Loading of Sphere

For membrane pressure stress conditions,

$$\epsilon_{11} = \epsilon_{22} = \epsilon_0, \quad \epsilon_{12} = 0, \quad \chi_{ik} = 0$$

$$T_{11} = T_{22} = \frac{pR}{2}, \quad T_{12} = 0, \quad M_{ik} = 0$$

From the extensional rigidity, $K = \frac{9}{8} EA$ one sees that the line loads $T_{11} = T_{22} = \frac{pR}{2}$ consisting of components

$$T_{11}^{(1)} = T_{22}^{(1)} \quad \text{in the plate composite}$$

$$T_{11}^{(2)} = T_{22}^{(2)} \quad \text{in the rib composite}$$

Direction of Rib and Plate Stresses

It is a compatibility requirement for composite rib and plate shell construction that strains in the shell surface coordinate directions be continuous at the attached surfaces as one traverses a normal to the shell. In particular, the Love-Kirckhoff assumption is that the strains are linear functions of the normal coordinate while membrane requirements are that they are constant along the normal coordinate.

Since the plate is subjected, however, to biaxial stresses while the ribs are stressed uniaxially, a local transition in the strains occur and the stresses, in general, are different in the two elements away from the attached surfaces.

Consider a typical segment shown in figure 4.9 where a set of surface coordinates are arbitrarily assigned parallel to and transverse to a rib.

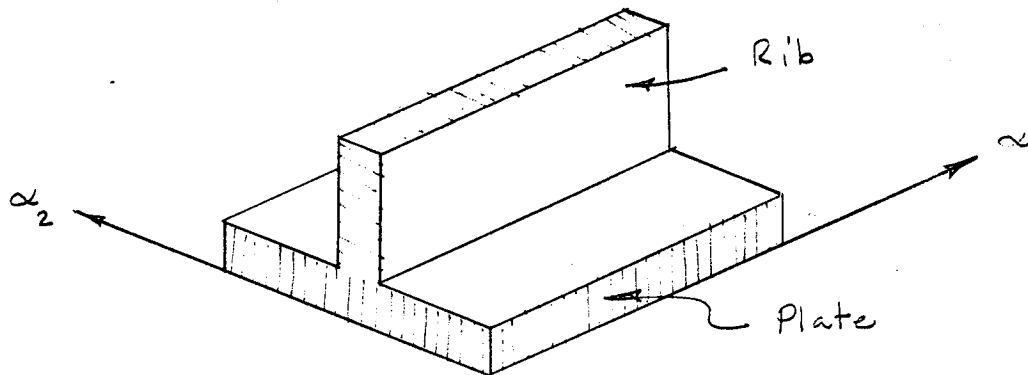


Figure 4.9 - TYPICAL SEGMENT SHOWING RIB AND PLATE

Assume, for example, a homogeneous isotropic condition such as would exist in a sphere subjected to internal pressure.

In the plate, the strains will be:

$$\epsilon_1 = \epsilon_2 = \epsilon$$

and Hooke's law for stresses in terms of strain is:

$$\sigma_1 = \frac{E}{1 - \nu^2} (\epsilon_1 + \nu \epsilon_2), \quad \sigma_2 = \frac{E}{1 - \nu^2} (\epsilon_2 + \nu \epsilon_1)$$

giving:

$$\sigma_1 = \sigma_2 = \frac{E \epsilon}{1 - \nu}$$

In the ribs, however, one has the strains,

$$\epsilon_1 = \epsilon, \quad \epsilon_2 = -\nu \epsilon_1 = -\nu \epsilon$$

since the transverse faces of the ribs are stress free (according to the usual approximations).

Thus, in the ribs, one obtains stresses of magnitude:

$$\begin{aligned} \sigma_1 &= E \epsilon \\ \sigma_2 &= 0 \end{aligned}$$

The plate and rib stresses in the rib direction will then be in the ratio:

$$\frac{\sigma_1(\text{plate})}{\sigma_1(\text{rib})} = \frac{1}{1 - \nu} = \frac{3}{2}, \quad \text{for } \nu = \frac{1}{3}$$

(This is exactly the ratio of the values previously obtained in equation 4.27 and 4.28).

One sees that a fundamental difference exists for stresses in ribbed plates or shells when the composite construction is stressed uni-axially or biaxially.

It is a consequence of this result that the ribs for 1:1 biaxial loading, regardless of the rib pattern, can be stressed to only 2/3 of the plate stresses. An optimum construction must then have a small value of α since

$$\alpha = \frac{bd}{th} \sim \frac{\text{rib area}}{\text{skin area}}$$

Such ribs will be thin and deep.

The rib and plate are shown separated in Figure 4.10 to illustrate the local character of the deformation transition between the plate and rib.

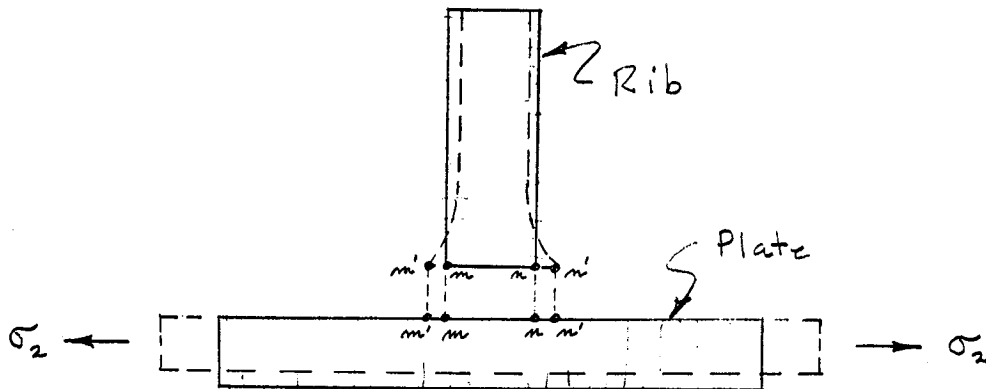


Figure 4.10 - LOCAL DEFORMATION BETWEEN RIB AND PLATE

Under load, the points $m n$ move to $m' n'$. Symmetric shear stresses exist across the attached edge of the rib having zero resultant force. By St. Venant's principle, the transition stress is of consequence only in a local region extending approximately one rib thickness into the rib.*

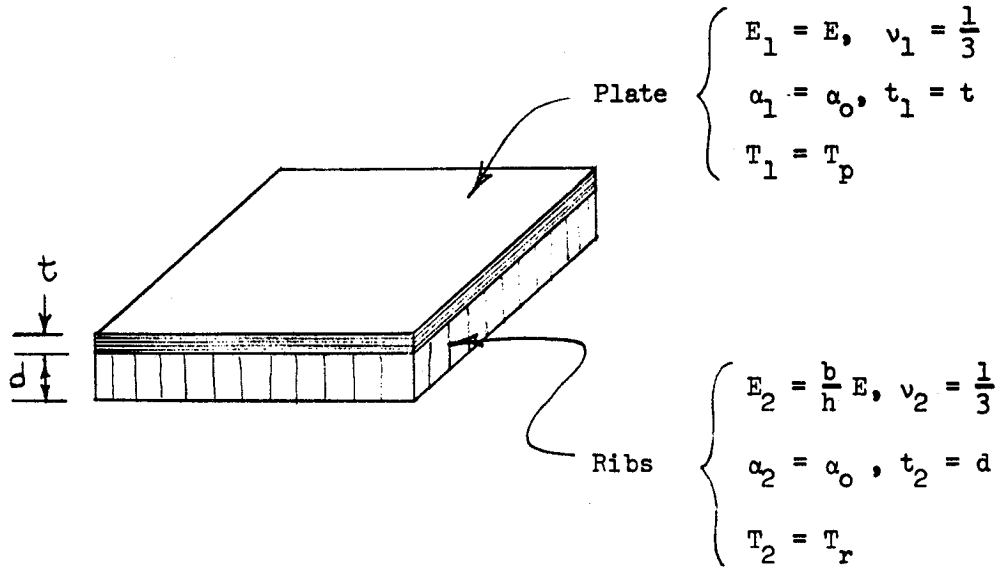
As a final comment, note that $\alpha \sim \frac{\text{rib area}}{\text{skin area}}$ is proportioned to but does not represent the ratio of rib weight to skin weight in the dome. This quantity is given by:

$$\frac{\text{rib weight}}{\text{skin weight}} = \frac{\bar{t} - t}{t} = \frac{t(1+3\alpha) - t}{t} = \underline{3\alpha}$$

*For St. Venant's principle, see "Theory of Elasticity", Timoshenko and Goodier p. 33 and "Theory of Elasticity", Novozhilov, Dept. of Comm. Trans. 1961, p. 208.

Thermal Stresses

The thermal stresses in the composite plate-rib shell may easily be computed from the composite elastic properties.



As a consequence of the 1:1 strain field, the solution of reference may be applied. This solution is:

$$\epsilon_0 = \frac{\sum_i \frac{t_i E_i \alpha_i}{1 - \nu_i} T_i}{\sum_i \frac{t_i E_i}{1 - \nu_i}}, \quad \sigma_j = \frac{E_j}{1 - \nu_j} (\epsilon_0 - \alpha_j T_j)$$

Where σ_j is positive for tensile stresses.

When ν_i and α_i are constant,

$$\epsilon_0 = \alpha_0 \frac{\sum_i t_i E_i T_i}{\sum_i t_i E_i}$$

For the values indicated,

$$\epsilon_o = \alpha_o \frac{(t E T_p + \frac{bd}{h} E T_r)}{t E + \frac{bd}{h} E} = \alpha_o \frac{(T_p + \alpha T_r)}{1 + \alpha}$$

The plate stresses are,

$$\begin{aligned} \tau_{11} = \tau_{22} = \sigma_p &= \frac{E_1}{1 - \nu_1} (\epsilon_o - \alpha_o T_p) \\ &= \frac{3}{2} E \alpha_o \left(\frac{T_p + \alpha T_r}{1 + \alpha} - T_p \right) \end{aligned}$$

$$\sigma_p = \frac{3}{2} E \alpha_o \frac{\alpha}{1 + \alpha} \Delta T$$

(4.29)

where

$$\Delta T = T_r - T_p$$

The composite rib stresses are,

$$\begin{aligned} \sigma_r &= \frac{E_2}{1 - \nu_2} (\epsilon_o - \alpha_o T_r) \\ &= \frac{3}{2} \frac{b}{h} E \alpha_o \left(\frac{T_p + \alpha T_r}{1 + \alpha} - T_r \right) \\ &= - \frac{3}{2} \frac{b}{h} E \alpha_o \frac{\Delta T}{1 + \alpha} \end{aligned}$$

As a check, equilibrium requires that,

$$\sum_i t_i \sigma_i = 0,$$

Thus

$$t \sigma_p + d \sigma_r = \frac{3}{2} E \alpha_o \frac{\Delta T}{1 + \alpha} \left(t \alpha - \frac{bd}{h} \right) = 0$$

As required.

The bar loads are related to edge stress resultants by the relation,

$$T_{xx} = T_{yy} = \sigma_r d = \frac{\sqrt{3}}{2a} (P_1 + P_2)$$

As a consequence of symmetry, $P_1 = P_2$ and one obtains,

$$\sigma_r d = \frac{\sqrt{3}}{a} P$$

The bar stresses are now,

$$\sigma_b = \sigma_1 = \sigma_2 = \sigma_3 = \frac{p}{bd} = \frac{a \sigma_r}{b \sqrt{3}}$$

Substituting the value for σ_r ,

$$\sigma_b = -\frac{3}{2} \frac{b}{h} E \alpha_o \frac{\Delta T}{1 + \alpha} \frac{a}{b \sqrt{3}}$$

$$\sigma_b = -E \alpha_o \frac{\Delta T}{1 + \alpha}$$

(4.30)

The plate and bar stresses are in the ratio,

$$\frac{\sigma_p}{\sigma_b} = -\frac{3}{2} \alpha = -\frac{3}{2} \frac{bd}{th}, \quad \text{i.e.}$$

$$\frac{2}{3} \sigma_p \cdot th + \sigma_b \cdot bd = 0$$

Primary Modes of Failure

General Instability

Since testing of the plastic specimens has demonstrated that satisfactory correlation exists between modified classical theory for a complete sphere and for spherical caps with half-opening angles in the range $33 \frac{1}{2}^\circ \leq \phi \leq 90^\circ$, this theory will be employed for calculation of general instability.

Further, as a consequence of the fact that geodesic stiffening is described by only three elastic constants, $\nu = 1/3$, D and K , a simple extension of the theory suffices to predict general stability.

In reference 20, p. 492, the equations of equilibrium (c) are unchanged. The Hooke's law relations, however, are replaced by their new values. Thus,

$$N_x = \frac{Et}{1 - \nu^2} (\epsilon_{11} + \nu \epsilon_{22}) + K (\epsilon_{11} + \nu \epsilon_{22})$$

$$N_y = \frac{Et}{1 - \nu^2} (\epsilon_{22} + \nu \epsilon_{11}) + K (\epsilon_{22} + \nu \epsilon_{11})$$

while the expression for M_x and M_y are already given in terms of D . This results in a redefinition of the quantities described as α' and ϕ' .*

$$\alpha' = \frac{D(1 - \nu^2)}{R^2 Et} \rightarrow \frac{D}{R^2 K}$$

$$\phi' = \frac{pR(1 - \nu^2)}{2Et} \rightarrow \frac{pR}{2K}$$

*Primes are used with the Timoshenko notation to avoid confusion with previous quantities.

All subsequent calculation of the eigenvalues of ϕ' remain unchanged, and one obtains:

$$\phi'_{\min} = 2 \sqrt{(1 - \nu^2) \alpha'}$$

neglecting the higher order term $6 \nu \alpha'$.

Thus:

$$p_{\min} \frac{R}{2K} = 2 \sqrt{(1 - \nu^2) \frac{D}{R^2 K}}$$

$$p_{\min} = \frac{4}{R^2} \sqrt{(1 - \nu^2) DK}$$

$$DK = \left(\frac{9}{8}\right)^2 E^2 \frac{t^4}{12} \{3\alpha(1 + \delta)^2 + (1 + \alpha)(1 + \alpha \delta^2)\}$$

Denoting the critical general instability pressure as p_o and substituting the given values for D and K, one obtains the classical value,

$$p_o = \sqrt{\frac{3}{2}} E \left(\frac{t}{R}\right)^2 \{3\alpha(1 + \delta)^2 + (1 + \alpha)(1 + \alpha \delta^2)\}^{1/2} \quad (4.31)$$

for $\nu = \frac{1}{3}$

where

$$\alpha = \frac{bd}{th}, \quad \delta = \frac{d}{t}$$

In terms of the equivalent weight $\bar{t} = t(1+3\alpha)$, one has

$$p_o = \sqrt{\frac{3}{2}} E \left(\frac{\bar{t}}{R}\right)^2 \frac{\gamma}{(1+3\alpha)^2} \quad (4.32)$$

$$\gamma = \{3\alpha(1 + \delta)^2 + (1 + \alpha)(1 + \alpha \delta^2)\}^{1/2}$$

The above formula reduces to that for monocoque construction when the rib area approaches zero. In such a case, one has the limiting values

$$\alpha \rightarrow 0, \quad \delta \rightarrow 0, \quad \gamma \rightarrow 1$$

$$\bar{t} \rightarrow t = t_o$$

$$p'_o \rightarrow \frac{\sqrt{3}}{\sqrt{2}} E \left(\frac{t_o}{R}\right)^2 = 2 C E \left(\frac{t_o}{R}\right)^2$$

$$c = 0.612 \quad \text{for } \nu = \frac{1}{3}$$

According to Huang, (reference 7)

$$p \leq 2 \bar{c} E \left(\frac{t_o}{R}\right)^2$$

where the buckling coefficient is approximately

$$\bar{c} = 0.80 c = 0.490 \quad \text{for } \nu = \frac{1}{3}$$

In order to compare the stiffened weight with monocoque weight for equal pressure, $p_o = p'_o$, one has,

$$t_o^2 = (\bar{t})^2 \frac{\gamma}{(1+3\alpha)^2}, \quad t_o = \bar{t} \frac{\sqrt{\gamma}}{1+3\alpha}$$

Since the weights are proportioned to the thickness,

$$\frac{\text{Stiffened weight}}{\text{Monocoque weight}} = \frac{\bar{t}}{t_o} = \frac{1+3\alpha}{\sqrt{\gamma}} = \text{weight ratio} = \eta$$

$$\eta = \frac{1+3\alpha}{\sqrt{\gamma}}$$

(4.33)

Rib Crippling - Ignoring the slight curvature of the rib, the allowable elastic crippling stress for a rectangular plate will be obtained under the conservative assumption that it is free on one edge and hinged on the other three edges. (See Figure 4.11)

According to reference 31 the critical allowable stress is:

$$\sigma_{cr} = \frac{\pi^2 E b^2}{12(1 - \nu^2)d^2} \left[\left(\frac{d}{a}\right)^2 + 0.425 \right]$$

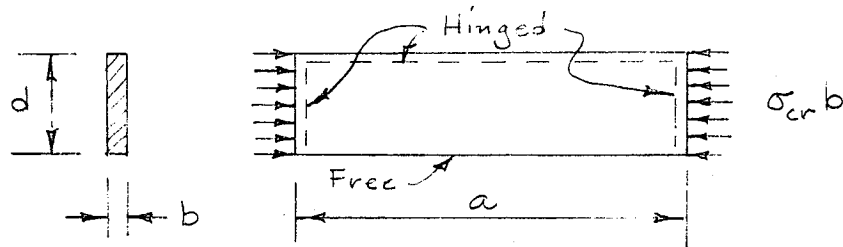


Figure 4.11 - LOADED RECTANGULAR PLATE

Substituting

$$a = \frac{2}{\sqrt{3}} h, \quad \nu = \frac{1}{3}$$

$$\sigma_{cr} = 0.693 E \left(\frac{b}{d}\right)^2 \left[\left(\frac{d}{h}\right)^2 + 0.567 \right]$$

Equating the actual stress (eq. 4.28) to the allowable stress, one obtains:

$$\frac{1}{1 + \alpha} \frac{p_1 R}{3t} = 0.693 E \left(\frac{b}{d}\right)^2 \left[\left(\frac{d}{h}\right)^2 + 0.567 \right]$$

and solving for the critical pressure,

$$p_1 = 2.08 E \left(\frac{t}{R}\right) \left(\frac{b}{d}\right)^2 (1 + \alpha) \left[\left(\frac{d}{h}\right)^2 + 0.567\right] \quad (4.34)$$

Panel Buckling - To obtain local panel buckling it will be assumed that the panels are small enough that they may be treated as equilateral triangular plates subjected to uniform compressive edge loads. This assumption will be justified and amplified. The edges are assumed free to rotate as a consequence of checkerboard (in-and-out) panel buckling. The critical allowable stress from reference 31 is:

$$\sigma_{cr} = \frac{\pi^2 E}{3(1 - \nu^2)} \left(\frac{t}{h}\right)^2$$

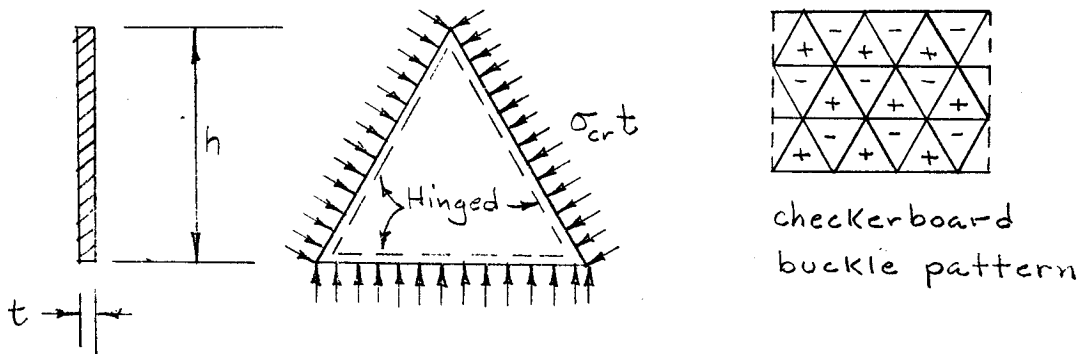


Figure 4.12 - LOADED TRIANGULAR PANEL

Equating this to the actual from eq. (4.27)

$$\frac{1}{1 + \alpha} \frac{p_2^R}{2t} = \frac{\pi^2 E}{3(1 - \nu^2)} \left(\frac{t}{h}\right)^2$$

and solving for the critical pressure: $(\nu = 1/3)$

$$p_2 = 7.40 E \left(\frac{t}{R}\right) \left(\frac{t}{h}\right)^2 (1 + \alpha) \quad (4.35)$$

Justification of Plate Buckling Approximation - In an examination of the experimental results of Krenzke and Kiernan (reference 17) plotted against theoretical curves obtained by Budiansky, Weinitschke and Thurston (reference 30) for shallow spherical shells with clamped edges depicted in figure 4.13 below, it appears that any plate regime must begin in the steeply rising portion of the curve to the left.

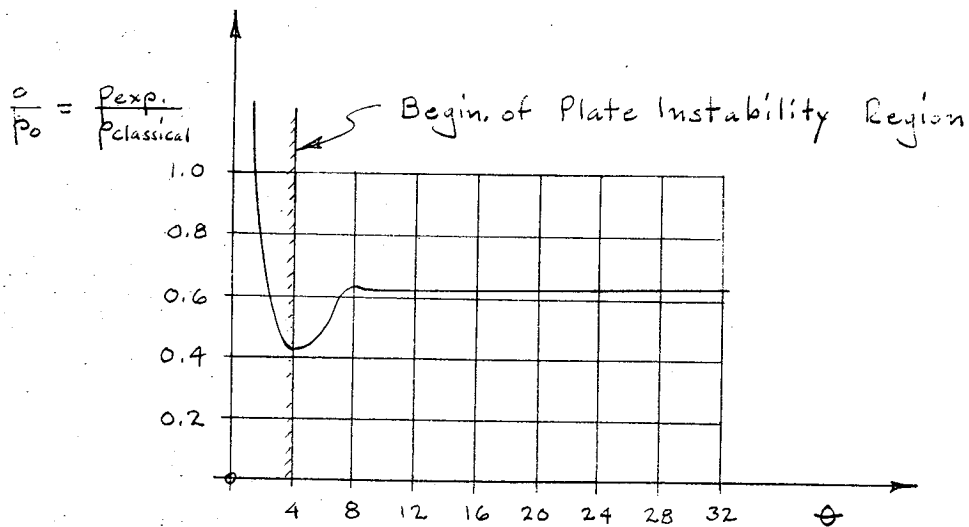
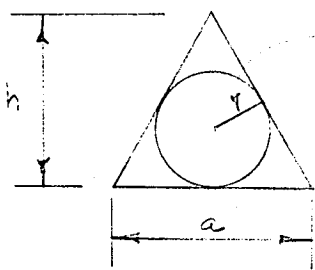


Figure 4.13 PLATE BUCKLING CURVE

$$\theta = \left[\frac{3}{4} (1 - \nu^2) \right]^{1/4} \frac{L_a}{\sqrt{Rt}} = 0.905 \frac{L_a}{\sqrt{Rt}}, \quad \nu = \frac{1}{3}$$

L_a is the chordal diameter of the spherical cap.

In order to put this conjecture on a more rational basis consider a dimple inscribed in an equilateral triangular grid as a smaller spherical cap.



$$\frac{1}{2} L_a = \frac{a}{2} \tan 30^\circ = \frac{a\sqrt{3}}{6} = \frac{h}{3}$$

$$L_a = \frac{2}{3} h$$

Then:

$$\theta = 0.905 \frac{2}{3} \frac{h}{\sqrt{Rt}} = A \frac{h}{\sqrt{Rt}}, \quad A = 0.603$$

Suppose the equation of the curve in the "plate instability" region to be given by the quadratic hyperbola:

$$\frac{p}{p_0} \theta^2 = B = \text{constant}$$

This equation appears to be a reasonable approximation in the steeply rising portion of the curve where $\theta < 4$.

Substituting for:

$$\theta = A \frac{h}{\sqrt{Rt}}, \quad p_0 = 2 C E \left(\frac{t}{R}\right)^2$$

one obtains:

$$p = p_0 \frac{B}{\theta^2} = 2 C E \left(\frac{t}{R}\right)^2 \frac{B}{A^2} \frac{Rt}{h^2} = D \frac{t^3}{Rh^2}$$

But:

$$\sigma = \frac{pR}{2t} = D \frac{t^3}{Rh^2} \frac{R}{2t} = \frac{D}{2} \left(\frac{t}{h}\right)^2$$

Which is precisely the form of the plate buckling equation.

The conclusion of Krenzke and Kiernan is that stiffening systems installed at spacings of θ greater than 2.2 - 2.5, will not increase the local buckling strength of the shell and may possibly weaken it (due to the dip in the curve at $\theta = 4$).

Thermal and Residual Stress Considerations

Thermal stresses and residual stresses are both initial stresses in internal equilibrium having like effects on dome stability. These effects are twofold: first, by introducing stresses which cause local yielding at reduced pressures and second, by introducing internal strain energy which might be relieved by the buckling deformation and thus reduce the buckling capacity.

Local buckling of the ribs and skin are governed by stress differences between the ribs and the skin. General instability of the dome is affected by local regions of compression extending over areas comparable in size to the dimple area.

Thermal gradients or residual stresses which vary through the dome thickness, but are otherwise uniform over the dome mid-surface are associated with a condition of pure moment stress resultants of the shell. The internal energy due to these moments will not be effected by primary instability modes of the type where positive changes of curvature integrated over the shell balance out negative changes of curvature. The variation in strain energy δw , is given as:

$$\delta w = \int_A \sum_{ij} (T_{ij} \delta \epsilon_{ij} + M_{ij} \delta \chi_{ij}) dA$$

$$i, j = 1, 2$$

where

$$T_{ij} = 0, \quad M_{ij} = M_0,$$

and A is the shell mid-surface.

Thus,

$$\delta w = M_0 \int_A \sum_{ij} \delta \chi_{ij} dA = 0$$

if

$$\int_A \sum_{ij} \delta x_{ij} dA = 0$$

as asserted.

A large number of uniform dimples such as are displayed by the tested domes should approximately satisfy this condition, so that general instability should not be affected, provided that the thermal gradients are fairly uniform over the dome surface.

Common bulkheads which are used on the Saturn S-IV are colder on the outside convex surface. A waffle design for this dome would have compressive stress in the relatively warmer ribs and tensile stress in the colder panels. Due to the high coefficient of conductivity of an integral metal dome, the temperature difference between the ribs and the panels will be small in the steady state condition. As a consequence, a design where rib thickness is dictated by fabrication tolerances will usually have a sufficient margin of rib strength to accommodate the small additional temperature stresses.

Another factor which enters into off-optimum design where either panels or ribs become non-critical is the support condition for the critical element. If the panels do not buckle, edge conditions for the ribs will become less severe than the assumed "free to rotate" edges. Similar consideration apply to edge condition for panels when the ribs do not fail. This fact provides an additional margin to prevent premature buckling of common domes in the presence of uniform thermal gradients. Insulation will also provide support to resist general instability or panel buckling.

Stresses Due to Hot Spot

Assume that over an angular region β from the apex a uniform temperature rise ΔT has occurred. A spherical cap of this size may be cut as a free body from the remainder of the dome and provided with a set of edge shears and moments which replace the internal stresses across the cut faces. These edge loads may be obtained by the method of compatible displacements. (See Figure 4.14)

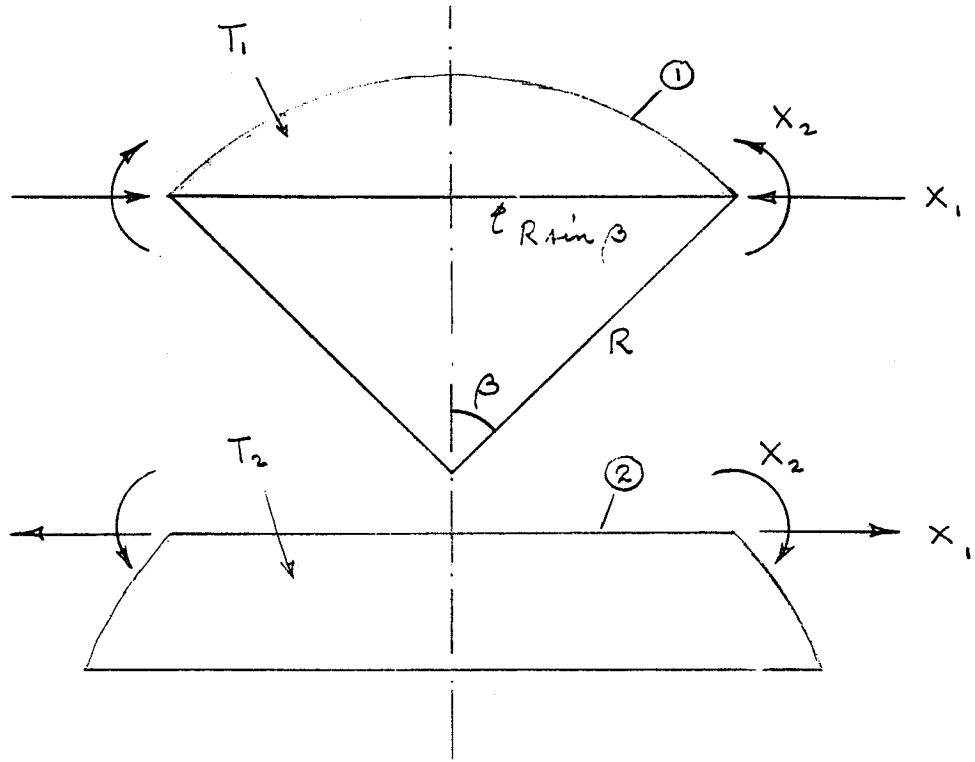


Figure 4.14 - FREE BODY OF SPHERICAL CAP

For part 1,

$$\Delta T = T_1 - T_2 = T > 0$$

$$\delta_{1p}^{(1)} = -\alpha R \sin \beta \Delta T, \quad \delta_{2p}^{(1)} = 0$$

$$\delta_{11}^{(1)} = \frac{2 \lambda R \sin^2 \beta}{Et}, \quad \delta_{12}^{(1)} = -\frac{2 \lambda^2 \sin \beta}{Et}$$

$$\delta_{22}^{(1)} = \frac{4 \lambda^3}{ERt}, \quad \lambda = 4 \sqrt{3(1-\nu^2) \left(\frac{R}{t}\right)^2}$$

Where the notation and influence coefficients have been obtained from reference 22 assuming that the angle is sufficiently large that the first Geckeler approximation may be used.

For part 2 similarly,

$$\delta_{1p}^{(2)} = \delta_{2p}^{(2)} = 0$$

$$\delta_{11}^{(2)} = \frac{2 \lambda R \sin^2 \beta}{Et}, \quad \delta_{12}^{(2)} = \frac{2 \lambda^2 \sin \beta}{Et}$$

$$\delta_{22}^{(2)} = \frac{4 \lambda^3}{ERt}$$

By summation, the differential displacements are now,

$$\delta_{1p} = -\alpha R \sin \beta \Delta T, \quad \delta_{2p} = 0$$

$$\delta_{11} = \frac{4 \lambda R \sin^2 \beta}{Et}, \quad \delta_{12} = 0$$

$$\delta_{22} = \frac{8 \lambda^3}{ERt}$$

The compatibility conditions are:

$$x_1 \delta_{11} + x_2 \delta_{12} + \delta_{1p} = 0$$

$$x_1 \delta_{21} + x_2 \delta_{22} + \delta_{2p} = 0$$

Since

$$\delta_{12} = \delta_{21} = 0, \quad \delta_{2p} = 0,$$

one obtains

$$x_2 = 0, \quad x_1 = -\frac{\delta_{lp}}{\delta_{ll}} = \frac{E \alpha t}{4 \lambda \sin \beta} \cdot \Delta T \quad (4.35)$$

The thermal stresses are seen to be a simple edge shear effect localized in the vicinity of the thermal jump across the two sections.

For small values of β , however, the Geckeler solution does not hold and the edge loads may propagate throughout the entire cap. This may be expected for values of $\beta \leq 8^\circ$. Since such angles are within the range of the dimple size, local hot spots should be avoided.

Thus, one may distinguish between local hot spots which enclose small β angles and have severe effects on general instability, and large hot regions enclosing large β angles which have a lesser effect on general instability. In the latter case, the edge effect may cause a drop of buckling load similar to that experienced by the torisphere at the juncture between the spherical cap and the torus.

Optimization

General Principles of Grid Optimization

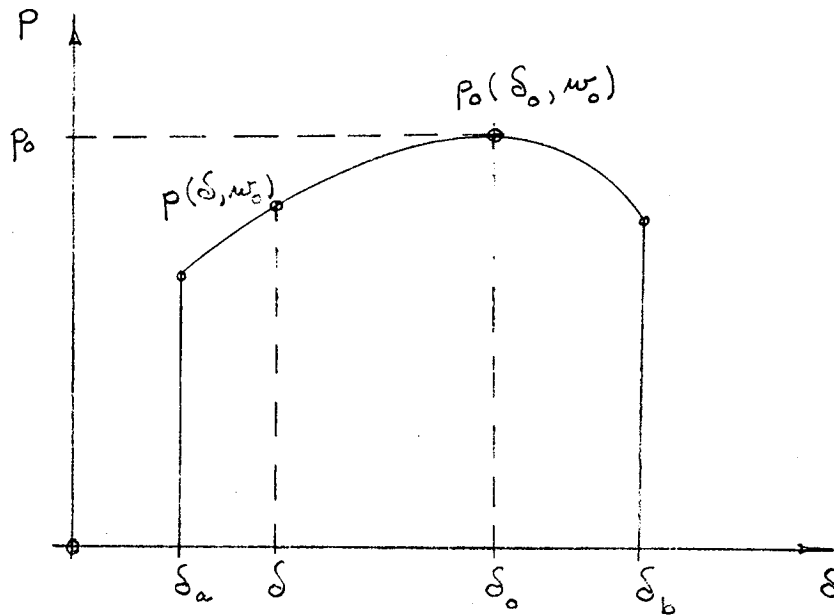
Two basic principles of grid optimization will be proven under assumptions of continuity and monotonicity which should be satisfied for the type of construction proposed here.

The first principle is the equivalence of the following statements:

- I. For a given dome shape and size, the optimum distribution of material between ribs and skin is that which maximizes the pressure for a specified weight of material.
- II. For a given dome shape and size, the optimum distribution of material between the ribs and skin is that which minimizes the weight of material for a specified pressure.

It will be assumed that the collapse pressure p is a continuous function of the material distribution δ between ribs and skin, and the dome weight w and that it is strictly increasing in w for a specified δ . Due to the continuity of p , for some distribution δ , p will reach a maximum in the closed interval $\delta_a \leq \delta \leq \delta_b$ where δ_a represents all the material concentrated in ribs and δ_b represents all the material concentrated in skin.

Consider hypothesis I. and plot collapse pressure p vs. material distribution δ for a specified weight $w = w_0$.



For distribution δ_0 , p reaches its maximum p_0 .

Now consider hypothesis II and assume that the specified pressure is p_0 .

At $\delta \neq \delta_0$, $p < p_0$ for a weight $w \leq w_0$.

Hence: $w > w_0$ to give a pressure p_0 for a distribution of material other than δ_0 .

The second statement to be proved is the "one horse shay" concept of failure. In essence, the principle states that the optimum construction is reached when all components collapse simultaneously. For the construction proposed, one considers failure due to general instability, rib crippling and panel instability between ribs.

For a given dome weight, \bar{w} , assign a weight distribution to the components:

δ_0 to general instability

δ_1 to rib crippling

δ_2 to panel instability

δ may be assumed normalized such that

$$\delta_0 + \delta_1 + \delta_2 = 1$$

Consider the collapse pressures p_i , ($i = 0, 1, 2$) for general instability, rib crippling and panel instability to be continuous monotonically increasing functions of δ_i and that p_i is not decreased by changes in δ_j , $j \neq i$.

$$p_i = p_i(\delta_i), \quad \frac{dp_i}{d\delta_i} > 0$$

Designate the least of the three values of p_i as $(p_i)_{\min}$.

If $(p_i)_{\min} = p_0 < p_1$ or p_2 , the collapse pressure of the structure is increased by taking increments of δ from δ_1 and δ_2 and adding them to δ_0 , thus increasing p_0 at the expense of p_1 and p_2 . This process may continue in a continuous manner due to the assumed continuity of p until all three pressures are equal. At this point $(p_i)_{\min}$ will have reached its maximum value.

Optimum Dimensions

The optimum dimensions are thus obtained from conditions that

$$p_{cr} = p_0 = p_1 = p_2$$

i.e

$$\begin{aligned} p_{cr} &= c_0 E \left(\frac{t}{R}\right)^2 [3\alpha(1+\delta)^2 + (1+\alpha)(1+\alpha\delta^2)]^{1/2} \\ &= 2.08 E \left(\frac{t}{R}\right) \left(\frac{b}{d}\right)^2 (1+\alpha) \left[\left(\frac{d}{h}\right)^2 + 0.567\right] \\ &= 7.40 E \left(\frac{t}{R}\right) \left(\frac{t}{h}\right)^2 (1+\alpha) \end{aligned}$$

(4.36)

$$c_0 = 2 \bar{c}$$

where

$$\alpha = \frac{bd}{th}, \quad \delta = \frac{d}{t}$$

For a given design, p, E, and R are determined by design requirements and optimum shape conditions.

The remaining four parameters b, d, t, h, are apparently restricted by only the three equations above, which presumably should leave one free parameter. This arbitrariness, however, disappears when one considers that the equation for obtaining panel instability was obtained under the assumption that the panel was small enough to be treated as a plate. In order for this to be true, h must be considerably smaller than the dimple diameter observed in the tests.

Solution Of The Optimization Equations

In terms of a non-dimensional pressure,

$$\bar{p} = \frac{p}{E}$$

the optimization equations in non-dimensional form are the following:

$$\left. \begin{aligned} \bar{p} &= c_0 \left(\frac{t}{R}\right)^2 \gamma \\ \bar{p} &= c_1 \frac{t}{R} \left(\frac{b}{d}\right)^2 (1 + \alpha) \left[\left(\frac{d}{h}\right)^2 + \bar{c}_1\right] \\ \bar{p} &= c_2 \frac{t}{R} \left(\frac{t}{h}\right)^2 (1 + \alpha) \end{aligned} \right\} \quad (4.37 \text{ a,b,c})$$

Where

$$\left. \begin{aligned} \gamma &= [3\alpha(1 + \delta)^2 + (1 + \alpha)(1 + \alpha \delta^2)]^{1/2} \\ \alpha &= \frac{bd}{th} \\ \delta &= \frac{d}{t} \end{aligned} \right\} \quad (4.38 \text{ a,b,c})$$

and

$$\begin{aligned}c_0 &= 0.8 \times 1.22474 & c_1 &= 2.08187 \\c_2 &= 7.40220 & \bar{c}_1 &= 0.566667\end{aligned}$$

c_0 is the upper limit value $0.8 \times 2 \times 0.61237$ and may be lowered by replacement by some reduced coefficient, c_0^* .

$$c_0^* < c_0$$

These equations are restricted by the plate approximation requirement that

$$h \leq 2 \sqrt{Rt}$$

In order to see the effect of this parameter, set

$$h^2 = \epsilon Rt, \quad \epsilon \leq 4 \quad (4.39)$$

and consider the solution for various values of ϵ . Lower bounds of ϵ will exist due to fabrication limitations.

Now for a fixed ϵ , equations (4.37 a,b,c,) and (4.39) represent four non-linear equations in four unknowns b , d , t , and h . A unique non-dimensional positive real solution for these variables will be obtained by elimination in terms of \bar{p} and ϵ .

Thus:

Substitute eq. (4.38c) and (4.39) into (4.37b)

$$\bar{p} = c_1 \frac{t}{R} \frac{b^2}{\delta^2 t^2} (1 + \alpha) \left(\frac{\delta^2 t}{\epsilon R} + \bar{c}_1 \right) \quad (4.40)$$

Substitute (4.39) into (4.37c)

$$\bar{p} = \frac{c_2}{\epsilon} \left(\frac{t}{R} \right)^2 (1 + \alpha) \quad (4.41)$$

Equate (4.40) and (4.41)

$$c_1 \frac{b^2}{\delta^2 t^2} \left(\frac{\delta^2 t}{\epsilon R} + \bar{c}_1 \right) = \frac{c_2 t}{\epsilon R}$$

Multiply by $\left(\frac{d}{h}\right)^2 \frac{\delta^2}{c_1}$ and use eq. (4.38b)

$$\alpha^2 \left(\frac{\delta^2 t}{\epsilon R} + \bar{c}_1 \right) = \frac{c_2 \delta^2}{c_1 \epsilon} \frac{t}{R} \frac{d^2}{h^2}$$

Use (4.38c) and (4.39)

$$\alpha^2 \left(\frac{\delta^2 t}{\epsilon R} + \bar{c}_1 \right) = \frac{c_2 \delta^4}{c_1 \epsilon^2} \left(\frac{t}{R} \right)^2$$

The quadratic in $\frac{t}{R}$ is:

$$\left(\frac{t}{R} \right)^2 = \frac{c_1 \epsilon}{c_2} \frac{\alpha^2}{\delta^2} \left(\frac{t}{R} \right) + \frac{c_1 \bar{c}_1 \epsilon^2}{c_2} \frac{\alpha^2}{\delta^4}$$

Define the quantities:

$$\boxed{c_3 = \frac{c_1 \epsilon}{c_2}, \quad c_4 = \frac{c_1 \bar{c}_1 \epsilon^2}{c_2}} \quad (4.42)$$

The quadratic in $\frac{t}{R}$ becomes:

$$\left(\frac{t}{R} \right)^2 = c_3 \frac{\alpha^2}{\delta^2} \left(\frac{t}{R} \right) + c_4 \frac{\alpha^2}{\delta^4} \quad (4.43)$$

Solving eq. (4.41) for $\frac{t}{R}$,

$$\frac{t}{R} = \sqrt{\frac{\bar{p}}{1 + \alpha} \frac{\epsilon}{c_2}} = f(\bar{p}, \alpha) \quad (4.44)$$

Substitute (4.44) into (4.43)

$$f^2 = c_3 \frac{\alpha^2}{\delta^2} f + c_4 \frac{\alpha^2}{\delta^4}, \quad \text{i.e.}$$

$$f^2 \delta^4 - c_3 \alpha^2 \delta^2 - c_4 \alpha^2 = 0$$

Solving the quadratic in δ^2 ,

$$\delta^2 = \frac{\alpha^2}{2f} \left[c_3 + \sqrt{c_3^2 + \frac{4c_4}{\alpha^2}} \right], \quad \text{since } \delta^2 > 0$$

Substituting back for $f(\bar{p}, \alpha)$,

$$\delta^2 = \frac{\alpha^2}{2} \sqrt{\frac{c_2}{\epsilon} \frac{1+\alpha}{\bar{p}}} \left[c_3 + \sqrt{c_3^2 + \frac{4c_4}{\alpha^2}} \right] \quad (4.45)$$

Again from eq. (4.37a) and (4.41)

$$\bar{p} = c_0 \frac{\bar{p}}{1+\alpha} \frac{\epsilon}{c_2} \gamma, \quad \gamma^2 = (1+\alpha) \left(\frac{c_2}{c_0 \epsilon} \right)^2$$

Expanding eq. (4.38a) for γ^2

$$(1+\alpha)^2 \left(\frac{c_2}{c_0 \epsilon} \right)^2 = 1 + 4\alpha + \alpha[6\delta + \delta^2(4+\alpha)]$$

i.e.

$$\delta^2(4+\alpha) + 6\delta - g(\alpha) = 0$$

where

$$g(\alpha) = \frac{(1+\alpha)^2}{\alpha} \left(\frac{c_2}{c_0 \epsilon} \right)^2 - \frac{1+4\alpha}{\alpha} \quad (4.46)$$

Again solving the quadratic in δ .

$$\delta = \frac{-3 + \sqrt{9 + (4 + \alpha) g(\alpha)}}{4 + \alpha} \quad (4.47)$$

since $\delta > 0$ as before.

Eliminating δ from (4.45) and (4.47)

$$\frac{\alpha^2}{2} \sqrt{\frac{c_2}{\epsilon} \frac{1 + \alpha}{\bar{p}}} \left[c_3 + \sqrt{c_3^2 + \frac{4 c_4}{\alpha^2}} \right] = \frac{[-3 + \sqrt{9 + (4 + \alpha) g(\alpha)}]^2}{(4 + \alpha)^2}$$

and solving for \bar{p} ,

$$\bar{p} = \left\{ \frac{\alpha^2 (4 + \alpha)^2 \sqrt{\frac{c_2}{\epsilon} (1 + \alpha)} \left[c_3 + \sqrt{c_3^2 + \frac{4 c_4}{\alpha^2}} \right]}{2[-3 + \sqrt{9 + (4 + \alpha) g(\alpha)}]^2} \right\}^2 \quad (4.48)$$

where

$$g(\alpha) = \left(\frac{c_2}{c_0 \epsilon} \right)^2 \frac{(1 + \alpha)^2}{\alpha} - \frac{1 + 4\alpha}{\alpha}$$

Off-Optimum Design

Due to constructional limitations, the theoretical optimum often cannot be realized and off-optimum designs must be obtained. The set of equations,

$$\left. \begin{aligned} \bar{p} &= c_0 \left(\frac{t}{R}\right)^2 [3\alpha(1+\delta)^2 + (1+\alpha)(1+\alpha\delta^2)]^{1/2} \\ \bar{p} &= c_1 \left(\frac{t}{R}\right) \left(\frac{b}{d}\right)^2 (1+\alpha) \left[\left(\frac{d}{h}\right)^2 + \bar{c}_1\right] \\ \bar{p} &= c_2 \left(\frac{t}{R}\right) \left(\frac{t}{h}\right)^2 (1+\alpha) \end{aligned} \right\} \begin{array}{l} 4.49 \\ a, b, c \end{array}$$

$$h^2 = \epsilon Rt, \quad \epsilon \leq 4 \quad (4.50)$$

with

$$\alpha = \frac{bd}{th}, \quad \delta = \frac{d}{t} \quad (4.51)$$

represent the solution for b, d, t, h , for chosen values of ϵ . Any additional geometric requirements must be obtained at the expense of satisfying these relations. For each such constraint relation, one of the equations must be discarded. The \bar{p} or h associated with the discarded equation must be not less than the design \bar{p} or h .

Generally one wishes to retain equation (4.49a) for general instability in the interest of efficiency. At the same time, eq. (4.50) is usually necessary to hold the panel size from becoming too small. Thus, one may wish to dispense with eq. (4.49b) or (4.49c).

Solution for Ribs of Non-Critical Width

If the dome is to be of integral construction, the panels must be milled or etched out. This usually results in a minimum rib width which is in excess of optimum requirements so that \bar{p} obtained from eq. (4.49b) will exceed the design pressure.

Combining eq. (4.49a) and (4.50),

$$\bar{p} = c_2 \left(\frac{t}{R}\right) \frac{t^2}{\epsilon R t} (1 + \alpha) = \frac{c_2}{\epsilon} \left(\frac{t}{R}\right)^2 (1 + \alpha)$$

$$\left(\frac{t}{R}\right)^2 = \frac{\epsilon}{c_2} \frac{\bar{p}}{1 + \alpha} \quad (4.52)$$

Substituting (4.41) into eq. (4.49a)

$$\bar{p} = \frac{c_o \epsilon}{c_2} \frac{\bar{p}}{1 + \alpha} [3\alpha(1 + \delta)^2 + (1 + \alpha)(1 + \alpha \delta^2)]^{1/2}$$

Squaring and rearranging,

$$3\alpha(1 + \delta)^2 + (1 + \alpha)(1 + \alpha \delta^2) = \left(\frac{c_2}{c_o \epsilon}\right)^2 (1 + \alpha)^2$$

Expanding,

$$1 + 4\alpha + 6\alpha\delta + 4\alpha\delta^2 + \alpha^2 \delta^2 = \left(\frac{c_2}{c_o \epsilon}\right)^2 (1 + 2\alpha + \alpha^2) \quad (4.53)$$

This is a quadratic requirement relating α and δ . It is the same relation between α and δ which has been previously developed (eq. 4.47).

From eq. (4.39) and (4.51),

$$\alpha = \frac{b}{h} \delta, \quad \alpha^2 = \frac{b^2 \delta^2}{\epsilon R t}$$

$$\frac{t}{R} = \frac{1}{\epsilon} \left(\frac{b\delta}{R\alpha}\right)^2 \quad (4.54)$$

Substitute (4.54) into (4.52),

$$\left(\frac{b\delta}{R\alpha}\right)^4 = \frac{\epsilon^3}{c_2} \frac{\bar{p}}{1 + \alpha}, \quad \frac{\delta}{\alpha} (1 + \alpha)^{1/4} = \frac{R}{b} \left(\frac{\bar{p} \epsilon^3}{c_2}\right)^{1/4}$$

Define

$$\beta = \frac{R}{b} \left(\frac{\bar{p} \epsilon^3}{c_2} \right)^{1/4} \quad (4.55)$$

then,

$$\delta = \frac{\alpha \beta}{(1 + \alpha)^{1/4}} \quad (4.56)$$

From eq. (4.47)

$$\beta = \frac{R}{b} \left(\frac{\bar{p} \epsilon^3}{c_2} \right)^{1/4} = \frac{(1 + \alpha)^{1/4}}{\alpha} \frac{-3 + \sqrt{9 + (4 + \alpha) g(\alpha)}}{4 + \alpha} \quad (4.57)$$

Eq. (4.57) establishes the relation between β and α to provide the solution.

One uses (4.57) to find β from R , b , and \bar{p} , then finds α from (4.57), δ from (4.56). Thus, all quantities may be determined. Of course, one must check to assure that the critical pressure for rib crippling associated with the discarded equation is at least equal to the design pressure. The easiest way to do this is to compare the p/E value of the design with that given in the table. One should have:

$$\left(\frac{p}{E} \right)_{\text{design}} \leq \left(\frac{p}{E} \right)_{\text{table}}$$

Other Boundary Conditions for Plate Buckling

For off-optimum designs with non-critical ribs, it appears reasonable to assume a clamped boundary condition for the panels if all panels buckle inward. This condition requires less distortion of the panel mid-surface for snap-through.

Both hinged and clamped boundaries are treated in the plate buckling summaries of Gerard and Becker (reference 19). Their allowable stresses are given in the form:

$$\sigma_{\text{cr}} = \frac{k \pi^2 E}{12(1 - \nu^2)} \left(\frac{t}{a} \right)^2$$

Since: $a = \frac{2}{\sqrt{3}} h$,

this may be written,

$$\sigma_{cr} = \frac{k \pi^2 E}{16(1 - \nu^2)} \left(\frac{t}{h}\right)^2$$

For hinged and clamped edges, their values of k are:

$$k(\text{hinged}) = 5.00$$

$$k(\text{clamped}) = 12.2 \quad (\text{from curve})$$

Their hinged values differ slightly from that of Timoshenko and Gere (reference 20) and Pfluger (reference 31) who both give

$$\sigma_{cr} = \frac{4 \pi^2 E}{12(1 - \nu^2)} \left(\frac{t}{h}\right)^2$$

The ratio between the hinged values is:

$$\frac{\sigma_{cr}(\text{G. \& B.})}{\sigma_{cr}(\text{T. \& G.})} = \frac{5}{16} \frac{12}{4} = \frac{15}{16}$$

Assuming the clamped values of Gerard and Becker as either correct or conservative, one obtains:

$$\begin{aligned} \sigma_{cr}(\text{clamped}) &= \frac{12.2}{16} \frac{\pi^2 E}{1 - \nu^2} \left(\frac{t}{h}\right)^2 \\ &= 8.45 E \left(\frac{t}{h}\right)^2 \end{aligned}$$

$$\text{for } \nu = \frac{1}{3}$$

Equating the actual panel stress to the allowable,

$$\frac{1}{1 + \alpha} \frac{PR}{2t} = 8.45 E \left(\frac{t}{h}\right)^2$$

one obtains the critical pressure

$$p_2(\text{clamped}) = 16.90 \frac{t}{R} \left(\frac{t}{h}\right)^2 (1 + \alpha)$$

and the constant c_2 is

$$c_2 = 16.90$$

which is an increase of $\frac{16.90}{7.4} = 2.29$ over the hinged value.

The effect of the increase in p_2 on the design will be to give thinner panels and heavier ribs² for a given grid size, thus increasing general stability and resulting in lower values of η , the weight ratio.

The jump in p_2 associated with the jump in c_2 from 7.4 to 16.9 violates the continuity assumption in the proof of the "one-horse shay" concept of failure associating δ_0 , δ_1 , and δ_2 with p_0 , p_1 , and p_2 . This discontinuous increase in p_2 may result in a lighter weight dome for the condition:

$$p_0 = p_2(\text{clamped}) = p_{cr} , \quad p_1 > p$$

than for the condition

$$p_0 = p_1 = p_2(\text{hinged}) = p_{cr}$$

CHAPTER V - EXPERIMENTAL DATA

Plastic Model Testing

Model Material

The plastic material used for the fabrication of the models tested in this program was "rigid-vinyl" manufactured by Union Carbide Company under the trademark "Bakelite." The material was purchased from Cadillac Plastic and Chemical Company in the form of planished sheets. The 21 x 51 sheets came in 13 standard thicknesses from 0.010 to 0.125 inches. They can be obtained in transparent, translucent, and opaque in various colors or clear. The surface finishes are pressed, polished, or matte, or any desired combination thereof. This plasticized poly-vinyl chloride material can be formed at 160°F (versus 275°F for unplasticized PVC). It is a mixture of 86% vinyl chloride and 14% vinyl acetate. The vinyl acetate is used as an internal plasticizer and acts on the monomer to soften it, to reduce its forming temperature, and in general, provide a more useful material.

Material Property Tests - To establish basic material properties of the polyvinyl chloride plastic material, the following tests were conducted at the start of the program:

Modulus of Elasticity - The modulus of elasticity of the material was determined in the direction of rolling and perpendicular to the direction of rolling by standard tensile coupons, 6 inches in length and 1/2 inch in width, cut from sheets of different thickness. The coupons were tested using a Baldwin Universal testing machine with a 2-inch gage length extensometer clamped to the specimen. Continuous load-deflection data was autographically recorded to fracture. The variation in Young's Modulus versus thickness is shown in Figure 5.1. The results show that the average modulus is 465,000 psi with a maximum deviation from the mean of 3.5%, that the material has nearly isotropic properties and the modulus of elasticity is somewhat dependent upon the thickness variation. A typical stress-strain curve is shown in Figure 5.2.

Strain Rate and Creep - Tests were conducted to measure the effect of strain rate and sensitivity to creep. Strain rates varying from .02 to .10 in/in/min. showed no discernable difference in the modulus of elasticity. Reference 22, however, showed that for loading rates $> .20$ in/in/min. that the material is rate dependent. There were no detectable creep effects on the material when constant loads below the proportional limit were maintained for several minutes.

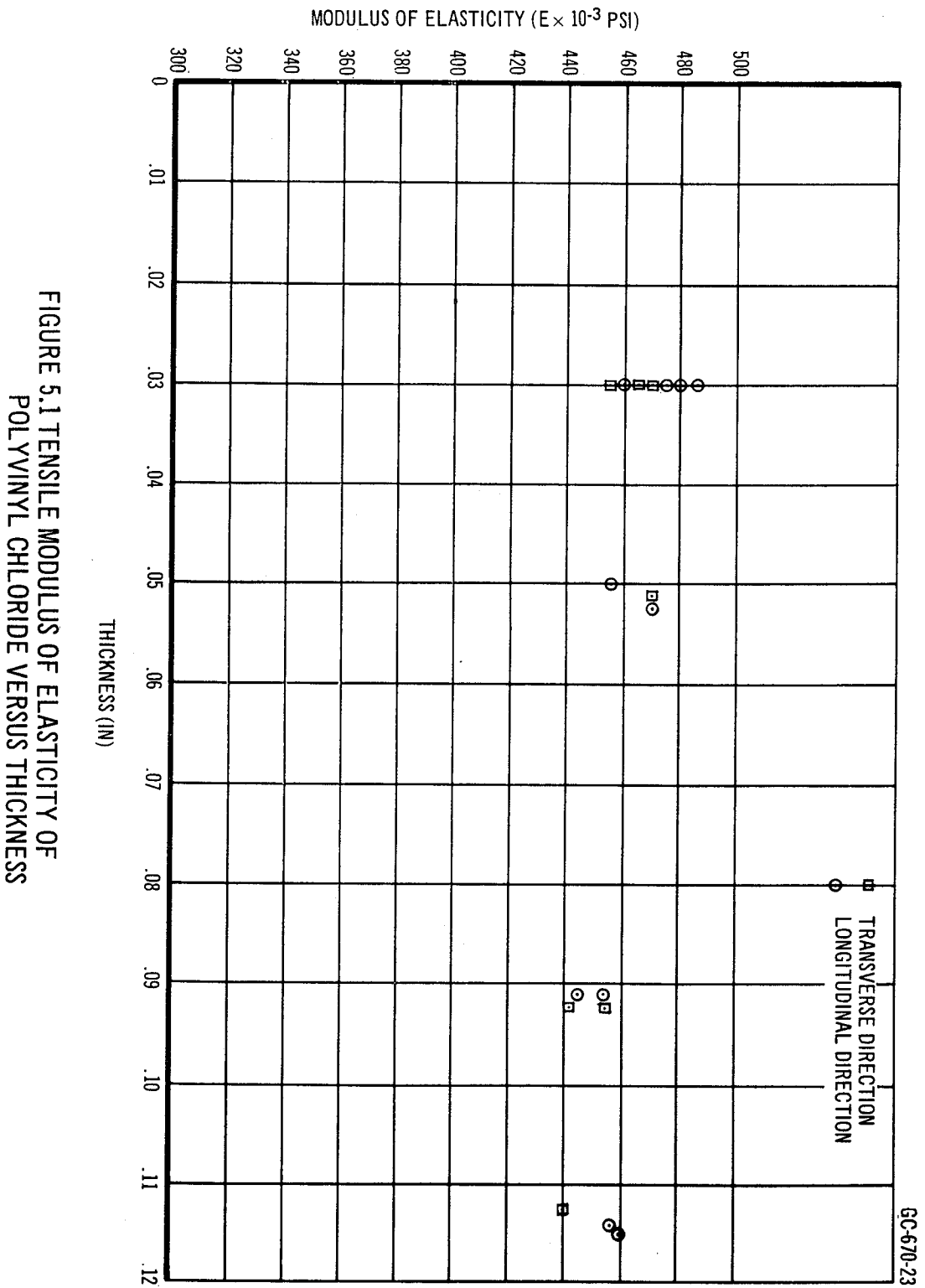


FIGURE 5.1 TENSILE MODULUS OF ELASTICITY OF POLYVINYL CHLORIDE VERSUS THICKNESS

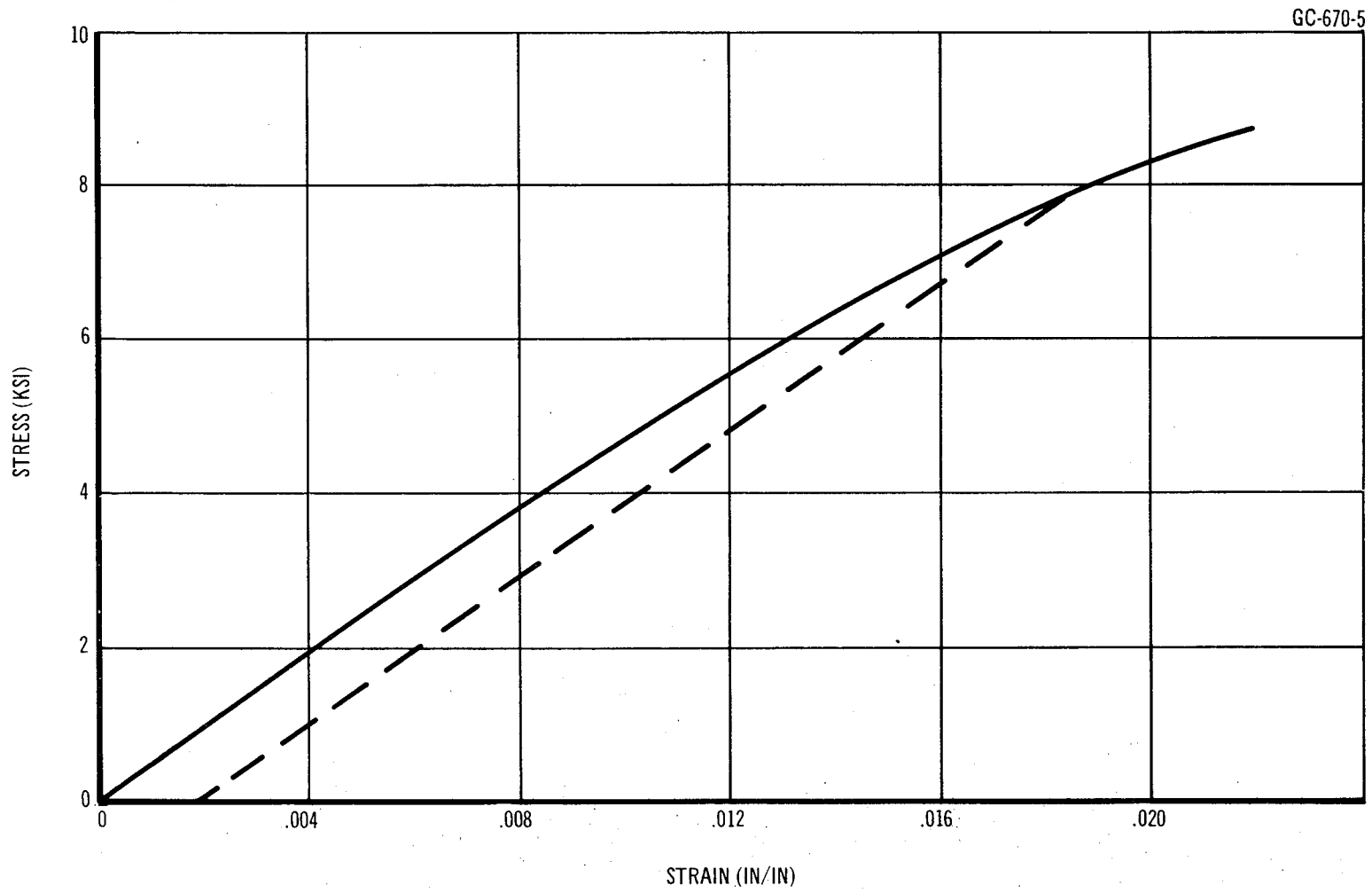


FIGURE 5.2 TYPICAL TENSILE STRESS-STRAIN CURVE
(POLYVINYL CHLORIDE PLASTIC)

Poisson's Ratio - Several tests were conducted to establish Poisson's ratio in the elastic region. The results showed this value to be 0.37 with a minimum of scatter.

The Poisson's ratio and the high ratio of elastic limit stress to modulus of elasticity are two explicit advantages. The Poisson's ratio approaches that of many metals. We, therefore, can achieve the same stress and strain distribution in the model and prototype. The high ratio of elastic limit stress to modulus of elasticity allows buckling to occur in the elastic range which makes possible the repeatability of testing one model. Another advantage in the use of the rigid vinyl material is the ease in cementing it to itself. Tetrahydrofuran, methyl ethylketone (MEK) were reasonably satisfactory solvent cements for this material, forming bonds up to 50 per cent of the strength of the original material. It has been recommended that when many joints are made that sufficient time should be allowed before testing in order to let the cement cure adequately. The softening process of the solvent type cement locally lowers the modulus of elasticity.

Fabrication of Domes

The shells of the basic monocoque dome configurations and the stiffened dome configurations were fabricated using the same technique. For the stiffened dome configurations, the appropriate ribs were bonded on the concave surface of the shell.

The seven dome shapes fabricated in this study had a constant base diameter of 16 inches. The configurations are shown in Table 5.1.

Table 5.1

Dome Configuration	a/b-Base Radius To Dome Height Ratio
Spherical	4.78; 3.33; 2.0; 1.0
Ellipsoidal	3.3; 2.0
Torispherical	2.0

The individual molds were designed to fit a standard base plate mounted on a 14 in. diameter lathe faceplate. The base plate served as the holding fixture when turning the mold and dome, and the mold's vacuum manifold cover. The formed shell was held in contact with the mold's

concave surface with vacuum during the machining of the inside radius of the plastic dome shell. All the aluminum dome molds and domes were machined on the same lathe and base plate, thus eliminating most of the concentricity problems and reducing the cost of multiple tooling. The female molds were machined from 6061-T651 aluminum plate. Each 20 in. diameter mold was turned on an 18 in. Monarch Lathe using a True-Trace hydraulic tracing attachment. The tracing attachment follows a template which duplicates the desired mold cavity contour. The spherical contour template $(a/b) = 3.33$ can be seen in the machining setup in Figure 5.3. (Note template in horizontal plane at right of center in the photograph.) Figure 5.4 shows a completed spherical mold and plastic dome with a radius to height, a/b of 3.33. The final step in the preparation of the mold is the through-drilling of many small holes (#70 to #80) normal to the contoured surface, but which are not visible in the photograph. These holes are part of the vacuum manifold for drawing the plastic into the cavity during vacuum forming and during machining the plastic dome to the required wall thickness. In the forming of the shallow domes air would become trapped under the plastic between the holes. This was eliminated by scribing rings and cross hatches on the surface of the mold. As mentioned before, the only tooling necessary to make plastic domes of one particular shape was the female mold and its corresponding tracing template. By changing the diameter of the tracing stylus to compensate for the dome thickness, it was possible to machine the inside surface of the plastic dome using the same template that was used for the mold surface. If two templates were used, the shell wall thickness variations would have been compounded by template differences, temperature changes, and cutting tool wear. This would also mean that for every shell shape with a different wall thickness, an internal surface template would also have been required.

The forming method used was vacuum forming, or negative pressure forming, with an additional amount of external pressure. The external pressure was added to minimize the dimensional difference between the mold and plastic dome caused by the difference of their coefficients of expansion during the transition temperature and to help form the rigid vinyl over the sharp radii.

A sheet of rigid-vinyl was clamped on the mold with a clamping ring (Figure 5.5). The external pressure plate was then bolted to the clamping ring (an O ring is used for the pressure seal). The whole assembly was placed in an oven mechanically connected to pressure and vacuum. After connecting the vacuum and external pressure lines, the temperature in the oven was raised to 240°F. The mold assembly was soaked at this temperature for a minimum of six hours. After soaking, the vacuum pump was turned on and the rigid-vinyl sheet was pulled down to conform to the mold cavity. When the plastic sheet pulled down, the space above it drew in oven air at 240°F into the space above the plastic sheet. This was done to eliminate cold spots while forming. While the negative pressure caused by the vacuum was holding down the plastic sheet, the additional external pressure was applied with factory air regulated to 15 psig. The oven heat was turned off, and the door opened so that the whole mold assembly could cool down to room temperature.

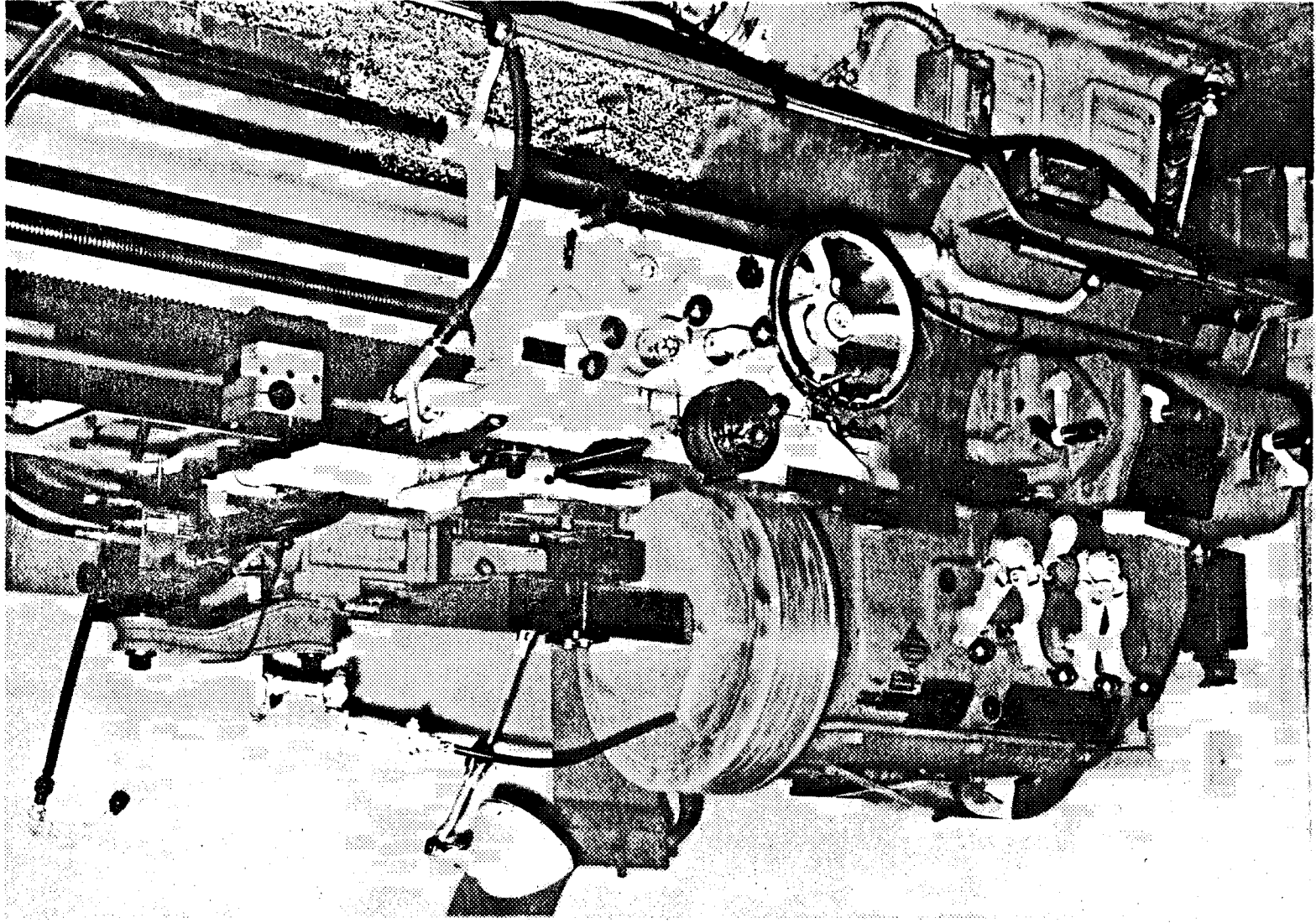


FIGURE 5.3 MACHINING VACUUM MOLD CAVITY USING
HYDRAULIC TRACING ATTACHMENT

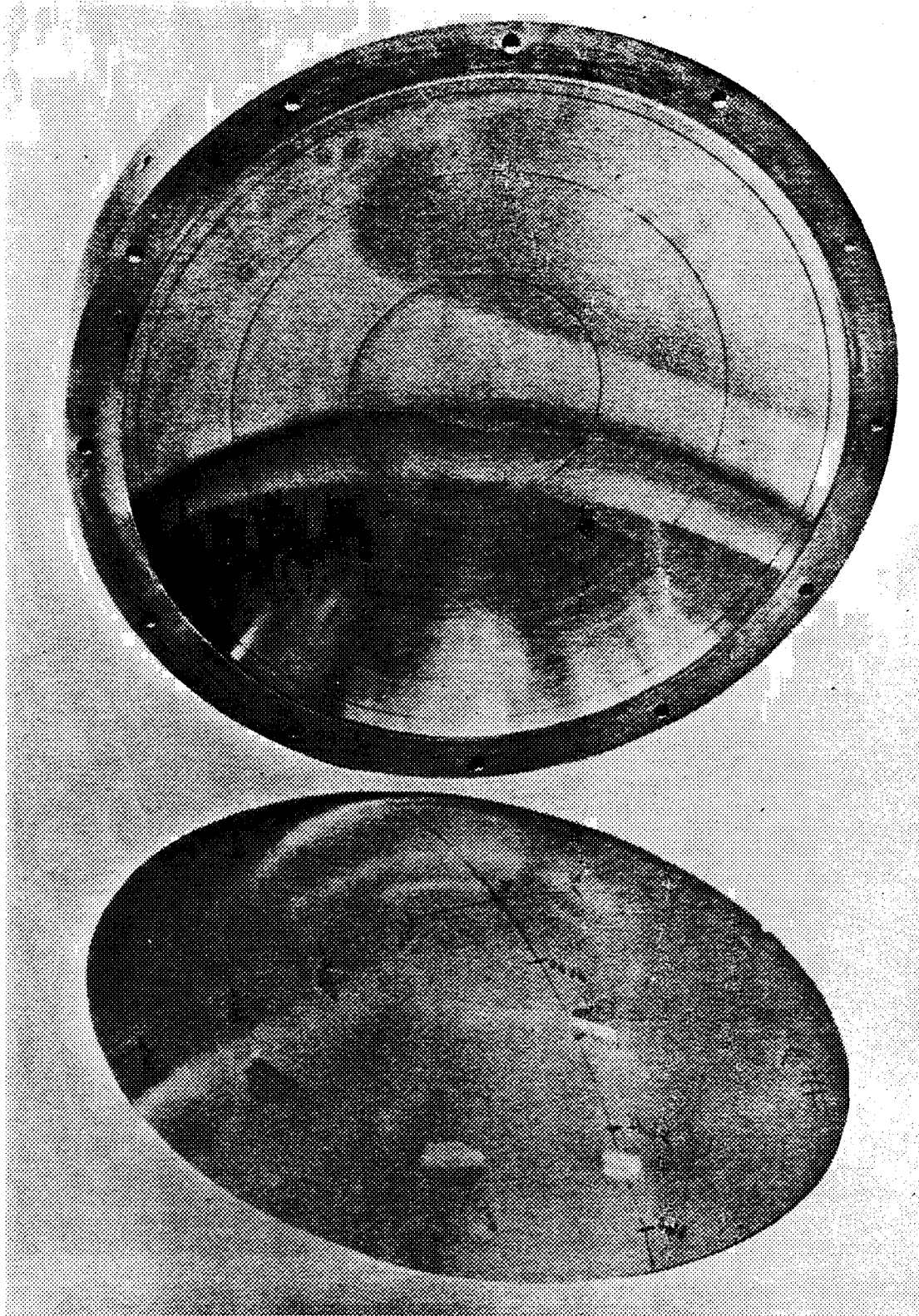


FIGURE 5.4 COMPLETED SPHERICAL MOLD AND PLASTIC DOME

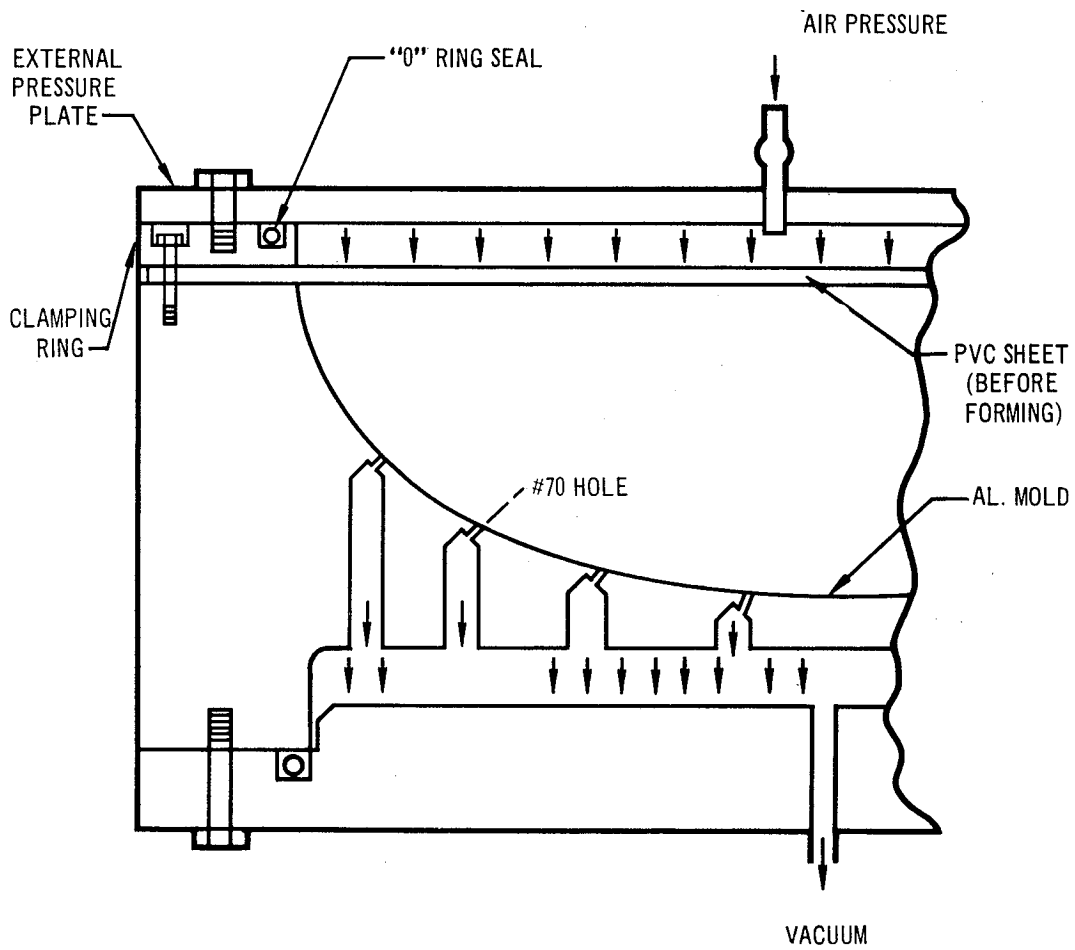


FIGURE 5.5 FORMING PLASTIC DOME MODEL

After the assembly had cooled to room temperature, the base plate was removed from the back of the mold and the mold was installed on the lathe base plate. The plastic dome was held tight to the mold cavity by vacuum while turning the internal surface of the vacuum formed dome. A Shrader rotating pressure joint was used between the rotating lathe spindle and the vacuum pump line.

The contraction of the plastic away from the aluminum mold was slight, but when the vacuum had been applied under the plastic dome, it was stretched slightly to conform to the mold cavity. In order to eliminate this stretching while machining, the plastic dome was parted from the excess clamping material. After parting, the edge was taped with a plastic coated fabric tape (Tuck) to restore the full 28-inch of vacuum used while turning the plastic dome to the required wall thickness. Soluble oil coolant was used while turning the rigid vinyl (PVC). This material turns well, but it should not be heated excessively. Tungsten carbide cutting tools were used to reduce wear since the accuracy of the dome wall was dependent upon the relationship of the radius of the cutting tool to the radius of the tracing stylus. The duplication of the hydraulic tracing attachment depends upon the conformity of the radius of the cutting tool and stylus.

When machining the plastic dome using the same template which was used to machine the aluminum mold cavity, the thickness dimension of the plastic dome had to be added to the radius of the stylus used to cut the mold cavity. The finished dome was then inspected for wall thickness variations. A dial indicator was mounted above a 1-inch diameter steel ball on an arm long enough to provide room for the indicator to reach the center of the 16-inch diameter plastic dome. For the stiffened domes, the ribs were routed from the same sheet material as the dome and cemented to the shell using Cadco No. 201 Solvent Cement. Figure 5.6 shows the small rectangular blocks that were used to position the ribs while cementing.

Test Set-Up

The testing fixture for the finished plastic dome models is shown in Figure 5.7. The dome shells were cemented to a stiff plexiglass ring. A 1/4 inch deep groove was cut into the ring, the shell placed into the groove, and this groove filled with Hysol 2039 epoxy cement with Hardner "C". The epoxy cement cured at room temperature. All of the shells made with an extra 1/4 inch for the epoxy cementing. This stiff ring, 1-inch thick by 2 inches wide, provided the fixed edge support for the dome model. The dome ring assembly is then clamped to a heavy Plexiglas base with provisions for pumping a vacuum from beneath the dome. For the monocoque and stiffened domes, a wooden block rests between the dome's inner surface and the base plate of the Plexiglas test fixture. The back up block protects the specimen from complete collapse so that tests can be repeated.

Test Procedure - Room Temperature

The test setup for the monocoque dome is shown in Figure 5.7a. The pressurization of the dome was accomplished by producing a negative pressure under the dome with a vacuum pump. The vacuum pressure was regulated with a Conoflow Type JH-20 vacuum regulator. The pressure was monitored and recorded from a 0 to 15 psia Statham pressure transducer. The output of the pressure transducer was conducted to the balance bridge and then to the X-axis of the four Mosely X-Y recorders (two double pen).

The deflection of the dome was monitored with six differential transformer displacement transducers held in place using a magnetic stand on the steel surface plate used to assemble the complete test setup. With this method, simultaneous plots were made of the test pressure versus deflections during a dome test.

The deflection transducers were calibrated before each test using a depth micrometer and reading the output on the X-Y recorders. This record was put on the same sheet of graph paper that was used during the test. The pressure channels were calibrated by shutting a known resistance across one leg of the transducer balance bridge. After calibrating the vacuum pump was turned on and the vacuum surge tank was evacuated to approximately 13 psia.

Test Procedure - Thermal Gradient

For the thermal gradient test ice was used as the cooling agent and water as the pressure medium. The test setup is shown schematically in Figure 5.8 and a photograph of it is Figure 5.9. Copper-Constantan Thermocouples were cemented to the model with "Eastman 910" cement. The standard thermocouple circuit was used with a switch introduced so only one reference thermocouple and only one voltmeter was used. Ice was first put into the lower cylinder and then the large upper ring holding the test specimen was bolted over the cylinder. Tap water was fed into the cylinder from the bottom and air bled from the top. During the soak period of two hours, the deflection transducers were put in place and periodic readings taken from the thermocouples. The pressure and deflection transducers were calibrated in the same manner as explained for the room temperature test procedure. Immediately before testing, a final temperature was recorded.

Monocoque Test Results

A total of seven monocoque domes were fabricated and tested in the experimental phase. The summary of test results are shown in Table 1.1 and a photograph of the buckling patterns are depicted in Figure 1.3.

Spherical Domes - Four spherical shapes were tested that had base radii to height ratios of 1:00, 2:00, 3.33 and 4.78 with a constant base radius of sixteen inches. Table 5.2 shows the measured thickness normal to the dome surface at the various locations. The buckling coefficient C is computed from the equation:

$$C = \frac{p}{2E t} (R)^2 \quad (5.1)$$

where

$$E = 465,000 \text{ psi}$$

Figure 5.10 shows the location of the displacement transducers on the appropriate shells. Figures 5.11 and 5.12 are plots of the radial deflection at failure transcribed from the autographic records.

Two effects of the test results deserve special mention. The first is the consistently high buckling coefficient for the range of R/t values of 245 to 345. These high buckling coefficients are a consequence of the minimization of imperfections and residual stresses and uniformity of the boundary conditions. The second effect is the remarkably complete buckle patterns over the spherical surfaces. In all tests, the formation of the pattern appeared to be instantaneous and occurred with a loud "bang." However, the backup block may have forced this condition. On the subsequent tests performed on the specimens, the initial collapse pressures were duplicated after a short relaxation time.

Ellipsoidal Domes - Two ellipsoidal domes were fabricated and tested with a/b ratios of 2.00 and 3.33. Table 5.3 shows the recorded thicknesses normal to the dome surface at the indicated locations. The buckling coefficients were computed using the theory of Mushtari-Galimov (Reference 8) where the maximum radius of curvature is substituted for (R) in equation (5.1). These coefficients are plotted in Figure 5.16 and compared with previous experimental data. The high buckling coefficients attained are indicative of the excellent fabrication and testing techniques employed in the study. Figures 5.13 and 5.14 are plots of the radial deflection at the buckling pressure.

Torispherical Domes - A single torispherical dome was tested with a spherical radius of 11.50 inches and a knuckle radius of 1.71 inches with an $a/b = 2.00$. The buckling coefficient for the torispherical dome was initially based upon the substitution of the spherical radius into equation (5.1). This assumption was shown to be incorrect by the visual observation of the buckle pattern at failure. A number of circumferential buckles occurred at the junction of the spherical cap and the torus, in the region of maximum discontinuity stress. This high discontinuity stress is thought to be the prime reason for the low experimental buckling coefficient. Figure 5.15 is a plot of the radial deflection at the failing pressure.



FIGURE 5.6 TYPICAL HOLDING BLOCK ARRANGEMENT FOR STIFFENED DOMES

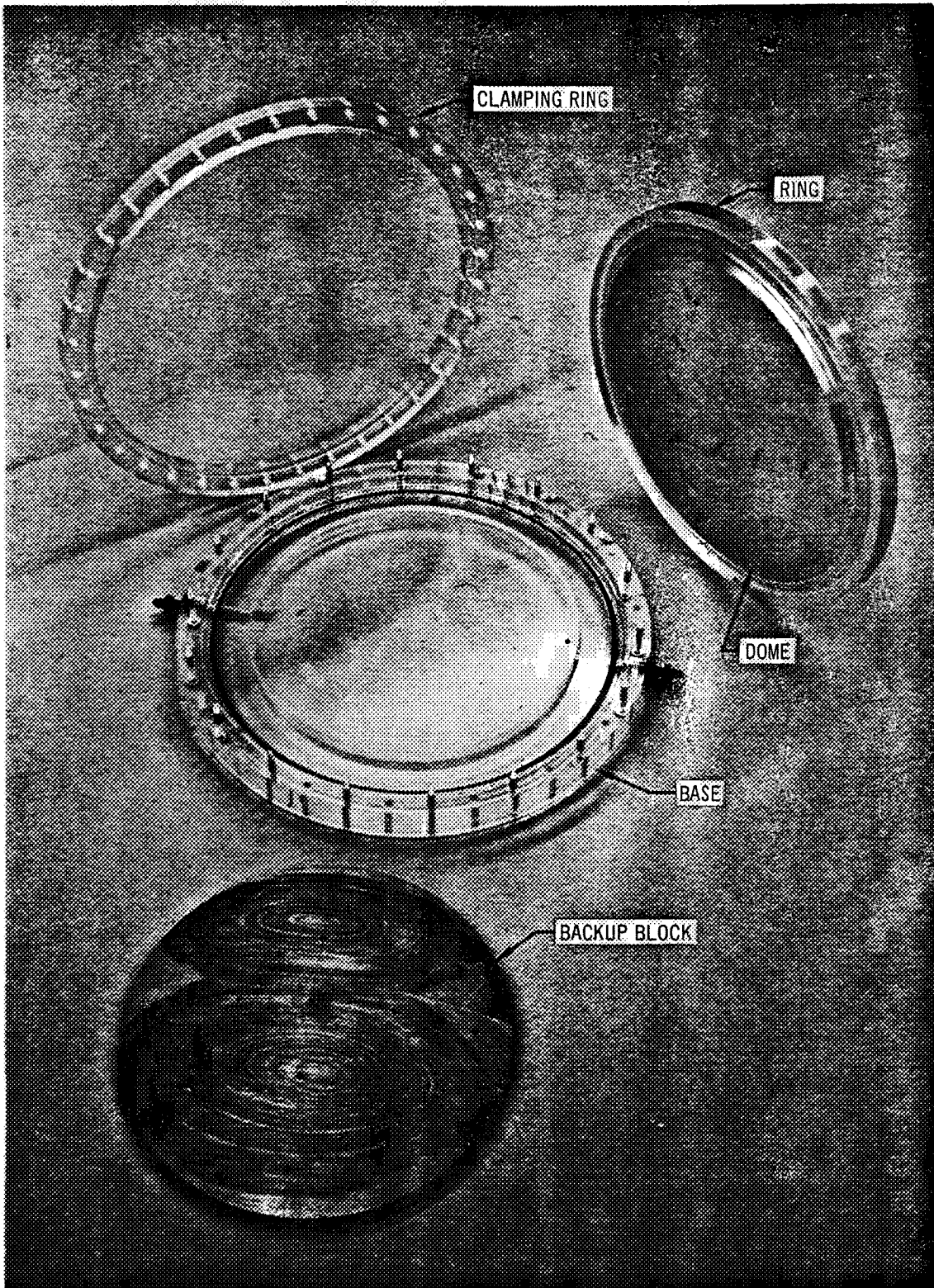


FIGURE 5.7 PLASTIC DOME TESTING FIXTURE

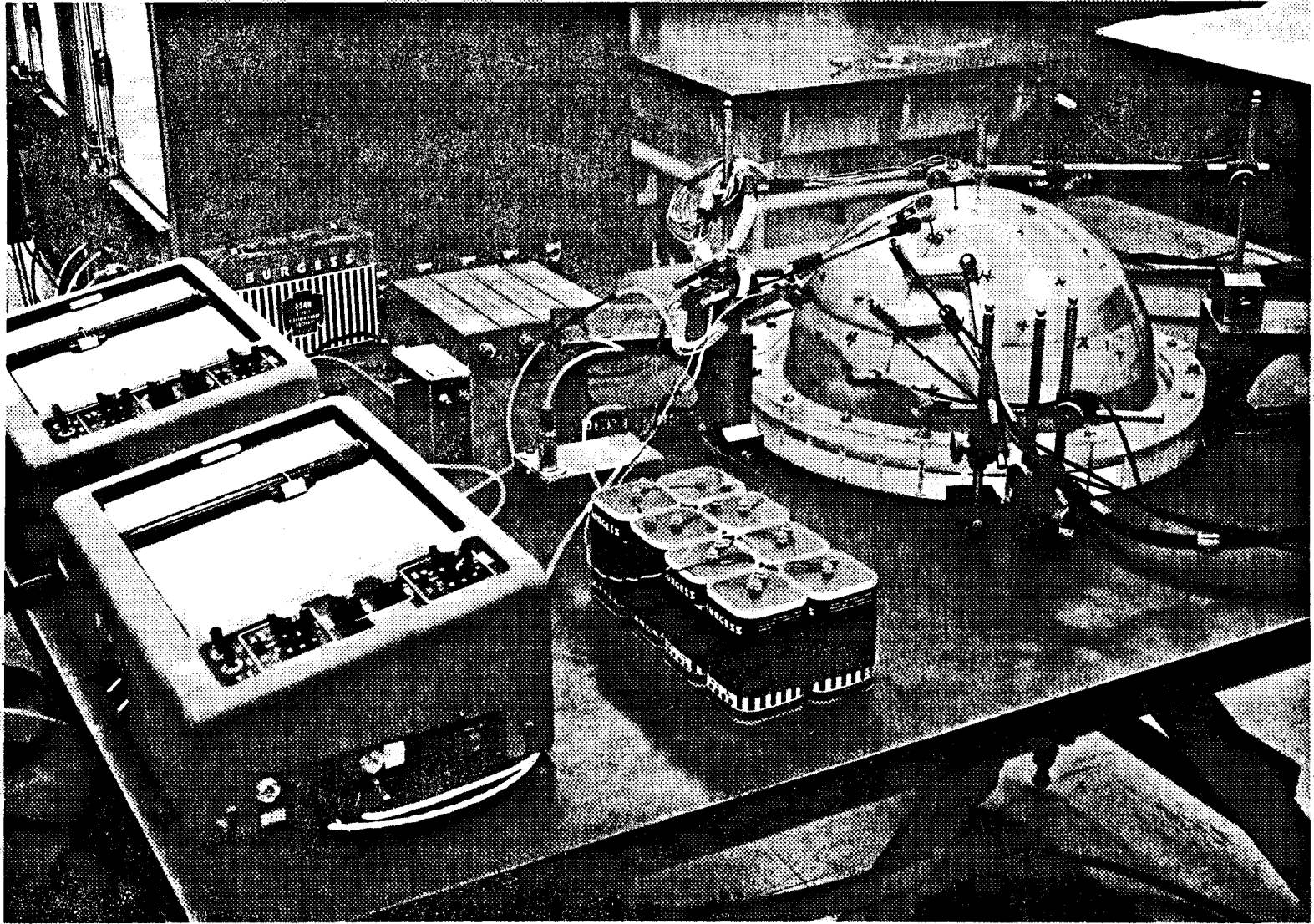


FIGURE 5.7a TYPICAL EXPERIMENTAL ARRANGEMENT

Howe, 1964

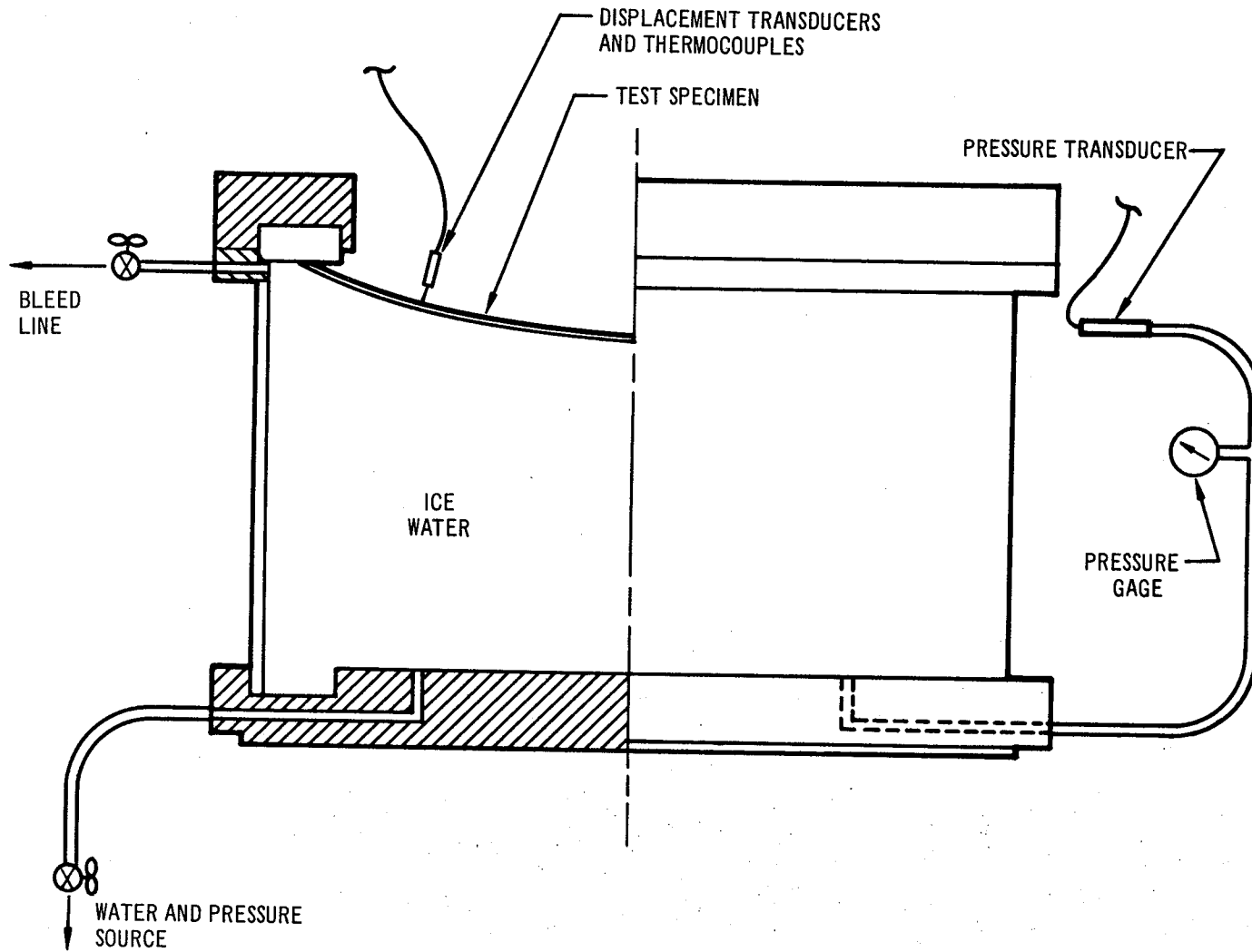


FIGURE 5.8 THERMAL GRADIENT BUCKLING TEST SETUP

FIGURE 5.9 THERMAL GRADIENT EXPERIMENTAL ARRANGEMENT

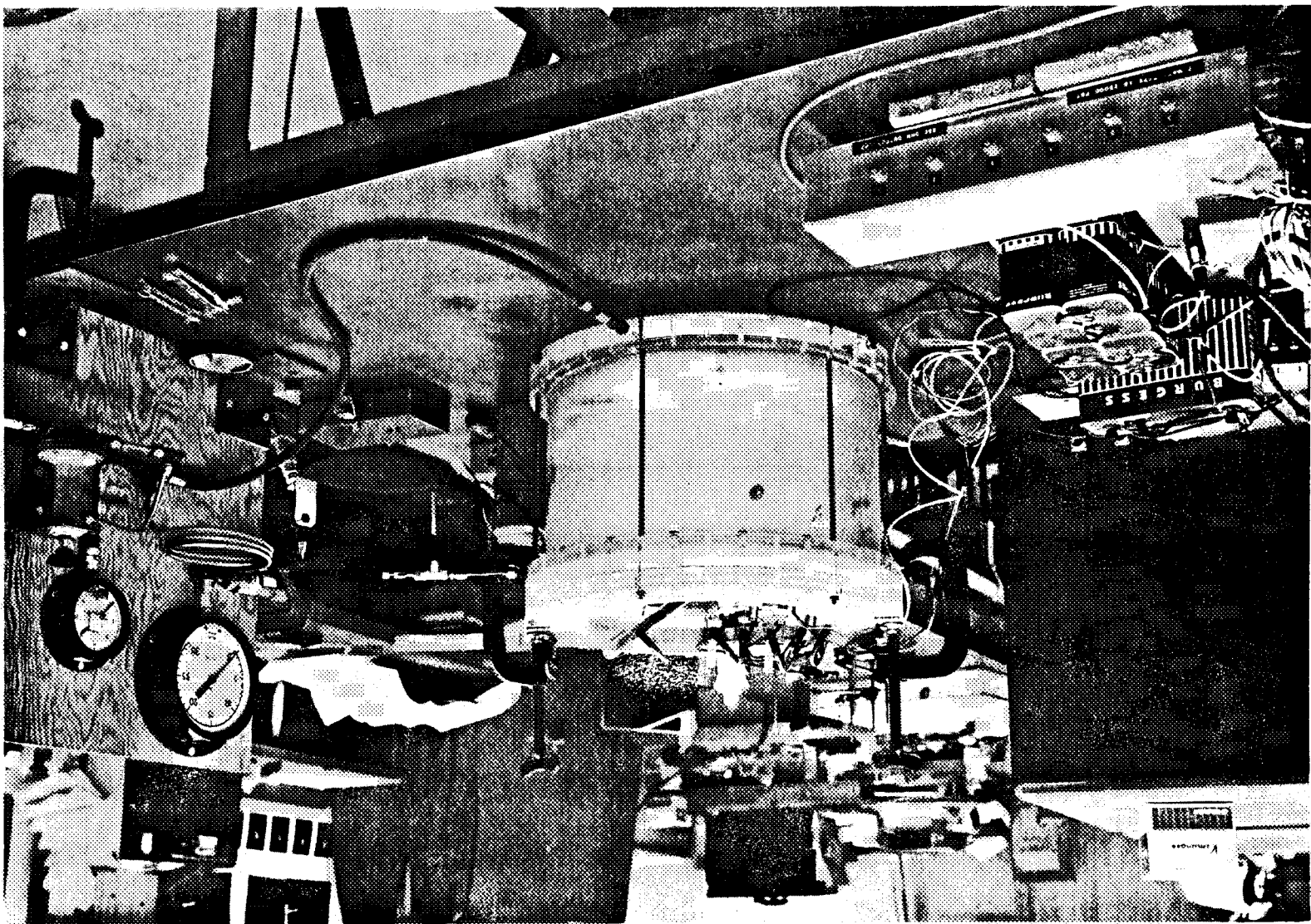
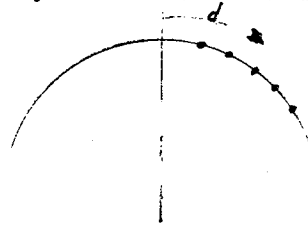
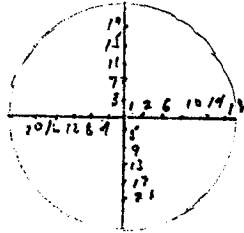


Table 5.2

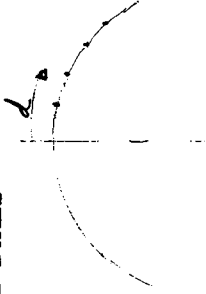
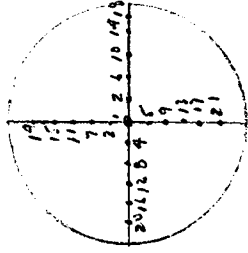
THICKNESS MEASUREMENTS FOR MONOCOQUE SPHERICAL DOMES



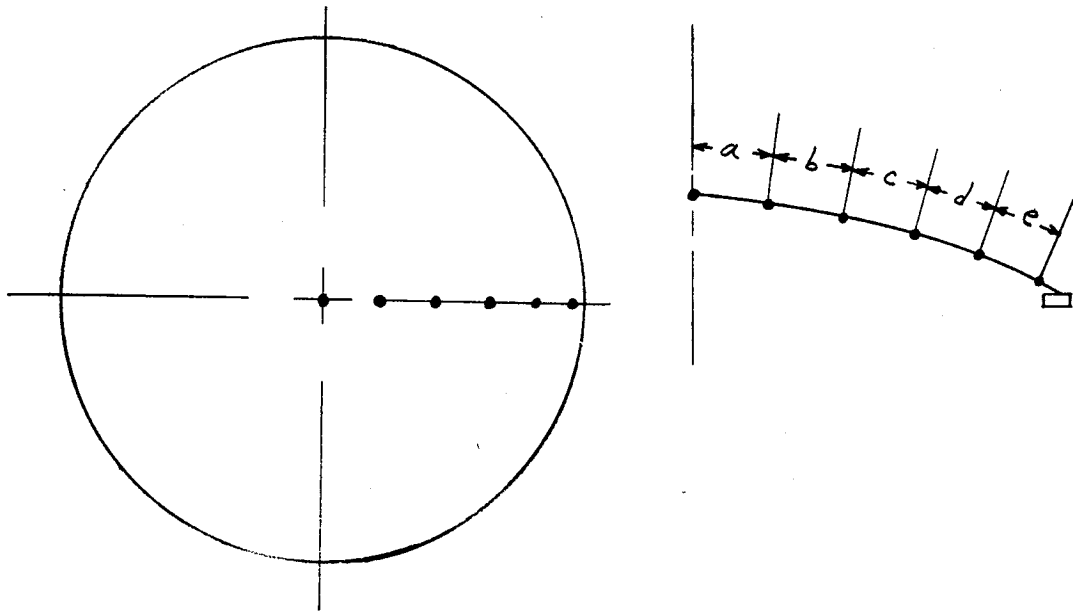
POINT NO.	d-Inches	THICKNESS - INCHES			
		#1-S a/b = 2.0	#2-S a/b = 3.33	#3-S a/b = 1.0	#4-S a/b = 4.78
1	0	.0405	.0500	.0288	.0560
2	2.0	.0405	.0490	.0285	.0559
3	2.0	.0405	.0590	.0285	.0559
4	2.0	.0405	.0484	.0285	.0560
5	2.0	.0405	.0480	.0282	.0560
6	4.0	.0404	.0482	.0280	.0560
7	4.0	.0404	.0492	.0280	.0561
8	4.0	.0405	.0490	.0280	.0563
9	4.0	.0405	.0500	.0280	.0561
10	6.0	.0405	.0500	.0283	.0560
11	6.0	.0405	.0490	.0282	.0561
12	6.0	.0405	.0490	.0282	.0561
13	6.0	.0406	.0482	.0275	.0560
14	8.0	.0415	.0484	.0275	.0563
15	8.0	.0415	.0484	.0275	.0565
16	8.0	.0415	.0490	.0272	.0566
17	8.0	.0418	.0500	.0273	.0565
18	9.25	10.5	.0415	.0270	
19	9.25	10.5	.0414	.0269	
20	9.25	10.5	.0415	.0270	
21	9.25	10.5	.0418	.0270	
22	12.6			.0268	
23	12.6			.0269	
24	12.6			.0269	
25	12.6			.0268	

Table 5.3

THICKNESS MEASUREMENTS FOR ELLIPSOIDAL AND TORISPHERICAL MONOCOQUE DOMES



POINT NO.	d-Inches	THICKNESS - INCHES		
		#5 - E a/b = 2.0	#6 - E a/b = 3.33	#7 - T a/b = 2.0
1	0	.0355	.0463	.0403
2	2.0	.0359	.0462	.0403
3	2.0	.0358	.0463	.0406
4	2.0	.0359	.0463	.0403
5	2.0	.0359	.0463	.0406
6	4.0	.0362	.0461	.0406
7	4.0	.0361	.0460	.0408
8	4.0	.0361	.0460	.0406
9	4.0	.0360	.0461	.0408
10	6.0	.0362	.0461	.0401
11	6.0	.0362	.0460	.0400
12	6.0	.0362	.0460	.0400
13	6.0	.0361	.0461	.0401
14	7.0	.0362	.0460	.0402
15	8.0	.0364	.0460	.0400
16	8.0	.0364	.0460	.0401
17	8.0	.0360	.0462	.0400
18	8.0	.0366	.0462	.0395
19	8.0	.0366	.0462	.0391
20	8.0	.0365	.0462	.0391
21	8.0	.0363	.0463	.0392
22	8.5	.0378	.0455	
23	8.5	.0378	.0454	
24	8.5	.0375	.0460	
25	8.5	.0380	.0460	
26	9.0	.0371		
27	9.0	.0381		
28	9.0	.0383		
29	9.0	.0378		
30	9.5	.0382		
31	9.5	.0381		
32	9.5	.0384		
33	9.5	.0381		



L_{OC}	1-S	2-S	3-S	4-S	4-E	5-E	6-T
a	1.5	1.50	2.0	2.0	2.0	2.0	2.0
b	1.5	1.50	2.0	1.0	2.0	2.0	2.0
c	1.5	1.50	2.0	1.0	2.0	2.0	2.0
d	1.5	1.50	2.0	1.0	2.0	1.0	2.0
e	1.5	1.50	2.0	1.0	1.0	1.0	1.0

FIGURE 5.10

LOCATION OF DISPLACEMENT TRANSDUCERS FOR MONOCOQUE DOMES #1-S, #2-S, #3-S, #4-S, #5-E, #6-E, #7-T.

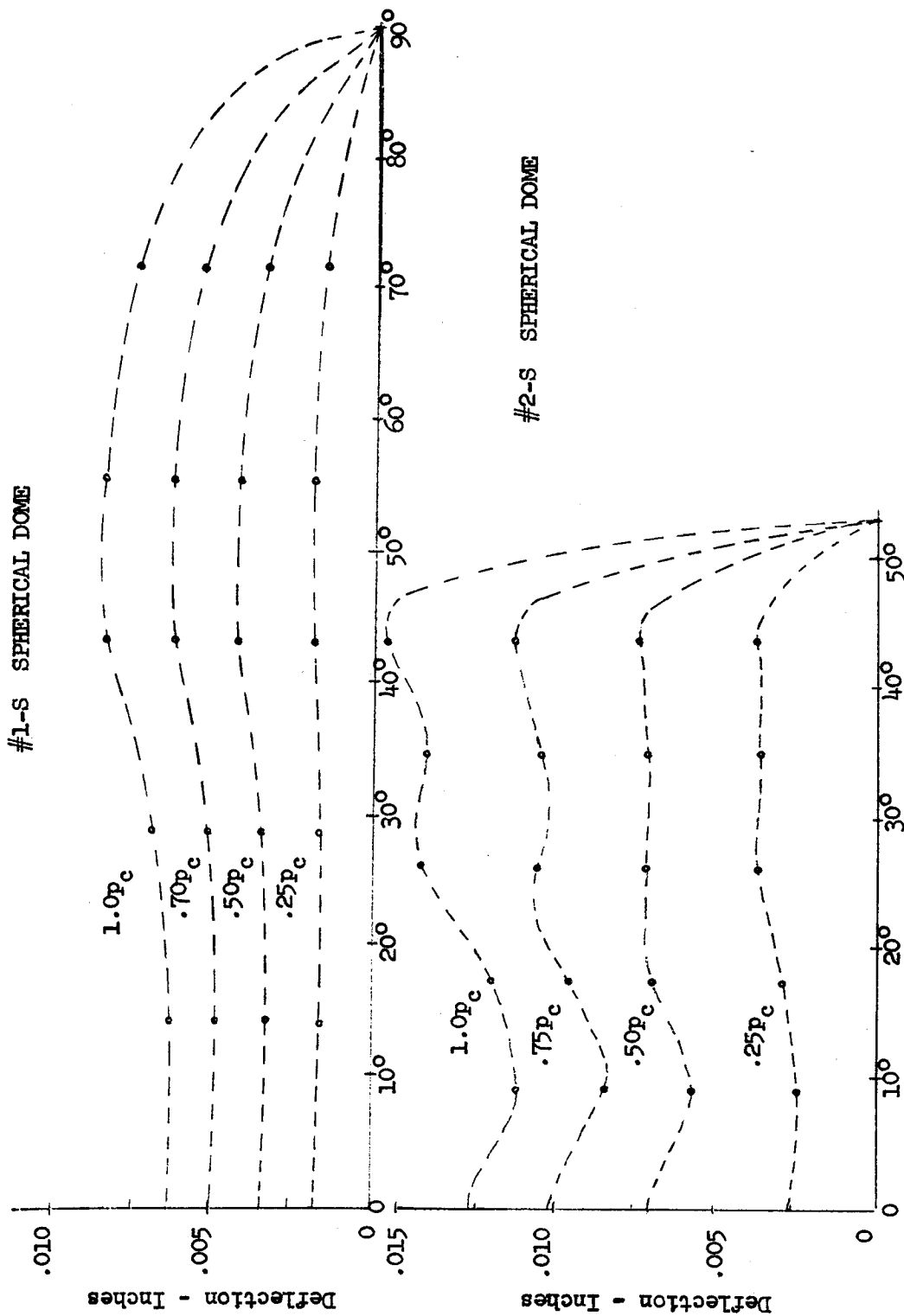


Figure 5.11 - Radial Deflections of Spherical Monocoque Domes Under External Pressure - #1-S and #2-S

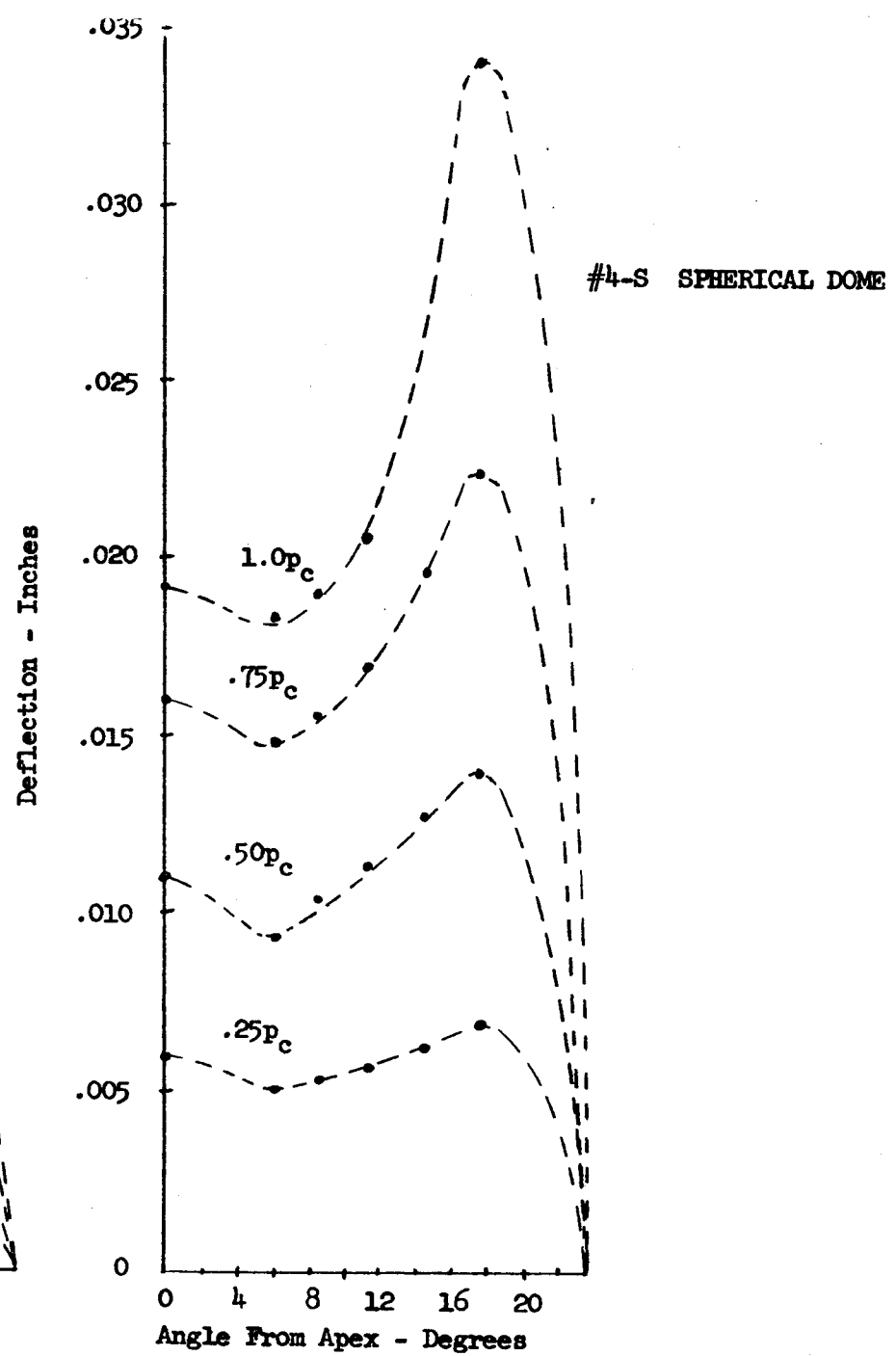
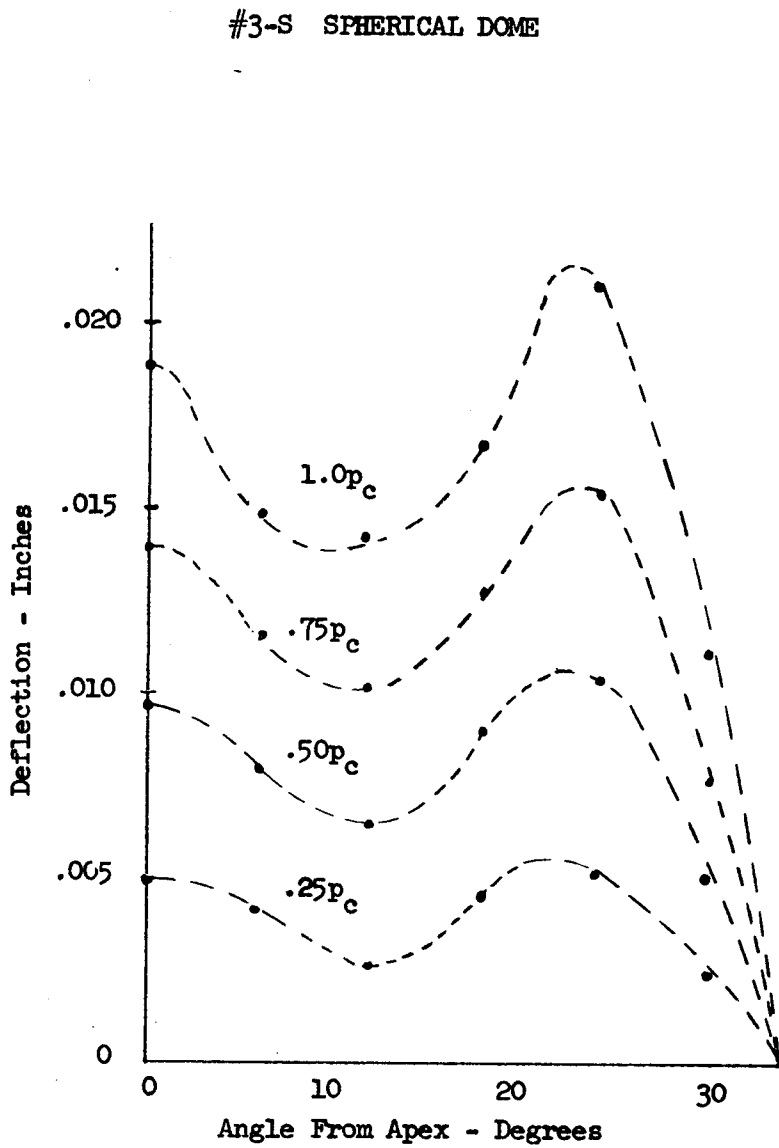
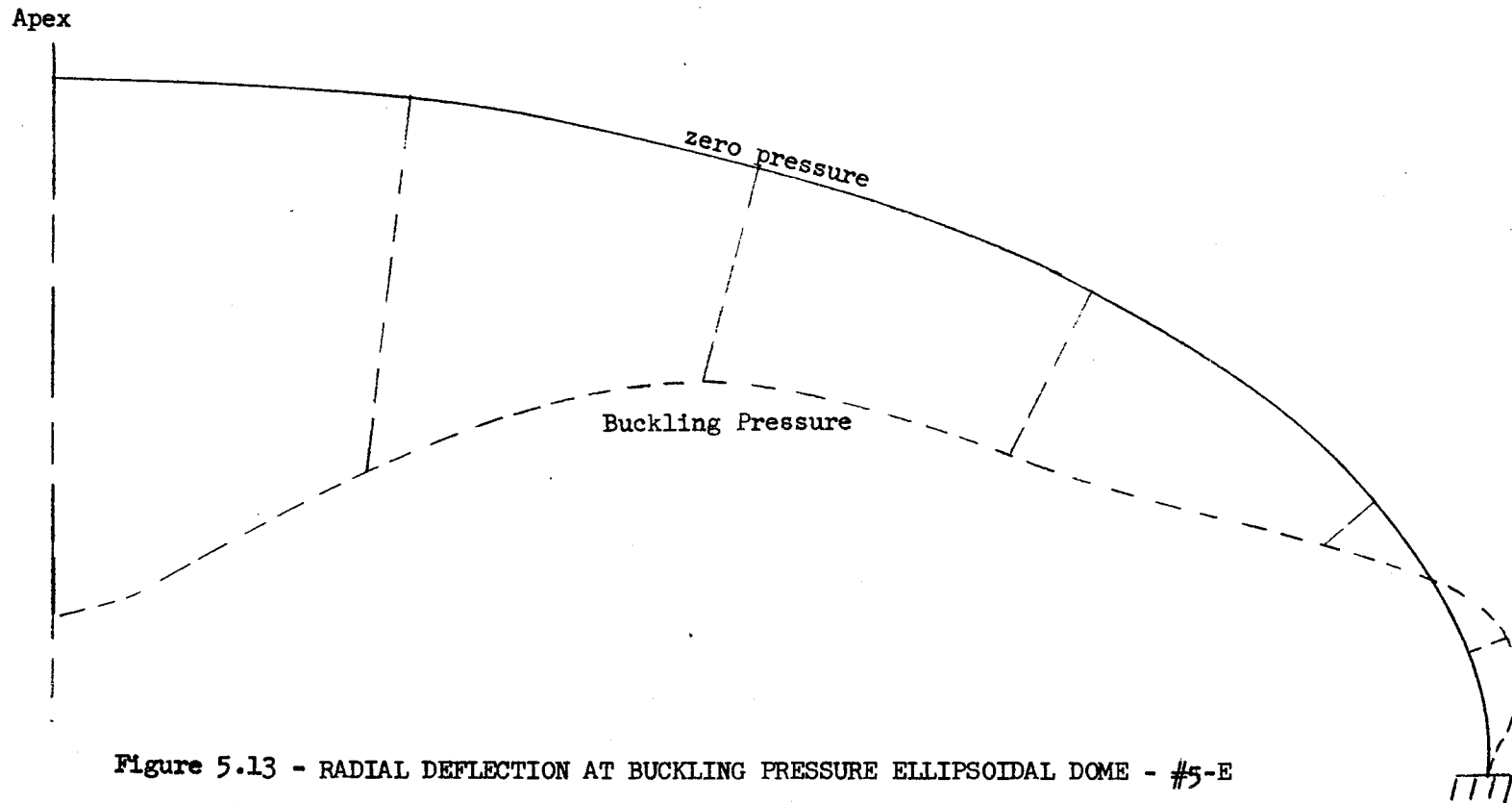


Figure 5.12 - Radial Deflections of Spherical Monocoque Domes Under Pressure #3-S and #4-S

Scale - 1.0" = .010" Deflection



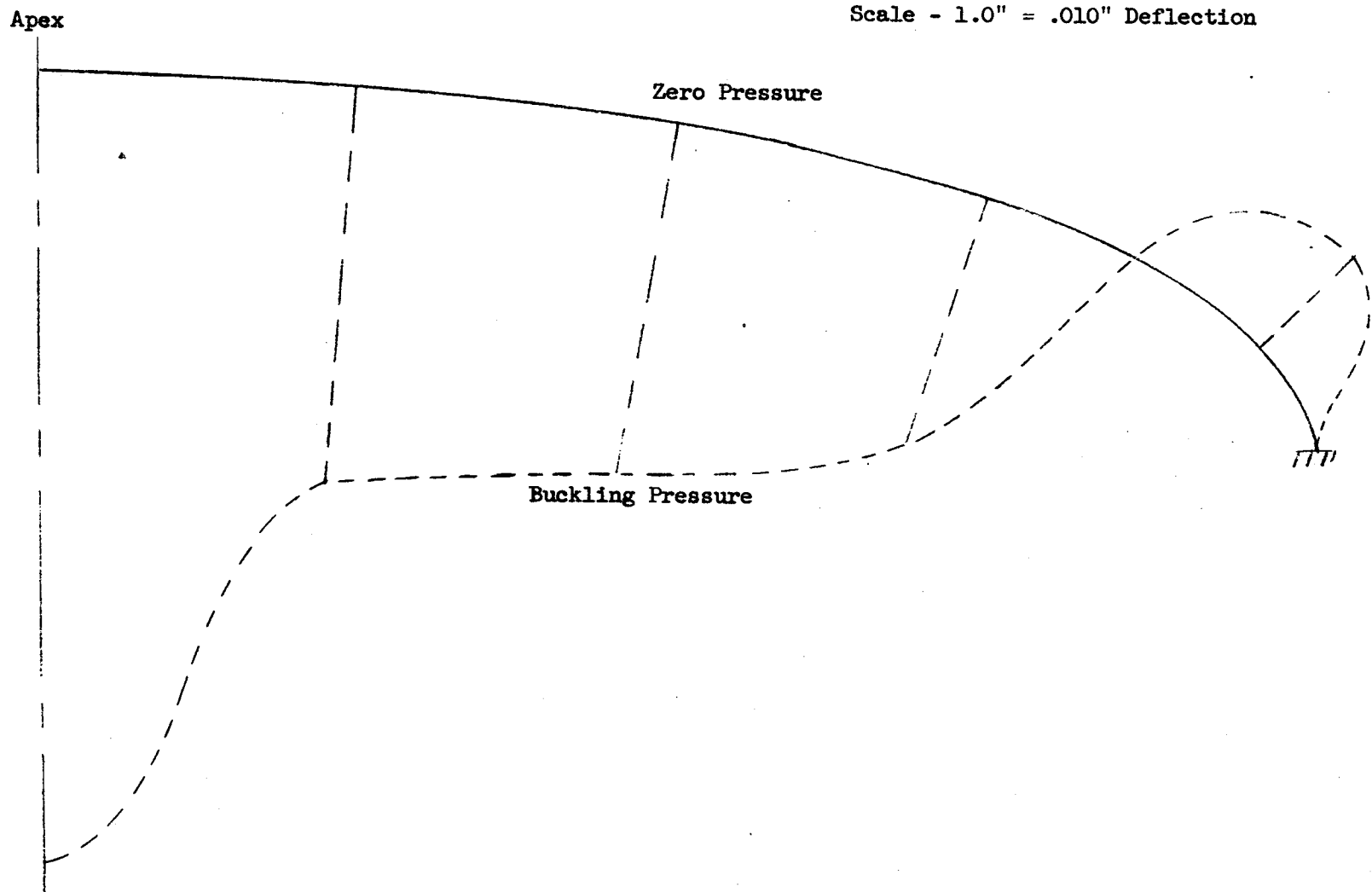


Figure 5.14 -RADIAL DEFLECTION AT BUCKLING PRESSURE ELLIPSOIDAL DOME - #6 E

Apex

Scale - 1.0" = .010" Deflection

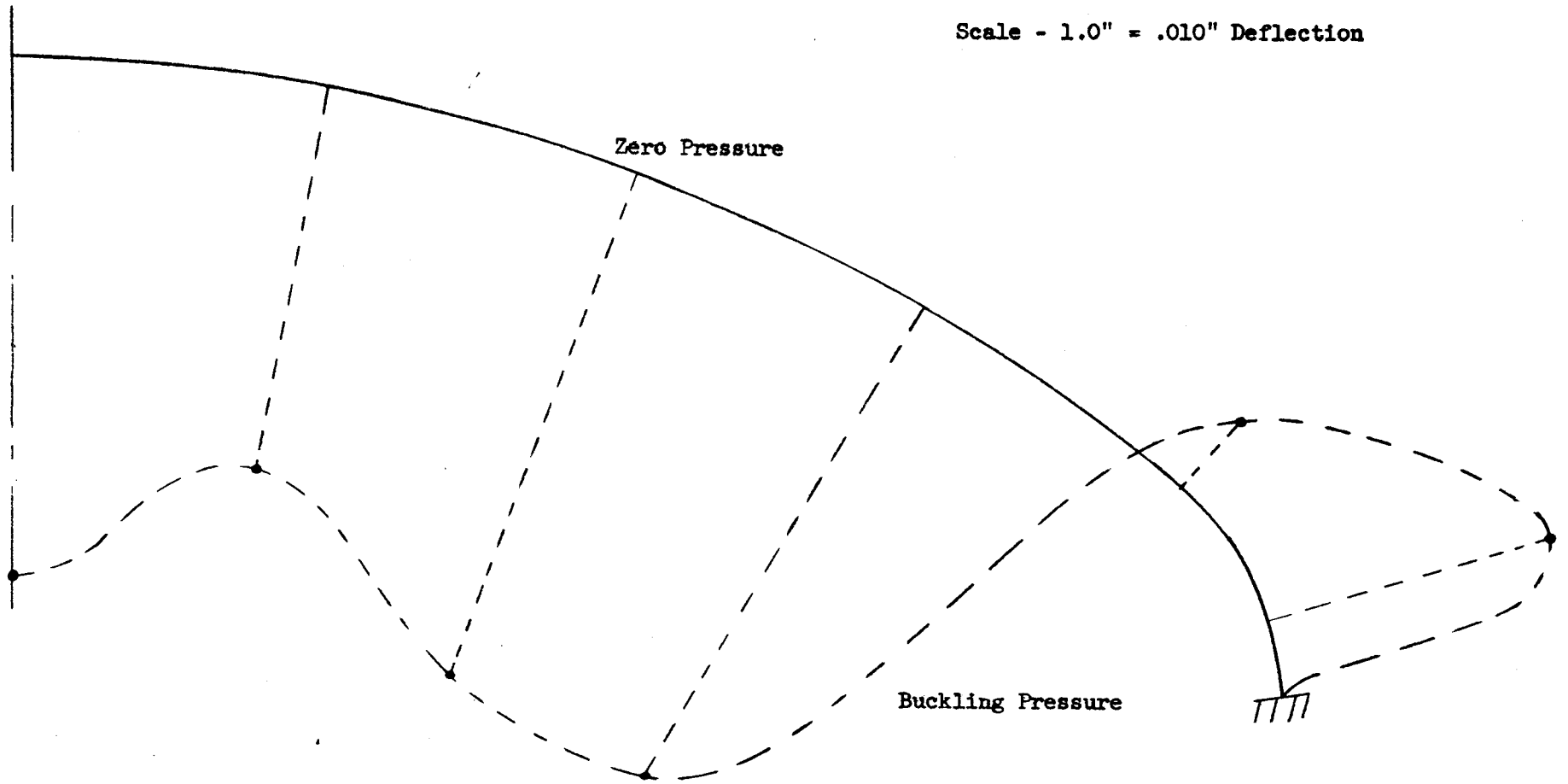


Figure 5.15 - RADIAL DEFLECTION AT BUCKLING PRESSURE TORISPHERICAL DOME - #7-T

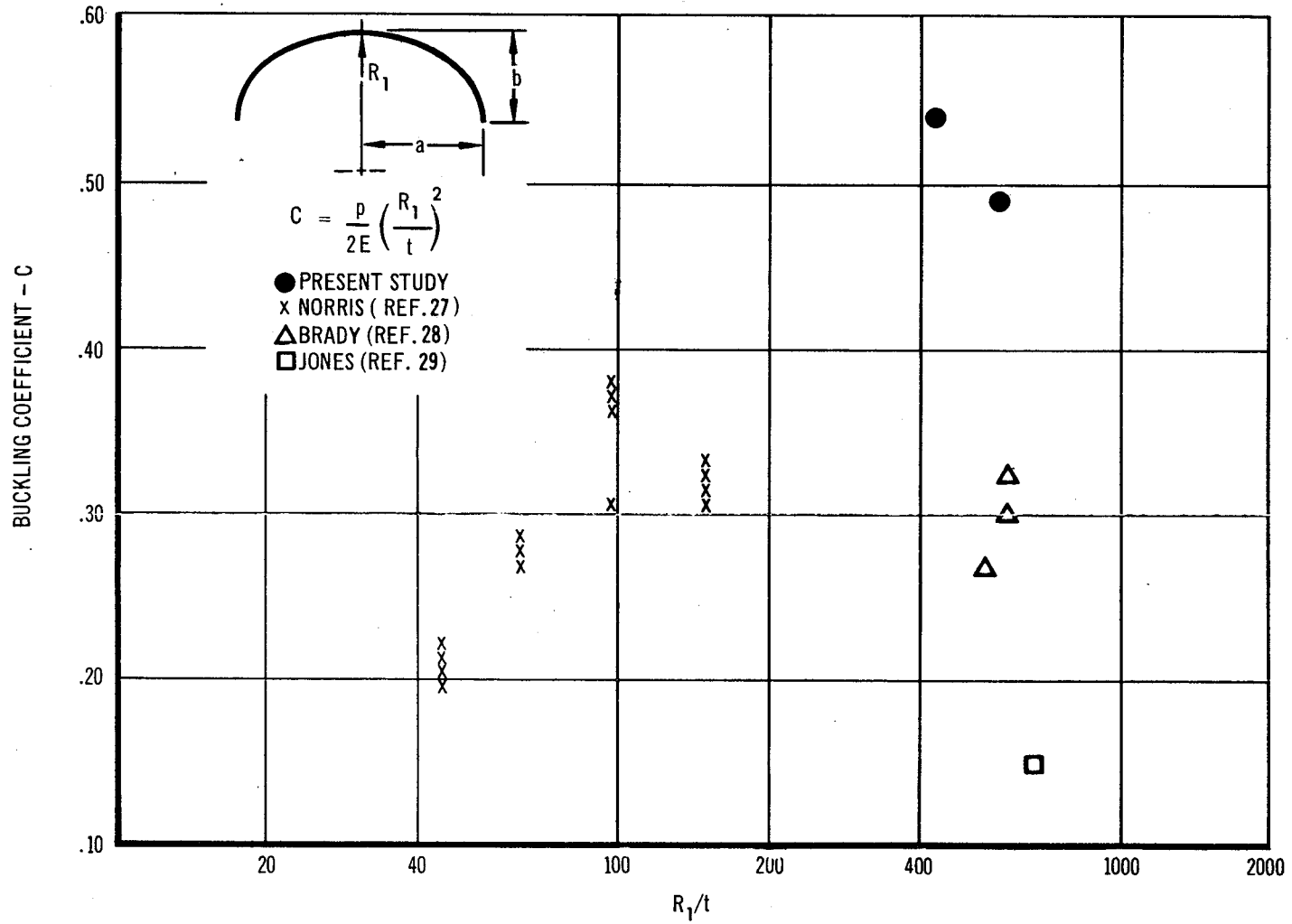


FIGURE 5.16 BUCKLING OF ELLIPSOIDAL DOMES-EXPERIMENTAL

Stiffened Spherical Domes - Room Temperature

A total of ten stiffened spherical dome configuration were fabricated and tested to arrive at an optimum stiffened dome arrangement. Stiffening configurations tested were:

- Meridional Stiffened
- Circumferential Stiffened
- Combined Meridional and Circumferential Stiffened
- Square-Grid Stiffened
- Geodesic Stiffened

Table 5.4 shows the measured thicknesses of the shell normal to the dome surface. Figures 5.17 - 5.20 show the location of the displacement transducers and Figures 5.21 - 5.24 are plots of the resulting deformation of the domes at the failing pressure. The summary of the experimental results are shown in Table 1.2 and Figure 1.5.

Meridional Stiffened Domes - Four meridionally stiffened domes (#1-M, #2-M, #3-M, #4-M) with 6, 26, 26, and 38 ribs respectively were fabricated therefore with modifications, it was used for the number 3 Meridional dome. The modification was the changing of the rectangular rib to a tee rib. The geometry and experimental results are shown in the table below.

		R	d	b	t _s	No of Ribs	p _s	\tilde{t}	$\frac{C}{C}$
	1 M	20	.25	.0191	.0349	6	1.41	.0371	.88
	2 M	20	.30	.0191	.0349	26	2.09	.0402	1.12
	3 M	20	.30	.0191	.0349	26	2.87	.0424	1.38
			d' .25	b' .0191					
4 M	20	.30	.0239	.0272	38	1.69	.0343	1.24	

Meridional Dome - #1-M - The intent of this arrangement was to verify a theory predicting that the radius of the largest inscribed circular plate within the bounds of the radial stiffeners define the allowable pressure for panel instability. To preclude that primary failure occurs by panel instability, rather than by rib instability, only six meridional ribs were used in this configuration. The axisymmetric buckle pattern at failure, clearly demonstrates that the buckling mode is by panel instability.

Meridional Dome - #2-M - The objective of testing #2-M was two fold:

1. To determine the allowable buckling stability of the rib.

2. To show an improvement of the buckling pressure of a meridionally stiffened dome compared to a monocoque dome having the same weight.

accomplish the first objective it was necessary to select an off-optimum condition where rib failure occurred prior to panel instability. To achieve the second objective, the non-dimensional parameter λ was selected such that $\lambda > 3$. From the theory in Chapter III the stiffening pattern is determined as follows:

$$\begin{aligned} \text{Let } R &= 20 \text{ inches} \\ \theta &= 23^{\circ}35' \\ a/b &= 4.78 \\ \nu &= 0.37 \\ E &= 465 \times 10^3 \\ t &= .035 \text{ inches} \end{aligned}$$

$$\text{assume } \lambda = 1.5$$

from equation 3.5 where λ is shown to be

$$\lambda = \left[12 (1-\nu^2) \right]^{1/4} \frac{r}{\sqrt{Rt}}$$

substituting into the above equation for λ , ν , R , t , and solving for the inscribed panel radius r gives

$$r = 0.70$$

$$\text{or } \psi = \frac{r}{R} = \frac{.70}{20} = .035$$

from Figure 3.1 the number of the ribs required to provide this ratio is selected as 26.

The predicted panel allowable from equation 3.10 is given as

$$p_p = \frac{2.44 Et^3}{(1-\nu^2) R r^2}$$

Substituting the proper values into the above equation results in

$$p_p = 5.75 \text{ psi}$$

Equating $p_p = p_r$ where from equation 3.15

$$p_r = \frac{B I_R E (k^2 - 1)}{r R^3}$$

where

$B = 5.0$ and $k^2 = 131$ for $\theta = 23^\circ 35'$
Solving for I_r results in

$$I_r = 106 \times 10^{-6}$$

To assure that rib failure occurs prior to panel instability the moment of inertia of the rib will be made considerably less than that required for simultaneous failure.

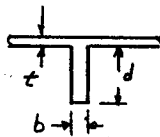
Arbitrarily the moment of inertia for the rib is selected as $0.4 I_r$

that is

$$I_r = .4 \times 106 \times 10^{-6} = 43.0 \times 10^{-6}$$

To satisfy this requirement for I_r

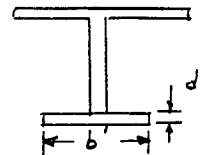
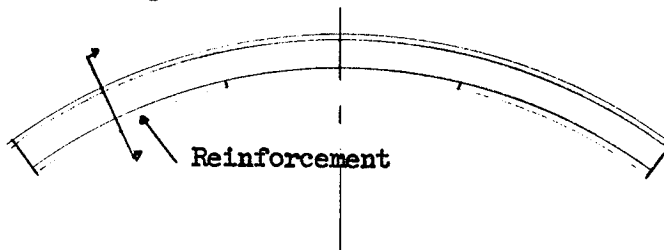
Let $d = .30$; $b = .0191$



therefore from the previous equation $p_r = 2.3$ psi (predicted failure of rib)

Meridional Dome #3-M - The objective of testing #3-M was to increase the buckling stability of the ribs such that panel and rib failure occur simultaneously.

Specimen - Meridional Dome #2 was used as the test specimen to meet this objective. The ribs were reinforced by the addition of a cap extending from the base to approximately $5/8$ of the original rib length. This is shown in the sketch below.

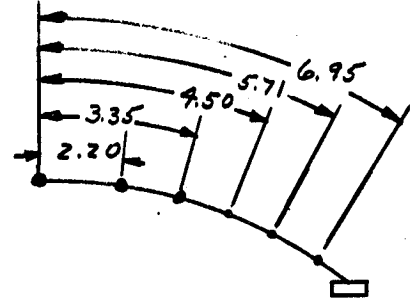
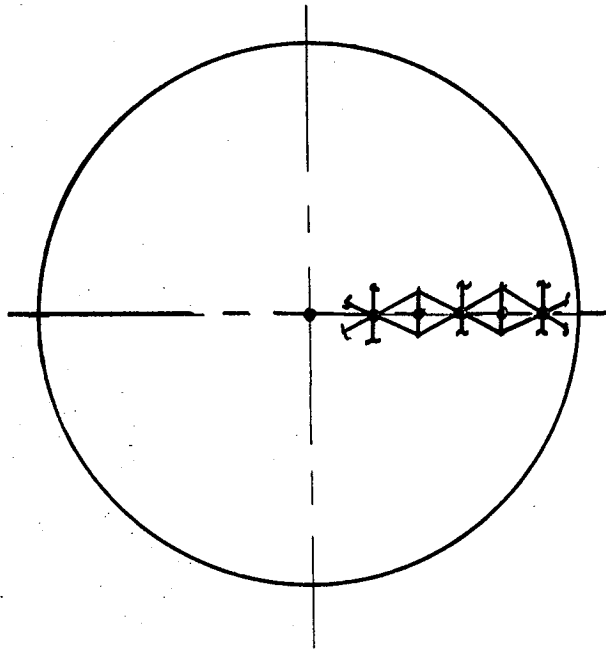


where $d' = .0191$

$b' = .250$

and I_r is computed to be 110×10^{-6}

#1-G, #2-G GEODISIC DOMES



#3-G GEODISIC DOME

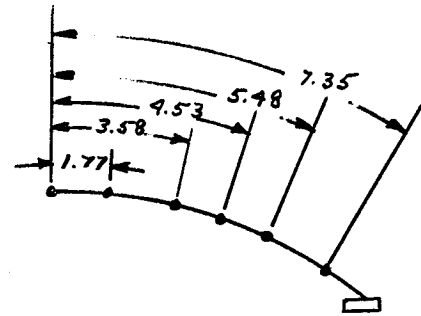
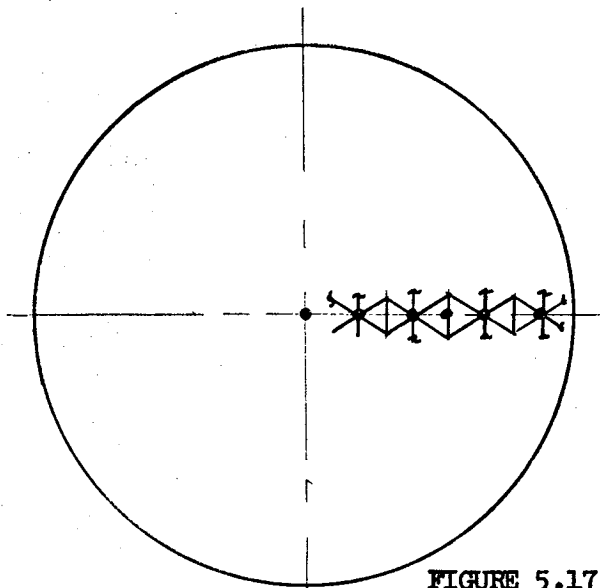
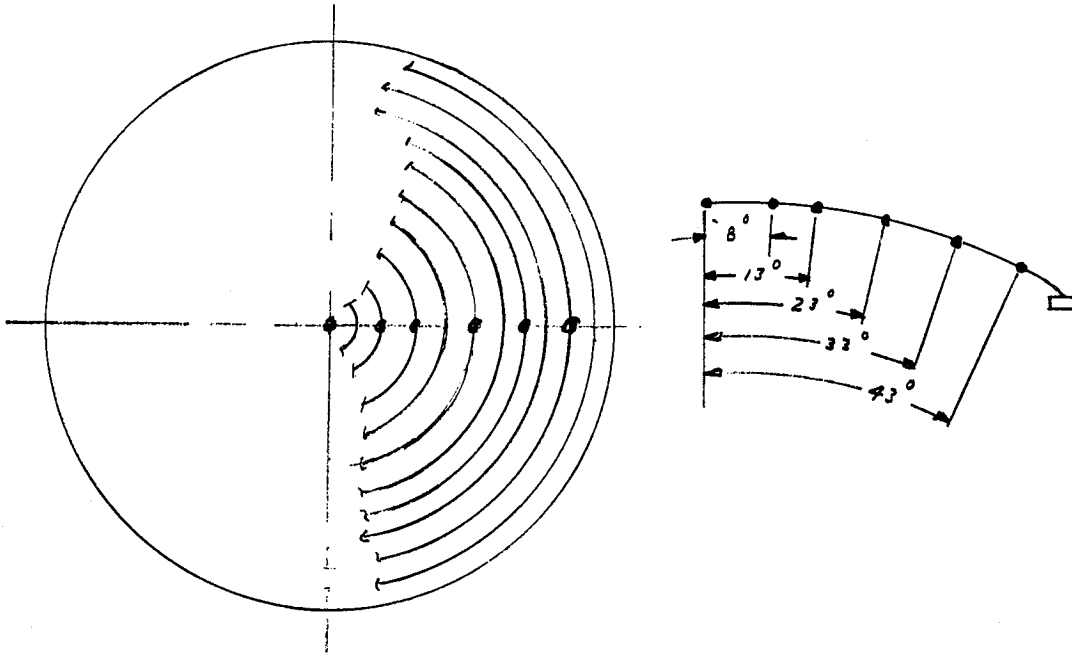


FIGURE 5.17

LOCATION OF DISPLACEMENT TRANSDUCERS ON #1-G, #2-G AND #3-G
GEODESIC DOMES

#1-C CIRCUMFERENTIAL DOME



#1-MC MERIDIONAL-CIRCUMFERENTIAL DOME

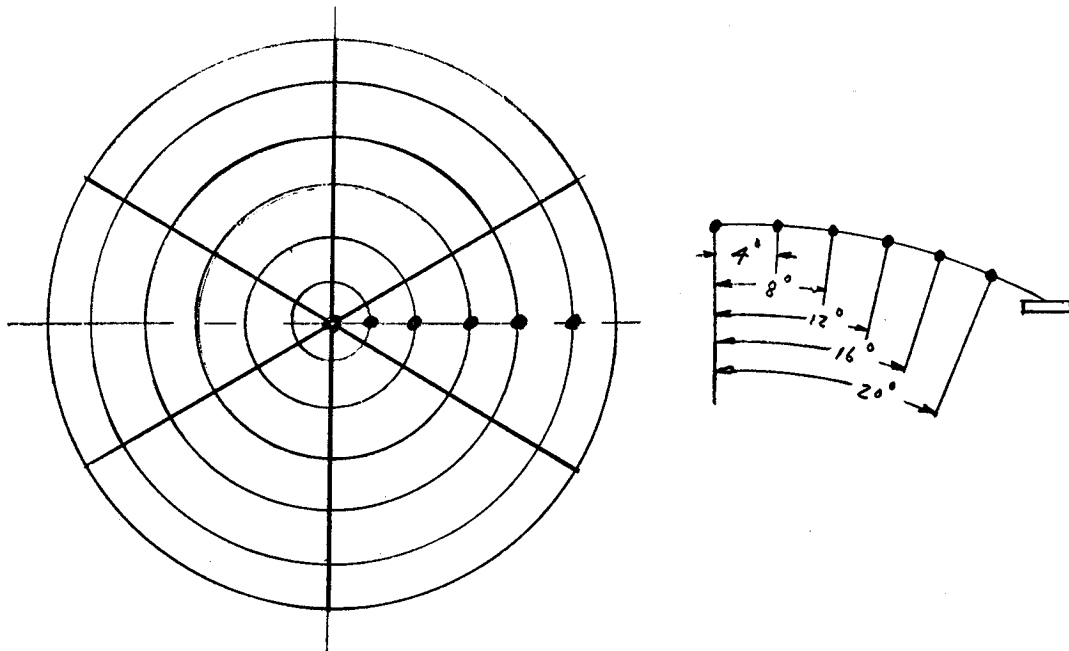
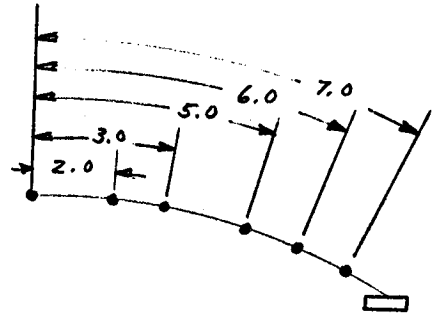
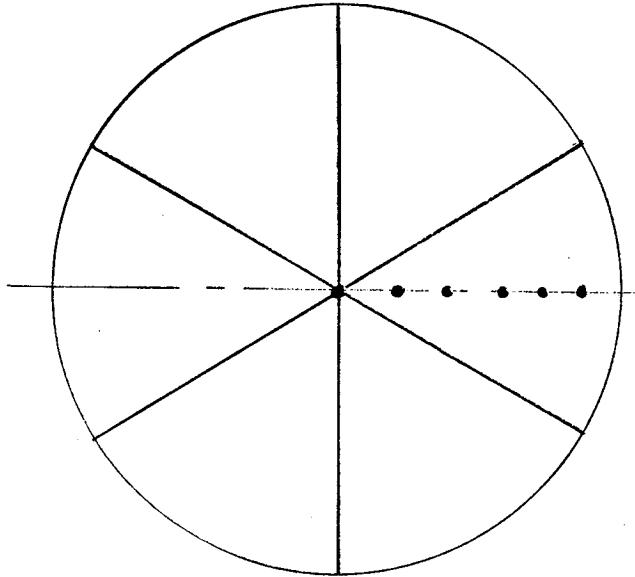


FIGURE 5.18

LOCATION OF DISPLACEMENT TRANSDUCERS ON #1-C and #1-MC CIRCUMFERENTIAL AND MERIDIONAL-CIRCUMFERENTIAL DOMES

#1-M MERIDIONAL DOME



#2-M, #3-M MERIDIONAL DOMES

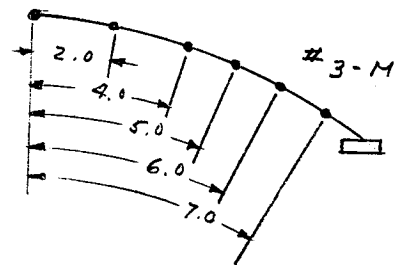
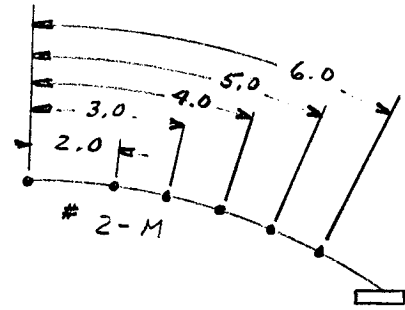
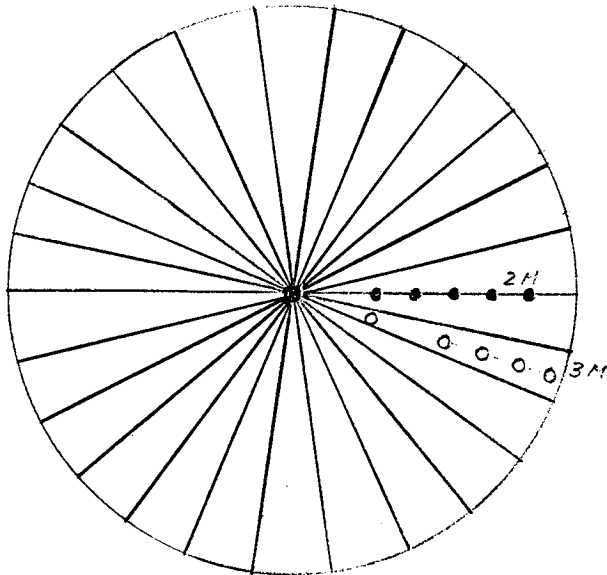
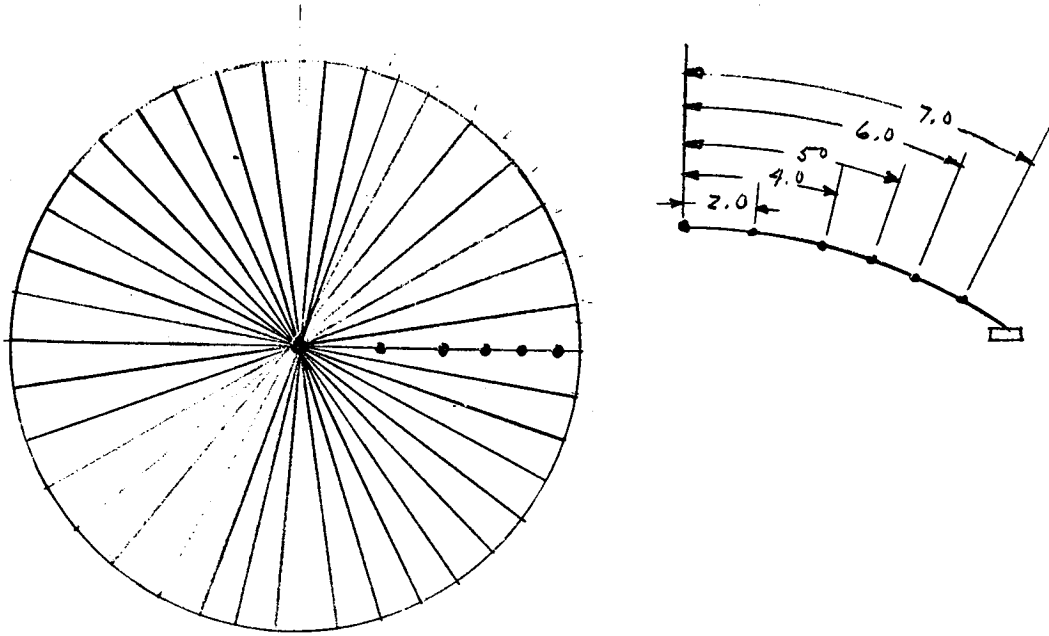


FIGURE 5.19

LOCATION OF DISPLACEMENT TRANSDUCERS ON #1-M, #2-M AND #3-M MERIDIONAL DOMES

#4-M MERIDIONAL DOME



#1-SG SQUARE STIFFENED DOME

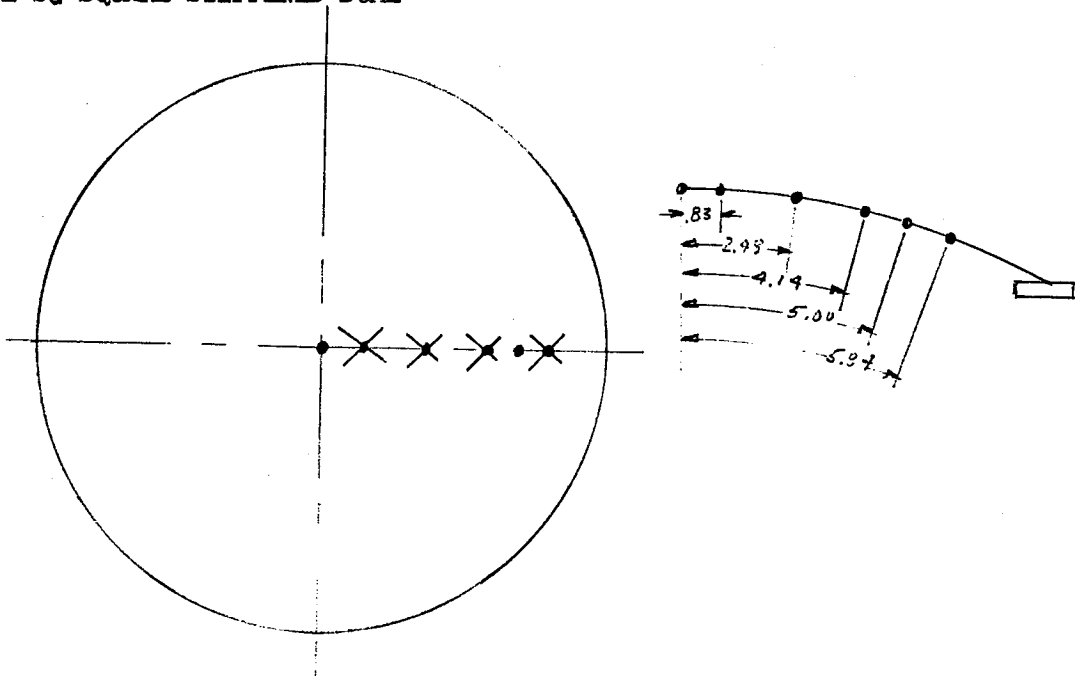


FIGURE 5.20

LOCATION OF DISPLACEMENT TRANSDUCERS ON #4-M AND #1-SG - MERIDIONAL AND SQUARE STIFFENED DOMES

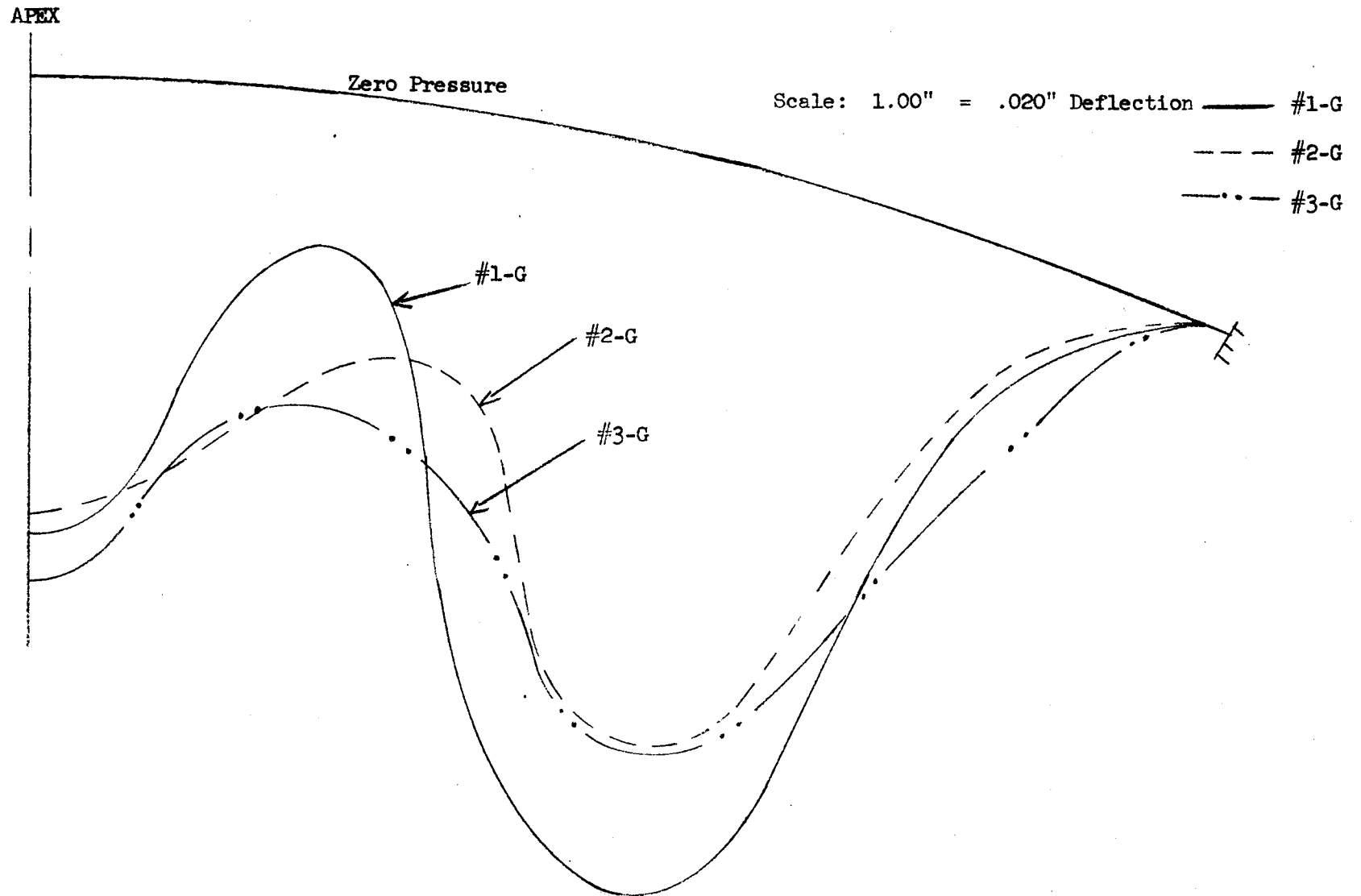


Figure 5.21 Radial Deflection at Buckling Pressure for Geodesic Stiffened Domes

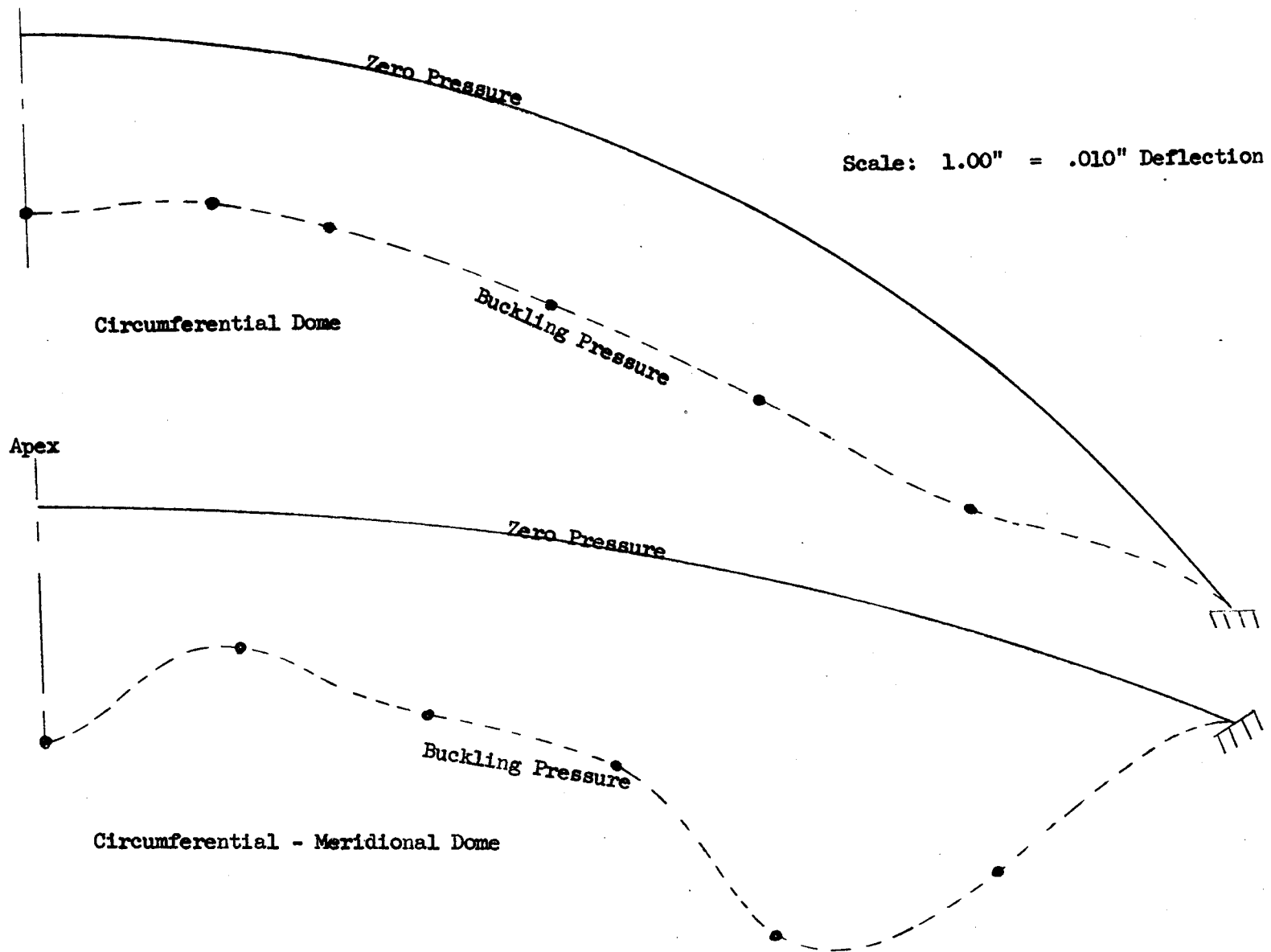


Figure 5.22 - Radial Deflection at Buckling Pressure For Circumferential and Circumferential - Meridional Stiffened Domes

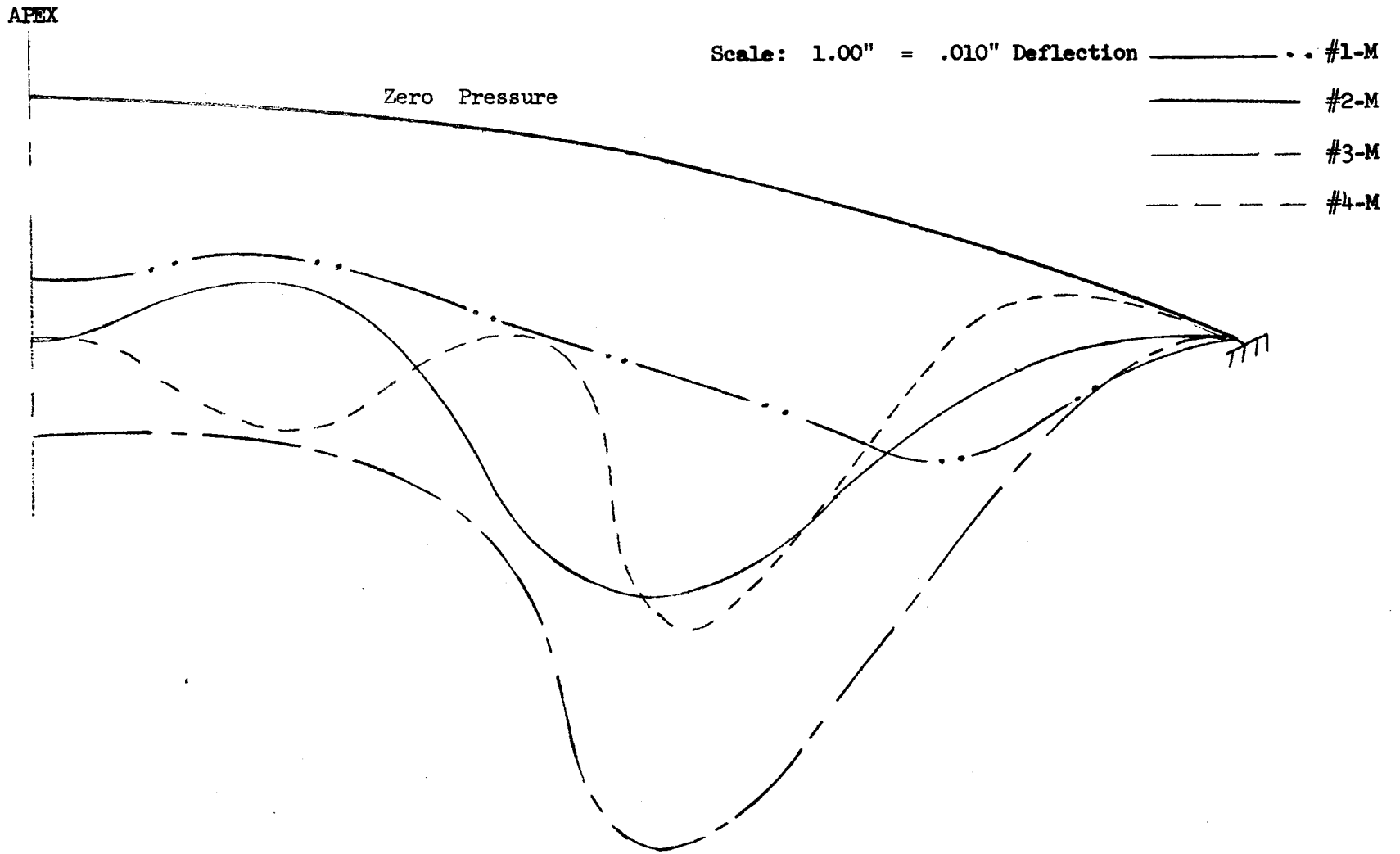


Figure 5.23 - Radial Deflection at Buckling Deflection at Buckling Pressure for Meridionally Stiffened Domes

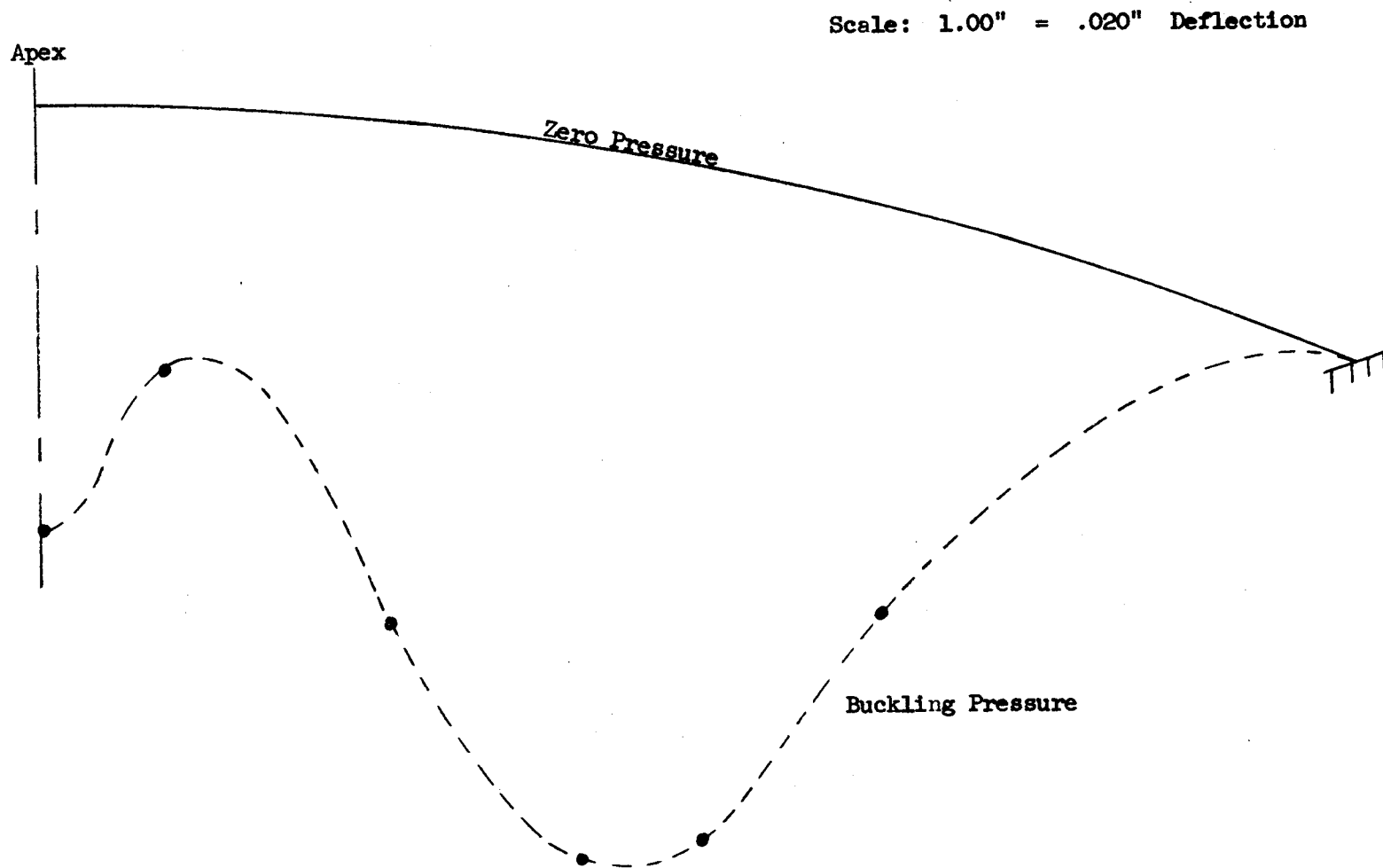


Figure 5.24 - Radial Deflection at Buckling Pressure
For Square-Grid Stiffened Dome

The above moment of inertia satisfies the requirement of sufficient rib stiffness such that panel and rib failure occur simultaneously as calculated for meridional dome #1.

The predicted failing pressure is therefore

$$p = 5.75 \text{ psi}$$

Meridional Dome #4 - The objective of testing #4-M was to optimize the dome configuration for a given ratio of $\left(\frac{t}{\bar{r}}\right)^2 = .10$

From Figure 3.3 for a value of $\left(\frac{t}{\bar{r}}\right)^2 = .10$ the optimum number of ribs required is given as 38 ribs, for an efficiency parameter of $\eta = 11.05$.

From Figure 3.1 for $N = 38$, $\psi = .024$

the inscribed radius is therefore computed as

$$r = R\psi = 20 \times .024 = .48 \text{ inches}$$

From equation 3.46 where the allowable panel stability is given as

$$p = \frac{2.44 E t^3}{(1-\nu^2) R r^2}$$

Letting $t = .0273$ and substituting appropriate values of E , R and r into the above equation results in

$$p = 5.88 \text{ psi}$$

From equation the necessary rib moment of inertia is expressed as

$$I_R = \frac{p R r R^3}{B E(k^2-1)} \quad \text{where } B = 5.0$$

Letting $p_p = p_R$ and solving for I_R gives

$$I_R = 75 \times 10^{-6}$$

Because of fabrication limitations it was not possible to meet this condition of I_R and still satisfy the condition of $\left(\frac{t}{\bar{r}}\right)^2 = .10$.

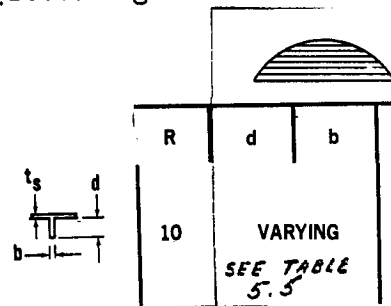
The I_R obtained for this configuration is

$$I_R = 54 \times 10^{-6}$$

For this value of I_R

$$p_R = 4.25 \text{ psi}$$

Circumferential Stiffened Domes - A circumferentially stiffened spherical cap with an $a/b = 2.0$ was tested to a buckling pressure of 4.09 psi. This is approximately 92% of the failing pressure that would be expected for a monocoque dome having the same equivalent weight. While the result was considerably higher than the previous experimental values, it clearly demonstrates that a circumferential stiffening arrangement is not expected to be a structurally efficient bulkhead design. The buckle pattern at failure, shows the buckles are aligned in the circumferential direction thus indicating that the primary failure was attributed to panel instability between the circumferential stiffeners. Although extensive rib failures occurred when the specimen collapsed against the restraining block, a secondary test of the failed shell resulted in a monocoque buckling coefficient that was within 3% of the previously reported unstiffened shell results. The geometry and test result is shown in the proceeding table.



R	d	b	t _s	No of Ribs	P _{sFail}	$\bar{\eta}$	$\frac{P}{\bar{c}}$
10	VARYING SEE TABLE 5.5		.0260	10	4.09	.0390	.92

Specimen Design - The following analysis is based upon the work developed in Chapter III. Assume that the results shown in Figure 3.8 for $\theta = 60^\circ$ is sufficiently close to $\theta = 53^\circ 10'$ so that the data is applicable.

Letting

$$\begin{aligned} \theta &= 53^\circ 10' \\ R &= 10.0 \text{ inches} \\ a &= 8.0 \text{ inches} \\ E &= 465 \times 10^3 \text{ psi} \\ \rho &= .05 \text{ lb/in}^3 \end{aligned}$$

From Figure 3.5 assuming $N = 400$ results in $\eta = 13$ with $\alpha_c = 55^\circ$. Substituting the values into equation 3.50 results in

$$\frac{P}{E} = 2.17 \times 10^{-8} \left(\frac{W_{\eta}}{\rho} \right)^{5/2}$$

A comparison of the efficiency of the stiffened dome to that of a monocoque dome was based upon equivalent weight. From the previous experimental monocoque dome result, it was reported that $\frac{W}{\bar{c}} = 10.2$ for a failing pressure of $p_m = 4.45$ psi.

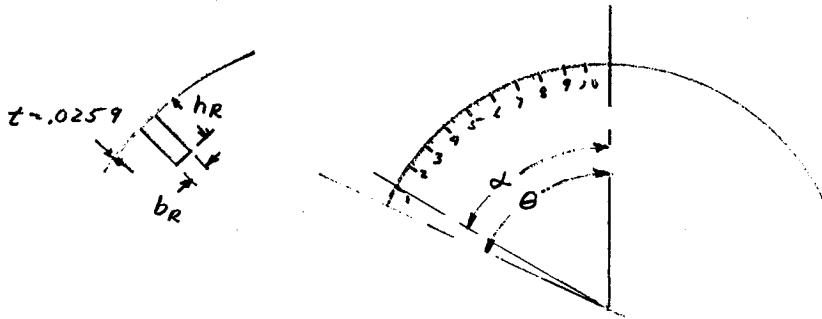


TABLE 5.5

Rib NO.	Rib Cross Sectional Area	$h_R = 12 b_R$		α°
		h_R	b_R	
1	.00821	.316	.026	48
2	.00692	.288	.024	43
3	.00565	.257	.022	38
4	.00441	.232	.019	33
5	.00328	.219	.015	28
6	.00228	.163	.014	23
7*	.00142	.142	.010	18
8*	.00100	.100	.010	13
9*	.00100	.100	.010	8
10*	.00100	.100	.010	3

*Note - Limitation of theory and consideration of minimum gage of plastic material available dictates design in this region.

Substituting $\frac{W}{\rho} = 10.2$ into the above equation results in $p = 3.39$ psi

or

$$\frac{p}{p_M} = \frac{3.39}{4.45}$$

Assuming that the developed optimum stiffening arrangement is realistic and that the value of $N = 400$ is indicative of the rib area required to prevent premature rib failure, the predicted efficiency of circumferentially stiffened domes was expected to be less than that of a monocoque shell. Since a negative result is sometimes as good as a positive result, an experimental test was conducted to substantiate the validity of the theory. The dome thickness was calculated from the following relationships.

$$\frac{p}{E} = J\lambda_1 (2\pi R^2 t \rho)^{5/2}$$

where $\lambda_1 = 4.12$

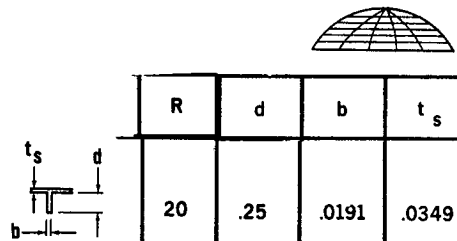
Substituting the values into the above equation and solving for t gives

$$t = .0259 \text{ inches}$$

The rib areas required for the design were calculated using the relationships developed in Chapter III. The resulting geometry is depicted in Table 5.5.

Combined Meridional and Circumferential Stiffened Dome #1-MC

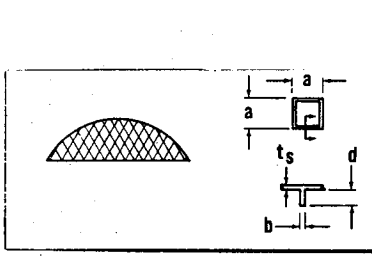
Meridional Dome #1-M with the addition of five equally spaced circumferential stiffeners of the same rib cross sectional area was tested to a failing pressure of 1.53 psi. A comparison with a monocoque dome of the same weight showed this pressure to be 82% of the expected monocoque buckling pressure. The primary mode of failure was in rib instability of the largest circumferential stiffener. Failure of this rib resulted in a secondary mode of panel instability. The geometry and failing pressure is shown in the preceding table.



R	d	b	t _s	No of Ribs		P _{sFail}	$\bar{\eta}$	$\frac{\bar{\eta}}{C}$
20	.25	.0191	.0349	6 M	5 C	1.53	.0401	.82

Square-Grid Stiffened Dome - The Square-Grid stiffening arrangement with an $a/b = 4.78$ was designed to a near optimum condition of efficiency. The geometric proportions and failing pressure is shown in

the proceeding table.



R	a	d	b	t _s	P _{sFail}	\tilde{t}	$\frac{t}{c}$
20	1.16	.302	.0287	.0576	9.48	.072	1.58

Specimen - The geometry selected for test was based upon the analysis by Crawford and Schwartz (reference 23). Due to the constraints imposed by fabrication and the available buckling pressure due to the vacuum method of test, the design of the specimen will be off-optimum. From the appropriate equations and figures in Reference 23 the selected parameters are:

$$N = 2.05$$

$$\frac{b}{t_s} = 0.50$$

$$\frac{d}{a} = 0.26$$

This results in the off-optimum equation

$$\frac{\tilde{t}}{R} = 2.05 \left(\frac{p}{E} \right)^{3/5}$$

The optimum equation (without restraints) is given as

$$\frac{\tilde{t}}{R} = 1.88 \left(\frac{p}{E} \right)^{3/5}$$

It may be seen that the off-optimum design is $\approx 9\%$ heavier than the optimum design.

Performing the necessary calculation using the dome geometry having a spherical radius of $R = 20$ inches and an a/b ratio = 4.78 at a limiting pressure of $p = 12$ psi results in:

$$a = 1.16$$

$$t_s = .0574$$

$$b = .0287$$

$$d = .302$$

$$\tilde{t} = .0723$$

As was previously shown, the predicted buckling pressure for a monocoque dome of the same geometry and weight may be expressed as

$$P_M = 2 E C \left(\frac{\tilde{t}}{R}\right)^2$$

where the buckling coefficient C as determined from experiment is C = 0.50. Substituting E = 465 x 10³ and $\tilde{t} = .0723$ into the above equation gives:

$$P_m = 6.1 \text{ Psi}$$

The predicted buckling pressure ratio for the square grid stiffened dome and the monocoque dome results in:

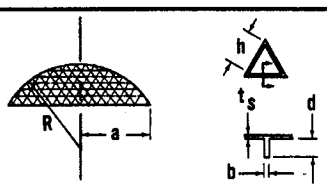
$$\frac{P}{P_m} = \underline{1.97}$$

Geodesic Stiffened Domes

Due to constructional limitations, the theoretical optimum shape having a half-opening angle $\theta = 60^\circ$ was not modeled for the stiffened configuration. Instead, a spherical cap with an a/b = 4.78 was used to test the validity of this stiffening theory. This larger spherical radius (R=20 in.) increased the grid pattern within tolerable fabrication techniques. The first two geodesic (#1-G, #2-G) domes are shown to have achieved pressures of 1.50 and 1.60 times the values which would be obtained for the same weight of material in monocoque construction. The general instability coefficient assumed in the design analysis of these domes was not achieved due to greater deviation of the stiffened specimens from membrane conditions in the prebuckled configuration. A redesign of the third specimen taking this into cognizance resulted in a pressure 2.27 times the monocoque pressure. The achieved pressure was within 1-1/2% of the redesign predicted value. When the No. 1 Geodesic dome was first tested, the resulting failing pressure was much less than predicted by theory. Cadco No. 202 bodied cement used at the rib intersections had softened the rib material enough to allow these rib intersections to act as vertical hinges instead of uniformly elastic ribs. Therefore, small 1/2 inch diameter by 0.015 inch thick PVC disks were cemented with "Eastman 910" cement at every rib intersection. This provided a more rigid joint to carry the rib compression through the intersections. The buckling pressure on retesting of this dome had increased to a more reasonable value.

On #2-G and #3-G domes 1/4 inch diameter by .020 inch thick disks were cemented with "Eastman 910" rather than "Cadco" No. 202. The chief reason for using disks on these domes was to provide an adhesive surface to hold a portion of the cement at the edge of the rib inter-

Section opposite the shell. The Eastman 910 cement has a low viscoelasticity and before setting up, would flow away from the area where the disk was placed. The geometry and test results shown in the proceeding table.

CONSTANT a = 8 IN.		R	h	d	b	t _s	P _{sFail}	$\bar{\epsilon}$	$\frac{\bar{\epsilon}}{c}$
		20	1.57	.230	.0191	.0474	5.86	.0580	1.50
		20	1.60	.226	.0239	.0479	6.54	.0592	1.60
		20	1.25	.205	.0153	.0296	3.96	.0387	2.27

Geodesic Dome #1-G - The specimen was sized using optimum design considerations. Since this was the first specimen tested, the classical buckling coefficient for monocoque domes was used for the general instability coefficient ($c_0 = 1.225$). The value of the buckling coefficient by test was calculated to be $c_0 = .696$.

Specimen Design - The plastic model specimen geometry and pressure was chosen as to give model sizes which are capable of being constructed and tested.

$$R = 20.0'' \quad E = 465000 \text{ psi}$$

$$\epsilon = 2.00 \quad P = 9.80 \text{ psi}$$

Thus

$$\frac{p}{E} \times 10^6 = \frac{9.8 \times 10^6}{0.465 \times 10^6} = 21.05$$

From Tables in Part II, one obtains the values:

$$\alpha = 0.0746, \quad \delta = 4.85, \quad \gamma = 3.11, \quad \eta = 0.672$$

One sees that this design indicates a "classical weight ratio" of 67.2% for the weight of the stiffened dome vs. a monocoque dome.

The ratio of rib weight to skin weight is 3, i.e.
 $3 \times .0746 \times 100\% = 22.4\%$

Since the classical c_0 is used for general instability, while the actual value will be somewhat smaller, the specimen should fail in general instability and give an indication of the reduction factor for c_0 .

Solving the general instability equation for $\frac{t}{R}$,

$$\frac{t}{R} = \sqrt{\frac{P_0}{1.225EY}} = \sqrt{\frac{9.80 \times 10^{-6}}{1.225 \times 0.465 \times 3.23}} = 2.37 \times 10^{-3}$$

$$t = 0.00237 \times 20 = \underline{0.0474''}$$

$$d = \delta t = 4.85 \times 0.0474 = \underline{0.230''}$$

$$h = \sqrt{\epsilon R t} = \sqrt{2 \times 20 \times 0.0474} = \underline{1.38''}$$

$$a = \frac{2}{\sqrt{3}} h = \underline{1.59''}$$

$$b = \alpha \frac{th}{d} = 0.0746 \times \frac{0.0474 \times 1.38}{0.230} = \underline{0.0212''}$$

Although these calculated dimensions do not exactly correspond to the measured dimensions little variation is expected in the predicted failing pressure.

Geodesic Dome #2-G - Attempts to machine sheets of polyvinyl chloride to arbitrary thickness were unsuccessful due to extreme deviations from flatness of the machined sheet. As a consequence, the chosen rib thickness for this specimen was obtained by measurement of rolled sheet 0.0239 in. as supplied by the manufacturer. In this case an off-optimum design for non-critical ribs is obtained by the analysis technique described in Chapter IV.

Specimen Design - From the Tables the following values are obtained:

α	δ	γ	η	β
.08	4.66	3.26	.686	59.4

From the formula:

$$\frac{\bar{p} \epsilon^3}{c_2} = \left(\frac{b\beta}{R}\right)^4 = \left(\frac{.0239 \times 59.4}{20.0}\right)^4 = 0.254 \times 10^{-4}$$

$$\bar{p} = \frac{c_2}{\epsilon^3} \times 0.254 \times 10^{-4}$$

For $c_2 = 7.4$ and $\epsilon = 2.0$

$$\bar{p} = \frac{7.4}{8} \times 0.254 \times 10^{-4} = 0.234 \times 10^{-4}$$

Since this is less than the value $\bar{p} = .365 \times 10^{-4}$ for an optimum design, rib crippling will not be critical.

For $E = 4.65 \times 10^5$ psi.,

$$p = 0.234 \times 10^{-4} \times 4.65 \times 10^5 = 10.9 \text{ psi.}$$

$$\frac{t}{R} = \sqrt{\frac{\bar{p}}{c_0 \gamma}} = \sqrt{\frac{0.234 \times 10^{-4}}{1.225 \times 3.26}} = 2.42 \times 10^{-3}$$

$$t = 20 \times 2.42 \times 10^{-3} = \underline{0.0484 \text{ in.}}$$

$$d = \delta t = 4.66 \times 0.0484 = \underline{0.226 \text{ in.}}$$

$$h^2 = \epsilon R t = 2 \times 20 \times 0.0484 = 1.94$$

$$h = 1.39 \text{ in. , } a = \frac{2}{\sqrt{3}} h = \underline{1.60 \text{ in.}}$$

Calculation of Geodesic Stiffened Configuration No. 3 - Since the general instability coefficients $C^* = 0.348$ and 0.377 obtained for tests #1-G and #2-G lie considerably below the "classical" value $C^* = c_o/2 = 0.6125$ the tables for α , δ , γ , η , \bar{p} and β were reworked assuming $c_o/2 = 0.4$. These values are shown in the table in Part II.

Specimen Design -

α	δ	γ	η	$\bar{p} \times 10^6$	β
.10	7.03	5.09	.576	11.38	72.02

Selecting the rib thickness $b = .0153$ in. and substituting in the previously developed formula:

$$\frac{\bar{p} \epsilon^3}{c_2} = \left(\frac{b\beta}{R}\right)^4 = \left(\frac{0.0153 \times 72.02}{20.0}\right)^2 = 0.0925 \times 10^{-4}$$

For $c_2 = 7.4$, $\epsilon = 2.0$,

$$\bar{p} = \frac{7.4}{8} \times 0.0925 \times 10^{-4} = 8.67 \times 10^{-6} < 11.38 \times 10^{-6}$$

$$\frac{t}{R} = \sqrt{\frac{\bar{p}}{c_o \gamma}} = \sqrt{\frac{8.67 \times 10^{-6}}{0.8 \times 5.09}} = 1.46 \times 10^{-3}$$

$$t = 20 \times 1.46 \times 10^{-3} = \underline{0.0292} \text{ in.}$$

$$d = \delta t = 7.03 \times 0.0292 = \underline{0.205} \text{ in.}$$

$$h^2 = \epsilon R t = 2 \times 20 \times 0.0292 = 1.170$$

$$h = 1.082 \text{ in.}, \quad a = \frac{2}{\sqrt{3}} h = \underline{1.25} \text{ in.}$$

$$p = 8.67 \times 10^{-6} \times 0.465 \times 10^6 = \underline{4.03} \text{ psi.}$$

Stiffened Domes - Thermal Gradient Tests

The objective of the thermal gradient test plan was to apply a known temperature differential through the thickness of a geodesic and square-grid stiffened dome and test to failure by a uniform external pressure. This would assess the influence of thermal stresses upon the critical buckling pressure.

The two stiffened domes selected for test were the #2-G (geodesic dome) and the #1-SG (square-grid dome). The table below shows the recorded temperatures and their locations prior to failure.

Loc.	Temp - °F	Temp - °F
	#2-G	#1-SG
1	+ 59.5	+ 63.5
2	+ 58.5	+ 63.5
3	+ 54.5	+ 63.5
4	+ 54.5	+ 58.0
5	+ 45.0	+ 58.0
6		+ 58.0
7		+ 43.5
8		+ 45.5
9		+ 45.5
10		+ 46.0

Under the maximum thermal gradient of 14.5°F for the Geodesic dome, the buckling pressure recorded was 8.29 psi. For the square stiffened dome the maximum thermal gradient recorded was 17.5°F, and failure occurred at a pressure of 10.83 psi. In both tests the applied thermal gradient produced a higher buckling pressure than was previously recorded under the room temperature condition. Since the back up blocks for these tests were removed, the resulting large deformations at failure caused damage to the domes. When the domes became unstable and buckled, the material fractured and blew out leaving a hole. The holes occurred in areas that had buckled in the previous tests. The

holes can be seen in Figure 5.25. The thermocouple locations are shown schematically in Figure 5.26. The external pressure versus radial deflection data just prior to buckling, for the two domes are found in Figure 5.28 and the location of the displacement transducers are illustrated in Figure 5.27. There was a definite change in the deflection mode from the room temperature tests reported previously.

The buckling pressures previously recorded for the #2 Geodesic dome and the #1 Square-Grid Stiffened dome for the room temperature condition were 6.54 psi and 9.48 psi respectively. This corresponds with the experimental buckling pressures of 8.29 psi and 10.83 psi with the additional condition of a thermal gradient. This apparent increase in the buckling pressure may be attributed to the difference between the coefficient of thermal expansion and soak temperature between the shell and the support ring which introduced a relieving tensile load in the shell.

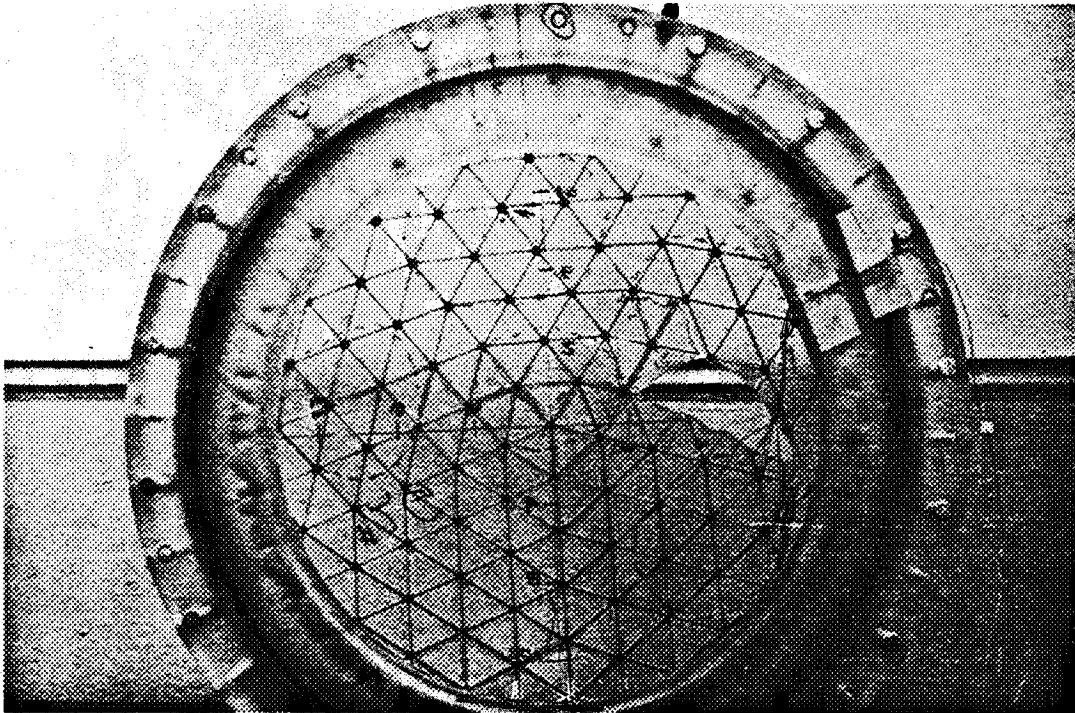
Metal Dome Testing

Fabrication of Dome

The geometric shape of the monocoque aluminum dome selected for test was a spherical cap with a half-opening angle $\theta = 60^\circ$ with a radius $R = 27.3$ inches. The basic material selected for fabrication of the spherically shaped dome was 2014-T6, in sheet size of 70 x 70 inches with a thickness of 3/4 inch. By a hot spinning process, the material was formed over steel mandrels in four successive passes at temperatures estimated to be between 500°F - 600°F. This hot forming process had an annealing effect such that coupons cut from the formed dome material had yield properties much less than that of the initial 2014-T6 material. The compressive and tensile stress strain curves in both the hoop and meridional direction is shown in Figure 5.29.

The dome was not heat treated after forming because of the possible detrimental effect of shape variation. While the dome was on the mandrel, the dome was machined to the required overall thickness of .200 inches. Measurements taken at random locations showed the tolerance to be within $\pm .002$ of the desired thickness. It was estimated that some of the residual stresses caused by the forming technique were removed during this machining process. The layout of the geodesic pattern was accomplished by dividing the pattern into five equal segments as shown in the working drawing in Figure 5.30. A fiberglass layup was formed on the concave surface of the metal dome and templates of both odd and even patterns were scribed on the fiberglass surface. This fiberglass liner was used to guide the hand router both in depth and contour. (Figure 5.31)

Based upon the geometry of the stiffening pattern and the quantity of only one dome, hand routing was selected as the fabrication method instead of numerically controlled machining or chemical milling which necessitates leaving large corner radii. To prevent the dome specimen from "popping out" into the router during machining, the dome was held in a handling fixture that was vacuum chucked to the dome. Figure 5.36 shows the machining setup.



FAILURE OF GEODESIC DOME (NO. 2-6) –
THERMAL GRADIENT TEST

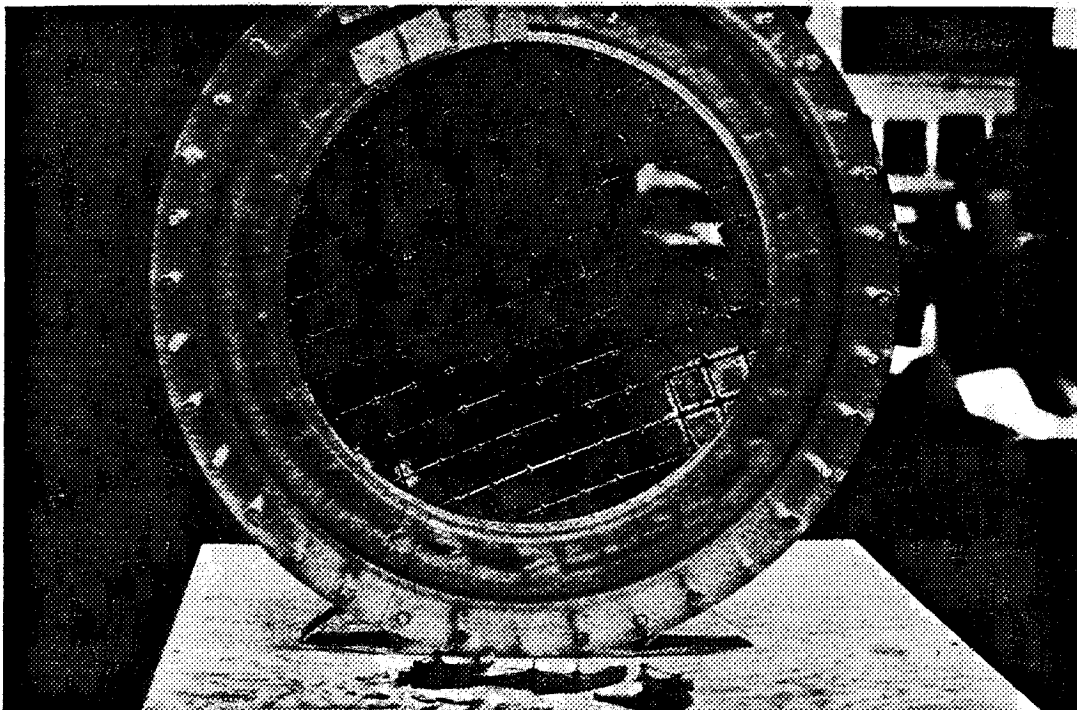
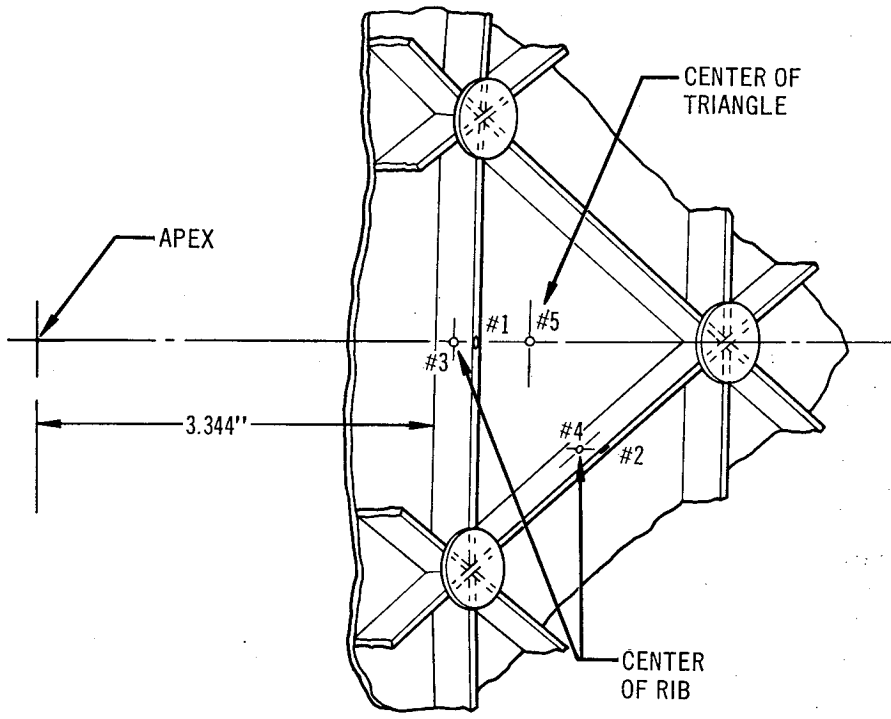


FIGURE 5.25 FAILURE OF SQUARE-GRID DOME (NO. 1-SG) –
THERMAL GRADIENT TEST



THERMOCOUPLE LOCATION
ON GEODESIC DOME (NO. 2-G)

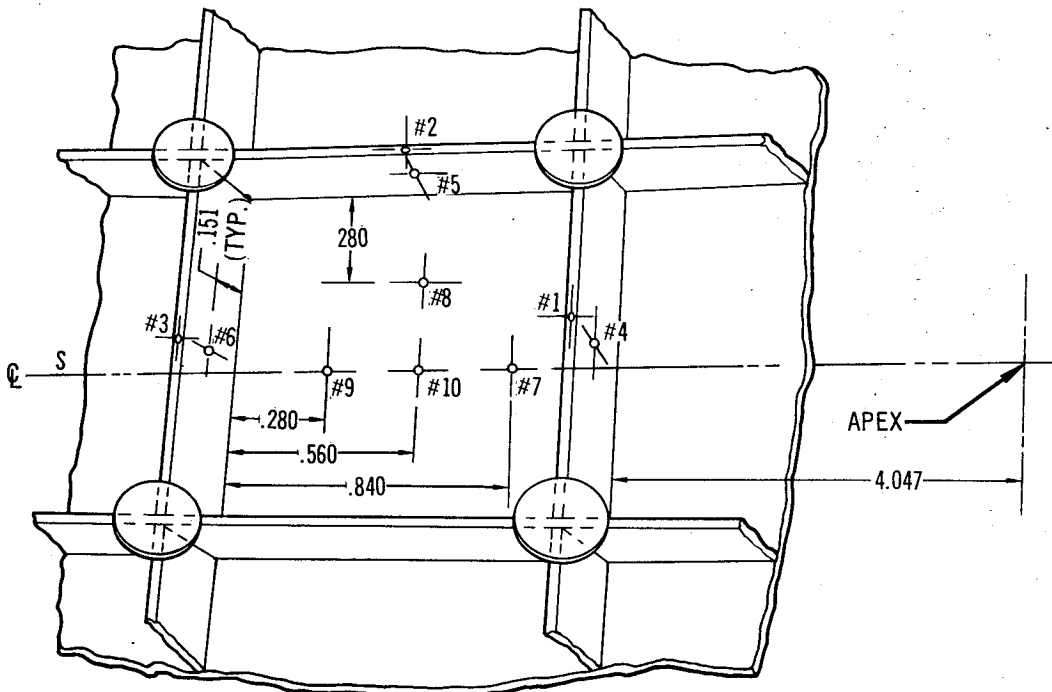
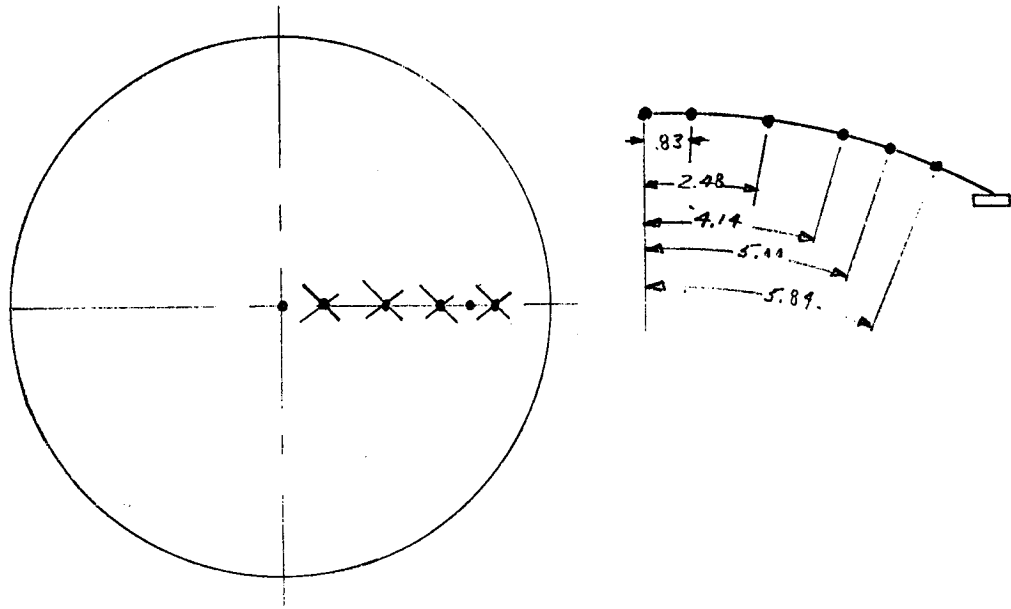


FIGURE 5.26 THERMOCOUPLE LOCATION ON
SQUARE STIFFENED DOME (NO. 1-SG)

#1-S SQUARE STIFFENED DOME



#2-G GEODESIC DOME

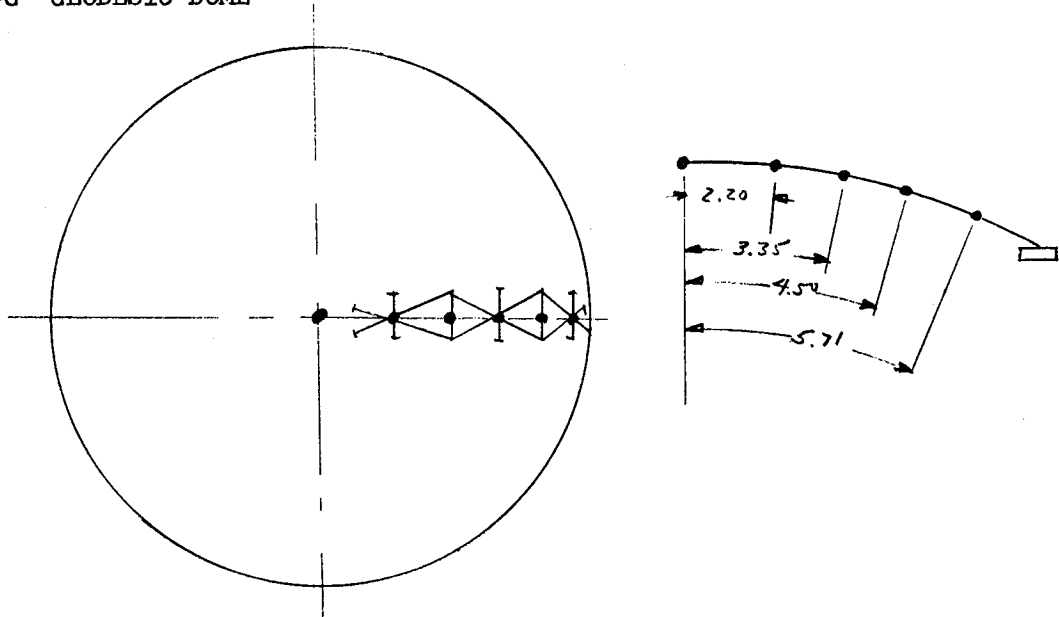


FIGURE 5.27

LOCATION OF DISPLACEMENT TRANSDUCERS ON #1-S AND #2-G SQUARE AND GEODESIC DOMES FOR COLD TEST

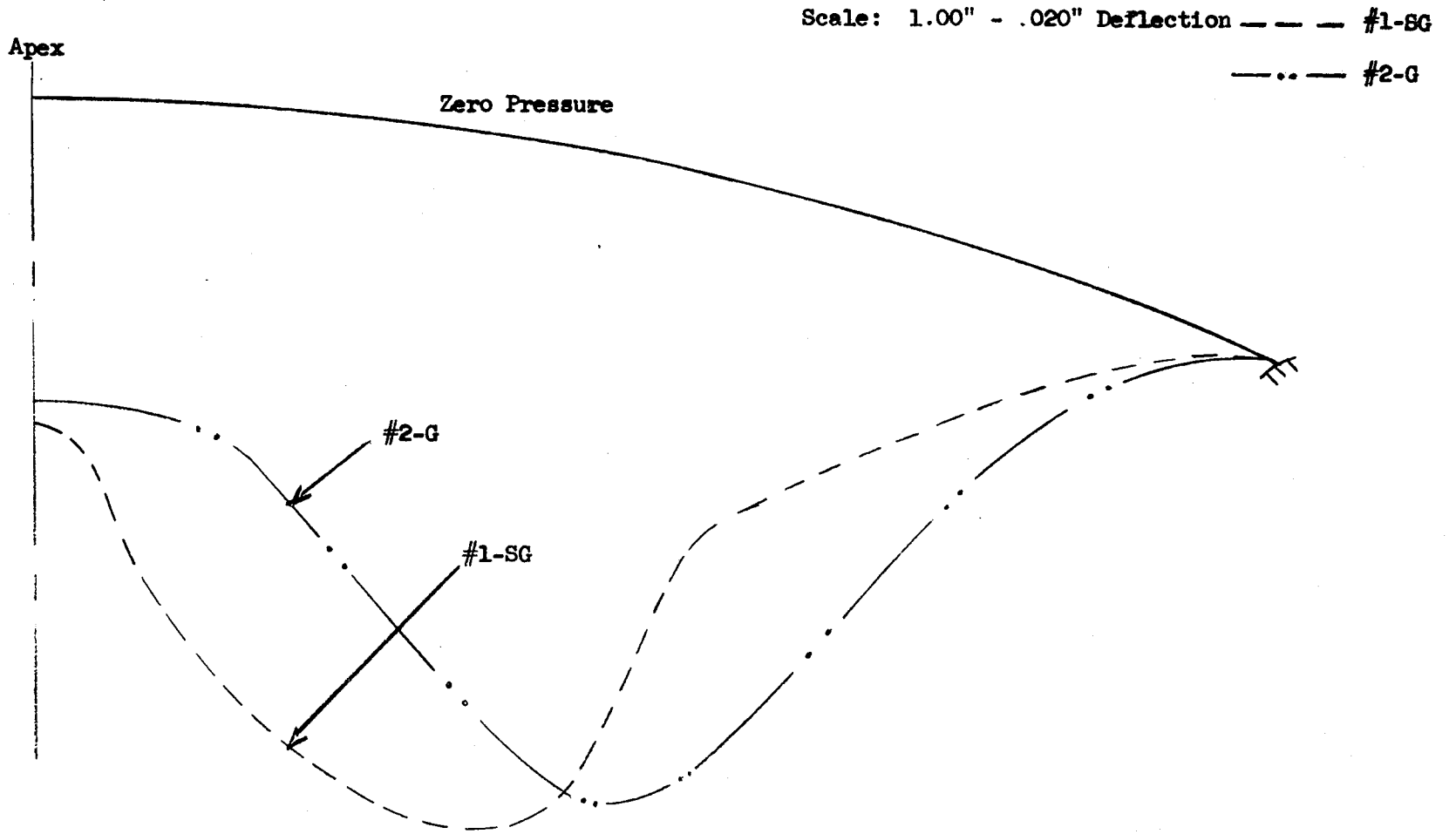


Figure 5.28 - Radial Deflection at Buckling Pressure Thermal Gradient Tests

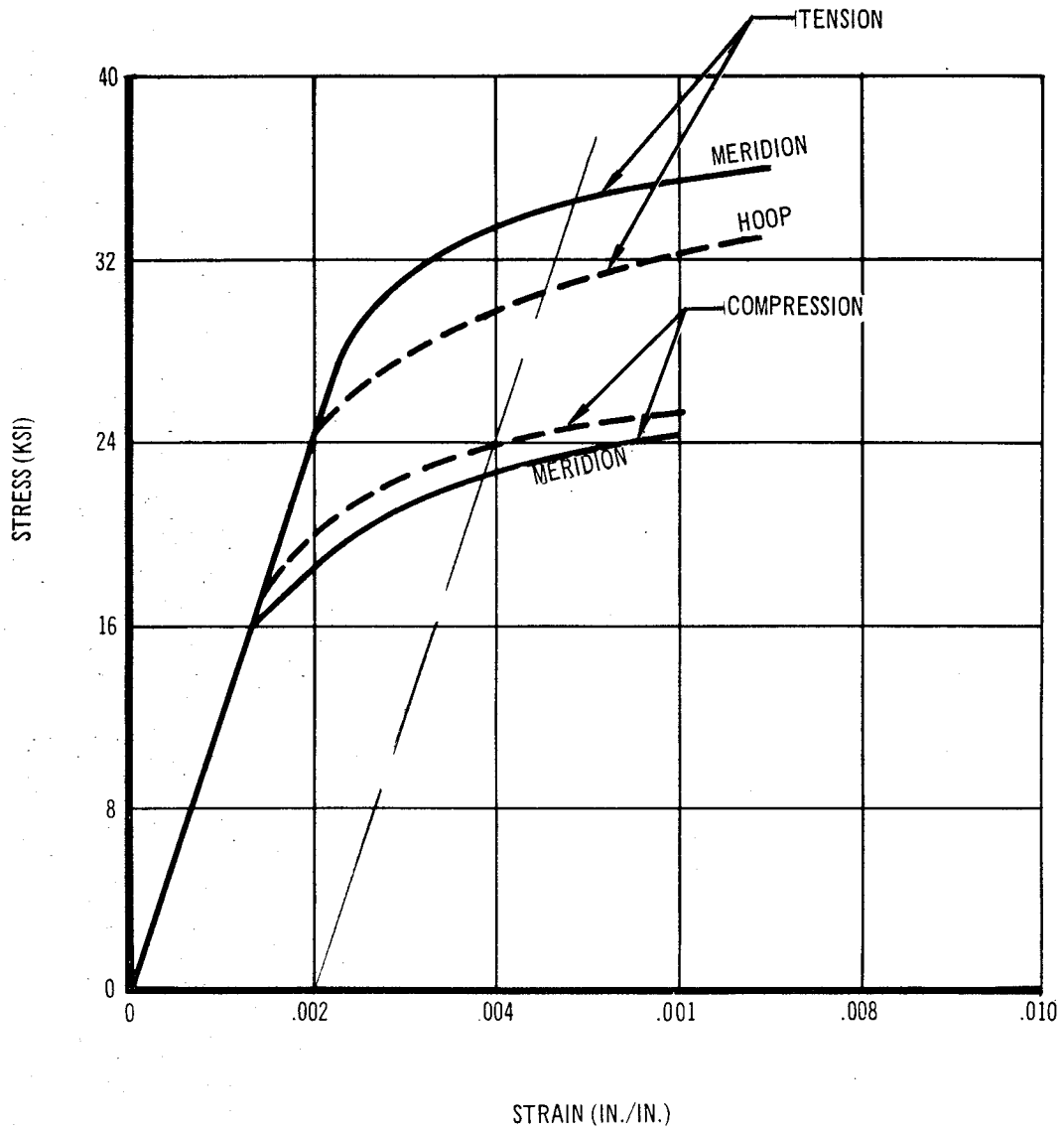


FIGURE 5.29 STRESS – STRAIN DIAGRAM FOR
ALUMINUM GEODESIC DOME
MAT'L 2014

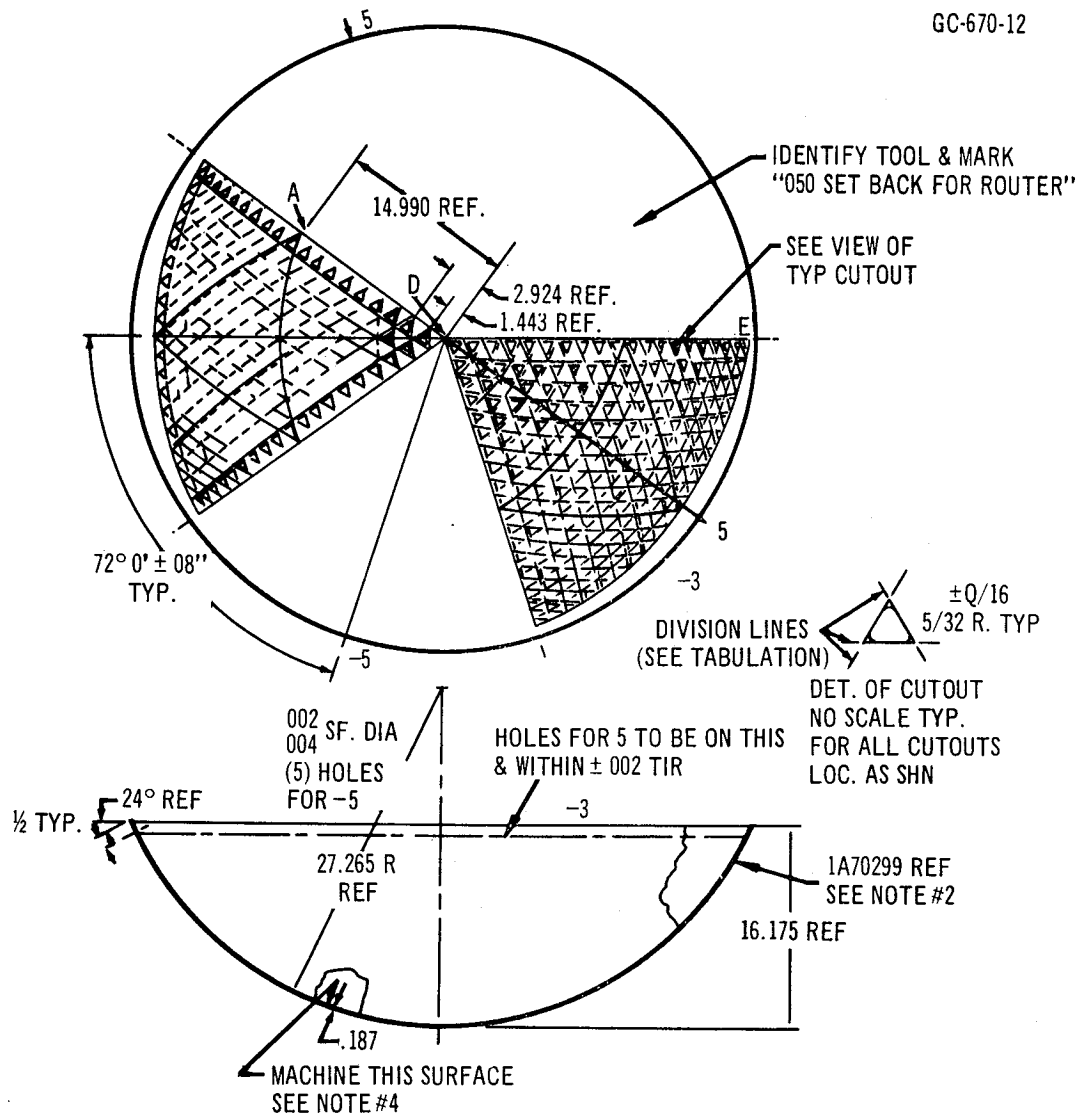


FIGURE 5.30 WORKING DRAWING OF GEODESIC
DOME LAYUP

As a result of machining difficulties encountered in the program to maintain the committed close tolerances and schedule, accurate machining was restricted to a circular area of approximately 20 inches in diameter. The remaining surface area was machined but not brought down to the specified tolerances. This overstrength region served as a support for the representative region.

Test Set-Up

The aluminum dome was mounted in a heavy steel base ring 4 inches thick with a 2 inch deep circular trough machined in the ring. The test specimen was seated into this trough and then filled with Cero-bend (low temperature melting alloy). This clamped boundary condition duplicated the edge fixity arrangement used for the plastic dome specimens. The base ring was then mounted on the pressure vessel fixture that allowed a maximum clearance between the test dome and the fixture of approximately 2 inches at the apex. This volume was filled with oil and the entrapped air was bled out. With the machined concave surface of the dome in the exposed position, the entire assembly was mounted on a supporting ground stand. This experimental arrangement is shown in Figure 5.32.

Test Procedure

The pressurization of the dome was accomplished by applying pressure on the convex surface of the dome slowly until a failure occurred. Pressure was accurately monitored by two pressure transducers that were automatically recorded with the other instrumentation on a continuous oscillograph recording. As a visual aid in estimating pressure, a calibrated hydraulic gage was mounted on the dome base ring. Single strain gages were located at 7 points within the predicted failure region on the stiffening ribs on the concave surface. Rosette strain gages were applied to a typical panel back to back so that bending effects could be recorded. Six deflectometers were bonded normal to the concave surface of the rib junctures to record the shapes of the surface under the applied pressure. The location of the instrumentation is shown in Figure 5.33.

Specimen Design

The rib dimensions of the small scale metal test dome is considerably off-optimum due to limitations of rib thickness and allowable yield stress in the metal. The method of fabrication requires two alternate templates to guide the routing tool which removes the material between the ribs. Template tolerances of 1/64" result in ribs not thinner than 1/10" in width for reasonable dimensional control.

Larger domes fabricated from sectors stretch formed, welded and program machined could be made closer to optimum dimensions with improved material properties. Efficiencies of such domes would more closely

approach ideal values.

With a choice of rib width, $b = 0.10''$ and a β value of 15.30 corresponding to $\alpha = 0.31$ and assuming that the general instability buckling coefficient is that obtained by the geodesic plastic domes ($c_o = .80$), one obtains from the tables in part II for $\epsilon = 2.0$

α	δ	γ	η	β
0.31	4.43	6.06	0.782	15.30

$$\left(\frac{b\beta}{R}\right)^4 = \left(\frac{.10 \times 15.3}{27.3}\right)^4 = 0.0990 \times 10^{-4} = \frac{\bar{p} \epsilon^3}{c_2}$$

$$\bar{p} = \frac{7.4}{8} \times 0.0990 \times 10^{-4} = 0.916 \times 10^{-5}$$

$$p = 9.16 \times 10^{-6} \times 10.3 \times 10^6 = \underline{94.3 \text{ psi.}}$$

$$\frac{t}{R} = \frac{\bar{p}}{c_o \gamma} = \frac{9.16 \times 10^{-6}}{0.8 \times 6.06} = 1.375 \times 10^{-6}$$

$$t = 27.3 \times 1.375 \times 10^{-3} = \underline{0.0375 \text{ in.}}$$

$$d = \delta t = 4.43 \times 0.0375 = \underline{0.166 \text{ in.}}$$

$$h^2 = \epsilon R t = 2 \times 27.3 \times 0.0375 = 2.045$$

$$h = \underline{1.43 \text{ in.}}, \quad a = \frac{2}{\sqrt{3}} h = \underline{1.65 \text{ in.}}$$

The predicted buckling stress in the plate is:

$$p = \frac{1}{1 + \alpha} \frac{pR}{2t} = \frac{1}{1.31} \frac{94.3 \times 27.3}{2 \times 0.0375} = \underline{26,200 \text{ psi.}}$$

Test Results

Failure of the dome occurred within the predicted region at a pressure of 62.2 psi. The failed dome shown in Figure 5.34, depicts a buckle that is approximately 12 inches in diameter and 4 to 5 inches in depth. Upon inversion of the dome for inspection purposes, a series of dimples had formed between many of the equilateral triangles at the failing pressure (Figure 5.34). The instrumentation data recorded is reduced and is shown for pressures of 20.6, 40.6, and 62.2 psi (just prior to failure) in the table below.

Strain Gage Readings Stress - Psi

P	S-1	S-2	S-3	S-4	S-5	Max. Norm.	
						Outer S-14	Inner S-17
20.6	4460	5170	4090	3890	3880	4875	4405
40.6	9160	10220	7700	7670	7540	9035	8544
62.2	15660	16360	12150	11680	10550	13850	11950

Deflection Readings - Inches

P	D-21	D-22	D-23	D-24	D-25	D-26
20.6	.013	.013	.013	.013	.013	.013
40.6	.025	.025	.024	.025	.026	.025
62.2	.042	.041	.038	.041	.043	.041

The buckling coefficient for this dome at the failing pressure was calculated to be $c_0 = 0.52$. This was much less than the classical buckling coefficient of $c_0 = 1.225$, and less than the results obtained for the plastic dome specimens where $c_0 = .70$. It is suspected that the lower buckling coefficient is attributed to the high stresses developed in the plate prior to failure as shown in the table of the strain gage readings. A comparison of the maximum recorded stresses, to that of Figure 5.29, indicates that failure occurred very close to the proportional limit of the material, thus introducing a plastic reduction factor in the stability equation. It is also suspected that the residual stresses inherently built into the dome during fabrication coupled with the high induced pressure stresses, combine to produce higher plastic stresses than indicated in the recorded stresses.

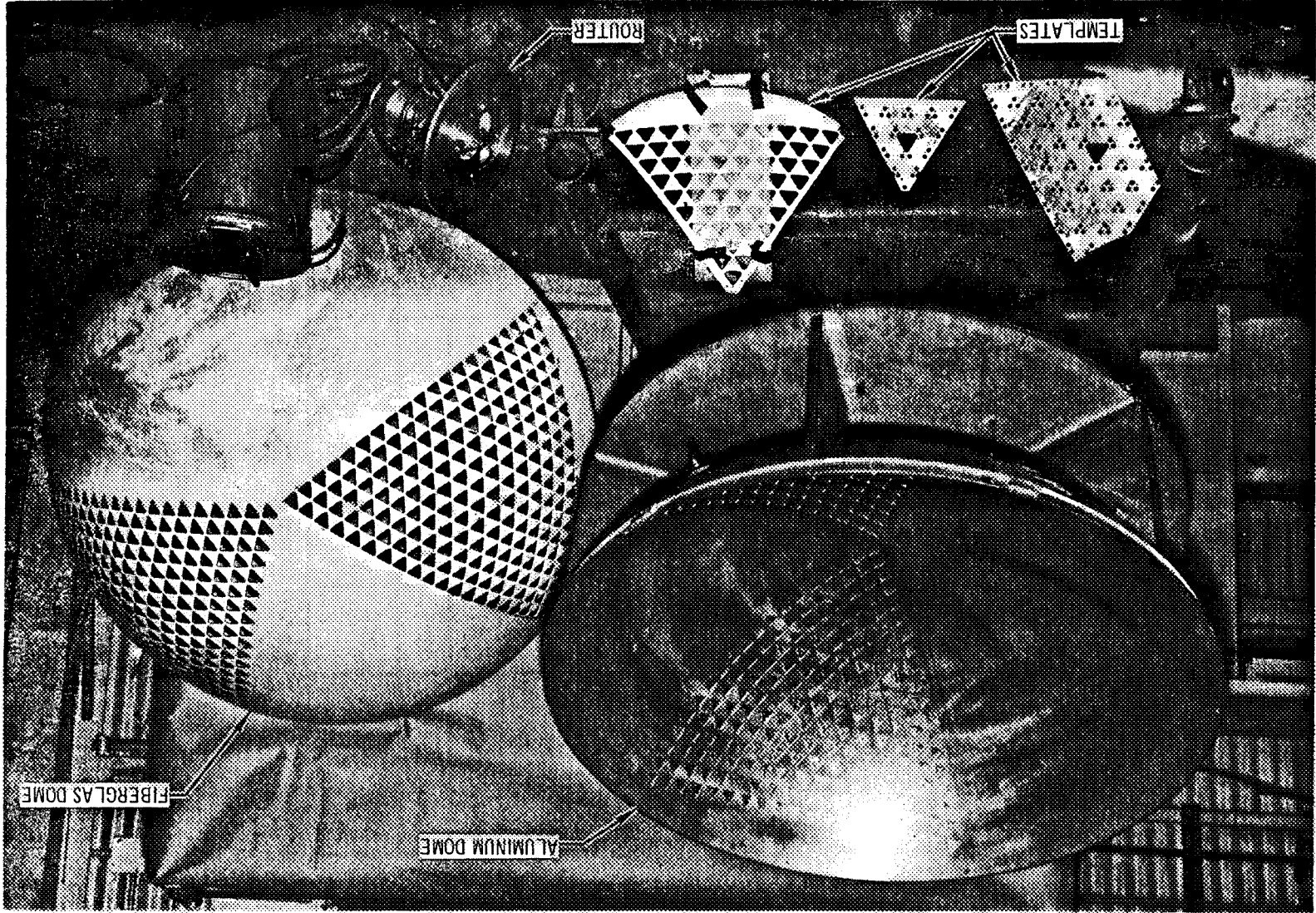


FIGURE 5.31 FABRICATION OF ALUMINUM GEODESIC DOME

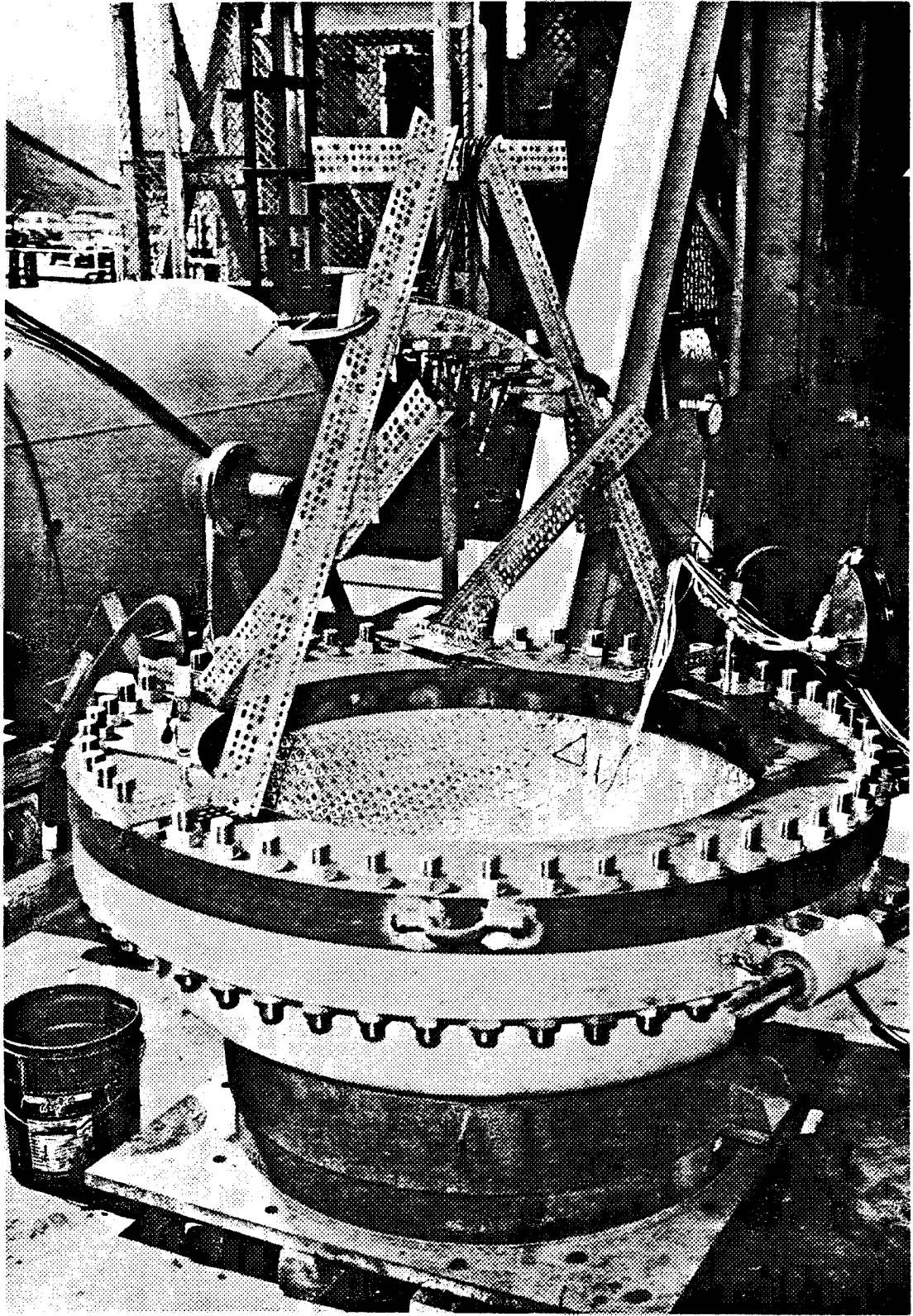


FIGURE 5.32 EXPERIMENTAL ARRANGEMENT FOR ALUMINUM GEODESIC DOME

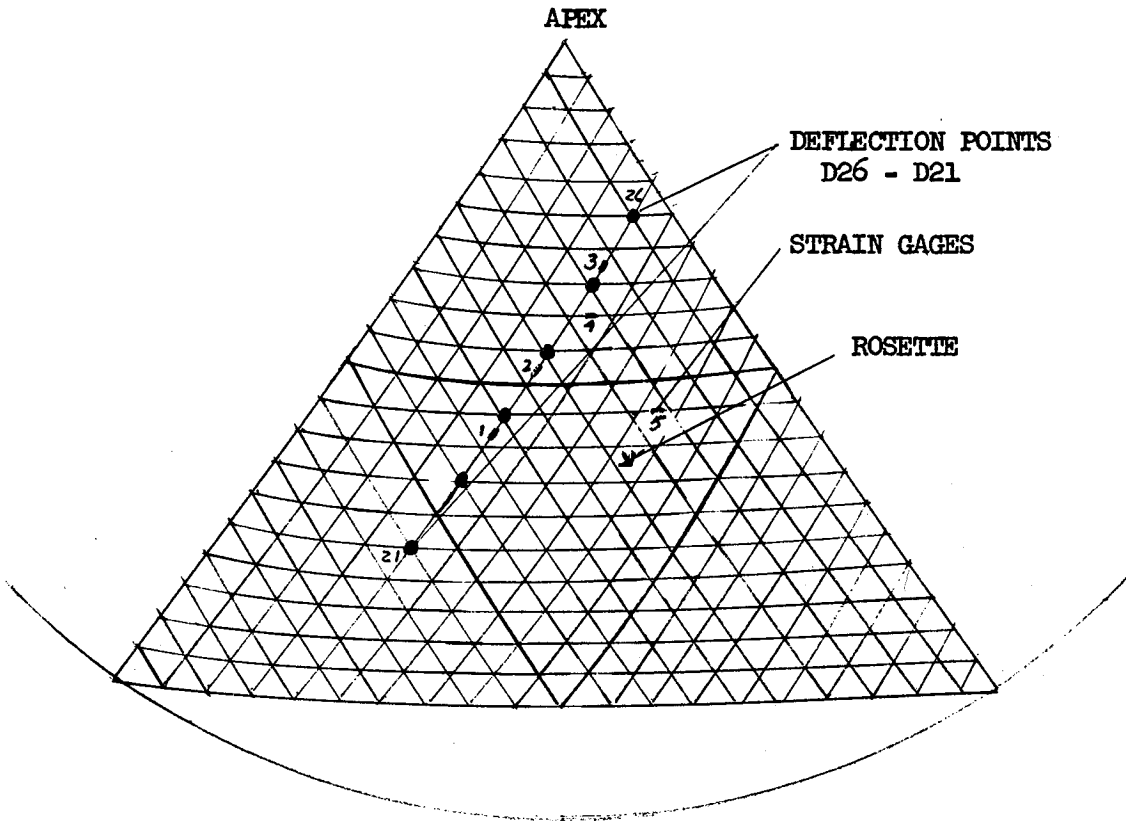
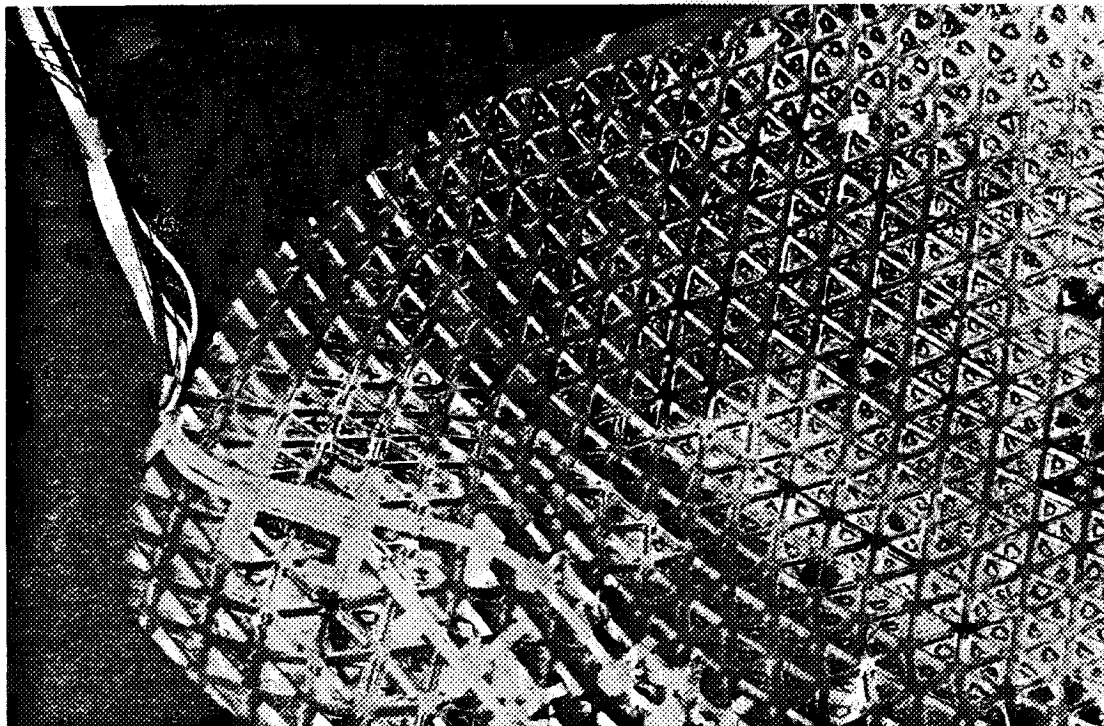


FIGURE 5.33 - LOCATION OF INSTRUMENTATION



FAILURE OF ALUMINUM GEODESIC DOME

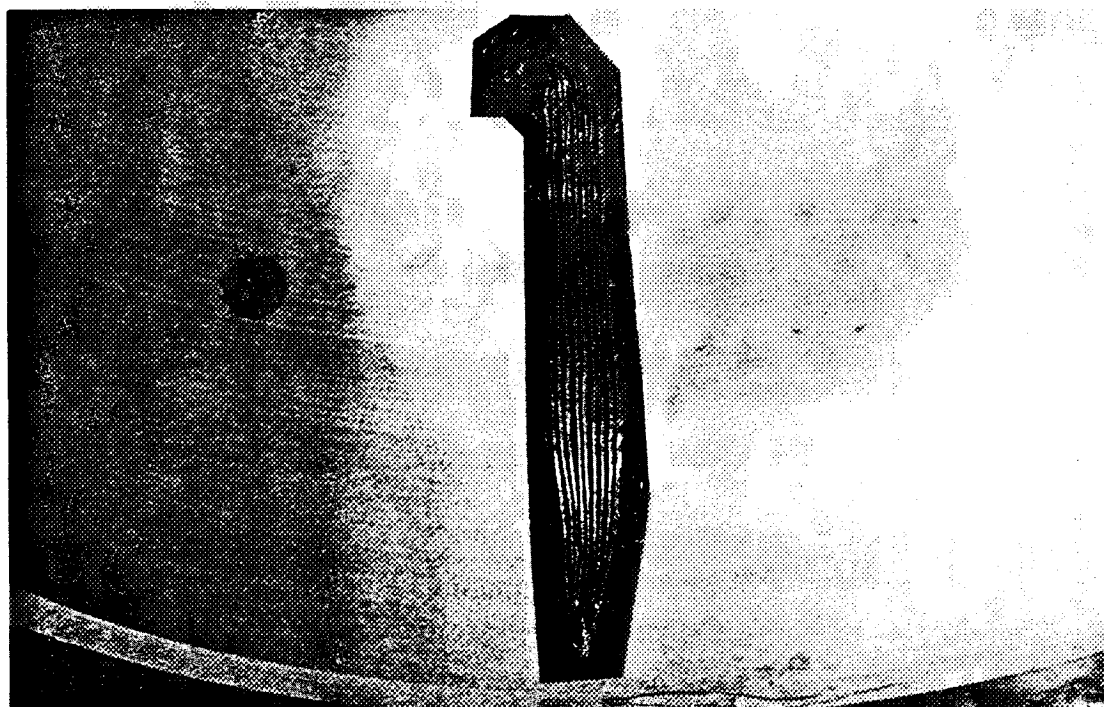


FIGURE 5.34 FAILURE OF ALUMINUM GEODESIC DOME
(REVERSE SIDE)

REFERENCES

1. Zoelly, R., Ueber ein Knickungsproblem an der Kugelschale Dissertation, Zurich, Techn. Hochschule, 1915.
2. Van der Neut, A., De Elastische Stabiliteit van den Dunwandigen Bol. Dissertation, Delft. 1932.
3. Donnell, L. H., A New Theory for the Buckling of Thin Cylinders Under Axial Compression and Bending. Trans. American Society Mech. Engineers, 56, November 1934.
4. Karman, Th. von and Tsien, H. S., The Buckling of Thin Cylindrical Shells Under Axial Compression, Journal Aeronautical Science, 1941.
5. Grigolyuk, E. I., On the Unsymmetrical Snapping of Shells of Revolution, Proc. of the I.U.T.A.M. on the Theory of Thin Elastic Shells. North Holland Publishing Co., 1960.
6. Parmerter, R. R., The Buckling of Clamped Shallow Spherical Shells Under Uniform Pressure. Ph.D. Thesis, California Institute of Technology, 1964.
7. Huang, N. C., Unsymmetrical Buckling of Thin Shallow Spherical Shells, TR Report No. 15, 1963.
8. Mushtari, Kh. M. and Galimov, K. Z., Non-Linear Theory of Thin Elastic Shells, 1957.
9. Homewood, R. H., Brine, A. C. and Johnson, A. E., Buckling Instability of Monocoque Shells, SESA Paper No. 547, Vol. 18, No. 1, 1961.
10. Kaplan, A. and Fung, Y. C., A Non-Linear Theory of Bending and Buckling of Thin Elastic Shallow Shells, NASA, TN-3212, 1954.
11. Bellinfante, R. J., Buckling of Spherical Caps Under Uniform External Pressure, Douglas Aircraft Co., Report No. SM-38938, 1962.
12. Kloppel and Jungbluth, Beitrag zum Durchschlagproblem Dunnwandiger Kugelschalen, Stahbau 22 (1953 H. 6S. 121/130).
13. Goerner, E., Buckling Characteristics of Spherical or Spherically-Dished Shells, ABMA, Report No. IR 9, 1956.
14. Dschou, D. D., Compressive Strength of Stiffened Cylindrical Shells, AFF Trans. 311, 1936.
15. Kloppel, K. and Roos, E., Contributions to the Problems of the Breakdown of Thin-Walled Reinforced and Unreinforced Spherical Shells for Full Load Conditions and for Conditions Under Which Only One-Half of the Shell is Loaded, Stahlbau, March 1956.

REFERENCES (Con't)

16. Ebner, H., Angenaherte Bestimmung der Tragfahigkeit Radial Versteifter Kugelschalen unter Druckbelastung, in the Symposium on "The Theory of Thin Elastic Shells," 1960, North Holland Publishing Co.
17. Krenzke, M. A. and Kiernan, T. J., Tests of Stiffened and Unstiffened Machined Spherical Shells Under External Hydrostatic Pressure, David Taylor Model Basin Report 1741, August 1963.
18. Shanley, F. R., Weight-Strength Analysis of Aircraft Structures, Dover Publications, Inc., New York.
19. Gerard and Becker, Handbook of Structural Stability, Part III - Buckling of Curved Plates and Shells, NACA TN-3783, 1957.
20. Timoskenko, S., Theory of Elastic Stability. Engineering Societies Monograph, McGraw-Hill Book Company, Inc., New York City, N.Y., 1936.
21. Adachi, J. and Benicek, M., Buckling of Torispherical Shells Under Internal Pressure, SESA Paper No. 884, May 1964.
22. Meyer, R. R., Discontinuity Stresses in Shells, Douglas Aircraft, Inc., Report No. SM-35652, 1959.
23. Crawford, R. F. and Schwartz, D. B., Preliminary Draft, issued November 1963, Martin Co., Baltimore, Md.
24. Krenzke, The Elastic Buckling Strength of Near Perfect Deep Spherical Shells with Ideal Boundaries, David Taylor Model Basin Report 1713, July 1963.
25. Seide, P., Weingarten, V. I. and Morgan, E. J., Final Report on the Development of Design Criteria for Elastic Stability of Thin Shell Structures, STL/TR-60-0000-19425, December 1960.
26. Little, W. A., Reliability of Shell Buckling Predictions Based Upon Experimental Analysis of Plastic Models, Paper presented during Engineering Mechanics Division Conference at MIT, April 1964.
27. Norris, C. H., Investigation of Strength and Buckling Characteristics of Transverse Bulkheads in Cylindrical Shells, MIT Contract No. DA 19-020-ORD-2800, July 1955.
28. Brady, M. S. and Goulet, W. J., Bulkhead Stability Tests, Eight Inch Diameter Monocoque Hemispheres and Spheroids, North American Aviation, Inc., Report No. SDL 361, January 1963.
29. Jones, E. O., The Effects of External Pressure on Thin-Shell Pressure Vessel Heads, ASME Paper No. 61-PET-10.

REFERENCES (Con't)

30. Evan-Iwanowski, R. M., Cheng, H. S. T. and Loo, T. C., Deformations and Stability of Spherical Shells Under Action of Concentrated Loads, TR-834
(1) No. 2, 1961.
31. Pflueger, Alf., Stabilitaetsprobleme der Elastostatik, Springer, Berlin, 1950.